DILATANCY: FURTHER STUDIES IN CRYSTALLINE ROCK

by

KATE HADLEY

SUBMITTED IN PARTIAL FULFILLMENT OF THE REQUIREMENTS FOR THE DEGREE OF DOCTOR OF PHILOSOPHY

at the

MASSACHUSETTS INSTITUTE OF TECHNOLOGY

September, 1975

Signature of Author _____
Department of Earth and Planetary Sciences

Certified by _____
Thesis Supervisor

Accepted by _____
Chairman, Departmental Committee on Graduate Students

DILATANCY: FURTHER STUDIES IN CRYSTALLINE ROCK

Kate Hadley

Submitted to the Department of Earth and Planetary Sciences on July 31, 1975 in partial fulfillment of the requirement for the degree of Doctor of Philosophy at the Massachusetts Institute of Technology.

ABSTRACT

When brittle rock is subjected to compressive loads dilatancy, an inelastic volume increase due to cracking, occurs. Even when the least and intermediate principal stresses are equal, the azimuthal distribution of dilatant cracks is not uniform. Anisotropy of dilatant strains and related properties in the plane perpendicular to the maximum stress may reach 100 percent or more at high stresses and generally exceeds 10-15 percent at stresses below the frictional strength of the rock. Dilatancy has previously been found under confining pressures up to 8 kbar. Preliminary investigations suggest that it can persist to temperatures in excess of 400°C. Dilatancy can therefore be expected under shallow to mid crustal conditions and its manifestations should be measurably anisotropic.

High differential stress is required to produce dilatancy during the first loading cycle of a rock. For granite and gabbro under less than about 2 kbar confining pressure this stress is in excess of the frictional strength. However, the application of cyclic loads reduces the minimum stress required for dilatancy in dry rocks at 500 bars confining pressure. At higher confining pressures, the effect of cyclic loading is uncertain. After repeated stress cycles at 5 kbar confining pressure dilatant volumetric strain persists at the level of a few parts in 10^4, but the minimum stress required to produce measurable dilatancy may increase, decrease or remain unchanged from its first cycle value. In some fracture zones, therefore, the kind of small scale dilatancy observed in the laboratory may not occur.

Where such microcrack dilatancy does occur, it can reduce seismic velocity ratios by a few percent per 10^{-3} dilatant volumetric strain if the region is dry. Decreases in seismic velocity ratio are difficult to generate in initially saturated rock even when pore pressures are low and strain rates reach 10^{-4}/sec. A liquid-vapor transition will not produce a significant drop in V_p/V_s.

Such results could not have been anticipated quantitatively with existing velocity theories due to a lack of knowledge of the geometry of dilatant cracks under stress.

Combining measured seismic velocities and dilatant strains with self-consistent models relating velocities to crack density it is found that the average aspect ratio of dilatant cracks increases with stress or dilatant porosity at an ever decreasing rate, reaching a maximum value of 2 to 3 parts in 10^3 at about 80 percent of the intact rock fracture strength.

Thesis supervisor: William F. Brace

Title: Professor of Geology

TABLE OF CONTENTS

TABLE OF TABLES

LIST OF FIGURES

Page

CHAPTER 1

CHAPTER 2

CHAPTER 3

CHAPTER 4

APPENDIX

INTRODUCTION

Dilatancy is a ubiquitous feature of rocks under stress and, as such, needs to be considered not only in theories of their mechanical behavior, but also in understanding how a wide range of physical properties of rock depend on differential load. One recent application has been to premonitory phenomena widely observed before earthquakes (Scholz et al., 1973). Two general models have been proposed to explain these precursors (Mjachkin et al., 1975); both depend on dilatancy. Yet little has been learned about dilatancy since it was first extensively described in crystalline rocks ten years ago (Brace et al., 1966). It has been frequently and somewhat indiscriminately applied to seismic problems, although the early laboratory work has never been extended above room temperature nor has the influence of major faults or stress cycling on the microcracking process been considered. The present study was undertaken to fill some of the gaps in our knowledge. Two basic questions were addressed: 1) over what range of conditions does dilatancy occur and 2) will dilatancy even in the laboratory, cause the premonitory effects ascribed to it. The particular effect we chose to look at was the decrease in seismic velocity ratio reported prior to some thrust-type earthquakes, because seismic velocity anomalies have received the most attention as earthquake precursors to date.

In the first 3 chapters which follow various aspects of the first question are explored; these are fundamental studies relevant to many geological problems. The specific effect of dilatancy on seismic velocities forms the subject matter of

chapters 4 and 5. We conclude with suggestions for future research. A few highlights of the present work are given below.

In the laboratory, dilatancy due to small scale cracking persists to 4 kbar in marble (Scholz, 1968a) and 8 kbar in granite (Brace et al., 1966) at room temperature. Some preliminary studies here extended this to 400°C at 2 kbar in granite. Therefore, dilatancy at least in the form of small microcracks can be expected at midcrustal depths. However, high shear stresses are required to produce measurable dilatancy in the laboratory. Supposing rocks were already faulted or had already been subjected to many stress cycles, would they still dilate before rupture?

In Chapter 1 it is shown that the differential stress required to induce dilatancy generally exceeds the stress at which sliding first occurs on any faults present when the confining pressure is less than about 2 kbar. The stress to cause dilatant volumetric strains of even 5×10^{-5} is on the order of kilobars.

Lack of a heat flow anomaly in seismic areas such as California seems to require stresses lower than this (Brune et al., 1969; Henyey and Wasserburg, 1971; Lachenbruch and Sass, 1973). Several mechanisms have been postulated to bring laboratory stresses down. In light of plate tectonics, rocks in seismic zones of the earth are thought to have experienced many cycles of stress, whereas laboratory experiments rarely involve more than 1. So one of the most attractive ideas is that the minimum differential stress for dilatancy, C' drops

after many cycles of stress. This has been recently confirmed by Scholz and Kranz (1974) and Haimson (1974) in uniaxial and low pressure triaxial experiments. Zoback and Byerlee (1975) however report no change in the stress required for dilatancy in cycling experiments at 0.5 and 2.0 kbar confining pressure. Chapter 2 of the present work represents an extension of Zoback and Byerlee's work to higher pressures, more rock types and more stress cycles. It was hoped that a trend in the value of C' would emerge with increased numbers of cycles. At 0.5 kbar confining pressure, a clear decrease in C' was observed after 20 cycles in most rock samples tested. At 1.5 and 5.0 kbar, trends were unclear owing probably to factors not carefully enough controlled in the experiments. On theoretical grounds (Martin, 1972) a slight decrease in C' might be expected simply because the amount of time spent under stress increases with each additional stress cycle. Yet for the very low frequency cycles found in the earth, healing processes might tend to push C' back up.

We also found (Chapter 2) that stress cycling has little effect on the amount of dilatant strain produced in a cycle. Thus, under nearly all conditions a dilatant volumetric strain of about 10^{-4} would have occurred were faults already present. This value is in accord with the most recent theoretical estimate (Brace, 1975) based on velocity and resistivity changes and the uplift actually observed before earthquakes, during the period when dilatancy is presumed to be taking place.

A characteristic feature of dilatancy is that the rock

becomes highly anisotropic (Brace et al., 1966). The exact form of the anisotropy is poorly understood, however, although the form is critical in a number of applications. For example, it seemed possible that even well below the fracture stress, the orientation of the eventual fault might in some way reveal itself by the detailed way in which expansion of the rock takes place. Fault orientation might therefore be predictable. Or, to determine how a seismic wave (Griggs et al., 1975) or an earth tide (Beaumont and Berger, 1975) traverses a dilatant zone the general form of the elastic stiffness tensor must be available.

It is usually assumed that dilatant strains are azimuthally symmetrical around the principal compression. Chapter 3 shows that this is not correct. Early in the stress history a strong anisotropy develops in directions normal to the principal compression. This anisotropy clearly reflects the future fault direction. The pseudo-elastic compliances are far from uniaxial; the variation of s_{iijj} in the plane normal to the maximum compression may reach 100 percent at high stress. Thus, calculations which assume spherical or cylindrical symmetry of the dilatant strain may be grossly inaccurate.

With this caution as to the possible magnitude of azimuthal anisotropies a series of measurements was undertaken to determine whether stress-induced cracking could produce a decrease in travel time ratio such as is sometimes observed in situ before thrust-type earthquakes. Although it is widely assumed that dilatancy is responsible for the field observations, various

combinations of dry, partially saturated or vapor-filled cracks have been postulated to account for the t_s/t_p decrease (Nur, 1972; Scholz et al., 1973; Whitcomb et al., 1973; Anderson and Whitcomb, 1975). Chapter 4 produces evidence that dry or vapor-filled cracks are the only likely candidates, the former being most probable. Simultaneous determination of strains and seismic velocities in triaxially loaded, water and CO_2 saturated rocks show that it is enormously difficult to cause V_p/V_s to decrease. Drops in V_p/V_s can only easily be generated in initially dry material. Such decreases are small, amounting at most to a few percent at dilatant volumetric strains of 10^{-3}.

In view of the complexity of seismic velocity measurement in triaxial experiments it would be convenient to have a theory which could predict seismic velocity from the degree of saturation, crack distribution and elastic moduli of the crack-free rock. Such theories exist for materials with isotropic crack distributions under hydrostatic pressure, most notably that of Toksöz et al.(1975). Chapter 5 looks at 2 existing isotropic theories, that of Toksöz et al. and the self-consistent model of O'Connell and Budiansky (1974). These formulations, constrained with new measurements of aspect ratio distributions in virgin granite, can accurately predict seismic velocities. However, neither one is sufficient to relate seismic velocities in dilatant rock to any measurable parameters. This stems from our continuing lack of knowledge about the details of dilatant crack growth rather than from any obvious failing in the

theories. Applying isotropic theory to a demonstrably anisotropic situation has its dangers, but if measurement paths are carefully selected the inverse problem can be worked, and information on the behavior of dilatant cracks with stress can be obtained from triaxial seismic velocity measurements. It is hoped that these results can one day be verified by means of direct scanning electron microscope observation of rock under stress and used to construct quantitative models of dilatant crack growth.

The 5 chapters are intended to be read as separate units. Each one has a general introduction to the problem, a section on experimental procedure, discussion of results and a conclusion or summary. Taken together, the chapters form a body of evidence which is generally in support of dilatancy as a mechanism for generating earthquake precursors. But beyond this, from detailed examination of the dilatant process new methods of exploiting dilatancy suggest themselves and new cautions as to its complexity arise.

CHAPTER 1

LABORATORY INVESTIGATION OF DILATANCY AND MOTION ON FAULT SURFACES AT LOW CONFINING PRESSURES

INTRODUCTION

Processes dependent upon dilatancy have recently been held responsible for certain premonitory effects of earthquakes (Nur, 1972; Scholz et al., 1973; Whitcomb et al., 1973). Comparison of laboratory measurements of both dilatancy (Brace et al., 1966) and friction (Byerlee, 1966; 1967) suggest, however, that the amount of dilatancy may be small or even zero at low confining pressure. A series of experiments was carried out to explore this possibility. In this note the results are reported and their implications for earthquake prediction discussed.

EXPERIMENTAL PROCEDURE

The first series of experiments involved determination of the stress-volumetric strain behavior. Right circular cylinders of San Marcos gabbro and Westerly granite about 2 cm in diameter and 4 cm long were jacketed in copper foil .05 mm thick. Strain gauges were attached axially and circumferentially (Brace, 1964). The rocks were axially stressed to near their compressive strength but unloaded before a violent stress drop occurred. The maximum axial stresses attained are plotted as filled circles in Figures 1-1 and 1-7. Stress-volumetric strain curves were computed for each rock by taking the sum of the measured axial and twice the measured circumferential strains.

Figure 1-1. Pressure dependence of fracture, sliding and dilatation stress (C') of Westerly Granite. Filled circles are from this study; open circles from Brace et al. (1966), Byerlee (1967), and Mogi (1966). Vertical bars are stress for sliding from this study; dashed-dot line is from Byerlee (1967).

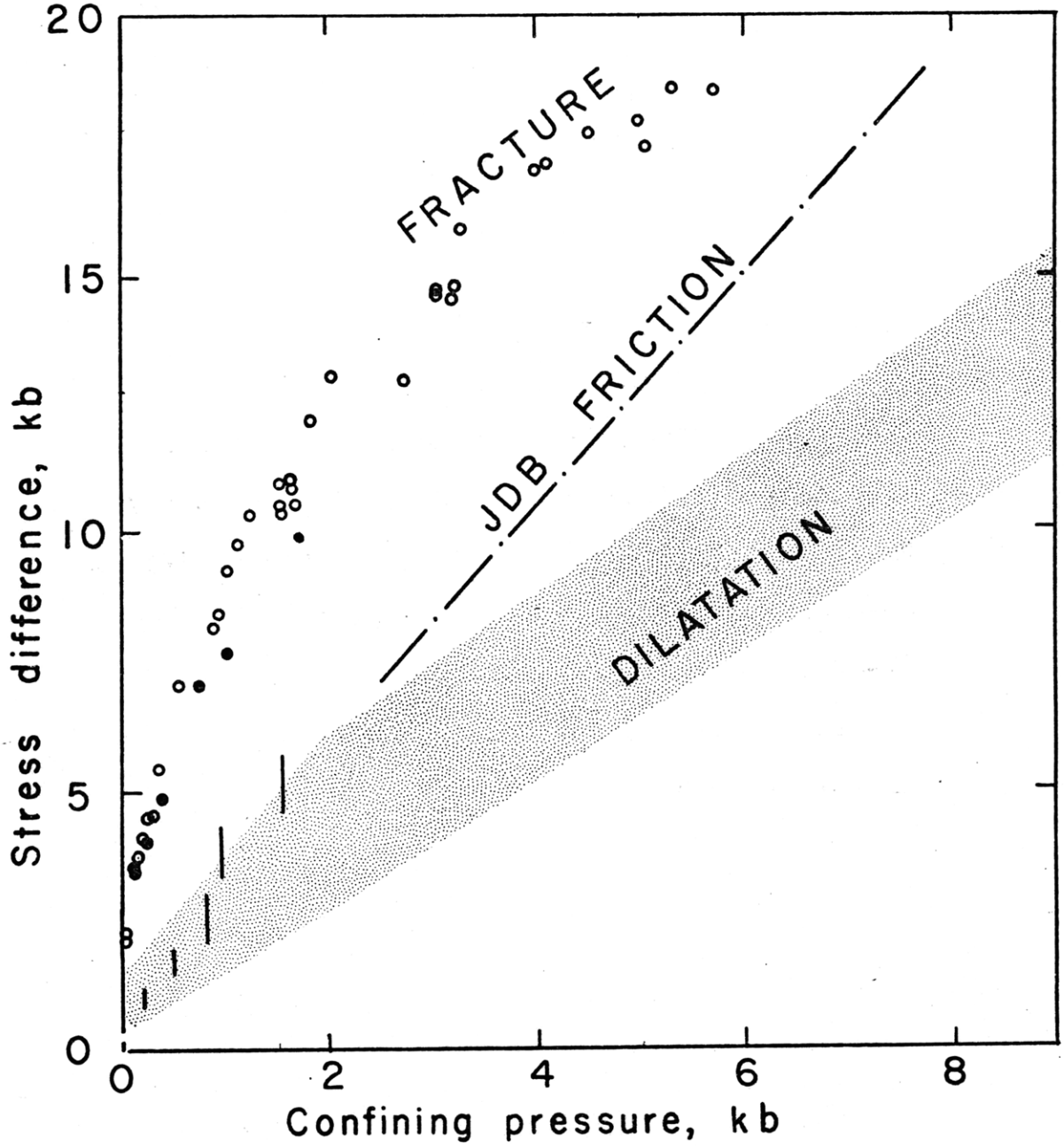
20
15
10
5
0
0
2
4
6
8
Stress difference, kb
Confining pressure, kb
FRACTURE
JDB FRICTION
DILATATION

The same samples were reused for the sliding tests. For these experiments, the strain gauge leads and one of the copper jacket end caps were removed. With the jacket otherwise intact, the samples were encased in polyurethane tubing and the ends sealed by clamping the tubing with wire to steel end pieces. Each specimen was faulted at the confining pressure for which its stress-strain curve had been obtained. The stress at failure was generally somewhat less than the maximum value reached in the stress-strain tests.

Three sliding stress determinations at different confining pressures were made on each sample. In all cases but one, the first value of confining pressure investigated was that at which the stress-strain curve of the sample had been obtained. Strain rates were nominally $2.5 \times 10^{-5} sec^{-1}$ and the confining pressure medium was argon gas.

RESULTS

For the granite, the initial curved portion of the stress-volumetric strain plot (Figure 1-2), associated with the closure of pre-existing cracks under applied load (Walsh, 1965b) is followed by a linear region. The point of departure from linear behavior as the load is increased, here called C', represents the stress at which axially-oriented cracks begin to grow in the sample (Brace et al., 1966; Scholz, 1968a). The volume increase due to these cavities, represented by the distance D' in Figure 1-2 will be referred to here as microcrack dilatancy.

Figure 1-2. Stress-volumetric strain relation for Westerly Granite. Distance D' represents microcrack dilatancy. C' is the axial stress at which the curve leaves the linear region.

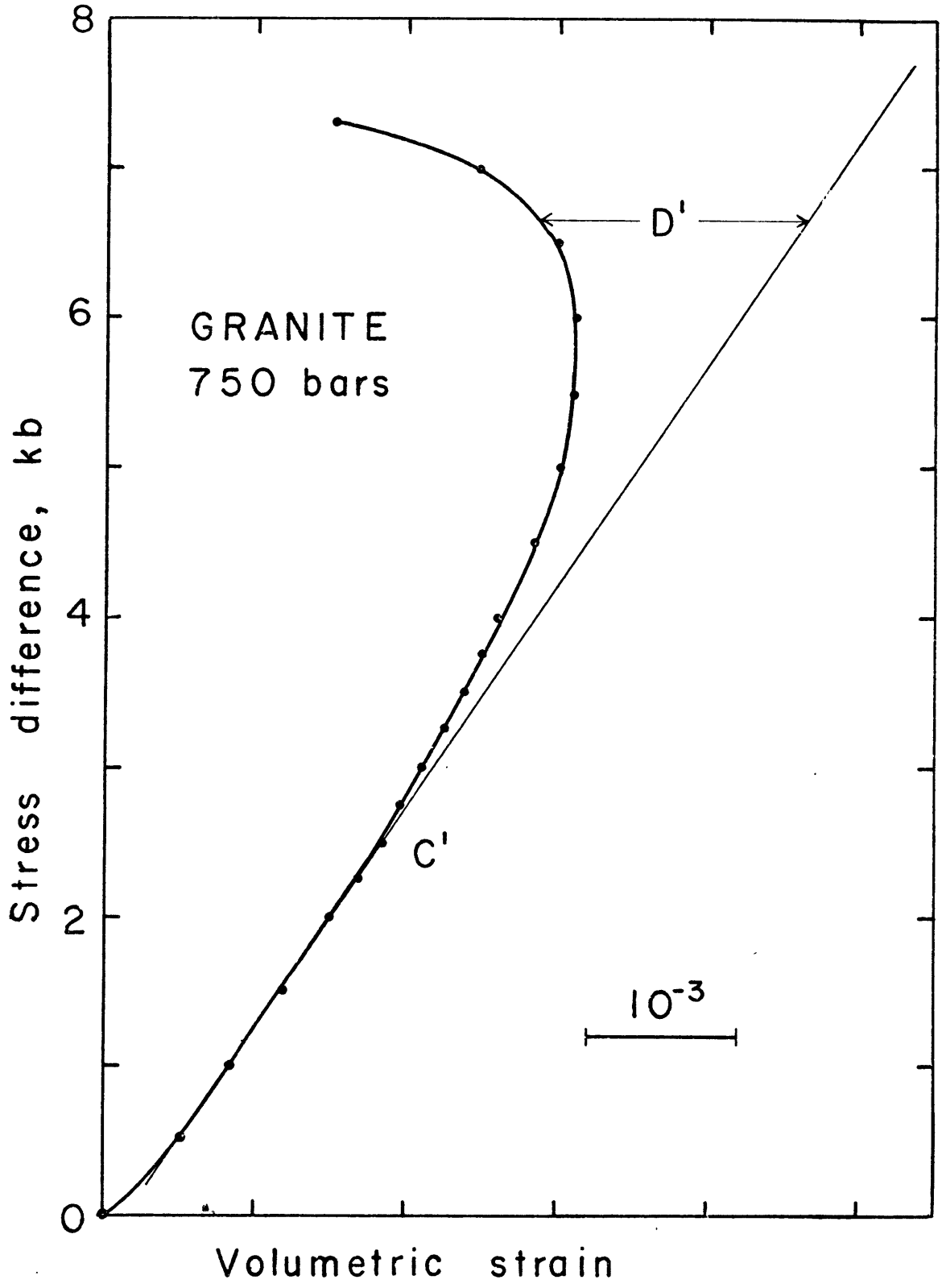
8
6
4
2
0
Stress difference, kb
GRANITE
750 bars
D'
C'
10^{-3}
Volumetric strain

The departure of the stress-volumetric strain curve from linearity is not abrupt, and C' could only be determined to within $\pm$ 100 bars. The variation in C' from sample to sample at any one confining pressure may be as much as 1 kbar for the granite, and twice that for the gabbro. The resolution of volumetric strain was 5×10^{-5}. Departures from linear elastic behavior smaller than this could have occurred at stress levels lower than the reported values (Figures 1-3 and 1-5).

For the gabbro, an additional complication arises in that the stress-volumetric strain curves generally exhibited two regions of linear behavior with distinct slopes. Consequently, two values for C' could have been assigned to any one sample. This ambiguity may arise because of the absence of a truly linear region for this pressure range, due perhaps to a bimodal distribution of crack shapes. For the purposes of this study, the lower value of C' was used, as the parameter of interest was the minimum stress for the onset of dilatancy at a given confining pressure.

No other determinations of C' were available for comparison with or extension of the gabbro data (Figure 1-5). For the granite, comparison with the data of Brace et al. (1966) suggests that the value of C' depends upon the strain rate at which experiments are conducted, lower values being associated with slower rates (Figure 1-3). Tests of Brace et al. using slow loading rates produced values of C' well below those obtained in this study, although agreement between the "fast" values and those of this study is good.

Figure 1-3. Pressure dependence of dilatancy of Westerly Granite. Filled symbols represent C'. Open symbols are stress associated with a dilatant volumetric strain of 10^{-3}. Lower solid line represents least value of C' as measured in this study. Shaded area bounds stress for onset of dilatancy as determined by Brace (1973) and Brace et al. (1966).

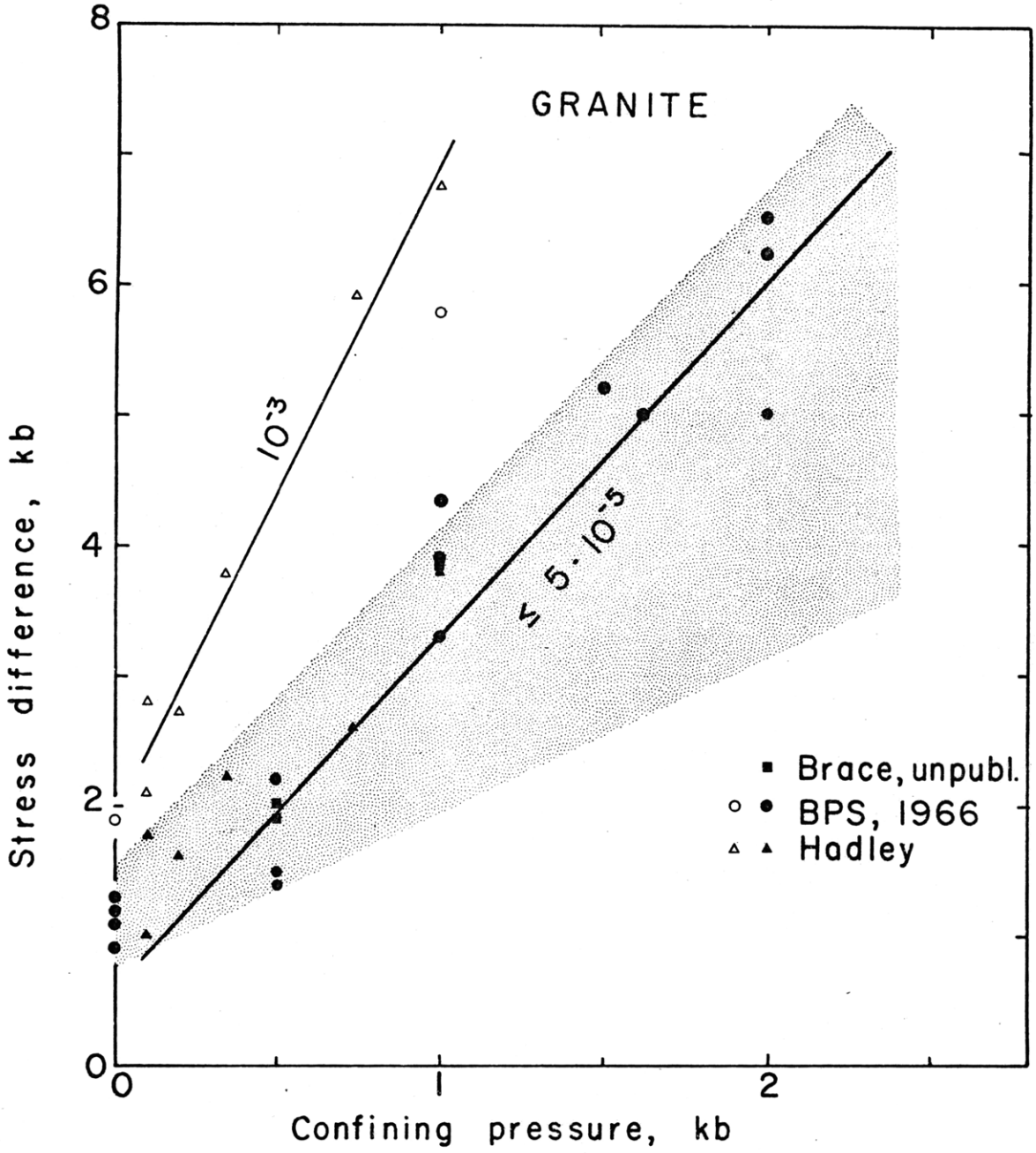
GRANITE
10-3
μ = 5 · 10-5
Brace, unpubl.
BPS, 1966
Hadley
Stress difference, kb
Confining pressure, kb
0
2
4
6
8
0
1
2

Figure 1-4. Pressure dependence of sliding stress of Westerly Granite. Diagonal line and stippled region are stress for onset of dilatancy as shown in Figure 1-3. Only that part of stippled region lying above the line in Figure 1-3 is reproduced here, as lower half of that region was defined by "slow" values of Brace et al. (1966).

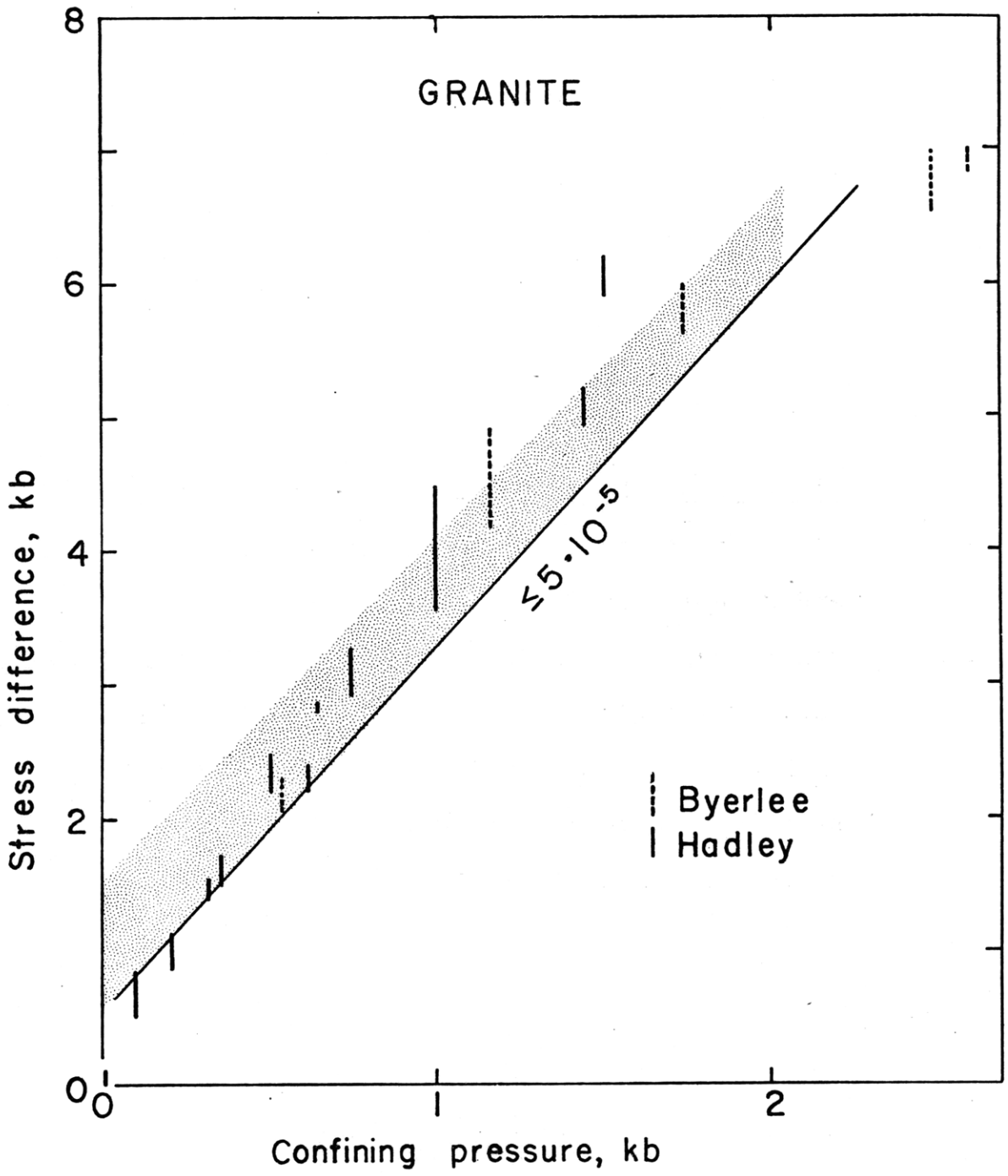
GRANITE
≤5·10⁻⁵
Byerlee
Hadley
Stress difference, kb
Confining pressure, kb
0
2
4
6
8
0
1
2

Sliding in all cases observed was stable, generally occurring over a small range of differential stress in any one sample, but with about a $\pm$ 15% variation from sample to sample at any particular confining pressure (Figures 1-4 and 1-6). The values reported from this study have not been corrected for change in contact area as sliding progressed, as this correction would have amounted to an increase of 5% or less in the stress. These new measurements of frictional stress also compare favorably with previous work (Figures 1-4 and 1-6) (Byerlee, 1966; 1967; 1973; Brace, 1973).

DISCUSSION

It is evident that below 2 kbar for the granite (Figure 1-1) and 0.5 kbar for the gabbro (Figure 1-7), the stress C' equals the frictional stress, within the rather large uncertainty in both measurements. Below these pressures, the amount of dilatancy in faulted rock is less than 5×10^{-5}, our level of detection. The maximum pressure, 2 kbar corresponds to a depth of 15 km, assuming hydrostatic pore fluid pressure. Since this is a region of major seismic activity, do the results of this study argue against dilatancy as being responsible for various premonitory effects as suggested by Nur (1972), Scholz et al. (1973) or Whitcomb et al. (1973)?

Firstly, it is not entirely clear how much dilatant strain is required to account for the observed precursory effects. Dilatant volumetric strain of less than 5×10^{-5} may be sufficient to account for many of them, although the work of

Figure 1-5. Pressure dependence of dilatancy of San Marcos Gabbro. Filled triangles represent C'. Open symbols are stress associated with a dilatant volumetric strain of 10^{-3}. Lower solid line represents least value of C'. Shaded area shows region of onset of dilatancy.

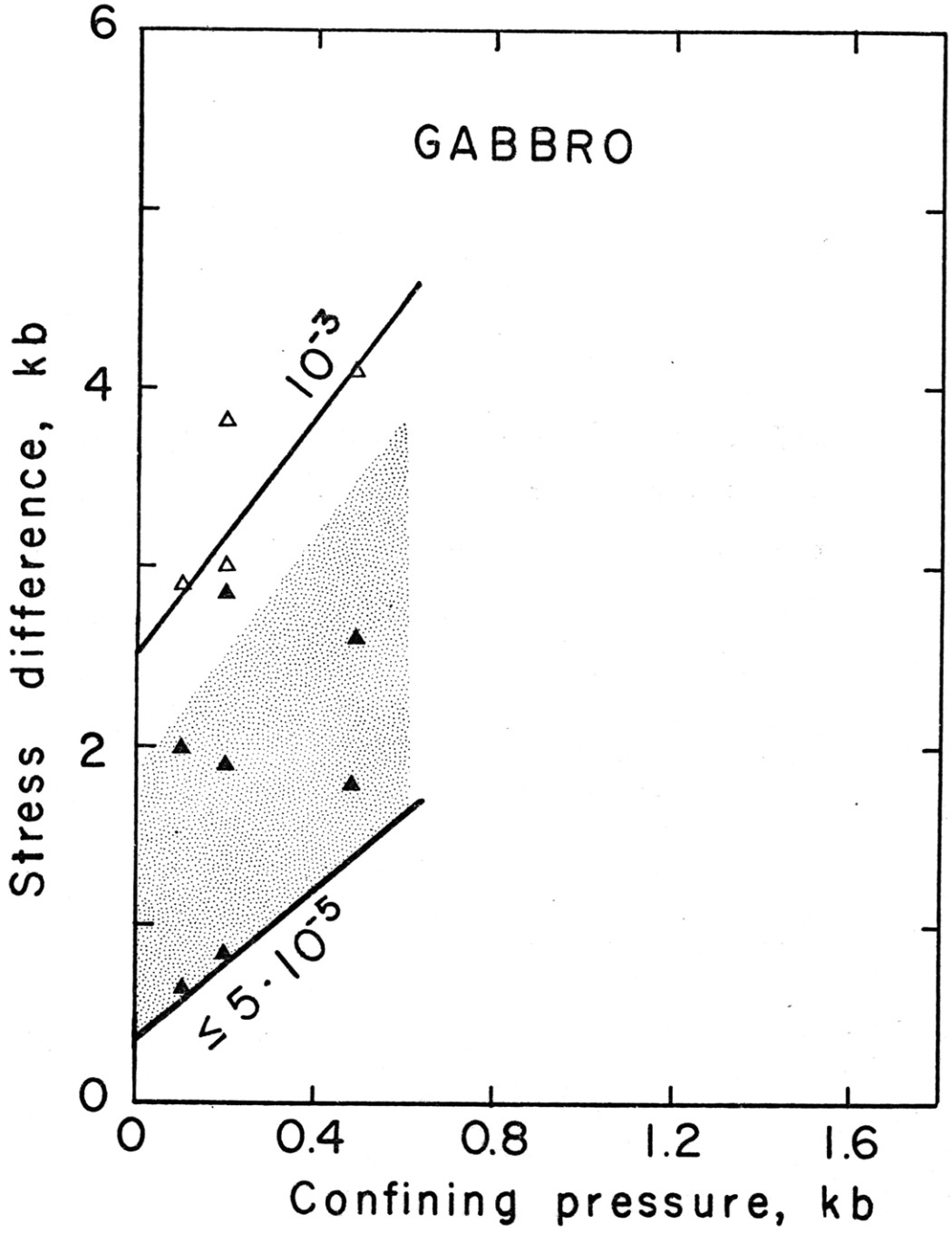
GABBRO
10^{-3}
$\leq 5 \cdot 10^{-5}$
Stress difference, kb
Confining pressure, kb
0
2
4
6
0
0.4
0.8
1.2
1.6

Figure 1-6. Pressure dependence of sliding stress of San Marcos Gabbro. Diagonal line and stippled region are stress for onset of dilatancy as shown in Figure 1-5.

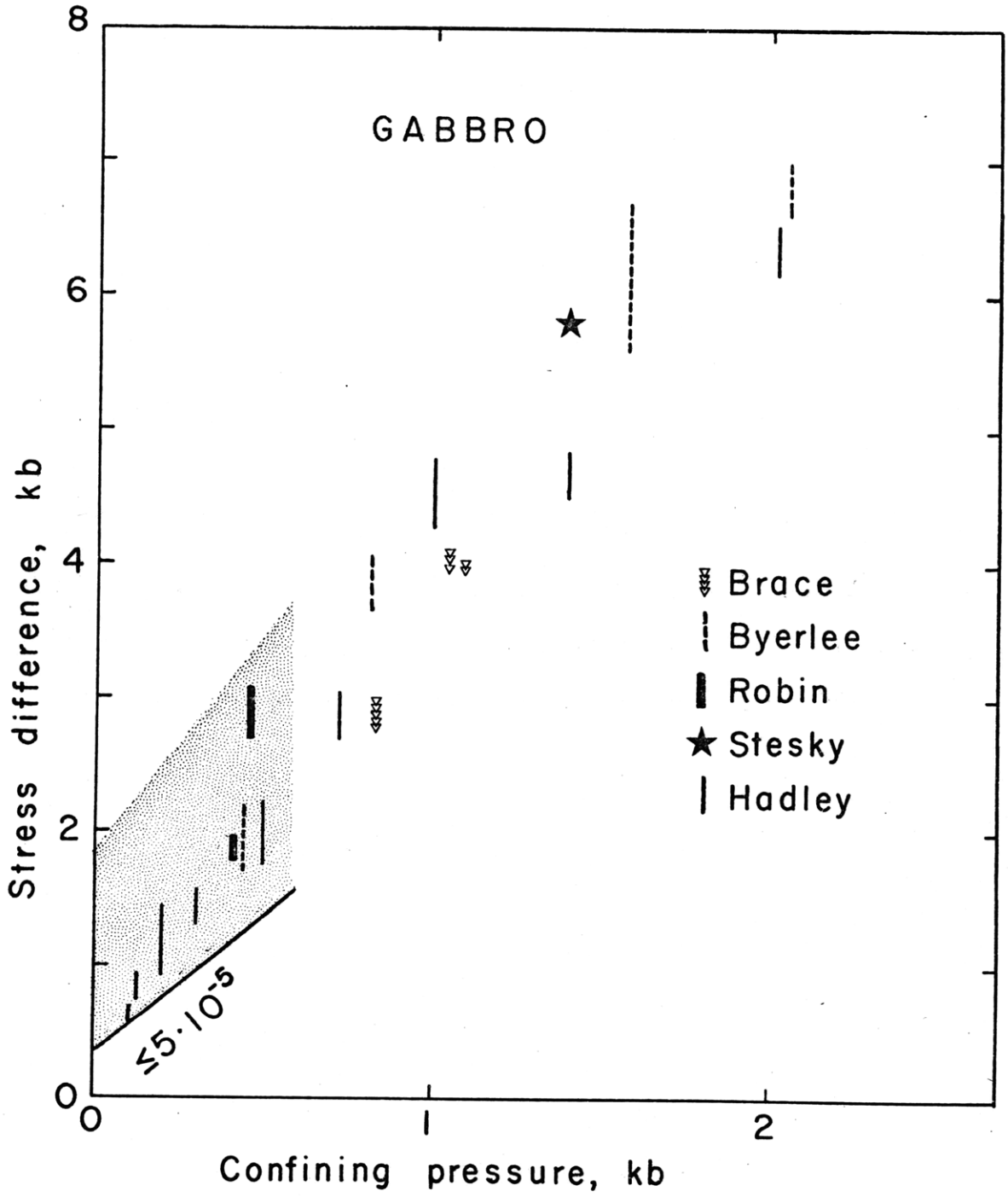
GABBRO
Brace
Byerlee
Robin
Stesky
Hadley
≤5·10⁻⁵
Stress difference, kb
Confining pressure, kb
0
2
4
6
8
0
1
2

Figure 1-7. Pressure dependence of fracture, sliding and dilatation stress (C') of San Marcos Gabbro. Filled circles are from this study; open circles from Brace (1973). Vertical bars are sliding stress from this study; the dashed-dot line represents an average of friction data of Byerlee, Brace and Robin (Brace, 1973).

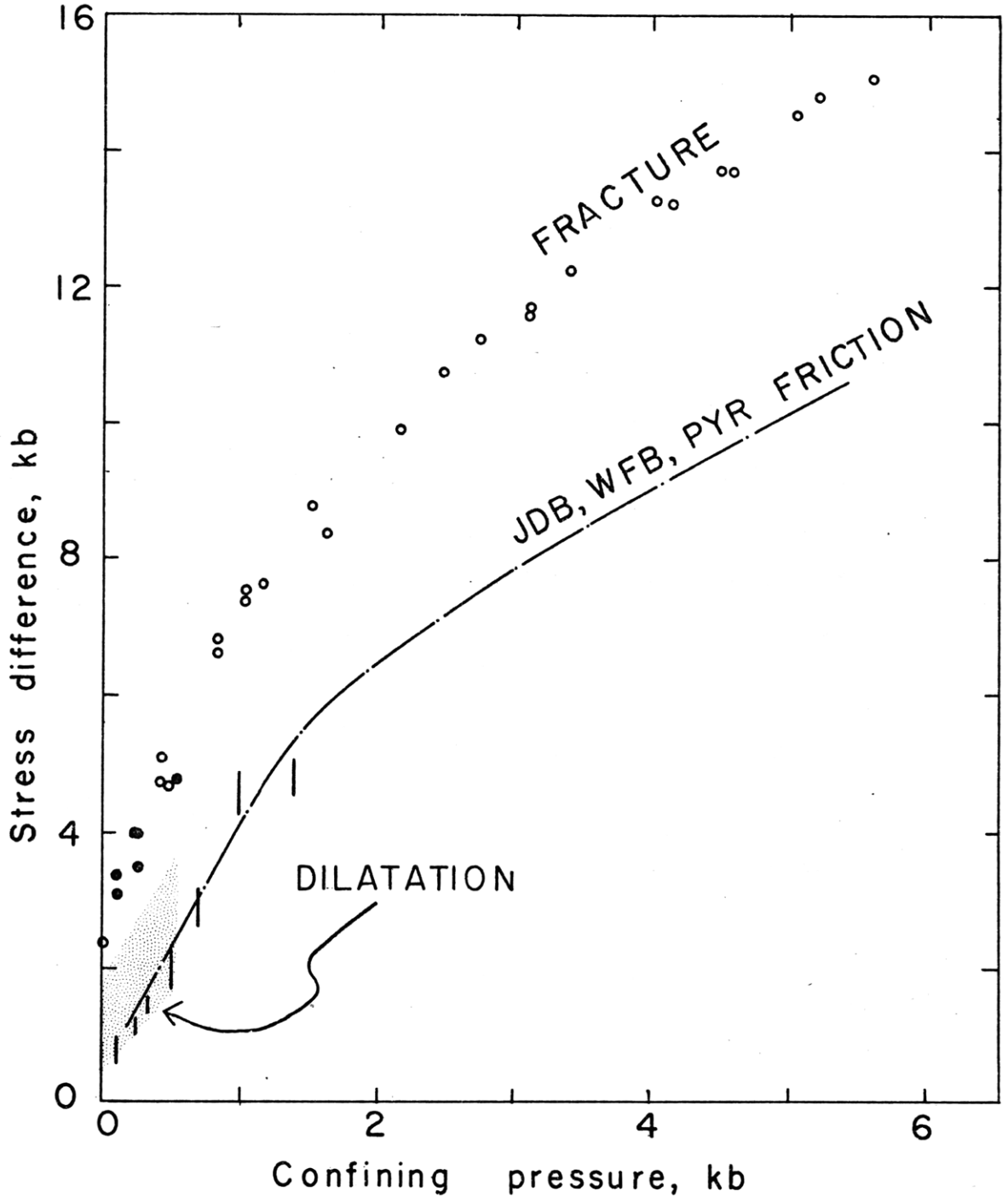
16
12
8
4
0
0
2
4
6
Stress difference, kb
Confining pressure, kb
FRACTURE
JDB, WFB, PYR FRICTION
DILATATION

Matsushima (1960a, b) and, more recently, Thill (1973) indicates that changes this small would be insufficient to cause significant variations in the seismic velocity of compressional waves.

Secondly, the stress-strain curves determined in this study apply to the initially intact material. The presence of a through-going fault may alter the stress state in the rock, changing the amount of strain and, in particular, the amount of dilatant strain associated with a given load. Further work in measuring volumetric strains under cyclic loading or in faulted rock is required to clarify this (Crouch, 1970). In addition, the strain rate used may affect C'. The slower strain rate may reduce C' without dramatically decreasing the sliding strength of the material.

In situ, other parameters than confining pressure and stress influence rock behavior. At depths of a few kilometers, temperature must be considered. The effect of temperature on C' is unknown. For sliding, Stesky (1973) has found that up to 500°C the frictional strength drops 2-3% per 100° and 20% per 100° at temperatures above this. It seems unlikely that at the temperatures reached in the first 6 km of the Earth's crust, any drastic change in C' would occur, but no data exist. Water or steam may also influence the relative values of C' and the sliding stress. Only meager information is available concerning the effect of water on the sliding strength of rock surfaces (Byerlee, 1967; Jaeger, 1971; Handin, 1973), and again, no data exist about its effect on C'.

In summary, the results of this study argue against micro-

crack dilatancy as a mechanism for precursory phenomena of many crustal earthquakes, but further work is required before any firm conclusion can be drawn. The concept of dilatancy may still be valid, however. Dilatancy associated with movement on joints (Goodman, 1972) and other large-scale features in response to stress could equally well account for compressional wave velocity and radon emission changes, small uplifts and other events now recognized as precursors of earthquakes.

CHAPTER 2

THE EFFECT OF CYCLIC STRESS ON DILATANCY

INTRODUCTION

One of the major problems associated with dilatancy models for earthquake precursors is the apparent requirement of high shear stress to produce inelastic volume increase in rocks. Heat flow data from the San Andreas Fault and other areas are inconsistent with such high stresses in the earth (Brune et al., 1969; Henyey and Wasserburg, 1971; Lachenbruch and Sass, 1973). Recently, Scholz and Kranz (1974) and Haimson (1974) have shown in uniaxial and low pressure triaxial experiments that the onset of dilatancy occurs at progressively lower stress in granite subjected to cyclic loading. Thus, in situ, cyclic stress might explain the apparent conflict between laboratory and field data. Zoback and Byerlee (1975) however, report no decrease in C', the minimum stress required for dilatant behavior, in stress cycling experiments at confining pressures of 2 kbar and a very small decrease in C' (200 $\pm$ 100 bars) at 0.5 kbar confining pressure. These results suggest the existence of a threshold confining pressure above which cyclic fatigue does not occur. This threshold may be as low as 500 bars. If such modest pressures -- corresponding to crustal depths of less than 2 km -- can indeed prevent any decrease in C' with repeated stress, then cyclic loading cannot be invoked as a means of lowering the stress required for dilatancy in the earth.

The present work is an extension of previous stress-cycling experiments to 5 kbar confining pressure and greater numbers of loading cycles. Zoback and Byerlee's single 2 kbar test was terminated by a jacket leak during the sixth cycle. Some doubt exists therefore about whether they failed to observe a decrease in C' because increased confining pressure inhibits such decreases, or whether their experiment was ended before any trend in stress-strain behavior could become apparent. We tried to resolve this question so that the more important question could be answered: Can *in situ* dilatancy occur at low shear stress?

PROCEDURE

We cycled 6 Westerly Granite and 7 San Marcos Gabbro samples at a strain rate of 10^{-4}/sec under confining pressures of 0.5, 1.5, 4.2 and 5.0 kbar. Except for the single gabbro sample run at 4.2 kbar 2 samples of each rock type were tested at each confining pressure. Samples were cycled in stress at least 20 times, unless failure terminated the test prematurely. Peak loads were chosen based on inspection of the stress-volumetric strain curves during cycling and ranged from 55 to 95 percent of the virgin fracture strength of the rock as previously determined by Stesky *et al.*, (1974) and Brace *et al.*, (1966) and given in Hadley (1973). Our present gabbro samples came from the same block used in the original fracture strength work and although the granite did not, the low pressure fracture strengths of the material agree well with the previously

determined values. Strains were measured using electric resistance foil gauges arranged axially, ε_z, and circumferentially, ε_θ, on copper-jacketed right circular cylindrical samples. Volumetric strain was computed assuming $\varepsilon_v = 2\varepsilon_\theta + \varepsilon_z$.

The onset of dilatancy was determined in 2 ways. In the first method, an elastic reference line was fitted to the stress-volumetric strain curve for each cycle of each sample. The departure of the curve from the line represents the beginning of dilatancy. In the second method, the slope of the elastic reference line was constrained to match that for the second loading cycle of each rock sample. The stress at which the stress-volumetric strain curve departed from this line was interpreted as C'.

The first method is deemed preferable because cyclic loading can change the crack geometry within the rock, resulting in changes in the elastic response of the crack-matrix aggregate. The second method is similar to that employed by Zoback and Byerlee and was used here in order to determine to what extent their method of determining C' influences the results.

At low to intermediate confining pressures, truly linear elastic behavior is not observed. Stress-volumetric strain curves for Westerly Granite below about 2 kbar and for San Marcos Gabbro below about 500 bars are continuously curved. Crack closure in the plane perpendicular to the applied load evidently overlaps the stress region in which dilatant cracks form or extend due to the applied load. Thus, the onset of dilatancy, although a convenient fiction, is not truly macro-

scopically discernible. The numerical value of C' under such conditions is subject to considerable uncertainty, and, owing to the simultanaeity of processes opening and closing cracks, not a particularly meaningful number anyway. However, trends in the numerical value of C' reflect the progress of the cracking process, the relative importance of crack closure vs. crack extension, and are therefore significant. The precision with which the onset of dilatancy can be determined by any one investigator is no doubt considerably greater than the accuracy of such a measurement at low confining pressures; thus trends may be detected despite large errors in the absolute magnitude of C'. The accuracy with which C' can be determined at low confining pressures in my experiments is $\pm$ 500 bars; the precision is about 2 percent of the fracture strength or $\pm$ 100 bars.

At high pressures, the picture is neater. The region of crack closure is separated from the dilatant portion of the stress-volumetric strain curve by a region of linear elastic behavior. For gabbro at 1500 bars this linear region extends over about 3 kbar in differential stress; at 500 bars, it is 2 kbar wide. Both these values represent about 40 percent of the stress span between zero and failure. The stress-volumetric strain curve for granite at 500 bars confining pressure displays continuous curvature, although the curvature is so small between about 0.3 and 1.9 kbar stress that any of that portion of the curve may be approximated to within 5×10^{-5} strain over 0.7 kbar by a straight line. At best then, any point between 1.0 and 1.9 kbar could reasonably be chosen as C'. Continuous curvature

is still displayed by the granite stress-strain curves at 1.5 kbar confining pressure, but at 5.0 kbar, they are linear over a discernible portion of the stress range: 2.5 kbar or 15 percent of the region between zero stress and failure. Values of C' determined at high confining pressures will therefore be more accurate than those determined at low pressure. In contrast to the low pressure case, the competing effect of crack closure has been removed from the picture: the measured values of C' now can be interpreted as the stress levels at which crack growth or crack opening becomes significant within the rock. Accuracy of measurement is now limited by precision. At 1.5 kbar this is 0.25 kbar stress, while at 5.0 kbar confining pressure the accuracy is 0.5 kbar.

There is no sharp demarcation between confining pressures at which the stress-volumetric strain curve for rock displays continuous curvature and those at which a linear elastic region clearly appears. That this should be so can be seen from examination of rock volumetric compressibility curves. These are just that -- curves -- below some confining pressure, while at high confining pressures the curvature decreases until the curves approach straight lines (Figure 2-4). Under confining pressures at which compressibility behavior is linear over several kilobars, one might confidently expect a region of linear elastic behavior in the stress-volumetric strain curve. At lower confining pressures, though, the mere application of a differential stress may not suffice to close all void space before that stress reaches a level great enough to begin inducing

cracking.

Of as much importance as the magnitude of C' is the amount of dilatant volumetric strain which can be produced, and whether this increases, remains constant or decreases with progressive loading cycles. The works cited earlier have demonstrated the persistence of dilatancy over the range of conditions studied, but no one has discussed the influence of stress cycling on the magnitude of the dilatant strains observed. The maximum stress attainable in established tectonic regions of the earth, and consequently, the maximum dilatant strain possible in any in situ stress cycle, is likely to be limited by the frictional strength of the rock. In the present study, therefore, dilatant volumetric strain for each loading cycle has been calculated at the sliding stress previously determined from faulted samples. The sliding stress at pertinent confining pressures is listed with a range and with the fracture strength of the virgin material in Table 2-1. Sliding stress has been shown to be unaffected by the amount of sliding (Byerlee, 1967) so the values given in Table 2-1, columns 3 and 4 are presumed appropriate for all stress cycles.

RESULTS

Variation of C' with cycling. Variation of C' with cyclic stress is plotted at the top of Figures 2-1 through 2-3. Shown at the bottom is the maximum stress reached in the cycle as a function of the fracture strength, F, of the virgin material. Trends in C' appear to be insensitive to the method of chosing the elastic reference line although the actual values of C' may

TABLE 2-1

Rock Type	Confining Pressure kb	Sliding Stress kb	Range kb	F kb
San Marcos Gabbro	5.00	10.14	1.00	14.50
	4.20	9.24	1.00	13.50
	1.50	5.00	1.00	8.30
	0.50	2.40	0.80	4.90
Westerly Granite	5.00	12.72	1.00	17.80
	1.50	5.20	0.60	10.60
	0.50	1.65	0.25	5.60

Source: Mogi (1966), Byerlee (1966), Stesky et al. (1974), Brace (1973, personal communication)

Figure 2-1. Stress at the onset of dilatancy, dilatant volumetric strain at the sliding stress and percentage of the virgin fracture strength represented by the maximum stress attained, all vs. loading cycle number. Open circles indicate C' determinations using an elastic reference line of constant slope; crosses indicate C' determined from elastic reference lines of variable slope. Confining pressure was 500 bars. SMG refers to gabbro; G1 to granite.

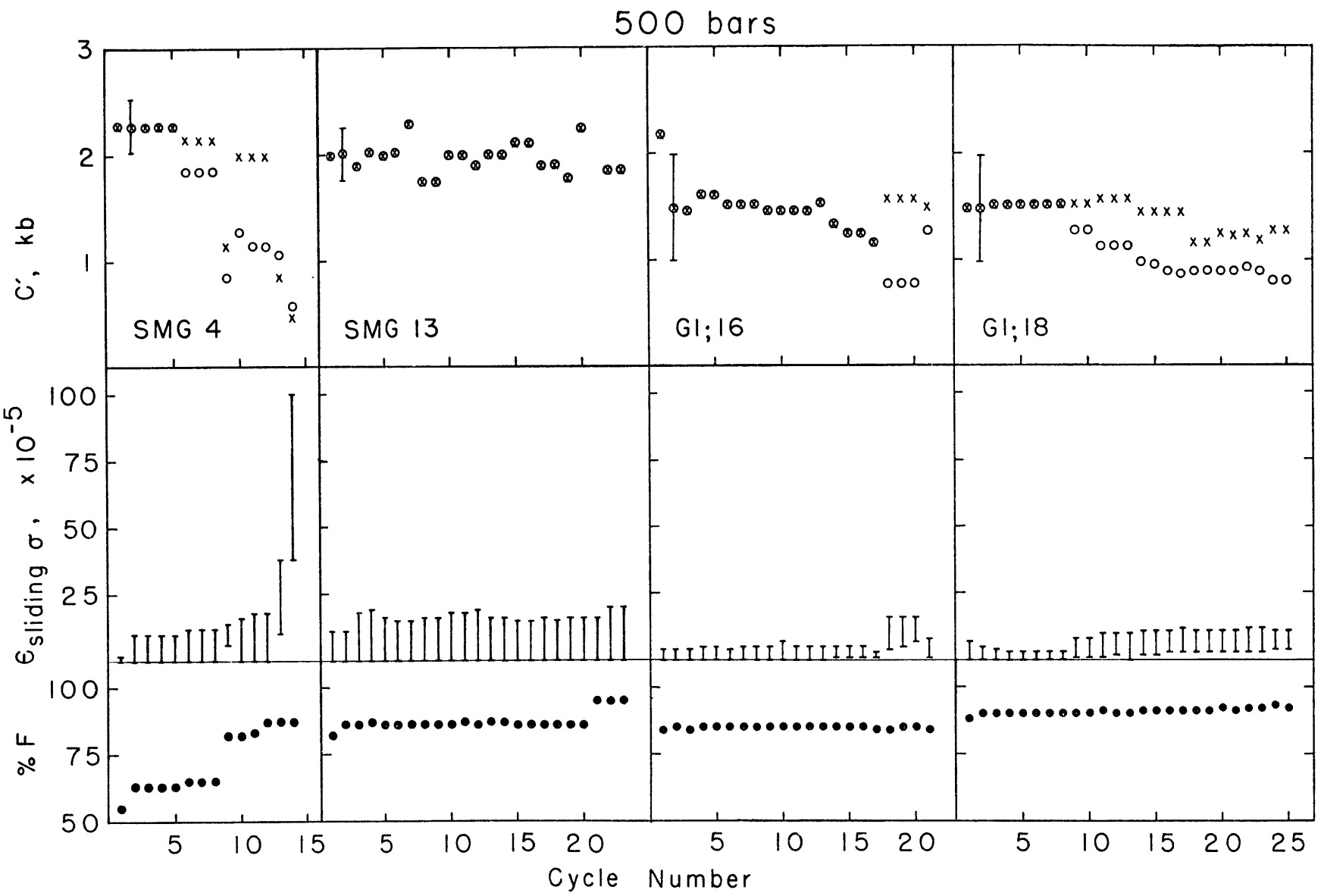
500 bars
C', kb
SMG 4
SMG 13
GI;16
GI;18
$\epsilon_{sliding}\,\sigma$, x 10^{-5}
% F
Cycle Number

Figure 2-2. Same as Figure 1., except that confining pressure was 1.5 kbar for SMG 7 and the granites, and 4.2 kbar for SMG 10. Heavy arrows indicate jacket leaks between loading cycles.

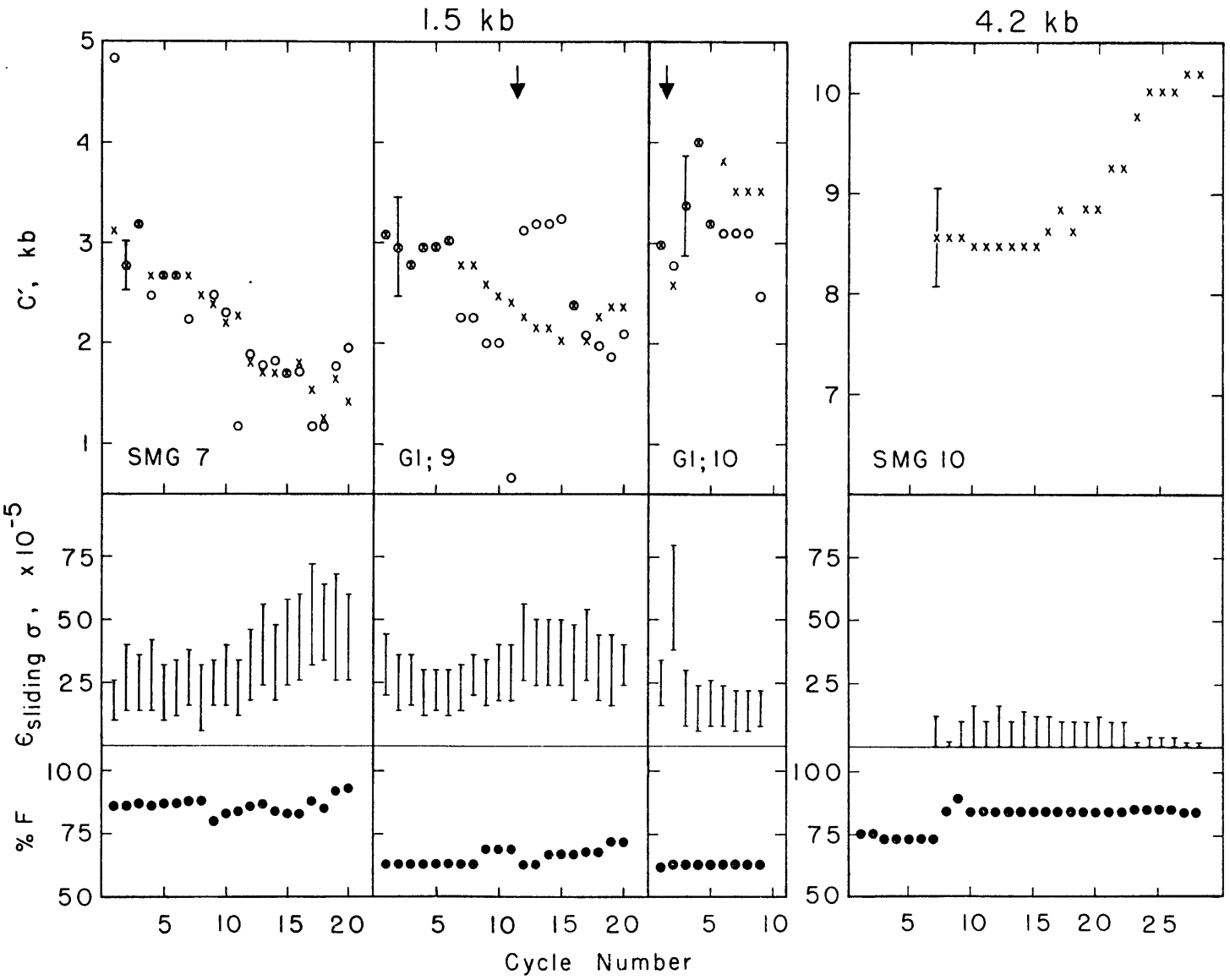
1.5 kb
4.2 kb
C', kb
SMG 7
GI; 9
GI; 10
SMG 10
$\epsilon_{sliding}\ \sigma$, x 10^{-5}
% F
Cycle Number

Figure 2-3. Same as Figure 2., except that confining pressure was 5.0 kbar. Arrow heads on the end of the bars giving dilatant volumetric strain at the sliding stress indicate that the maximum value of the sliding stress was not attained during the cycle, and the maximum strain would have exceeded the maximum value shown. Triangles indicate that the minimum value of the sliding stress was not achieved, and the minimum dilatant volumetric strain at sliding must be greater than the value shown. Horizontal bars mark the value of dilatant volumetric strain at the minimum stress for sliding, for cycles in which that stress was barely reached.

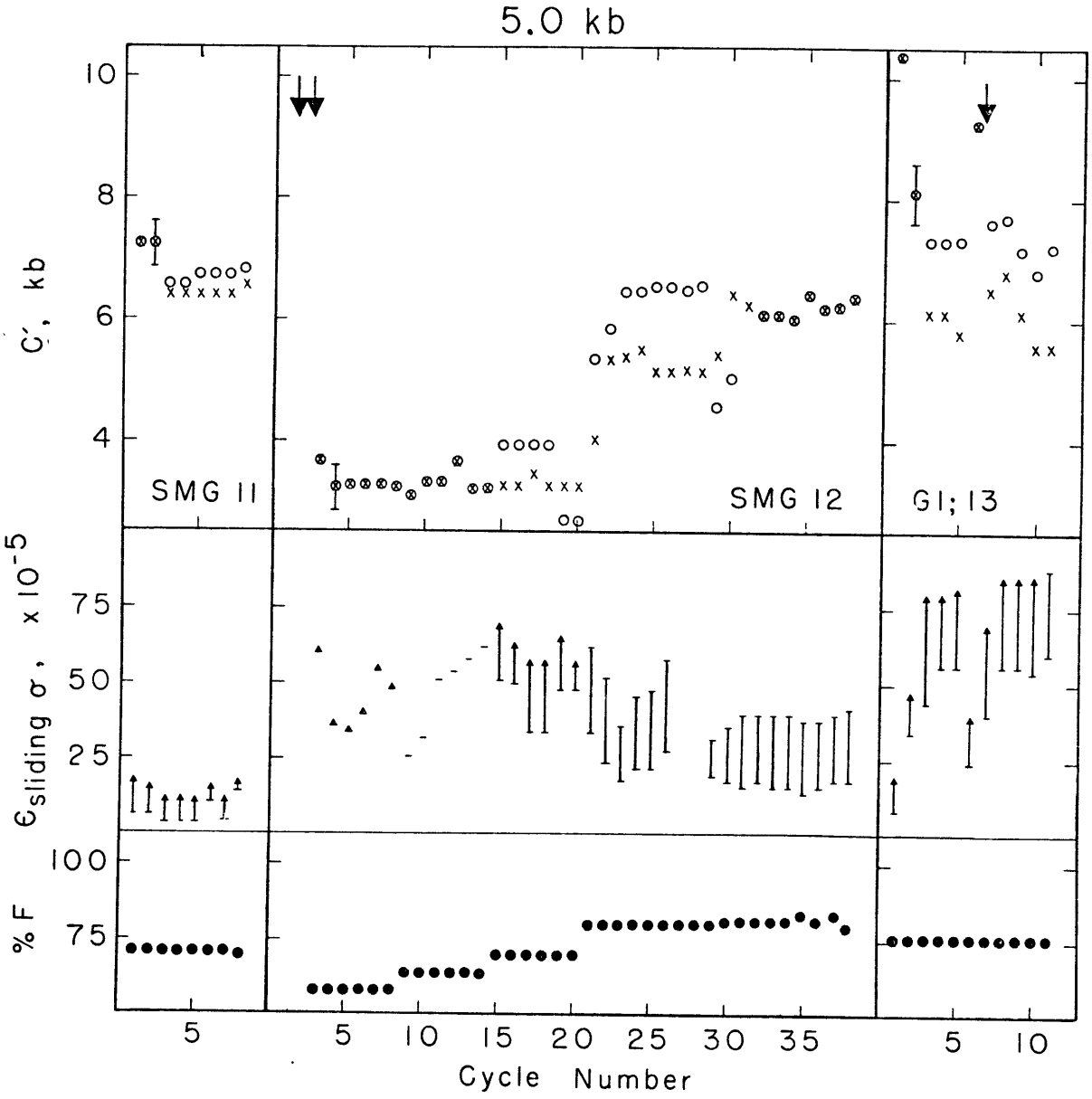
5.0 kb
C', kb
10
8
6
4
SMG 11
SMG 12
G1; 13
$\epsilon_{sliding}$ σ, x 10^{-5}
75
50
25
% F
100
75
5
5
10
15
20
25
30
35
5
10
Cycle Number

differ depending upon whether one assigns that line a fixed slope throughout the cycling history or not. Except at 0.5 kbar confining pressure, where a decrease is indicated in 3 of the 4 rocks tested, no consistent patterns in C' are discernible.

Dilatant volumetric strain at sliding. The amount of dilatancy expected at the sliding stress is also given in Figures 2-1 through 2-3. Like C', the dilatant volumetric strain has been determined both with reference to the elastic line for the specific cycle in question and with reference to a line with the slope of the elastic line for the second cycle. Because the results are nearly identical, only those obtained using the first method are shown. The range of values arises from the range of stress at which sliding may commence and is usually larger than the scatter due to the uncertainties in the determination of volumetric strain ($\pm$ 5 parts in 10^5) or in picking the elastic reference line ($\pm$ 10 parts in 10^5 or less between the method 1 and method 2 numbers). Over the range of confining pressure investigated, dilatancy persists at the level of a few parts in 10^4 and occasionally increases to as much as 1 part in 10^3 during cycles immediately preceding failure.

Evidence for cracking during cycling. Changes in both the number of cracks and crack geometry during cycling are supported by inspection of the low and high pressure regions of the volumetric compressibility curves obtained during confining pressure application and release. For example (Figure 2-4), volumetric compressibility at high pressure increased from $\beta_1 = 1.22$ mbar^{-1} before the first stress cycle to $\beta_{12} = 1.30$ mbar^{-1}

Figure 2-4. Compressibility curves for cycled gabbro and granite. The number of the stress cycle following hydrostatic compression is given next to each curve. All paths are loading paths.

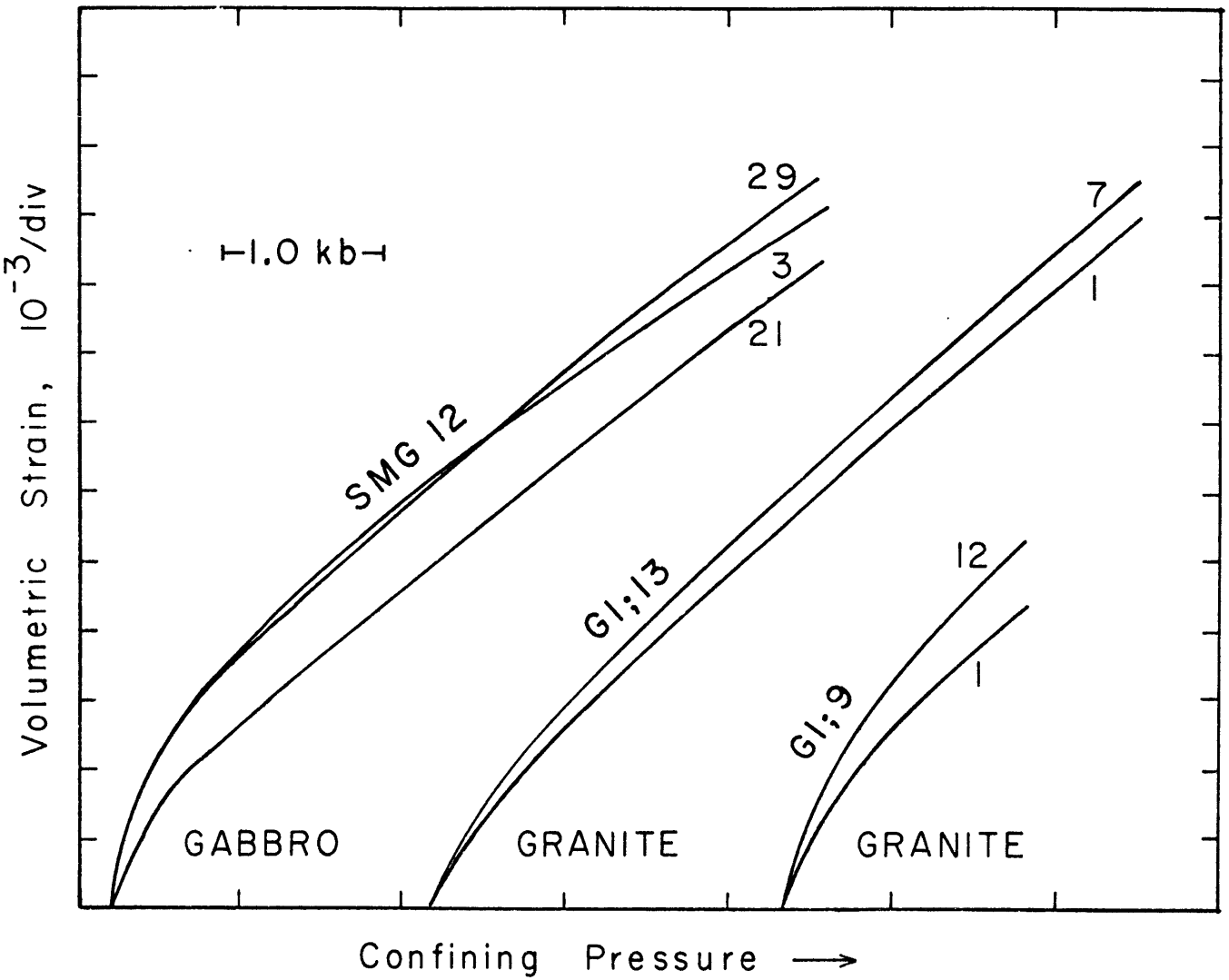
Volumetric Strain, 10^{-3}/div
1.0 kb
29
3
21
SMG 12
7
1
G1;13
12
1
G1;9
GABBRO
GRANITE
GRANITE
Confining Pressure →

for a granite at 1.5 kbar confining pressure, where the subscript for compressibility indicates the cycle number of the stress cycle following. For a gabbro at 5.0 kbar, $\beta_3 = 0.84$ mbar^{-1}, while $\beta_{21} = \beta_{29} = 0.88$ mbar^{-1}.

The initial part of successive stress-volumetric strain curves also provides an indication of changing crack geometry within the rock. The usual curve for rock under low confining pressure has a knee caused by crack closure in the plane perpendicular to the applied load (Figure 2-6, dashed line). At high confining pressure, the knee is suppressed. Occasionally (Zoback, 1974, personal communication) the knee is reversed, indicating initial expansion rather than contraction. With cycling, the tendency at all confining pressures is for reversed knees to develop.

Dilatancy associated with major flaws. Although it initially displayed a normal stress-volumetric strain curve at 1.5 kbar confining pressure, a granite sample which suffered an almost through-going fault during the first stress cycle subsequently showed a large reversed knee (Figure 2-5, solid line) which was reproducible over eight subsequent cycles. A reversed knee was also observed in granite during a post-failure cycle at 5.0 kbar confining pressure (Figure 2-6). This behavior could not be duplicated using a sawcut granite specimen. Strains associated with transverse shearing of the circumferential strain gauge due to motion on the underlying sawcut occurred only after some threshold stress had been exceeded and were non-recoverable. Attempts to find such low-stress dilatancy in a gabbro containing

Figure 2-5. Stress-volumetric strain curves for a granite damaged at 5.0 kbar confining pressure. Dotted lines represent the cycle in which extensive fracturing occurred. Note the anomalous volume increase with initial loading in the damaged sample (solid curve).

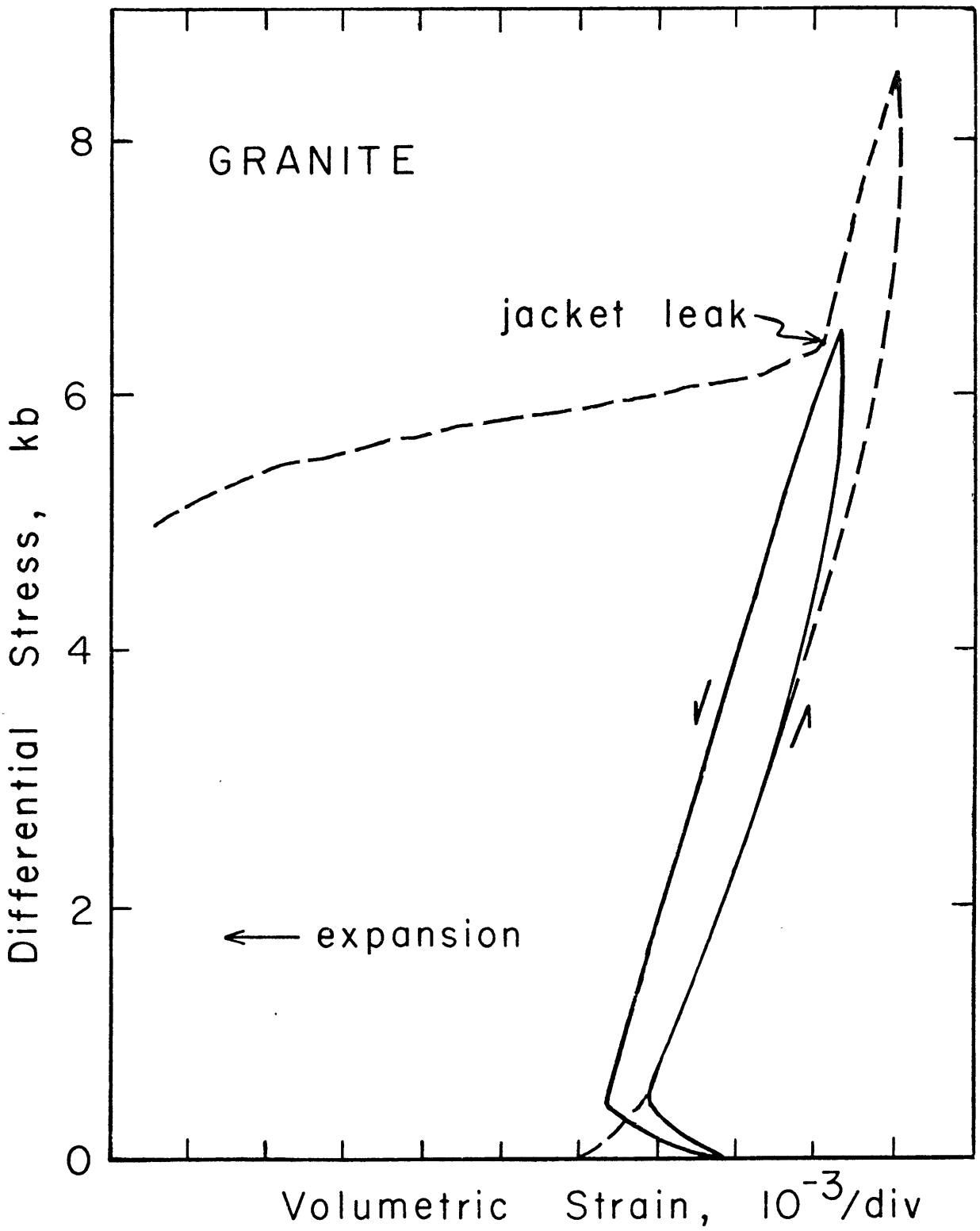
GRANITE
jacket leak
expansion
Differential Stress, kb
0
2
4
6
8
Volumetric Strain, 10^{-3}/div

Figure 2-6. Stress-volumetric strain curves for a granite at 1.5 kbar confining pressure. Dotted portions show regions of unstable behavior. Note the similarity in initial loading behavior between this sample and the one shown in Figure 5.

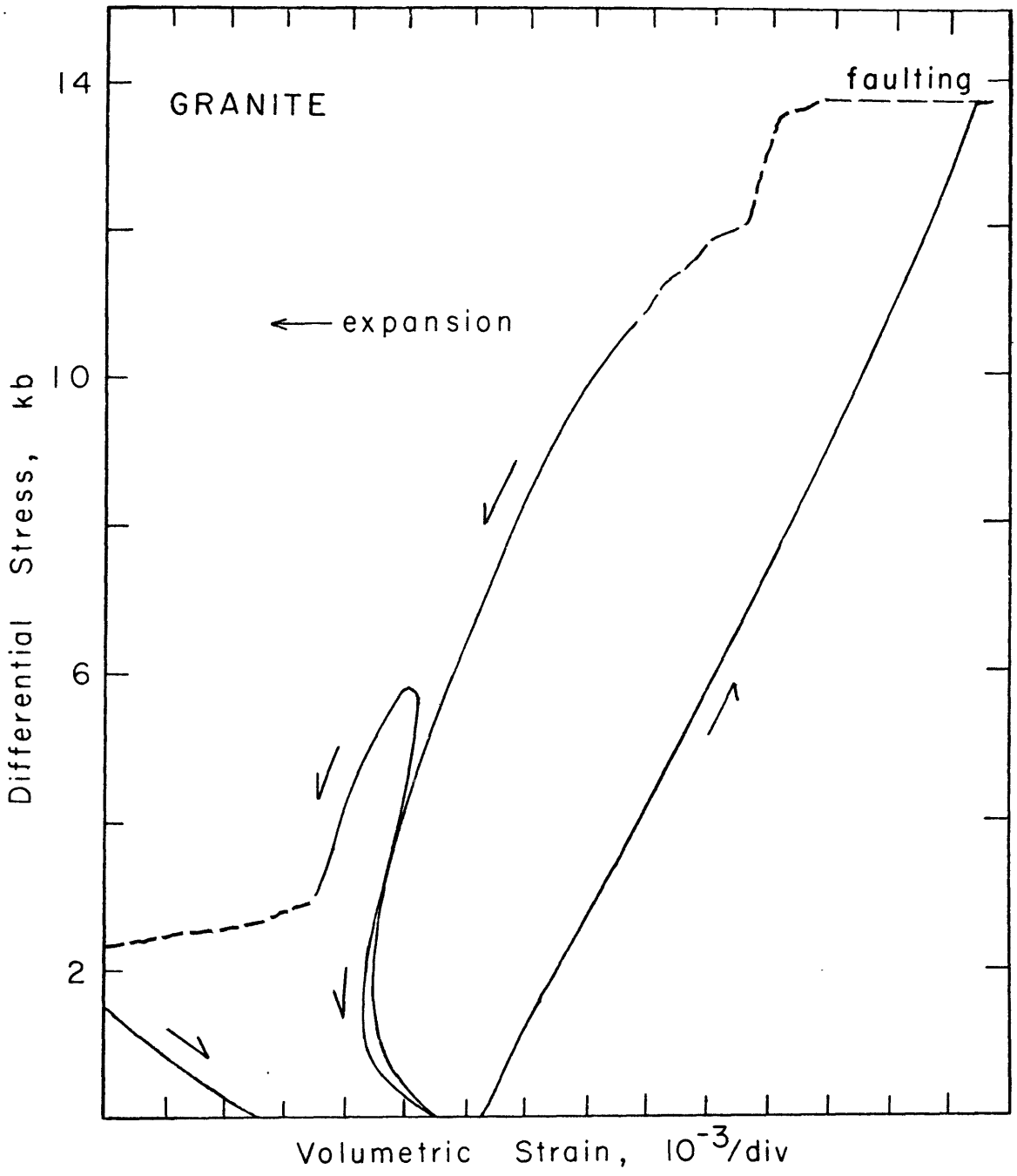
GRANITE
faulting
expansion
14
10
6
2
Differential Stress, kb
Volumetric Strain, 10^{-3}/div

a small, healed joint were unsuccessful, but the fracture ultimately induced by loading did not stay in the plane of the joint, indicating that healing was at an advanced stage. Also, the fracture strength of the supposedly flawed sample was well within the range expected for virgin gabbro.

Contraction prior to failure. At confining pressures of 1.5 kbar and above, the failure mode of both granite and gabbro after many stress cycles is always characterized by rapid volumetric contraction immediately prior to volumetric expansion and stress drop associated with rupture. Often, it is associated with accoustic events. This contraction -- not observed in single-cycle fracture experiments or 0.5 kbar cycling experiments -- appears to be due to accelerating axial compaction accompanied by steady or even decelerating circumferential expansion (Figure 2-7, beginning at point A). In two cases, ε_θ began to decrease before failure.

DISCUSSION

All of the tests described here were terminated before deformation became identical from cycle to cycle over many cycles. Because of this failure to reach an entirely reproducible deformation condition, absolute values of C' and the steady-state dilatant volumetric strains at sliding are not known. The indications are, from trials with jacket leaks that these properties may be strongly history dependent so that their long-term numerical values need not be unique. At 0.5 kbar confining pressure, there is a clear indication of a decrease in C' with cyclic stress, but at higher pressures, the data are inconclusive.

Figure 2-7. Stress-strain curves for granite at 5.0 kbar confining pressure showing region of volumetric contraction immediately prior to failure. Magnification of the upper (circled) portion of the curves is 2x. Rapid volumetric contraction begins at point A and continues until the peak strength is achieved.

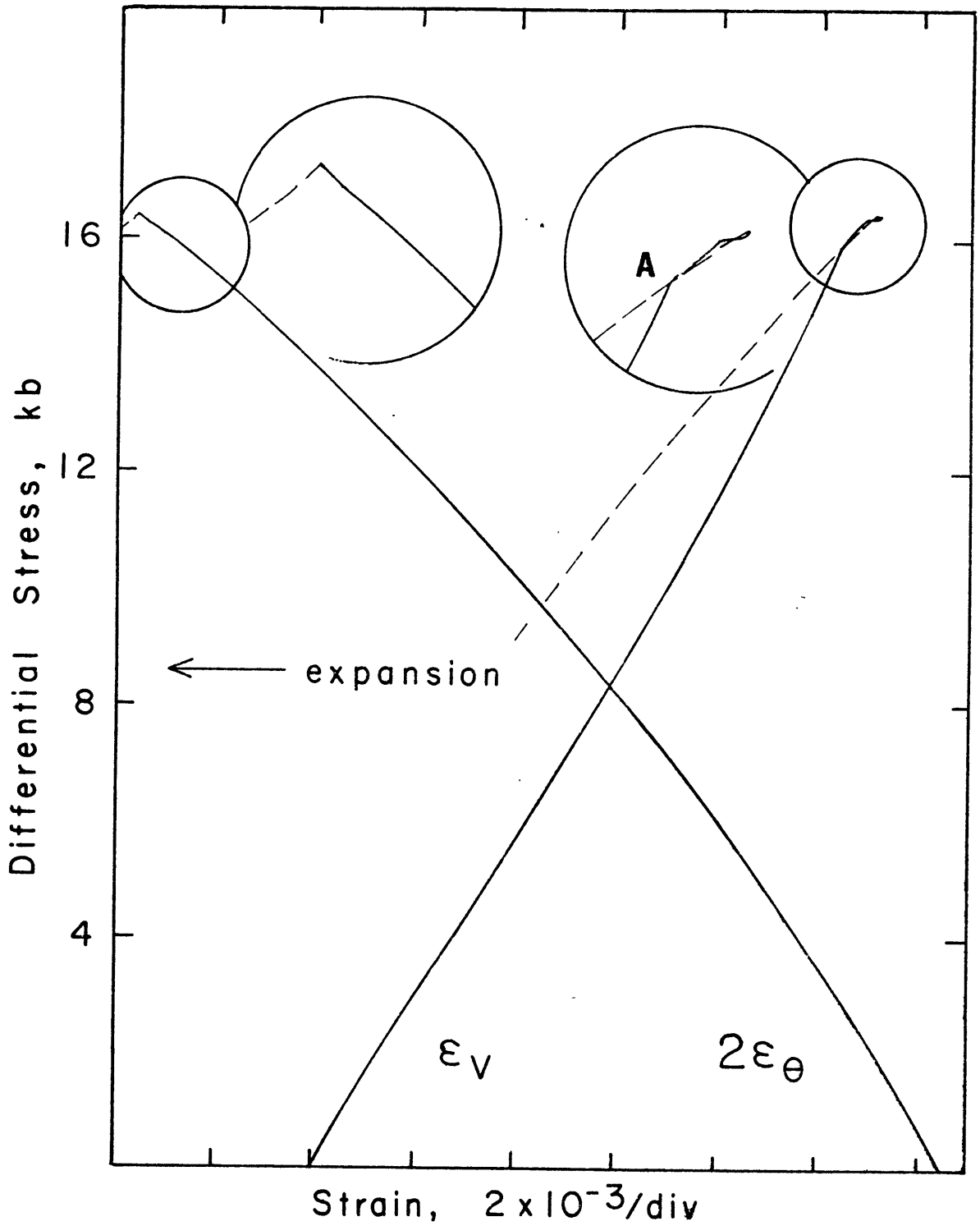
16
12
8
4
A
expansion
ε_v
$2\varepsilon_\theta$
Differential Stress, kb
Strain, 2×10^{-3}/div

The amount of dilatant volumetric strain at sliding is not strongly tied to the behavior of C', although one might have anticipated a reciprocal relationship between the two.

The first cycle values of C' and dilatant volumetric strain at sliding agree well with published values (Brace et al., 1966; Hadley, 1973). The later-cycle values of C' in granite tend to fall below published minima by about a kilobar at all confining pressures. This is particularly significant because the previously determined minima were invariably associated with strain rates of 10^{-6}/sec. Faster strain rates, such as used in this study, yielded considerably higher values of C'. The same pattern applies to the gabbro at 0.5 and 1.5 kbar; unfortunately, no previous data are available for higher pressure comparison. It is at these higher pressures that the significance of the present results are the most uncertain.

The inconsistency of the high pressure data evidently has a dual cause. Firstly, we may not have completed sufficient numbers of stress cycles to determine any trends in deformation. To circumvent this problem would require the use of a servo-controlled loading system and faster strain rates. Secondly, strict uniformity in experimental parameters may be required to produce self-consistent results. If a sample once suffers a jacket leak, it may never be comparable with a sample which has not. Cycled samples, decompressed and then recompressed to the same confining pressure and recycled may behave differently from samples which were held under constant confining pressure, all other experimental variables being equal.

At 0.5 kbar confining pressure, C' decreased in both of my granite samples by about 400 ± 100 bars over 20 stress cycles. This is not significantly different from the change reported by Zoback and Byerlee (1975) although strain rates used in these experiments were an order of magnitude faster. In the gabbro sample which failed during the eighth stress cycle at 0.5 kbar confining pressure, a marked decrease in C' was observed. This is consistent with Zoback and Byerlee's uniaxial observations associating a decrease in the minimum stress for dilatancy with progressive failure of the sample (Zoback, personal communication). But another gabbro sample, SMG 13, survived 20 stress cycles intact and exhibited no change in C' with cycling.

Two previously unreported phenomena have been identified in this study. The first, low-stress dilatancy associated with through-going or nearly through-going fractures, requires further documentation to substantiate its occurrence. The volume increase may be only apparent, having its origins in alignment problems which develop bending moments in the flawed specimens, but the increase in volumetric strain is due as much to a rapid increase in ε_θ as to ε_z behavior. Alternatively, even if the expansion is real, it may arise due to the intersection of the macroscopic flaw with the free surface of the sample. The sample size is no longer infinite with respect to the fracture, and boundary effects may dominate. Certainly, the strains will be as inhomogeneous as the sample has become and the approximation $\varepsilon_v = 2\varepsilon_\theta + \varepsilon_z$ is no longer applicable. However, unless substantial compression occurs in some part of the rock specimen not moni-

tored by a strain gauge, the net volume change will still be large and positive.

The second phenomenon, volumetric contraction immediately preceeding failure, was found to be associated with all rock samples which failed during stress cycling at confining pressures of 1.5 kbar or more. As few as 8 or 9 stress cycles are sufficient to produce this behavior although it has not been reported in single-cycle fracture experiments. It is not known whether this phenomenon is general to all crystalline or other rock types, nor has the range of confining pressures, strain rates, and other experimental conditions over which it might occur been delineated. In view of the possible significance of this effect as a short-term precursor for catastrophic failure, more work should be done to characterize it.

CONCLUSIONS

Dilatancy in granite and gabbro occurs at progressively lower stress due to cyclic loading at 500 bars confining pressure. At higher confining pressures the results are inconclusive. First cycle values of C' agree with previously published numbers in all cases. Dilatant volumetric strain at differential stresses corresponding to the frictional strength of the rock persists at the level of a few parts in 10^4, also consistent with results previously reported.

Volumetric contraction occurs immediately prior to failure in samples cyclically stressed under confining pressures of 1.5 kbar and higher. This phenomenon may be useful as a short-term

precursor of catastrophic rupture.

In samples containing large fractures, we have apparently generated significant amounts of dilatancy (1 part in 10^4) with stresses of less than 100 bars at confining pressures as high as 5 kbar. Thus, fault rubble, joints and large-scale crack-like features in the earth might generate sufficient dilatancy to account for observed premonitory effects of earthquakes at very low shear stresses.

CHAPTER 3

AZIMUTHAL VARIATION OF DILATANCY

INTRODUCTION

Anisotropy in dilatancy has been identified for some years in laboratory studies (Brace et al., 1966), yet only one possible example of dilatancy-related anisotropy has been recognized in situ, (Gupta, 1973b). Current thinking about dilatancy generally revolves around axisymmetric models (Anderson et al., 1974; Stuart and Dieterich, 1974) owing to the axisymmetric stress conditions imposed in most laboratory experiments and the presumed axial symmetry of the resulting microcracks. No one has tested the vailidity of axial symmetry although all possible azimuthal variations in dilatancy must be understood before one can attempt to separate measurement path effects from changes in the rock medium itself with time. While this uncertainty can always be circumvented in the laboratory by maintaining constant source-receiver geometries in the various measurements, this does not hold true in the field. Many reported observations of the temporal variation of seismic velocities or other vector properties may in fact represent variations in measurement path rather than material state. In the laboratory, reported sample to sample variability may only reflect poor control on specimen orientation. Moreover, by discounting possible directional variations in physical properties valuable information may be thrown away. For example, in complex tectonic regions, consideration of variation in path dependent properties over restricted

azimuths might allow one to distinguish which of several active faults posed the immediate threat.

To examine the magnitude of possible path effects and to study the localization of the fracture process we measured the variation of circumferential strain (ε_θ) in Westerly Granite cylinders loaded triaxially ($\sigma_1 = \sigma_2 < \sigma_3$, compression positive). In related experiments, pseudoelastic compliances (s_{ijkl}) have been obtained for the granite and a specimen of San Marcos Gabbro. These studies indicate that developing fault orientation and anisotropy in dilatant strain can be related early in the deformation history of the rock. Moreover, the anisotropy in strains and pseudoelastic constants is sufficiently large for these relatively homogeneous rocks that similar anisotropy should be easily detectable <u>in situ</u>.

Previous measurements of stress-induced anisotropy in rocks are restricted to seismic velocities. These are customarily measured along one circumferential and one axial path, and although two separate polarizations of S may be monitored along the former, the net result is to sample only the axial and one circumferential direction. Nur and Simmons (1969a), working at low stresses measured variations in velocity due to crack closure at several angles in the 1,3-plane but did not consider the 1,2-plane. Gupta (1973a), in quasi-uniaxial experiments ($\sigma_1 \simeq \sigma_2 < \sigma_3$) controlled fault orientation by means of C-clamps and measured seismic velocities in 3 perpendicular directions, 1 in the fault plane ($0x_2$) and 2 inclined 15° ($0x_3$) and 75° ($0x_1$) to it. Not surprisingly, he

found little change in P and S velocities along the first two directions and a large decrease in both quantities in the latter direction beginning at about 50 percent of the fracture strength. At fracture V_{p1} and V_{p2} differed by about 33 percent. The initial difference was zero within experimental error.

Gupta's results are suggestive, but owing to the presence of the C-clamp, the stress state in his samples was not truly uniaxial.

PROCEDURE

In our experiments, $\sigma_1 = \sigma_2$ = confining pressure (p_c). During the first type of test, run at 500 bars p_c, variations in circumferential strains were measured directly by means of 4 pairs of circumferential foil resistance strain gauges spaced equally about the copper-jacketed sample at mid-section. Pairs were used to eliminate any possible effects of bending. Each gauge pair was assumed to measure the strain along a line perpendicular to the diametral line joining the gauge midpoints (Figure 3-1a). The effect of finite gauge length on the value of the measured strain is discussed in Appendix I. The net effect is to reduce any apparent anisotropy in measured strain by as much as 1.7x for small strains and perhaps 1.1x for large strains. Thus any reported strain anisotropies will be conservative.

From the measured strains, a circumferential strain ellipse (Figure 3-1b) was constructed by computer using a least squares method given in Nye (1957). The ellipse was

Figure 3-1. (a) Schematic cross sectional view of Cu-jacketed rock sample showing location of strain gauge pairs and eventual position of fault trace (dashed line). (b) Circumferential strain ellipse showing data points corresponding to each gauge pair of Figure 3-1a. Note that the strains are measured perpendicular to gauge pair midpoint tie-lines. This solid line locates principal axes of the ellipse. This is an actual example (sample #2, cycle #2, 4.47 kbar stress); strain scale is indicated.

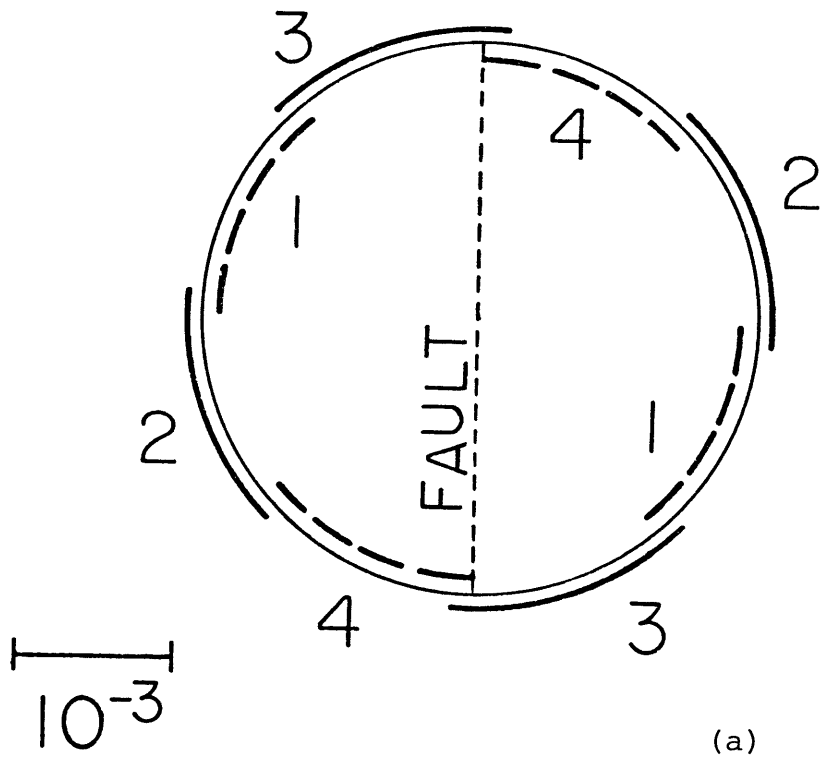

(a)

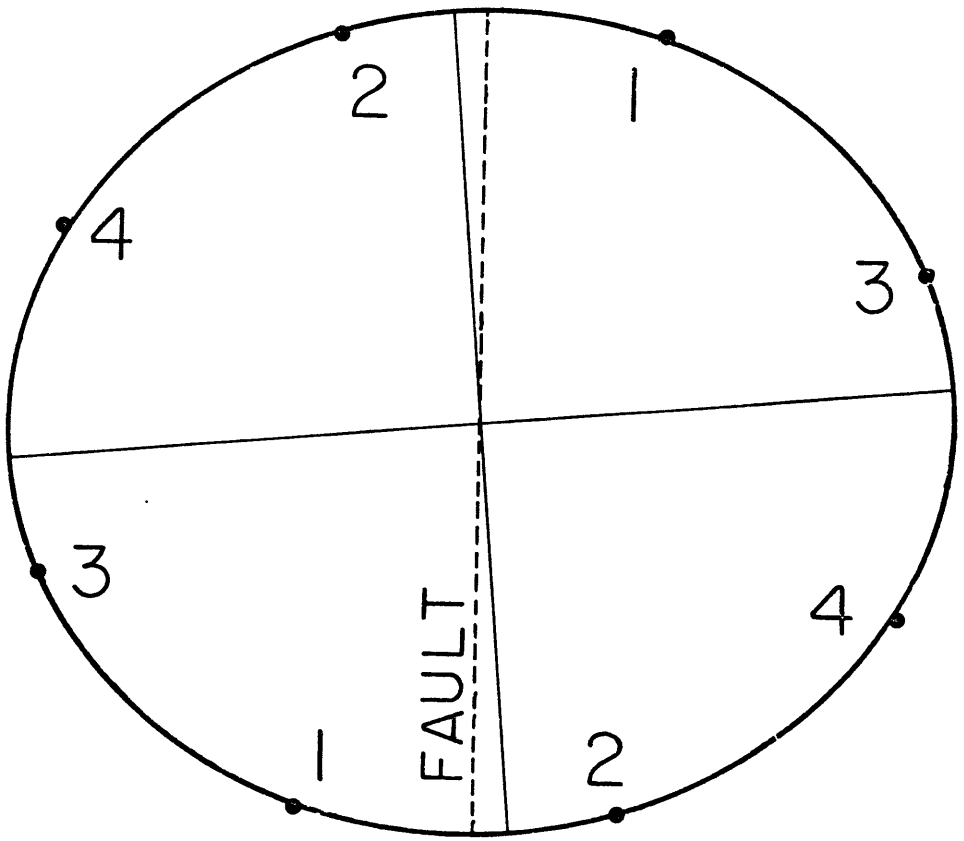

(b)

constrained to be centro-symmetrical, but otherwise was unrestricted. The orientation of the principal strain axes was expressed as the angle between the major axis and the eventual trace of the developing fault.

In the second type of test, small cycle excursions in confining pressure and stress were made during large-scale cyclic loading of copper-jacketed rock samples at 500 bars and 1500 bars confining pressure. These samples had only a single axial and a single circumferential strain gauge, but from the small excursions in axial load and confining pressure s_{13}, s_{23} and s_{33} could be independently determined using:

$$\Delta\varepsilon_i = s_{ij}\,\Delta\sigma_j. \tag{1}$$

$$s_{13} = \left(\Delta\varepsilon_1 / \Delta\sigma_3 \right) \Big|_{\text{constant } p_c} \tag{2}$$

$$s_{33} = \left(\Delta\varepsilon_3 / \Delta\sigma_3 \right) \Big|_{\text{constant } p_c} \tag{3}$$

$$s_{23} = -s_{13} + \Delta\varepsilon_3 / \Delta p_c - s_{33}\ \Delta\sigma_3 / \Delta p_c \tag{4}$$

where $\Delta\sigma_3$ in (4) is related to the confining pressure increment and the measured change in force per sample cross-sectional area, F*, as indicated by the external load cell through:

$$\Delta\sigma_3 = -(A_p - A_s)\,\Delta p_c / A_s + F^*. \tag{5}$$

A_p and A_s are the cross-sectional areas of the piston and the sample respectively. The remaining relationship gives the sum

$$(s_{11} + s_{12}) = \Delta\varepsilon_1 / \Delta p_c - s_{13}\ \Delta\sigma_3 / \Delta p_c \tag{6}$$

where $\Delta\sigma_3$ is as in (5).

RESULTS AND DISCUSSION

Representative strain ellipses for experiments of the first type are shown in Figures 3-1b, 3-2a and b. Below 90 percent of the sample fracture strength, the measured points deviate from the computed ellipse by strains which are always less than 5 parts in 10^5, indicating that the measured strain is homogeneous within experimental resolution. Above about 90 percent of the fracture strength, however, the points deviate from the best-fit ellipse by larger amounts indicating that the strain near fracture is no longer homogeneous. This is especially true of samples which failed in a complex manner with several intersecting pairs of conjugate faults. These results are consistent with those of Scholz (1968b) and Mogi (1968) who showed that somewhere above 90 percent of the fracture strength, microfractures which previously had a random distribution within their rock samples began to cluster along the developing fault.

The orientation and magnitude of the principal axes of the circumferential strain ellipses are shown in Figures 3-3 and 3-4 at various points in the loading history of the rock samples. Results for the four samples tested are tabulated in Table 3-1. In the case of simple faulting, the major axis of the strain ellipse becomes nearly perpendicular to the ultimate fracture trace fairly early and more or less remains that way. Such an orientation is to be expected inasmuch as the fault represents an expression of a preferred direction of cracking in the rock. Although the strain ellipses shown here are for total strain --

Figure 3-2. Representative strain ellipses for samples under loads less than (a) and greater than (b) 90 percent of the peak sample strength.

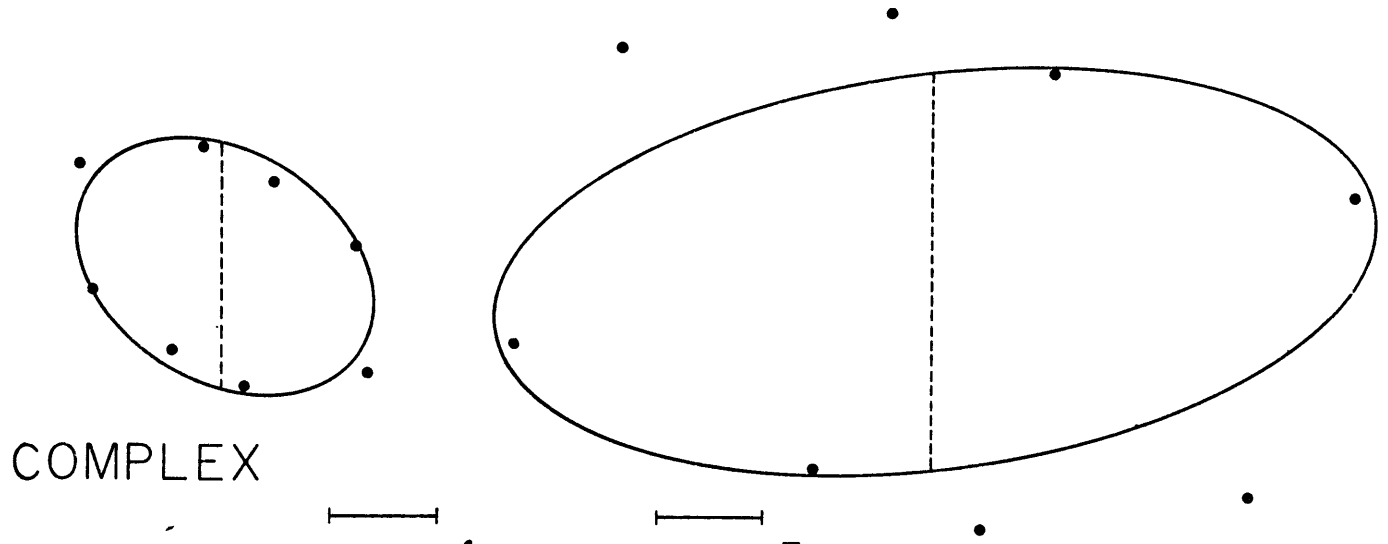

35 % FRACTURE STRENGTH 100

(a) (b)

Figure 3-3. Magnitude and orientation of principal circumferential strains during loading history for a sample which failed on a single through-going fracture. Stress-volumetric strain curve is shown to the left; dashed lines indicate the stress to which principal strains drawn at the same horizontal position refer. Dotted lines schematically place each set of strain axes in the loading sequence. Strains are also symbol-coded to their respective stress cycles. Orientation of the ultimate fault would plot as a vertical line with respect to the coordinate system of the principal strain axes.

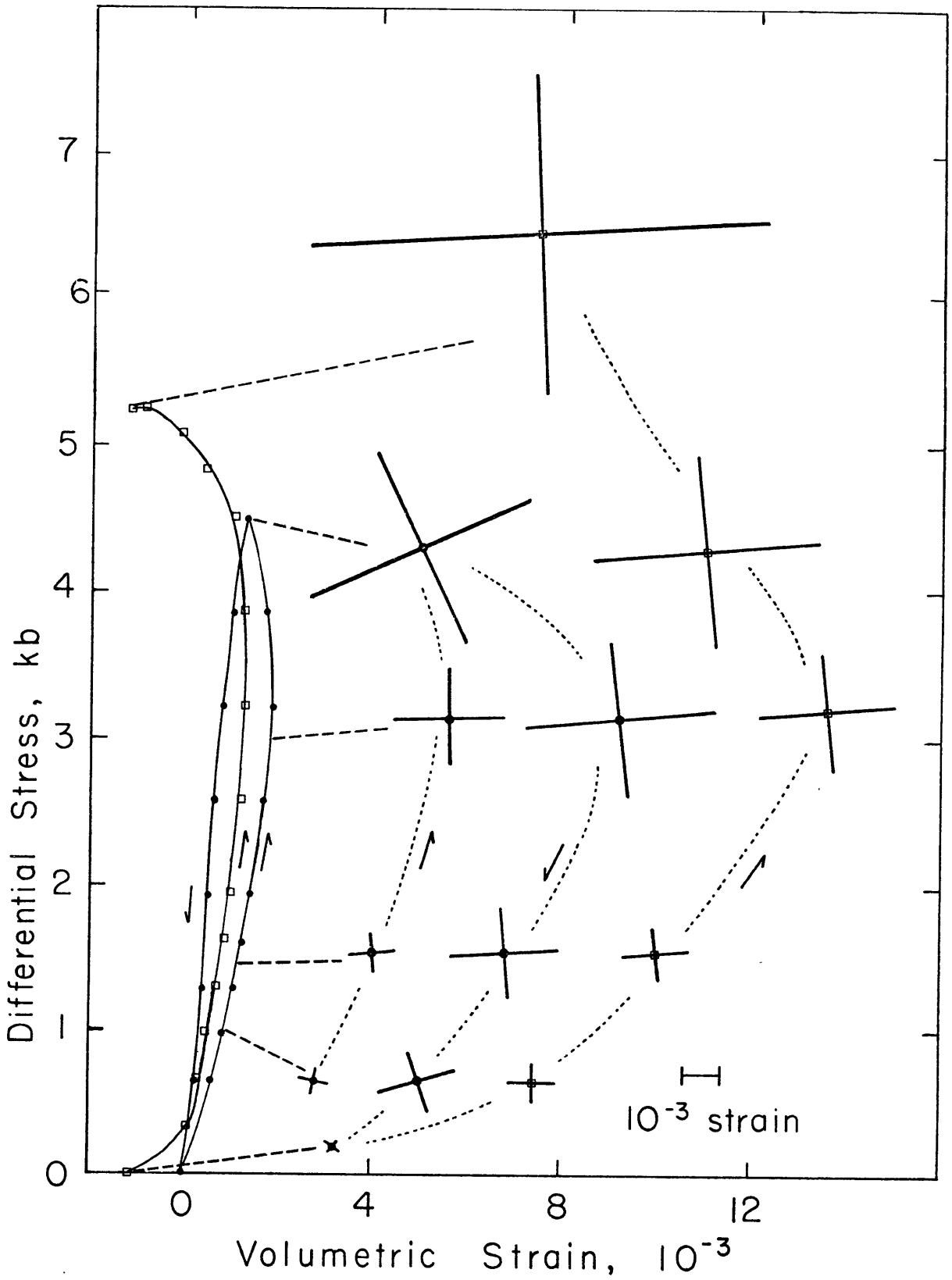
Differential Stress, kb
0
1
2
3
4
5
6
7
0
4
8
12
Volumetric Strain, 10^{-3}
10^{-3} strain

Figure 3-4. Magnitude and orientation of principal circumferential strains during loading for a sample which failed on several intersecting fractures. Stress-volumetric strain curve is shown at right; dashed lines and orientation of the main fault trace as in Figure 3-3. Strain axes illustrated are for the loading portion of the stress cycles only.

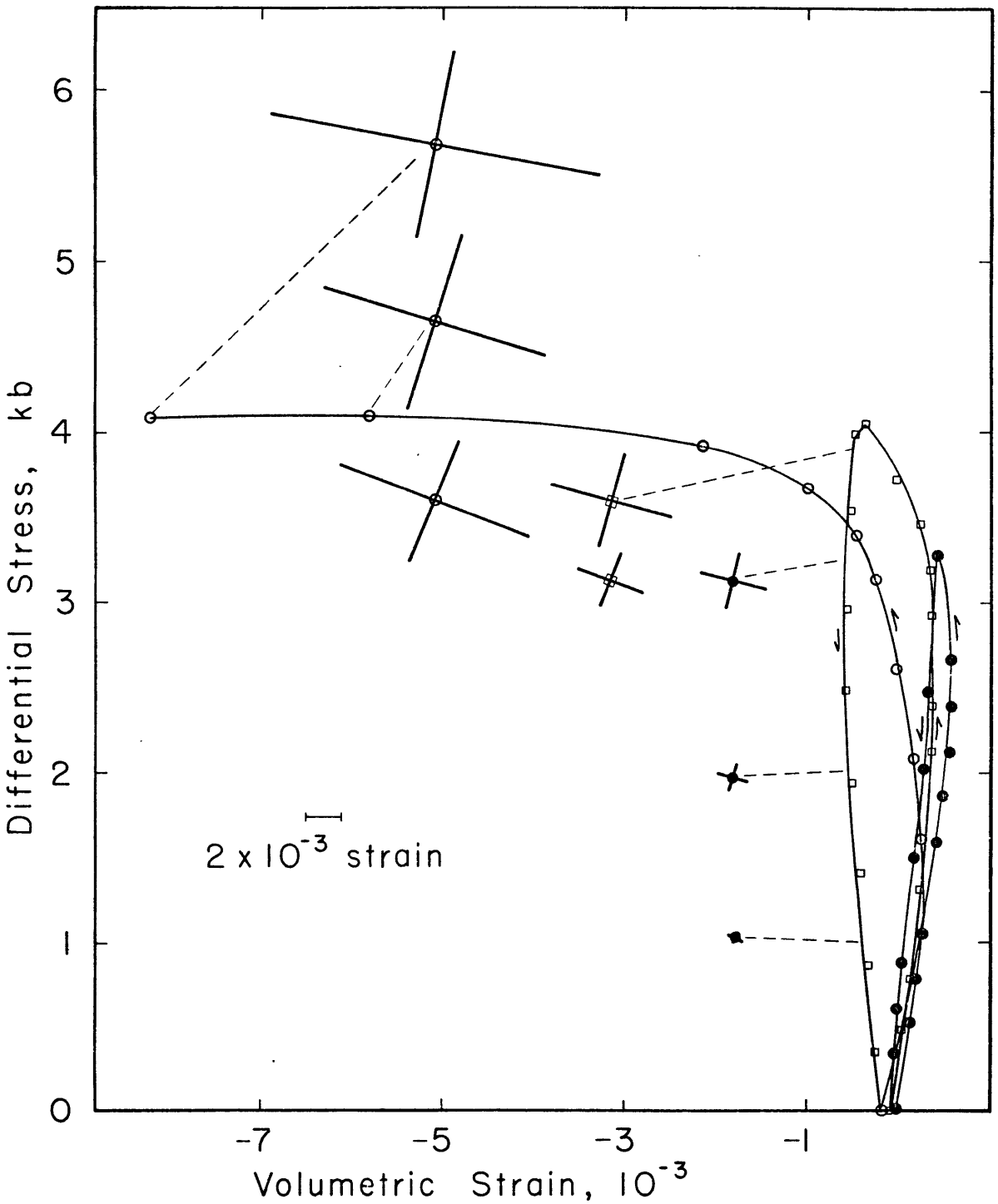
Differential Stress, kb
6
5
4
3
2
1
0
-7
-5
-3
-1
Volumetric Strain, 10^{-3}
2×10^{-3} strain

TABLE 3-1

Cycle #	Stress (kb)	A Λ Fault trace (o)	-A (10^{-3} strain)	-B strain)
Sample #1	(complex)			
1	1.00	-23	0.35	0.43
1	2.00	-21	0.75	0.87
1	3.26	-14	1.61	1.89
2	3.26	-20	1.60	1.92
2	3.95	-16	2.77	3.46
3	3.95	-21	3.62	5.63
3	4.08	-17	5.06	7.49
3	F	-10	5.38	9.33
Sample #2	(simple)			
1	1.00	-12	0.33	0.40
1	1.50	- 5	0.55	0.63
1	3.00	2	1.34	1.50
1	4.47	25	2.82	3.19
1	3.00	5	2.10	2.53
1	1.50	4	1.24	1.47
1	1.00	7	0.87	1.09
2	0.00	-16	0.19	0.24
2	1.00	- 1	0.53	0.64
2	1.50	4	0.73	0.90
2	3.00	5	1.58	1.84
2	4.47	5	2.61	3.00
2	5.20	6	4.23	6.10
2	F	4	4.32	6.15
Sample #3	(complex)			
1	1.00	12	0.38	0.40
1	1.50	3	0.56	0.60
1	3.20	- 5	1.30	1.50
2	1.50	1	0.65	0.73
2	3.20	- 3	1.27	1.50
2	4.50	- 1	2.20	2.86
2	5.77	9	5.02	8.57
2	F	8	4.76	9.36

TABLE 3-1 (continued)

Cycle #	Stress (kb)	A ∧ Fault trace (°)	-A (10^{-3} strain)	-B
Sample #4	(simple)			
1	1.00	40	0.35	0.46
1	1.50	26	0.66	0.76
1	1.88	11	1.05	1.24
2	1.88	8	0.79	0.97
2	4.41	10	2.61	3.39
3	1.88	7	0.82	0.93
3	4.41	8	2.55	3.54
3	5.12	10	4.37	6.54

including the contribution from the poisson expansion of the constituent mineral phases as well as that due to cracking -- previous studies on Westerly Granite (Brace, 1965) revealed a directional anisotropy in linear compressibility of less than 5 percent at high confining pressures; thus the intrinsic strains developed in response to an applied stress should be very nearly the same as those of an isotropic material. Yet the strain anisotropy exceeds 10 percent very quickly after the onset of dilatancy as determined from the stress-volumetric strain curve, and persists through repeated cycling. $(\varepsilon_{max} - \varepsilon_{min})/\varepsilon_{min}$ at the stress equal to the frictional strength of the rock at 500 bars confining pressure is about 15 percent. Anisotropy prior to failure always exceeds 30 percent; specimens in which complex faults are developing show even greater strain anisotropy at the higher stress levels.

In our loading system, complex faulting probably results from the interference of at least two sets of subequally preferred failure directions. The orientation of the main fracture cannot be predicted from the measured strain anisotropy until quite late in the loading sequence, suggesting that the manner in which the competing systems interfere is as important as the initial crack anisotropy in determining the location of the main fault.

Measured pseudoelastic compliances for 4 granites and a gabbro are given in Table 3-2 and illustrated for the granites in Figures 3-5 and 3-6. If the rocks were axisymmetric, s_{13} and s_{23} should be equal. Indeed, at 500 bars confining

TABLE 3-2

Cycle #	Stress	$-s_{13}$ ($mbar^{-1}$)	$-s_{23}$ ($mbar^{-1}$)	s_{33} ($mbar^{-1}$)	$s_{11}+s_{12}$ ($mbar^{-1}$)
Granite p_c = 500 bars					
2	2.52	0.37±.05	0.20±.10	1.14±.05	1.11±.10
2	3.64	0.41	0.23	1.21	1.25
2	2.99	0.42	0.36	1.26	1.34
2	1.99	0.37	0.31	1.26	1.12
6	0.64	0.37	0.28	1.35	1.04
6	2.47	0.38	0.42	1.18	1.22
6	3.61	0.41	0.41	1.19	1.36
6	3.23	0.42	0.45	1.21	1.42
6	1.14	0.39	0.32	1.30	1.18
13	0.72	0.30	0.39	1.19	1.10
13	2.47	0.39	0.23	1.20	1.15
13	3.09	0.41	0.63	1.25	1.38
13	1.31	0.36	0.37	1.31	1.20
17	0.70	0.35	0.23	1.34	1.07
17	2.50	0.40	0.37	1.22	1.25
17	3.61	0.41	0.45	1.19	1.32
17	3.09	0.38	0.37	1.12	1.33
17	1.31	0.38	0.18	1.25	1.15
21	0.72	0.36	0.30	1.37	1.09
21	2.47	0.38	0.30	1.22	1.21
21	3.61	0.40	0.34	1.16	1.39
21	4.64	0.41	0.32	1.18	1.45
21	2.68	0.40	0.38	1.19	1.34
21	1.17	0.36	0.10	1.28	1.11
Granite, p_c = 500 bars					
3	0.63	0.36	0.38	1.43	1.16
3	2.68	0.36	0.31	1.25	1.29
3	4.19	0.38	0.29	1.28	1.53
3	3.58	0.40	0.37	1.32	1.63
8	0.57	0.34	0.37	1.37	1.16
8	2.48	0.37	0.44	1.26	1.33
8	4.09	0.40	0.35	1.34	1.61
14	2.37	0.38	0.42	1.28	1.37
14	4.44	0.41	0.71	1.31	1.99
14	3.03	0.41	0.27	1.31	1.60
14	1.42	0.40	0.43	1.37	1.34

TABLE 3-2 (continued)

Cycle #	Stress	$-s_{13}$ ($mbar^{-1}$)	$-s_{23}$ ($mbar^{-1}$)	s_{33} ($mbar^{-1}$)	$s_{11}+s_{12}$ ($mbar^{-1}$)
Granite, p_c = 500 bars (continued)					
19	0.57	0.35	0.35	1.41	1.19
19	2.63	0.38	0.36	1.31	1.37
19	4.50	0.40	0.30	1.30	1.71
19	3.07	0.41	0.36	1.31	1.65
19	1.25	0.38	0.24	1.37	1.22
Gabbro, p_c = 500 bars					
2	2.26	0.27	0.31	1.02	0.91
2	3.44	0.26	0.45	0.95	1.03
2	2.86	0.34	0.18	1.09	1.02
2	1.12	0.35	0.27	0.94	0.89
7	0.36	0.38	0.04	1.09	1.23
7	2.23	0.33	0.13	1.09	0.89
7	3.44	0.36	0.10	1.17	1.00
7	2.87	0.35	0.35	1.11	1.10
7	1.12	0.32	0.27	1.07	0.94
12	2.23	0.35	0.20	1.17	0.96
12	3.44	0.36	0.25	1.09	1.07
12	2.84	0.35	0.47	1.14	1.12
12	1.11	0.33	0.12	1.08	1.00
19	0.40	0.38	0.25	1.22	1.27
19	2.26	0.35	0.24	1.14	0.96
19	3.47	0.35	0.33	1.11	1.06
19	2.89	0.35	0.25	1.11	1.03
19	1.17	0.33	0.46	1.08	1.06
Granite, p_c = 1500 bars					
1	2.02	0.32	0.32	1.22	0.92
1	5.97	0.34	0.48	1.22	1.00
6	1.54	0.29	0.36	1.19	0.96
6	3.62	0.31	0.26	1.19	0.99
6	6.09	0.35	0.04	1.25	0.95
6	3.81	0.35	0.16	1.25	1.00
6	1.23	0.31	0.27	1.18	1.00

TABLE 3-2 (continued)

Cycle #	Stress	$-s_{13}$ ($mbar^{-1}$)	$-s_{23}$ ($mbar^{-1}$)	s_{33} ($mbar^{-1}$)	$s_{11}+s_{12}$ ($mbar^{-1}$)
Granite, p_c = 1500 bars					
1	1.23	0.31	0.20	1.18	0.89
1	2.43	0.38	0.04	1.30	0.86
1	6.21	0.40	0.03	1.26	0.87
1	4.61	0.34	0.30	1.19	0.95
1	1.23	0.33	0.24	1.24	0.92
6	1.54	0.33	0.29	1.19	0.93
6	3.87	0.31	0.33	1.15	0.96
6	6.09	0.36	0.10	1.19	0.90
6	3.95	0.34	0.17	1.19	0.95
6	0.98	0.33	0.24	1.22	0.92
11	1.17	0.39	0.28	1.30	1.06
11	3.54	0.38	0.39	1.24	1.11
11	6.68	0.40	0.00	1.26	0.95
16	1.07	0.33	0.14	1.31	0.93
16	3.42	0.36	0.15	1.29	0.94
16	6.03	0.39	-0.01	1.33	0.94
16	4.18	0.37	0.14	1.29	0.97
16	2.32	0.34	0.20	1.29	0.93
20	1.08	0.34	0.20	1.31	0.93
20	3.96	0.34	0.17	1.27	0.94
20	6.88	0.39	-0.06	1.25	1.06
20	4.99	0.37	0.15	1.26	1.00
20	1.67	0.34	0.21	1.31	0.95

Figure 3-5. Variation of pseudoelastic compliances s_{23} (circles) and s_{13} (squares) with mean pressure. Open symbols, samples at 500 bars confining pressure; filled symbols, samples at 1500 bars confining pressure. Squares are $\pm$ 0.05 $mbar^{-1}$; circles, $\pm$ 0.10 $mbar^{-1}$. Dashed line is the crack free value of s_{ij} ($i,j = 1,2,3$; $i \neq j$) computed from the constituent mineral compliances.

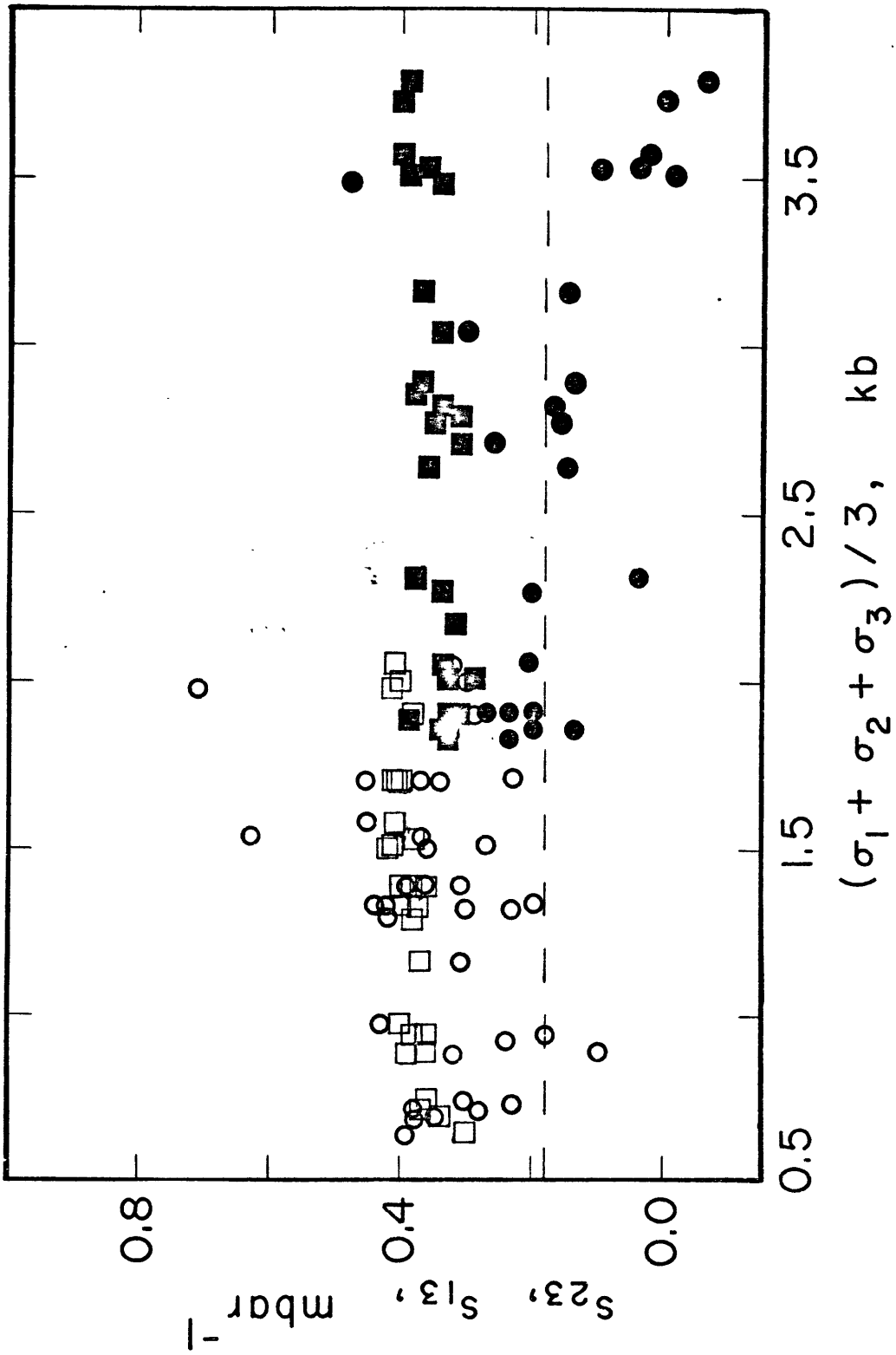
0.8
0.4
0.0
S_{23}, S_{13}, mbar^{-1}
0.5
1.5
2.5
3.5
$(\sigma_1 + \sigma_2 + \sigma_3)/3$, kb

Figure 3-6. Same as Figure 3-5 except that circles are now $s_{11} + s_{12} + 0.35$, squares are s_{33}. Dashed line is the crack free value of s_{ii} $(i = 1,2,3)$.

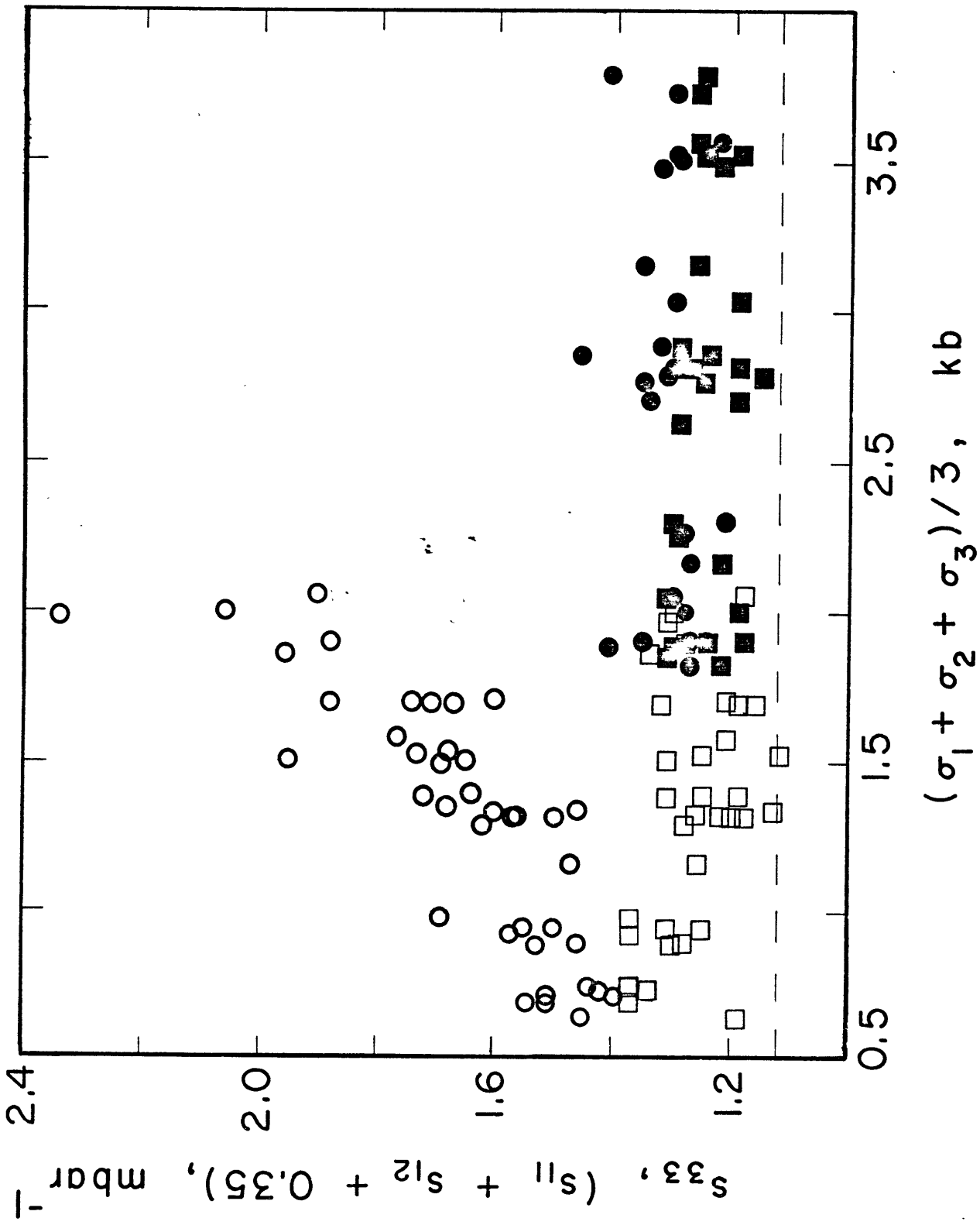
s_{33}, $(s_{11} + s_{12} + 0.35)$, mbar^{-1}
2.4
2.0
1.6
1.2
0.5
1.5
2.5
3.5
$(\sigma_1 + \sigma_2 + \sigma_3)/3$, kb

pressure (open symbols, Figure 3-5), they appear to be. At 1500 bars however (solid symbols, Figure 3-5), the values diverge at high stress. Unfortunately, the patterns seen here are not unique to the rock. They depend, as do all the elastic properties, on stress level and loading path. $|s_{13}|$, which increases by perhaps 10 percent with increasing axial stress, is determined by making small cycles in σ_3. Its slight increase in magnitude may be attributed to either more abundant or longer open axial cracks at higher stresses. s_{23} is determined from excursions in confining pressure. These excursions were in all cases 300 bars. This apparently represents a substantial change in conditions for a rock under only 500 bars confining pressure, and a less significant change at 1500 bars. Indeed at 500 bars, the excursions are much greater than necessary to close up the stress-induced cracks and the rock responds in the axial direction as if those cracks were not present. Within the scatter of the data, $s_{13} = s_{23}$. At 1500 bars confining pressure, however, 300 bars additional confining pressure does not close up all the cracks, especially at high stress. Above the onset of dilatancy (mean pressure = 2.9 kbar at 1500 bars confining pressure), changing σ_1 and σ_2 may act merely to close down some of the crack space, leaving ε_3 unaffected. s_{23} falls to zero, just as poisson's ratio would do in an orthotropic solid composed of alternate layers of air and rock compressed parallel to the layers. The apparent anisotropy in s_{13} and s_{23} determined from the small stress cycle and confining

pressure excursion tests is thus a function of the method of measurement. The 3 different variables affecting these pseudoelastic constants (actual azimuthal anisotropy of the crack + rock aggregate, amount of crack closure, and energy dissipated in inelastic processes) cannot be separated.

Anisotropy between the axial and diametral directions shows up clearly, however, in the disparate behavior of s_{33} and $s_{11} + s_{12} + 0.35$ (Figure 3-6). At 500 bars confining pressure, s_{33} (squares) decreases to a constant level of about 1.25 $mbar^{-1}$. The decrease in compliance presumably results from the closure of cracks oriented normal or sub-normal to $0x_3$. Once these cracks have been closed the compliance maintains a constant value near the intrinsic one (dashed line, Figure 3-6). 1500 bars evidently suffices to close most cracks initially present in the unconfined rock; at this pressure, no change in s_{33} is observed as axial load increases.

At 500 bars, the sum $s_{11} + s_{12} + 0.35$ to a first approximation represents the behavior of s_{11}, taking s_{12} = constant = -0.35 $mbar^{-1}$. At this confining pressure, s_{11} increases greatly indicating that the rock becomes progressively more compliant perpendicular to the loading direction as the load is applied. Again, this requires more or longer axial cracks in the stressed material.

At 1500 bars pressure, there is no suggestion of such behavior. The constancy in $s_{11} + s_{12} + 0.35$ may occur because opening cracks are very narrow features under such confinement, or because changes in s_{11} are offset by changes in s_{12}.

Unfortunately, small confining pressure and stress excursions were not made for samples with multiple sets of circumferential strain gauges so direct comparison between the two types of test we conducted is not possible. However, the observed changes in elastic compliances are in qualitative agreement with changes in seismic velocities previously reported from laboratory studies (Matsushima, 1960; Thill, 1972; Hadley, 1975). An exact comparison cannot be made as we have only 3^{+} of the possible 21 elastic compliances necessary to solve the characteristic equation completely.

$$|s_{ijkl}^{-1} \ell_k \ell_l - \rho v^2 \delta_{ij}| = 0 \qquad (7)$$

where the compliance is now given its full tensor notational subscripts, the ℓ_i are direction cosines of the wave front normal and ρ is the aggregate density (Hearmon, 1961). If we assume that the starting material is isotropic and that all unknown elastic constants retain their initial values, then the decrease in diametral seismic velocity at high stress calculated from the change in the s_{ijkl} is of the order of 20 percent.

CONCLUSIONS

While the results of our experiments are consistent with the opening of cracks perpendicular to the direction of maximum compression, $0x_3$, their azimuthal distribution is not uniform. Anisotropy of strains in the 1,2-plane may reach

100 percent or more at high stress levels, and generally exceeds 10-15 percent at stresses below the frictional strength of the rock. Thus, aximuthal variations in dilatancy may produce apparent sample to sample variations in laboratory measurements of directional physical properties in relatively isotropic rocks unless measurement path orientations are standardized with respect to preferred directions of cracking within the rock.

Regarding dilatant rock as having hexagonal symmetry is suitable for order of magnitude calculations and extrapolations in the case of intrinsically nearly isotropic material under axially symmetric loading. When rocks have a modest fabric or when the intermediate stress is even slightly different from the minimum value, this assumption could be grossly inacurrate. Worse, ignoring possible azimuthal variations in rock properties when processing field data may result in erroneous or incomplete interpretations. The strain anisotropy reported in our laboratory experiments is in all cases sufficient such that a directional variation in strain dependent properties should be observable <u>in situ</u> when measurements are made in the plane perpendicular to the greatest principal stress and the in-plane stresses are equal. In a tectonically active area, it is unlikely that any combination of stress states and measurement paths would result in less strain anisotropy than observed here. Consequently, an azimuthal variation of dilatancy dependent properties should be the observed rule rather than the exception. Failure to recognize it as such could result

in the incorrect reporting of a temporal variation of some material property. On the positive side, such anisotropy might be exploited to determine the strike of a future fault break, or the next site of motion.

CHAPTER 4

V_p/V_s ANOMALIES IN DILATANT ROCK SAMPLES

INTRODUCTION

Ever since Russian seismologists first correlated large changes in the travel time ratio of transverse to longitudinal seismic waves with the time of occurrence of earthquakes (Semenov, 1969; Nersesov, et al. 1969; Whitcomb, et al. 1973), considerable controversy has existed about their cause. New field data from California and New York State (Anderson and Whitcomb, 1973; Aggarwal, et al. 1975) imply that the drop in t_s/t_p is due to a large drop in compressional wave velocity coupled with a somewhat smaller drop in shear wave velocity.

Although it is widely assumed in this country that dilatancy is responsible for the field observations, various combinations of dry, partially saturated or vapor-filled cracks have been invoked to account for the t_s/t_p decrease (Nur, 1972; Scholz, et al. 1973; Anderson and Whitcomb, 1973). Existing laboratory data are insufficient to eliminate any one of these mechanisms, or even to answer the more fundamental questions: Starting with a saturated rock, can dry or partially saturated cracks be created such that t_s/t_p will drop? Or, starting with a water-saturated rock above 100°C, can enough of that water be converted to vapor in the dilating material such that t_s/t_p will decrease? To date, with one exception (Bonner, 1975), the only laboratory measurements of dilatancy-related velocity changes have been conducted on dry materials (Tocher, 1957;

Matsushima, 1960a; Thill, 1973). Only in two investigations was the shear wave velocity measured (Bonner, 1974, personal communication; Gupta, 1973a), and only in Gupta's work were V_p and V_s (of unknown polarization) measured simultaneously. Since strains were not recorded simultaneously in any of these experiments, one cannot quantitatively relate velocity changes to dilatant strains.

In this paper, results are presented from a set of laboratory experiments in which V_p and V_s and volumetric strains have been simultaneously recorded in dilating dry and saturated rocks. For the first time, this permits quantitative comparison of seismic velocities or their ratio and dilatant strains. Also for the first time, the crux of the dilatancy-fluid flow model has been tested.

PROCEDURE

The sample configuration is shown in Figure 4-1. Flats were ground into the surface of a right circular cylinder of Westerly granite or San Marcos gabbro 6.3 cm long and 3.2 cm in diameter. A thin (.05 mm) copper jacket surrounded the sample, excluding the confining pressure medium. Two HDT-31 ceramic transducers, one shear and one compressional, were mounted on the copper jacket in each flat region with conducting epoxy. The frequency of each was approximately 1 MHz. Only one transducer was driven at a time; velocities were determined at discrete points in the loading sequence using a mercury delay-line technique (Birch, 1961). Although the P arrival was clear,

Figure 4-1. Sample configuration.

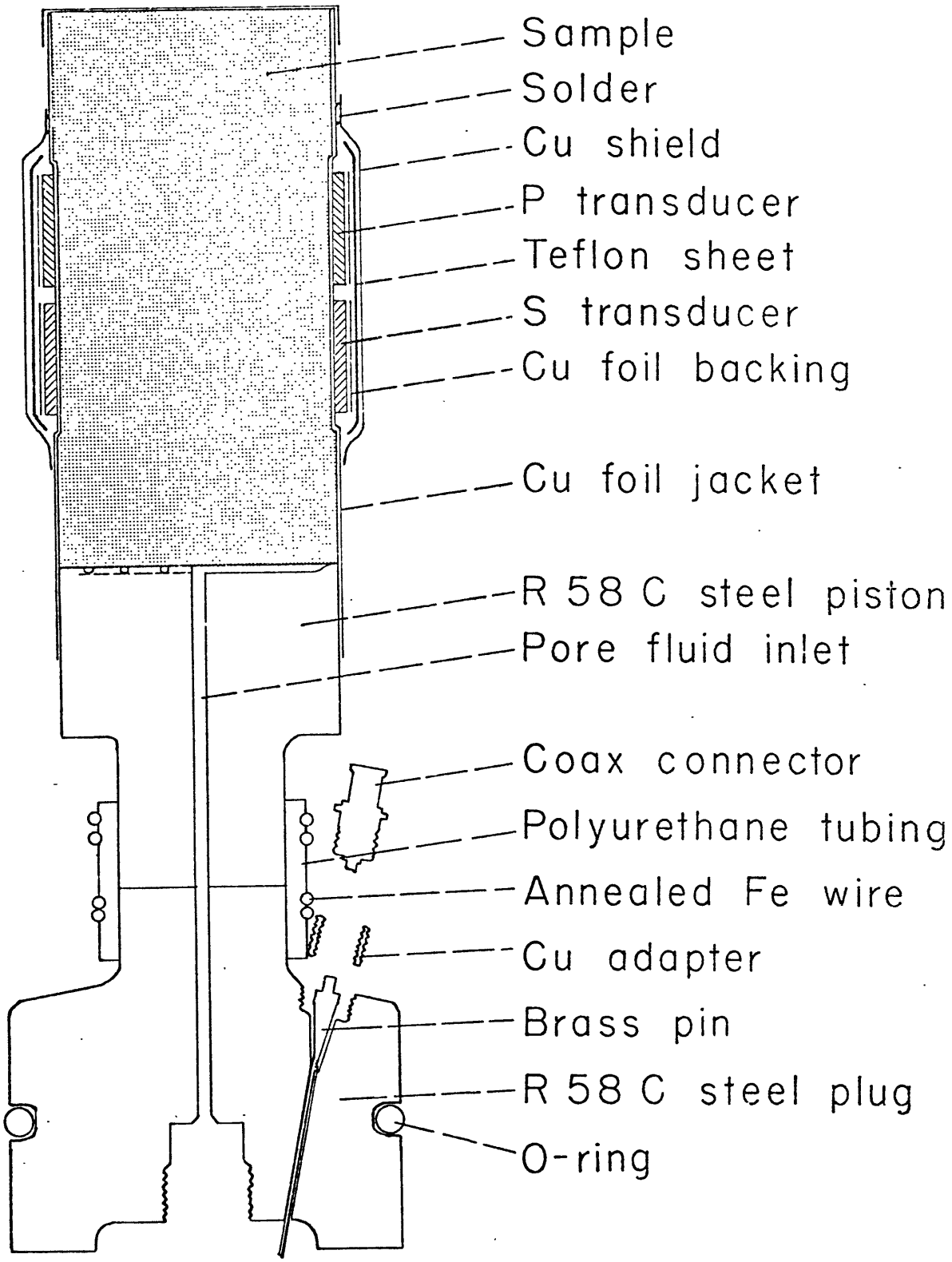
Sample
Solder
Cu shield
P transducer
Teflon sheet
S transducer
Cu foil backing
Cu foil jacket
R 58 C steel piston
Pore fluid inlet
Coax connector
Polyurethane tubing
Annealed Fe wire
Cu adapter
Brass pin
R 58 C steel plug
O-ring

the P coda prevented exact determination of the first arrival of S, especially at high stress when the signals became attenuated. For this reason, the peak of the first S pulse was chosen as the S arrival (Figure 4-2). This results in 10-12 percent lower values of V_S than are correct. Thus, the percent change in V_S will be somewhat smaller than reported here.

The effect of folding the P coda into the S arrival usually works in the opposite sense. The shear transducers generate a low amplitude compressional wave signal which precedes the larger shear pulse. Depending upon the changing delay in P arrival relative to S, this P signal may increase the apparent S velocity by about 1 percent as loading progresses. Thus the true decrease in V_S may be greater than the decrease reported here by as much as 10 percent of the reported value.

Velocities were measured in a direction transverse to the greatest principal stress. Large changes in velocity are observed in this direction compared with the direction parallel to the greatest principal stress (Matsushima, 1960a; Gupta, 1973a). The polarization of the shear waves was also chosen to be in the plane perpendicular to this stress, as this polarization was anticipated to give the greatest possible change in shear wave velocity in response to the opening of axial cracks under load. That it does indeed do so is shown by the results in Figure 4-3, and confirmed by Bonner, (personal communication).

Confining pressure was 390 bars. This low value was chosen so that large dilatant strains could be achieved easily

Figure 4-2. Typical P and S arrivals in granite with 350 bars pore water pressure, 390 bars confining pressure.

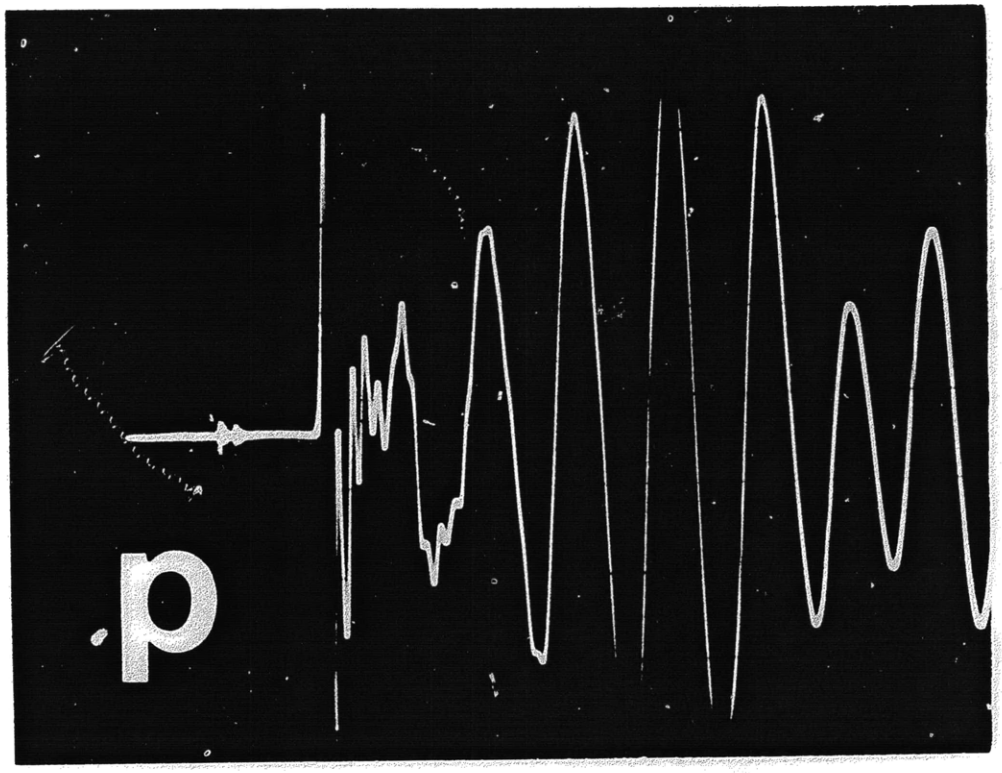
p

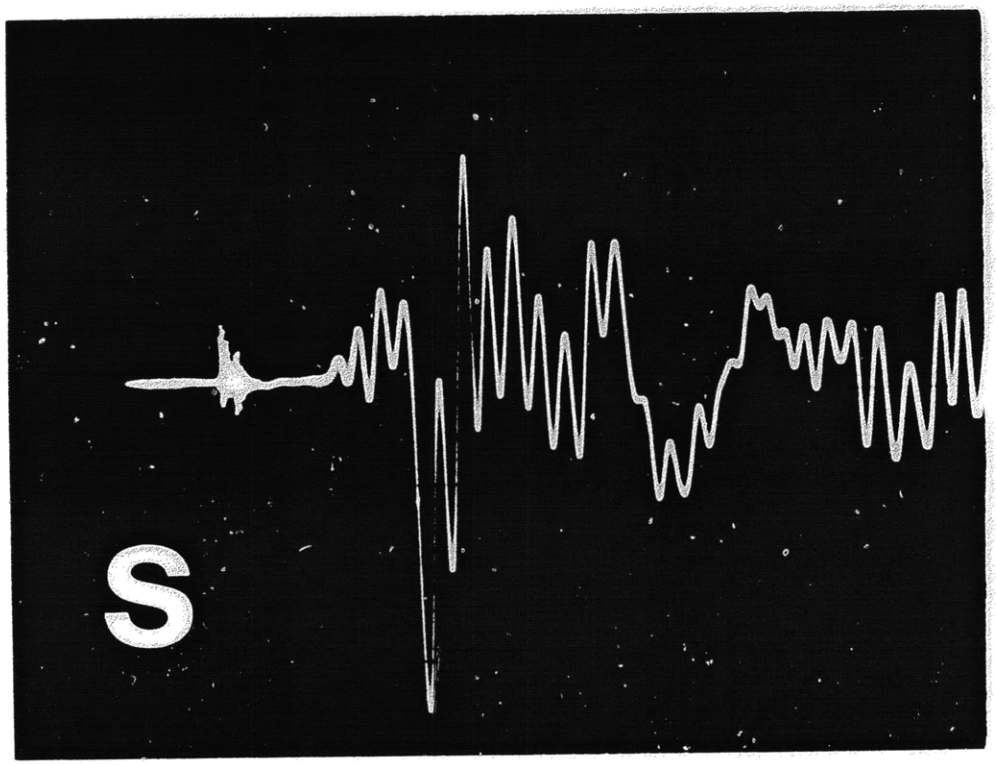
S

Figure 4-3. Change in shear wave velocity with dilatant volumetric strain for two polarizations of S. Circles, polarization parallel to σ_{max}; crosses, polarization perpendicular to σ_{max}.

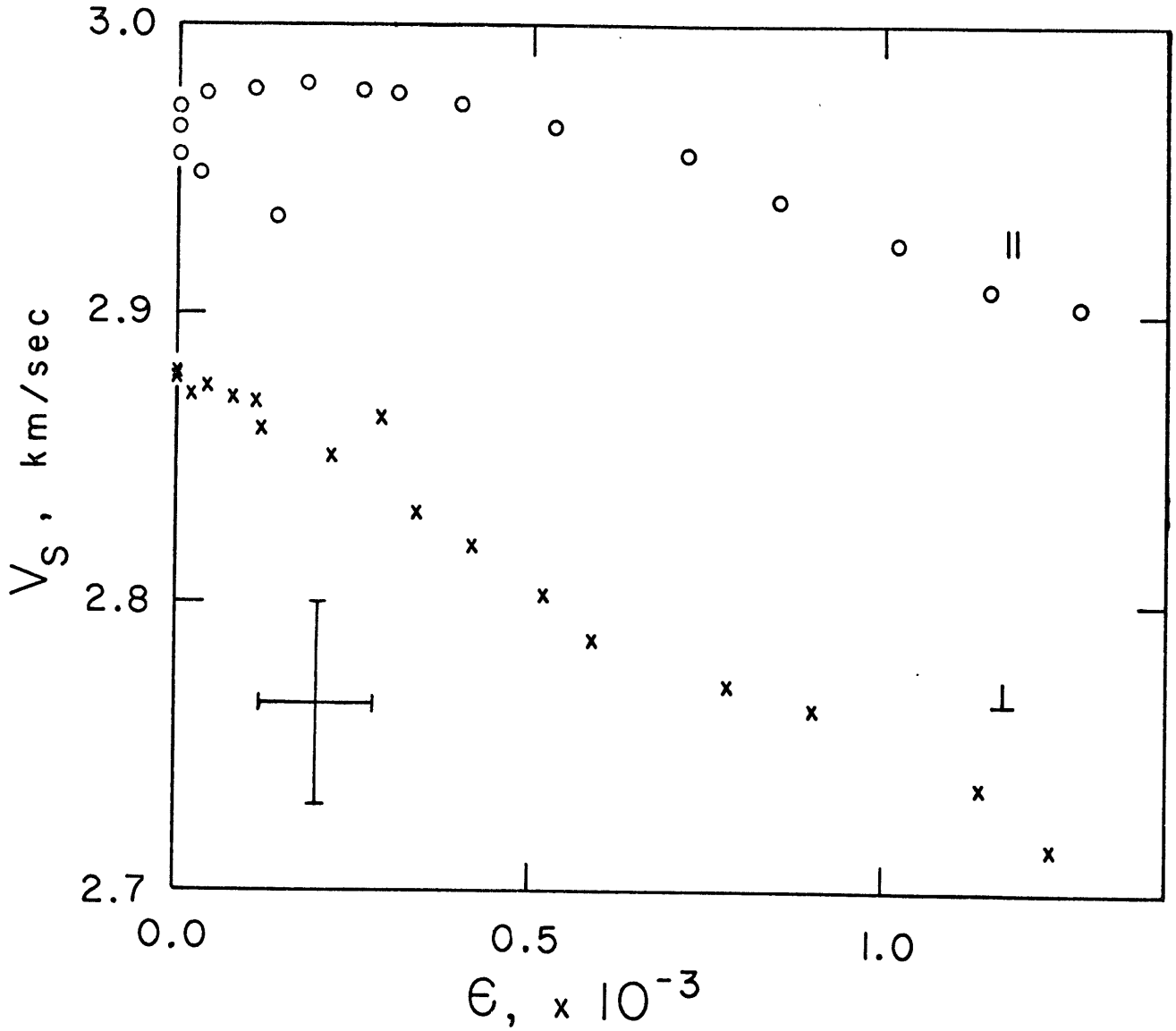
3.0
2.9
2.8
2.7
V_S, km/sec
0.0
0.5
1.0
ϵ, x 10^{-3}
||
⊥

and large variations in seismic velocity could be observed. Pore water pressure was initially chosen to be 350 bars. Later experiments were carried out with a pore pressure of 1 bar when it became apparent that partial saturation could not be developed at available strain rates with the higher pore pressure.

Because it was not possible to heat the sample assembly to temperatures in excess of 100°C, CO_2 was used instead of water to determine the effect of a liquid vapor pore fluid transition on seismic velocities. 62 bars is the liquid-vapor transition pressure of CO_2 under ambient laboratory temperatures. Initially, CO_2 pore pressures used were in excess of this value, 112 and 68 bars, but when no decrease in V_p/V_s developed, an experiment was run at the transition pressure.

All of the experiments run with CO_2 as the pore fluid were run with a constant mass of fluid available to the sample. When water was used as the pore fluid, the reservoir fluid pressure was usually maintained at a constant value by addition or subtraction of water from the system. Pore pressure values stated in this report are those measured at the reservoir; local fluid pressures within the rock departed from those values during the experiments.

For comparison with wet results, some tests were performed on air dry samples. These rocks were soaked in acetone for several days after machining to dissolve any oil in them, and then evacuated for 24 hours at room temperature. They were then exposed to the atmosphere before jacketing. Relative

humidity in the laboratory is about 60-80 percent, but these rocks will be referred to as dry in this paper.

Strain rate is not so important in the case of dry rocks because no kinetics of pore fluid motions are involved, but it becomes crucial when pore fluids are present as seismic velocities may be expected to behave differently when there is insufficient time for fluids to communicate between cracks. The fastest controllable loading rate available for these experiments was 1.5×10^{-4}/sec; the slowest rate practical was 1.5×10^{-7}/sec. Unloading had to be performed manually with pauses at each stress where velocities were measured.

Using a permeability of 10^{-6} darcies (= 10^{-14}cm/sec) for the granite at 40 bars effective pressure and a fluid viscosity of 1.4×10^{-8}bar-sec for water at 350 bars pressure (Brace, et al., 1968), equilibration of pore pressure to within 10 percent throughout the rock specimen requires a time, t, given by:

$$t > \lambda^2 \mu \beta / k$$

where λ is the sample length, μ the fluid viscosity, β the aggregate compressibility and k the permeability (Carslaw and Jaeger, 1959). Since this time is approximately 2 minutes, it is unlikely that the wet rock could be driven to undersaturation even at the fastest strain rates. Therefore, the wet granite was run at 1.5×10^{-5} and 1.5×10^{-6}/sec, the most convenient strain rates to use, with the expectation that saturated behavior would be observed as the rock dilated. Experimentally, this was the observed case.

Based on electrical resistivity measurements (Brace, et al.,

1965; Brace and Orange, 1968) and using the empirical formula of Brace et al. (1968) relating resistivity and permeability, the initial permeability of the gabbro is probably 20 times less than that of the granite. The compressibility is probably half as large, so the resulting equilibration time for the gabbro under comparable conditions is about 80 minutes. Therefore it seemed likely that the gabbro would be under-saturated at strain rates of 10^{-4}/sec, when peak load was reached in a few minutes but saturated at 10^{-6}/sec, when 5 or 6 hours were required to reach peak load.

Rock specimens were not loaded to failure but rather cycled in stress. Apart from the convenience of being able to use a single sample for many different tests, repeatedly stressed specimens more accurately reflect the properties of in situ rocks near active fault zones than does the virgin material. During each stress cycle, therefore, the rock was loaded to within 80 percent of its initial fracture strength. There is no need to investigate higher stresses, as in an active shallow to midcrustal fault zone, where pre-existing planes of weakness exist, stresses could reach no more than 60 percent to 70 percent of the intact fracture strength before sliding on fault surfaces occurred (Hadley, 1973).

Axial and circumferential strains were monitored continuously with conventional foil gauges glued to the sample jacket. These were summed electronically to produce a volumetric strain: $\varepsilon_v = 2\varepsilon_\theta + \varepsilon_z$. Because this study sought to clarify the effect of dilatancy on seismic velocities, it was necessary,

for each experiment, to determine an elastic reference line (Brace, et al. 1966) from which all dilatant volumetric strains, θ, could be measured ($\theta = \frac{\Delta V_{elastic} - \Delta V_{observed}}{\Delta V}$). This reference line presumably represents an intrinsic property of the material and should not change from cycle to cycle or from sample to sample of the same homogeneous rock type. However, several kilobars of confining pressure are required to close the crack space in most rocks, pressures clearly not achieved in these experiments. Due to the presence of open cracks, small differences in the elastic reference line were noted from sample to sample, regardless of rock type. Larger differences showed up in individual samples from cycle to cycle because effective confining pressure and therefore the number of open cracks varied. Moreover, the population of cracks in the sample may have changed slightly during each loading. However, consecutive cycles run at the same effective pressure and strain rate showed nearly identical behavior in strain and velocities (Figure 4-4, open circles and crosses). It was thus decided to take one elastic reference line for each specimen, specifically the one determined from the stress-volumetric strain curve for the second stress cycle. For any single specimen, therefore, all dilatant strains are referred back to the elastic reference line for the second stress cycle, and that cycle was conducted dry, so that the effective confining pressure was equal to the total confining pressure, 390 bars. When referenced that way, dilatant volumetric strain and velocities match closely for two different samples having similar stress histories (open and

→ Pg 102

Figure 4-4. Change in compressional wave velocity with θ in dry granite. Crosses, sample W1, cycle 3; open circles, sample W1, cycle 2; filled circles sample W2, cycle 2.

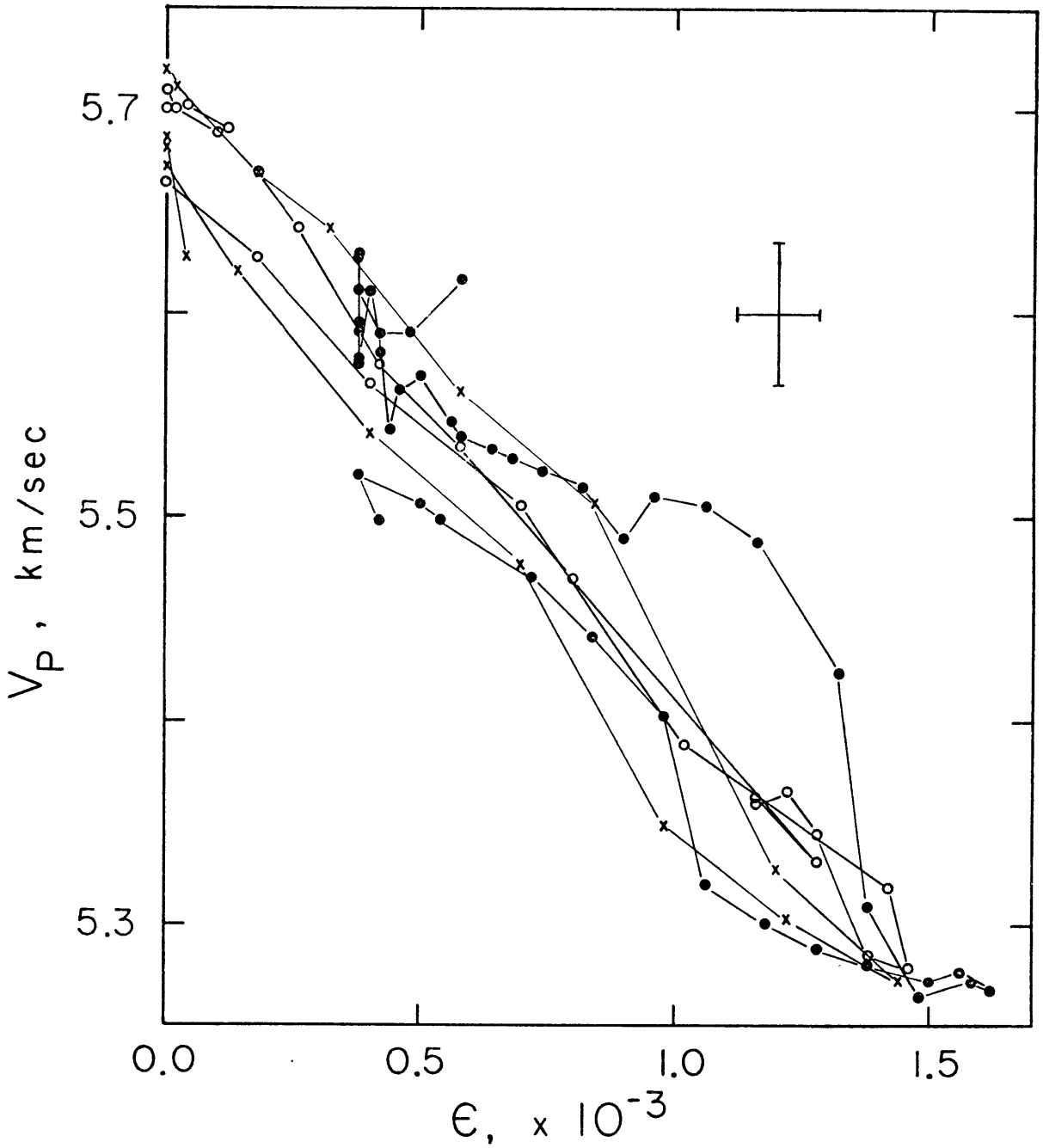
5.7
5.5
5.3
V_P, km/sec
0.0
0.5
1.0
1.5
ϵ, x 10^{-3}

TABLE 4-1

Sample #W1, Cycle #2, Dry, $\dot{\varepsilon} = 10^{-6}$/sec

Stress kb	V_p km/sec	V_s km/sec	V_p/V_s	$V_p/(V_p)_o$	$V_s/(V_s)_o$	$(V_p/V_s)/(V_p/V_s)_o$	$e \times 10^{-3}$
0.0	5.690	not recorded	-	0.997	-	-	0.12
0.14	5.701		-	0.999	-	-	0.04
0.41	5.700		-	0.998	-	-	0.00
0.66	5.709		-	1.-	-	-	0.00
0.96	5.700		-	0.998	-	-	0.02
1.21	5.688		-	0.996	-	-	0.10
1.52	5.669		-	0.993	-	-	0.18
1.82	5.641		-	0.988	-	-	0.26
2.22	5.575		-	0.977	-	-	0.42
2.49	5.534		-	0.969	-	-	0.58
2.87	5.470		-	0.958	-	-	0.80

TABLE 4-1 (continued)

Sample #W1, Cycle #2, Dry, $\dot{\varepsilon} = 10^{-6}$/sec (continued)

Stress kb	V_p km/sec	V_s km/sec	V_p/V_s	$V_p/(V_p)_o$	$V_s/(V_s)_o$	$(V_p/V_s)/(V_p/V_s)_o$	$e \times 10^{-3}$
3.14	5.331		-	0.934	-	-	1.28
2.64	5.363		-	0.939	-	-	1.16
2.64	5.359		-	0.939	-	-	1.16
2.89	5.366		-	0.940	-	-	1.22
3.11	5.344		-	0.936	-	-	1.28
3.41	5.285		-	0.926	-	-	1.38
3.17	5.279		-	0.925	-	-	1.46
2.62	5.318		-	0.932	-	-	1.42
2.07	5.388		-	0.944	-	-	1.02
1.53	5.506		-	0.964	-	-	0.70
0.96	5.566		-	0.975	-	-	0.40
0.55	5.627		-	0.986	-	-	0.18
0.0	5.664		-	0.992	-	-	0.0
Sample #W1, Cycle #3, Dry, $\dot{\varepsilon} = 10^{-5}$/sec							
0.0	5.628		-	0.984	-	-	0.04
0.14	5.681		-	0.993	-	-	0.0
0.44	5.686		-	0.994	-	-	0.0
0.87	5.720		-	1.-	-	-	0.0
1.24	5.711		-	0.998	-	-	0.02
1.71	5.669		-	0.991	-	-	0.18
2.07	5.641		-	0.986	-	-	0.32
2.62	5.561		-	0.972	-	-	0.58
2.98	5.507		-	0.963	-	-	0.84
3.36	5.326		-	0.931	-	-	1.20

TABLE 4-1 (continued)

Sample #W1, Cycle #2, Dry, $\dot{\varepsilon} = 10^{-6}$/sec (continued)

Stress kb	V_p km/sec	V_s km/sec	V_p/V_s	$V_p/(V_p)_o$	$V_s/(V_s)_o$	$(V_p/V_s)/(V_p/V_s)_o$	$\epsilon \times 10^{-3}$
1.55	5.477		-	0.958	-	-	0.70
1.00	5.541		-	0.969	-	-	0.40
0.46	5.621		-	0.983	-	-	0.14
0.0	5.671		-	0.991	-	-	.0.0

Sample #W1, Cycle #7, Dry, $\dot{\varepsilon} = 10^{-6}$/sec

0.0	5.501	2.942	1.870	0.997	0.997	1.001	0.20
0.7	5.507	2.942	1.872	0.998	0.997	1.002	0.14
0.16	-	2.949	-	-	0.999	-	0.06
0.28	5.510	2.950	1.868	0.999	1.000	0.999	0.02
0.51	5.507	2.950	1.867	0.998	1.000	0.999	0.0
0.65	5.516	2.951	1.869	1.-	1.-	1.000	0.0
0.76	5.514	2.951	1.869	1.000	1.-	1.000	0.0
0.85	5.536	2.944	1.880	1.004	0.998	1.006	0.0
0.92	5.524	2.943	1.877	1.001	0.997	1.004	0.0
0.99	5.502	2.941	1.871	0.997	0.997	1.001	0.0
1.06	5.496	2.935	1.872	0.996	0.996	1.001	0.0
1.13	5.494	2.935	1.872	0.996	0.995	1.002	0.0
1.20	5.495	2.933	1.874	0.996	0.994	1.003	0.02
1.27	5.478	2.929	1.870	0.993	0.993	1.001	0.06
1.34	5.454	2.924	1.865	0.989	0.991	0.998	0.10
1.41	5.446	2.919	1.866	0.987	0.989	0.998	0.10
1.49	5.427	2.911	1.864	0.984	0.986	0.997	0.12
1.56	5.403	2.904	1.861	0.980	0.984	0.996	0.14
1.64	5.405	2.899	1.864	0.980	0.982	0.997	0.16
1.77	5.399	2.883	1.873	0.979	0.977	1.002	0.18
1.93	5.397	2.860	1.887	0.978	0.969	1.010	0.24
2.05	5.343	2.841	1.881	0.969	0.963	1.006	0.28
2.26	5.293	2.820	1.877	0.960	0.956	1.004	0.30

TABLE 4-1 (continued)

Sample #W1, Cycle #8, p_w = 350 bars, $\dot{\varepsilon} = 10^{-6}$/sec (continued)

Stress kb	V_p km/sec	V_s km/sec	V_p/V_s	$V_p/(V_p)_o$	$V_s/(V_s)_o$	$(V_p/V_s)/(V_p/V_s)_o$	e x 10^{-3}
0.37	5.590	2.650	2.109	0.995	1.-	-	0.80
0.47	5.590	2.647	2.112	0.995	0.999	-	0.84
0.57	5.573	2.634	2.116	0.992	0.994	-	0.96
0.65	5.571	2.626	2.121	0.992	0.991	-	1.06
0.74	5.557	2.613	2.127	0.989	0.986	-	1.18
0.85	5.542	2.602	2.130	0.987	0.982	-	1.30
0.93	5.529	2.592	2.133	0.985	0.978	-	1.42
1.03	5.515	2.581	2.137	0.982	0.974	-	1.58
1.13	5.504	2.564	2.147	0.980	0.968	-	1.74
1.22	5.491	2.555	2.149	0.978	0.964	-	1.90
1.30	5.481	2.540	2.158	0.976	0.958	-	2.04
1.41	5.447	2.523	2.159	0.970	0.952	-	2.24
1.49	5.431	2.505	2.168	0.967	0.945	-	2.40
1.56	5.416	2.487	2.178	0.964	0.938	-	2.56
1.63	5.399	2.465	2.190	0.961	0.930	-	2.70
1.70	5.396	2.448	2.204	0.961	0.924	-	2.84
1.75	5.379	2.419	2.224	0.958	0.913	-	2.98
1.81	5.353	2.398	2.232	0.953	0.905	-	3.18
1.87	5.353	2.387	2.243	0.953	0.901	-	3.28
1.92	5.332	2.361	2.258	0.942	0.891	-	3.42
1.98	5.258	2.346	2.241	0.936	0.885	-	3.60
1.98	5.269	2.339	2.253	0.938	0.883	-	3.68
1.84	5.263	2.334	2.255	0.937	0.881	-	3.64
1.56	5.271	2.323	2.269	0.939	0.877	-	3.56
1.56	5.270	2.326	2.266	0.938	0.878	-	3.52
1.27	5.301	2.323	2.282	0.944	0.877	-	3.32
0.99	5.313	2.321	2.289	0.946	0.876	-	2.98
0.71	5.347	2.333	2.292	0.952	0.880	-	2.84
0.71	5.361	2.359	2.273	0.955	0.890	-	2.48
0.42	5.414	2.400	2.256	0.964	0.906	-	1.96
0.14	5.438	2.502	2.173	0.968	0.944	-	1.36

TABLE 4-1 (continued)

Sample #W1, Cycle #8, p_w = 350 bars, $\dot{\varepsilon} = 10^{-6}$/sec (continued)

Stress kb	V_p km/sec	V_s km/sec	V_p/V_s	$V_p/(V_p)_o$	$V_s/(V_s)_o$	$(V_p/V_s)/(V_p/V_s)_o$	$\theta \times 10^{-3}$
0.0	5.477	2.533	2.162	0.975	0.956	-	1.38
0.0	5.429	2.538	2.139	0.967	0.958	-	1.30
0.0	5.455	2.551	2.138	0.971	0.963	-	1.30 ?

Sample #W1, Cycle #9, p_w = 350 bars, $\dot{\varepsilon} = 10^{-5}$/sec

0.0	5.473	2.550	2.146	0.989	0.986	1.003	1.38
0.08	5.503	2.550	2.158	0.994	-	1.008	1.34
0.14	-	-	-	-	0.986	-	1.36
0.18	5.524	-	-	0.998	-	-	1.14
0.24	-	2.557	2.160	-	0.989	1.009	1.14
0.28	5.545	-	-	1.002	-	-	1.16
0.34	-	2.571	2.157	-	0.994	1.008	1.16
0.44	5.563	-	-	1.005	-	-	1.20
0.52	-	2.583	2.154	-	0.999	1.007	1.26
0.62	5.534	-	-	1.-	-	-	1.30
0.71	-	2.586	2.140	-	1.-	1.-	1.36
0.82	5.533	-	-	1.000	-	-	1.42
0.91	-	2.576	2.148	-	0.996	1.004	1.50
0.99	5.519	-	-	0.997	-	-	1.58
1.09	-	2.567	2.150	-	0.993	1.005	1.70
1.16	5.503	-	-	0.994	-	-	1.82
1.25	-	2.551	2.157	-	0.986	1.008	1.92
1.37	5.496	-	-	0.993	-	-	2.12
1.46	-	2.528	2.174	-	0.978	1.016	2.26
1.54	5.454	-	-	0.986	-	-	2.42
1.61	-	2.497	2.184	-	0.966	1.021	2.54
1.70	5.431	-	-	0.981	-	-	2.68
1.78	-	2.492	2.179	-	0.964	1.018	2.84
1.90	5.389	-	-	0.974	-	-	3.08

TABLE 4-1 (continued)

Sample #W1, Cycle #8, p_w = 350 bars, $\dot{\varepsilon} = 10^{-6}$/sec (continued)

Stress kb	V_p km/sec	V_s km/sec	V_p/V_s	$V_p(V_p)_o$	$V_s/(V_s)_o$	$(V_p/V_s)/(V_p/V_s)_o$	$e \times 10^{-3}$
1.98	-	2.386	2.259	-	0.923	1.055	3.33
1.98	5.279	2.308	2.287	0.954	0.892	1.069	4.19
1.84	5.267	2.297	2.293	0.952	0.888	1.071	4.23
1.56	5.269	2.290	2.301	0.952	0.886	1.075	3.89
1.27	5.268	2.289	2.301	0.952	0.885	1.075	3.63
0.99	5.279	2.294	2.301	0.954	0.887	1.075	3.49
0.69	5.309	2.306	2.302	0.959	0.892	1.076	3.24
0.69	5.348	2.325	2.300	0.966	0.899	1.075	2.76
0.57	5.350	2.344	2.282	0.967	0.906	1.066	2.66
0.42	5.397	2.336	2.310	0.975	0.903	1.079	2.40
0.42	5.413	2.377	2.277	0.978	0.919	1.064	2.08
0.28	5.389	2.388	2.257	0.974	0.923	1.055	2.04
0.28	5.432	2.431	2.234	0.982	0.940	1.044	1.80
0.14	5.439	2.405	2.182	0.983	0.930	1.020	1.72
0.14	5.464	2.492	2.192	0.987	0.964	1.024	1.46
0.0	5.480	2.493	2.198	0.990	0.964	1.027	1.44
0.0	5.445	2.520	2.161	0.984	0.974	1.010	1.40

Sample #W1, Cycle #10, p_w = 350 bars, $\dot{\varepsilon} = 10^{-6}$/sec

0.0	5.466	2.530	2.160	0.995	0.983	1.012	1.26
0.07	5.459	2.543	2.147	0.994	0.988	1.006	1.04
0.14	5.472	2.553	2.143	0.996	0.992	1.004	0.94
0.21	5.472	2.560	2.138	0.996	0.995	1.001	0.90
0.28	5.519	2.564	2.152	1.005	0.997	1.008	0.94
0.37	5.505	2.565	2.146	1.002	0.997	1.005	0.96
0.47	5.475	2.567	2.133	0.997	0.998	0.999	1.00
0.57	5.493	2.573	2.135	1.-	1.-	1.-	1.08
0.69	5.501	2.551	2.156	1.001	0.991	1.010	1.20
0.75	5.519	2.544	2.169	1.005	0.989	1.016	1.26

TABLE 4-1 (continued)

Sample #W1, Cycle #10, p_w = 350 bars, $\dot{\varepsilon} = 10^{-6}$/sec (continued)

Stress kb	V_p km/sec	V_s km/sec	V_p/V_s	$V_p/(V_p)_o$	$V_s/(V_s)_o$	$(V_p/V_s)/(V_p/V_s)_o$	$\epsilon \times 10^{-3}$
0.85	5.465	2.525	2.164	0.995	0.981	1.014	1.44
0.93	5.448	2.509	2.171	0.992	0.975	1.017	1.54
1.02	5.430	2.492	2.179	0.989	0.969	1.021	1.70
1.13	5.431	2.450	2.217	0.989	0.952	1.038	1.92
1.32	5.391	2.397	2.249	0.981	0.932	1.054	2.28
1.41	5.375	2.371	2.267	0.979	0.921	1.062	2.46
1.51	5.359	2.358	2.273	0.976	0.916	1.065	2.64
1.58	5.322	2.345	2.278	0.969	0.911	1.067	2.82
1.63	5.337	2.336	2.285	0.972	0.908	1.070	2.96
1.70	5.341	2.328	2.294	0.972	0.905	1.074	3.12
1.75	5.318	2.322	2.290	0.968	0.902	1.073	3.20
1.75	5.282	2.318	2.279	0.962	0.901	1.067	3.37
1.56	5.279	2.310	2.285	0.961	0.898	1.070	3.30
1.27	5.286	2.308	2.290	0.962	0.897	1.073	3.14
0.99	5.293	2.313	2.288	0.964	0.899	1.072	2.84
0.71	5.368	2.335	2.299	0.977	0.908	1.077	2.38
0.56	5.375	2.349	2.288	0.979	0.913	1.072	2.12
0.42	-	2.343	-	-	0.911	-	2.06
0.42	5.394	2.380	2.266	0.982	0.925	1.061	1.80
0.28	-	2.365	-	-	0.919	-	1.78
0.28	5.416	2.423	2.235	0.986	0.942	1.047	1.52
0.14	-	2.409	-	-	0.936	-	1.48
0.14	5.440	2.486	2.188	0.990	0.966	1.025	1.26
0.0	5.461	2.510	2.176	0.994	0.976	1.019	1.28
0.0	5.438	2.523	2.155	0.990	0.981	1.009	1.50

TABLE 4-1 (continued)

Sample #W1, Cycle #11, p_w = variable, $\dot{\epsilon} = 10^{-6}$/sec

Stress kb	V_p km/sec	V_s km/sec	V_p/V_s	$V_p/(V_p)_o$	$V_s/(V_s)_o$	$(V_p/V_s)/(V_p/V_s)_o$	$\epsilon \times 10^{-3}$
0.0	5.440	2.534	2.147	1.-	1.-	1.-	1.40
0.07	5.469	2.531	2.161	1.005	0.999	1.006	1.16
0.14	5.476	2.529	2.165	1.007	0.998	1.008	1.10
0.21	5.481	2.530	2.166	1.008	0.998	1.008	0.88
0.28	5.481	2.530	2.166	1.008	0.998	1.008	1.12
0.37	5.471	2.532	2.161	1.006	0.999	1.006	1.16
0.47	5.447	2.529	2.154	1.001	0.998	1.003	1.20
0.57	5.476	2.525	2.169	1.007	0.996	1.010	1.26
0.65	5.394	2.521	2.140	0.992	0.995	0.997	1.34
0.74	5.437	2.514	2.163	0.999	0.992	1.007	1.42
0.85	5.426	2.503	2.168	0.997	0.988	1.009	1.54
0.93	5.420	2.499	2.169	0.996	0.986	1.010	1.62
1.02	5.432	2.495	2.177	0.999	0.985	1.013	1.72
1.13	5.413	2.479	2.184	0.995	0.978	1.017	1.82
1.22	5.398	2.476	2.180	0.992	0.977	1.015	1.94
1.30	5.412	2.468	2.193	0.995	0.974	1.021	2.04
1.41	5.393	2.461	2.191	0.991	0.971	1.020	2.16
1.49	5.379	2.453	2.193	0.989	0.968	1.021	2.26
1.56	5.383	2.445	2.202	0.990	0.965	1.025	2.32
1.63	5.378	2.440	2.204	0.989	0.963	1.026	2.40
1.70	5.361	2.435	2.202	0.985	0.961	1.025	2.48
1.77	5.368	2.428	2.211	0.987	0.958	1.029	2.56
1.84	5.352	2.419	2.212	0.984	0.955	1.029	2.64
1.91	5.344	2.415	2.213	0.982	0.953	1.030	2.74
1.98	5.337	2.401	2.223	0.981	0.948	1.036	2.84
1.99	5.335	2.402	2.221	0.981	0.948	1.034	2.86
1.84	5.335	2.396	2.227	0.981	0.946	1.037	2.82
1.56	5.329	2.374	2.245	0.980	0.937	1.046	2.74
1.56	5.354	2.385	2.245	0.984	0.941	1.046	2.70
1.27	5.353	2.361	2.267	0.984	0.932	1.056	2.58
1.27	5.392	2.377	2.268	0.991	0.938	1.056	2.50

TABLE 4-1 (continued)

Sample #W1, Cycle #11, p_w = variable, $\dot{\varepsilon} = 10^{-6}$/sec (continued)

Stress kb	V_p km/sec	V_s km/sec	V_p/V_s	$V_p/(V_p)_o$	$V_s/(V_s)_o$	$(V_p/V_s)/(V_p/V_s)_o$	$\Theta \times 10^{-3}$
0.99	5.352	2.360	2.268	0.984	0.931	1.056	2.40
0.99	5.381	2.385	2.256	0.989	0.941	1.051	2.28
0.71	5.352	2.361	2.267	0.984	0.932	1.056	2.16
0.71	5.397	2.399	2.250	0.992	0.947	1.048	1.98
0.57	5.396	2.377	2.270	0.992	0.938	1.057	1.92
0.57	5.396	2.411	2.238	0.992	0.951	1.042	1.74
0.42	5.387	2.396	2.248	0.990	0.946	1.047	1.74
0.42	5.426	2.432	2.231	0.997	0.960	1.039	1.60
0.28	5.432	2.416	2.248	0.999	0.953	1.048	1.54
0.28	5.431	2.453	2.214	0.998	0.968	1.031	1.42
0.14	5.411	2.436	2.221	0.995	0.961	1.034	1.36
0.14	5.428	2.477	2.191	0.998	0.978	1.020	1.22
0.0	5.438	2.484	2.189	1.000	0.980	1.020	1.30
0.0	5.438	2.515	2.162	1.000	0.993	1.007	1.26
Sample #W1, Cycle #12, Dry, $\dot{\varepsilon} = 10^{-6}$/sec							
0.0	5.347	2.372	2.254	1.-	1.-	1.-	1.40
0.0	5.322	2.339	2.375	0.995	0.986	1.009	1.40
0.07	5.278	2.294	2.301	0.987	0.967	1.018	1.44
0.14	5.262	2.315	2.273	0.984	0.976	1.008	1.44
0.21	5.295	2.325	2.277	0.990	0.980	1.010	1.40
0.28	5.295	2.326	2.276	0.990	0.981	1.010	1.44
0.37	5.284	2.355	2.286	0.988	0.993	1.014	1.52
0.47	5.236	2.322	2.255	0.979	0.979	1.000	1.64
0.57	5.183	2.291	2.262	0.969	0.966	1.004	1.88
0.69	5.150	2.270	2.269	0.963	0.957	1.007	2.14
0.75	5.112	2.263	2.259	0.956	0.954	1.002	2.20
0.85	5.091	2.263	2.250	0.952	0.954	0.998	2.36
0.93	5.060	2.253	2.246	0.946	0.950	0.996	2.56

TABLE 4-1 (continued)

Sample #W1, Cycle #12, Dry, $\dot{\epsilon} = 10^{-6}$/sec (continued)

Stress kb	V_p km/sec	V_s km/sec	V_p/V_s	$V_p/(V_p)_o$	$V_s/(V_s)_o$	$(V_p/V_s)/(V_p/V_s)_o$	$\epsilon \times 10^{-3}$
1.06	5.049	2.239	2.255	0.944	0.944	1.000	2.86
1.13	5.004	2.257	2.217	0.936	0.952	0.984	3.04
1.25	4.975	2.214	2.247	0.930	0.933	0.997	3.29
1.32	4.948	2.208	2.241	0.925	0.931	0.994	3.41
1.43	4.975	2.244	2.217	0.930	0.946	0.984	3.47
1.51	4.928	2.230	2.210	0.922	0.940	0.980	3.57
1.58	4.917	2.225	2.210	0.920	0.938	0.980	3.71
1.63	4.921	2.225	2.212	0.920	0.938	0.981	3.81
1.70	4.904	2.224	2.205	0.917	0.938	0.978	3.93
1.77	4.869	2.216	2.197	0.911	0.934	0.975	4.07
1.84	4.780	2.200	2.173	0.894	0.927	0.964	4.23
1.91	4.624	2.175	2.126	0.865	0.917	0.943	4.51
1.98	4.574	2.138	2.139	0.855	0.901	0.949	4.73
1.98	4.489	2.129	2.109	0.840	0.898	0.937	4.83
1.84	4.485	2.127	2.109	0.839	0.897	0.937	4.71
1.58	4.574	2.124	2.153	0.855	0.895	0.955	4.53
1.58	4.569	2.128	2.147	0.854	0.897	0.953	4.57
1.27	4.692	2.141	2.191	0.878	0.903	0.972	4.19
1.27	4.720	2.147	2.198	0.883	0.905	0.975	4.13
0.99	4.877	2.165	2.253	0.912	0.913	1.000	3.71
0.99	4.889	2.185	2.238	0.914	0.921	0.993	3.57
0.71	4.887	2.164	2.258	0.914	0.912	1.002	3.35
0.71	4.898	2.155	2.273	0.916	0.910	1.008	3.39
0.57	4.885	2.145	2.277	0.914	0.904	1.010	3.29
0.57	4.921	2.179	2.258	0.920	0.919	1.002	2.94
0.42	4.922	2.157	2.282	0.921	0.909	1.012	2.90
0.42	4.942	2.183	2.264	0.924	0.920	1.004	2.72
0.28	5.007	2.170	2.307	0.936	0.915	1.024	2.64
0.28	5.023	2.200	2.283	0.939	0.927	1.013	2.40
0.14	5.008	2.183	2.294	0.937	0.920	1.018	2.42

TABLE 4-1 (continued)

Sample #W1, Cycle #12, Dry, $\dot{\varepsilon} = 10^{-6}$/sec (continued)

Stress kb	V_p km/sec	V_s km/sec	V_p/V_s	$V_p/(V_p)_o$	$V_s/(V_s)_o$	$(V_p/V_s)/(V_p/V_s)_o$	$\theta \times 10^{-3}$
0.14	4.996	2.174	2.298	0.934	0.917	1.020	2.38
0.0	5.002	2.146	2.331	0.935	0.905	1.034	2.28
0.0	4.912	2.105	2.333	0.919	0.887	1.035	2.38

Sample #W2, Cycle #3, Dry, $\dot{\varepsilon} = 10^{-6}$/sec

0.0	5.617	3.047	1.843	0.998	0.992	1.007	0.58
0.09	5.590	3.055	1.830	0.993	0.994	0.999	0.48
0.19	5.590	3.055	1.830	0.993	0.994	0.999	0.42
0.43	5.627	3.073	1.831	1.-	1.-	1.-	0.38
0.60	5.629	3.046	1.848	1.000	0.991	1.009	0.38
0.72	5.591	3.026	1.848	0.994	0.985	1.009	0.38
0.90	5.596	3.017	1.855	0.994	0.982	1.013	0.38
1.04	5.577	3.015	1.850	0.991	0.981	1.010	0.38
1.18	5.575	3.008	1.853	0.991	0.979	1.012	0.38
1.30	5.611	3.007	1.866	0.997	0.979	1.019	0.40
1.47	5.580	3.003	1.858	0.992	0.977	1.015	0.42
1.59	5.542	2.996	1.850	0.985	0.975	1.010	0.44
1.73	5.563	2.989	1.861	0.989	0.973	1.016	0.46
1.88	5.569	2.983	1.867	0.990	0.971	1.020	0.50
2.02	5.546	2.977	1.863	0.986	0.969	1.017	0.56
2.17	5.539	2.971	1.864	0.984	0.967	1.018	0.58
2.31	5.533	2.964	1.867	0.983	0.965	1.020	0.64
2.46	5.528	2.956	1.870	0.982	0.962	1.021	0.68
2.60	5.522	2.948	1.873	0.981	0.959	1.023	0.74
2.75	5.515	2.940	1.876	0.980	0.957	1.025	0.82
2.89	5.490	2.930	1.874	0.976	0.953	1.024	0.90
3.03	5.510	2.918	1.888	0.979	0.950	1.031	0.96
3.18	5.505	2.907	1.894	0.978	0.946	1.034	1.06
3.32	5.489	2.891	1.897	0.975	0.941	1.036	1.16

TABLE 4-1 (continued)

Sample #W2, Cycle #3, Dry, $\dot{\varepsilon} = 10^{-6}$/sec (continued)

Stress kb	V_p km/sec	V_s km/sec	V_p/V_s	$V_p/(V_p)_o$	$V_s/(V_s)_o$	$(V_p/V_s)/(V_p/V_s)_o$	$e \times 10^{-3}$
3.52	5.424	2.868	1.891	0.963	0.933	1.033	1.32
3.61	5.309	2.854	1.866	0.943	0.929	1.019	1.38
3.68	5.264	2.845	1.863	0.935	0.926	1.017	1.48
3.76	5.277	2.831	1.864	0.938	0.921	1.018	1.56
3.78	5.264	2.826	1.863	0.935	0.920	1.014	1.62
3.61	5.267	2.831	1.860	0.936	0.921	1.016	1.58
3.32	5.272	2.833	1.861	0.937	0.922	1.016	1.50
3.03	5.280	2.840	1.859	0.938	0.924	1.015	1.38
2.75	5.287	2.845	1.858	0.940	0.926	1.015	1.28
2.46	5.301	2.851	1.859	0.942	0.928	1.015	1.18
2.17	5.320	2.860	1.860	0.945	0.931	1.016	1.06
1.81	5.403	2.868	1.884	0.960	0.933	1.029	0.98
1.59	5.441	2.878	1.891	0.967	0.937	1.033	0.84
1.30	5.471	2.887	1.895	0.972	0.939	1.035	0.72
1.01	5.498	2.893	1.900	0.977	0.941	1.038	0.54
0.72	5.507	2.902	1.898	0.979	0.944	1.037	0.50
0.43	5.520	2.915	1.894	0.981	0.949	1.034	0.38
0.14	5.505	2.920	1.885	0.978	0.950	1.029	0.38
0.0	5.498	2.925	1.880	0.977	0.952	1.027	0.42
Sample #W3, Cycle #1, Dry, $\dot{\varepsilon} = 10^{-5}$/sec, shear polarization $\parallel \sigma_{max}$							
0.0	5.682	2.909	1.953	0.996	0.979	1.018	0.20
0.0	5.682	2.917	1.948	0.996	0.981	1.015	0.20
0.14	-	2.930	-	-	0.986	-	0.05
0.28	5.682	-	1.939	0.996	-	1.010	0.0
0.41	-	2.949	-	-	0.992	-	0.0
0.51	5.722	-	1.940	1.003	-	1.011	0.0
0.61	-	2.950	-	-	0.993	-	0.0

TABLE 4-1 (continued)

Sample #W3, Cycle #1, Dry, $\dot{\varepsilon} = 10^{-5}$/sec, shear polarization $\| \sigma_{max}$ (continued)

Stress kb	V_p km/sec	V_s km/sec	V_p/V_s	$V_p/(V_p)_o$	$V_s/(V_s)_o$	$(V_p/V_s)/(V_p/V_s)_o$	$\theta \times 10^{-3}$
0.70	5.730	-	1.942	1.000	-	1.012	0.0
0.87	-	2.957	-	-	0.995	-	0.0
0.96	5.744	-	1.943	1.007	-	1.012	0.0
1.04	-	2.963	-	-	0.997	-	0.03
1.07	5.729	-	1.934	1.004	-	1.007	0.03
1.25	-	2.966	-	-	0.998	-	0.08
1.32	5.719	-	1.928	1.003	-	1.005	0.09
1.44	-	2.971	-	-	1.000	-	0.12
1.52	5.695	-	1.917	0.998	-	0.999	0.13
1.70	-	2.969	-	-	0.999	-	0.16
1.77	5.709	-	1.923	1.001	-	1.002	0.17
1.90	-	2.972	-	-	1.-	-	0.24
1.99	5.704	-	1.919	1.-	-	1.-	0.25
2.09	-	2.969	-	-	0.999	-	0.30
2.16	5.696	-	1.918	0.999	-	1.000	0.30
2.29	-	2.969	-	-	0.999	-	0.36
2.38	5.660	-	1.906	0.992	-	0.993	0.39
2.46	-	2.965	-	-	0.998	-	0.42
2.57	5.653	-	1.907	0.991	-	0.993	0.46
2.70	-	2.960	-	-	0.996	-	0.56
2.76	5.598	-	1.891	0.981	-	0.985	0.56
2.76	5.593	2.955	1.893	0.981	0.994	0.986	0.56
2.46	5.610	2.962	1.894	0.984	0.997	0.987	0.52
2.18	5.609	2.964	1.892	0.983	0.997	0.986	0.44
1.88	5.609	2.965	1.892	0.983	0.998	0.986	0.34
1.60	5.628	2.961	1.901	0.987	0.996	0.990	0.28
1.30	5.652	2.961	1.909	0.991	0.996	0.995	0.18
1.02	5.652	2.956	1.912	0.991	0.995	0.996	0.09
0.72	5.655	2.951	1.916	0.991	0.993	0.998	0.00
0.44	5.668	2.949	1.922	0.994	0.992	1.001	0.00

TABLE 4-1 (continued)

Sample #W3, Cycle #1, Dry, $\dot{\varepsilon} = 10^{-5}$/sec, shear polarization $\parallel \sigma_{max}$ (continued)

Stress kb	V_p km/sec	V_s km/sec	V_p/V_s	$V_p/(V_p)_o$	$V_s/(V_s)_o$	$(V_p/V_s)/(V_p/V_s)_o$	$\theta \times 10^{-3}$
0.14	5.681	2.934	1.936	0.996	0.987	1.009	0.00
0.0	5.673	2.928	1.938	0.995	0.985	1.010	0.14
0.0	5.687	2.934	1.938	0.997	0.987	1.010	0.14

Sample #W3, Cycle #2, Dry, $\dot{\varepsilon} = 10^{-5}$/sec, shear polarization $\parallel \sigma_{max}$

0.0	5.682	2.933	1.937	1.003	0.984	1.019	0.14
0.23	-	2.948	-	-	0.989	-	0.03
0.35	5.703	-	1.935	1.007	-	1.018	0.00
0.51	-	2.955	-	-	0.992	-	0.00
0.57	5.705	-	1.931	1.007	-	1.016	0.00
0.72	-	2.965	-	-	0.995	-	0.00
0.81	5.693	-	1.920	1.005	-	1.010	0.00
0.99	-	2.972	-	-	0.997	-	0.00
1.06	5.700	-	1.918	1.006	-	1.009	0.00
1.35	-	2.976	-	-	0.999	-	0.04
1.39	5.704	-	1.917	1.007	-	1.008	0.06
1.58	-	2.978	-	-	0.999	-	0.11
1.67	5.701	-	1.914	1.006	-	1.007	0.14
1.83	-	2.980	-	-	1.-	-	0.18
1.91	5.665	-	1.901	1.-	-	1.-	0.20
2.07	-	2.977	-	-	0.999	-	0.26
2.13	5.671	-	1.905	1.001	-	1.002	0.26
2.32	-	2.977	-	-	0.999	-	0.31
2.39	5.658	-	1.901	0.999	-	1.000	0.34
2.57	-	2.973	-	-	0.998	-	0.40
2.67	5.613	-	1.888	0.991	-	0.993	0.42
2.87	-	2.964	-	-	0.995	-	0.53
2.97	5.575	-	1.881	0.984	-	0.989	0.58
3.16	-	2.955	-	-	0.982	-	0.72

TABLE 4-1 (continued)

Sample #W3, Cycle #2, Dry, $\dot{\varepsilon} = 10^{-5}$/sec, shear polarization $\| \sigma_{max}$ (continued)

Stress kb	V_p km/sec	V_s km/sec	V_p/V_s	$V_p/(V_p)_o$	$V_s/(V_s)_o$	$(V_p/V_s)/(V_p/V_s)_o$	e x 10^{-3}
3.25	5.484	-	1.856	0.968	-	0.976	0.76
3.36	-	2.939	-	-	0.986	-	0.85
3.48	5.398	-	1.837	0.953	-	0.966	0.96
3.55	-	2.925	-	-	0.982	-	1.02
3.62	5.344	-	1.827	0.943	-	0.961	1.10
3.68	5.261	2.909	1.809	0.929	0.976	0.951	1.15
3.68	5.246	2.904	1.806	0.926	0.974	0.950	1.28
3.41	5.253	2.907	1.807	0.927	0.976	0.951	1.18
3.12	5.252	2.909	1.805	0.927	0.976	0.950	1.09
2.83	5.272	2.910	1.812	0.931	0.977	0.953	0.98
2.46	5.315	2.909	1.827	0.938	0.976	0.961	0.83
2.18	5.339	2.910	1.835	0.942	0.977	0.965	0.74
1.88	5.385	2.913	1.849	0.951	0.978	0.972	0.61
1.60	5.410	2.916	1.855	0.955	0.979	0.976	0.50
1.30	5.477	2.919	1.876	0.967	0.980	0.987	0.36
0.96	5.547	2.927	1.895	0.979	0.982	0.997	0.22
0.72	5.588	2.930	1.907	0.986	0.983	1.003	0.14
0.44	5.602	2.934	1.909	0.989	0.985	1.004	0.04
0.14	5.652	2.929	1.930	0.998	0.983	1.015	0.02
0.0	5.633	2.926	1.925	0.994	0.982	1.013	0.28
0.0	5.664	2.928	1.934	1.000	0.983	1.018	0.28

Sample #W3, Cycle #3, Dry, $\dot{\varepsilon} = 10^{-5}$/sec

0.0	5.664	2.864	1.978	-	-	1.004	0.29
0.14	-	2.869	-	-	-	-	0.11
0.26	5.652	-	1.970	-	-	1.000	0.08
0.41	-	2.872	-	-	-	-	0.02
0.51	5.689	-	1.981	-	-	1.006	0.0
0.67	-	2.879	-	-	-	-	0.0

TABLE 4-1 (continued)

Sample #W3, Cycle #3, Dry, $\dot{\varepsilon} = 10^{-5}$/sec (continued)

Stress kb	V_p km/sec	V_s km/sec	V_p/V_s	$V_p/(V_p)_o$	$V_s/(V_s)_o$	$(V_p/V_s)/(V_p/V_s)_o$	$\epsilon \times 10^{-3}$
0.77	5.670	-	1.968	-	-	1.000	0.0
0.97	-	2.878	-	-	-	-	0.0
1.06	5.694	-	1.978	-	-	1.005	0.03
1.23	-	2.875	-	-	-	-	0.04
1.32	5.663	-	1.970	-	-	1.000	0.04
1.45	-	2.871	-	-	-	-	0.08
1.55	5.656	-	1.970	-	-	1.000	0.10
1.70	-	2.860	-	-	-	-	0.12
1.83	5.638	-	1.971	-	-	1.001	0.18
1.97	-	2.851	-	-	-	-	0.22
2.13	5.600	-	1.964	-	-	0.997	0.26
2.28	-	2.832	-	-	-	-	0.34
2.35	5.573	-	1.968	-	-	0.999	0.38
2.49	-	2.820	-	-	-	-	0.42
2.58	5.529	-	1.961	-	-	0.996	0.48
2.70	-	2.803	-	-	-	-	0.52
2.87	5.422	-	1.934	-	-	0.982	0.60
3.03	-	2.787	-	-	-	-	0.69
3.10	5.378	-	1.930	-	-	0.980	0.76
3.22	-	2.771	-	-	-	-	0.78
3.28	5.326	-	1.922	-	-	0.976	0.84
3.38	-	2.763	-	-	-	-	0.90
3.52	5.302	-	1.919	-	-	0.974	1.02
3.68	-	2.736	-	-	-	-	1.14
3.73	5.228	-	1.911	-	-	0.970	1.18
3.73	5.186	2.715	1.910	-	-	0.970	1.24
3.48	5.187	2.717	1.909	-	-	0.969	1.10
3.19	5.186	2.720	1.907	-	-	0.968	1.03
3.04	5.242	2.728	1.922	-	-	0.976	0.99
2.67	5.251	2.730	1.923	-	-	0.977	0.90

TABLE 4-1 (continued)

Sample #W3, Cycle #3, Dry, $\dot{\varepsilon} = 10^{-5}$/sec (continued)

Stress kb	V_p km/sec	V_s km/sec	V_p/V_s	$V_p/(V_p)_o$	$V_s/(V_s)_o$	$(V_p/V_s)/(V_p/V_s)_o$	e x 10^{-3}
2.46	5.257	2.735	1.922	-	-	0.976	0.70
2.18	5.276	2.744	1.923	-	-	0.977	0.56
1.88	5.338	2.756	1.937	-	-	0.983	0.48
1.60	5.366	2.774	1.934	-	-	0.982	0.33
1.30	5.442	2.788	1.952	-	-	0.991	0.11
1.00	5.498	2.811	1.956	-	-	0.993	0.06
0.72	5.547	2.827	1.962	-	-	0.996	-0.02
0.44	5.599	2.848	1.966	-	-	0.998	-0.16
0.14	5.635	2.861	1.970	-	-	1.000	-0.16
0.0	5.625	2.870	1.960	-	-	0.995	+0.29
0.0	5.631	2.862	1.968	-	-	0.999	+0.29

Sample #W3, Cycle #4, p_{CO_2} = 112 bars, $\dot{\varepsilon} = 10^{-5}$/sec

0.0	5.624	3.014	1.867	-	-	0.975	0.44
0.0	5.687	2.972	1.914	1.000	1.000	1.000	0.44
0.14	5.712	2.965	1.926	1.004	0.998	1.006	0.10
0.55	5.712	-	-	1.004	-	-	0.08
0.69	-	2.963	1.928	-	0.997	1.007	0.10
0.80	5.724	-	-	1.007	-	-	0.11
0.94	-	2.952	1.939	-	0.993	1.013	0.13
1.07	5.572	-	-	0.980	-	-	0.16
1.24	-	2.930	1.902	-	0.986	0.993	0.24
1.35	5.547	-	-	0.975	-	-	0.28
1.49	-	2.916	1.903	-	0.981	0.994	0.33
1.68	5.530	-	-	0.972	-	-	0.46
1.82	-	2.874	1.924	-	0.967	1.006	0.56
1.95	5.499	-	-	0.967	-	-	0.70
2.09	-	2.837	1.938	-	0.955	1.013	0.80
2.19	5.412	-	-	0.952	-	-	0.90

TABLE 4-1 (continued)

Sample #W3, Cycle #4, p_{CO_2} = 112 bars, $\dot{\varepsilon} = 10^{-5}$/sec (continued)

Stress kb	V_p km/sec	V_s km/sec	V_p/V_s	$V_p/(V_p)_o$	$V_s/(V_s)_o$	$(V_p/V_s)/(V_p/V_s)_o$	$e \times 10^{-3}$
2.31	-	2.782	1.946	-	0.936	1.017	1.02
2.45	5.326	-	-	0.937	-	-	1.15
2.53	5.304	2.747	1.939	0.933	0.924	1.013	1.23
2.64	-	2.719	1.951	-	0.915	1.019	1.42
2.75	5.235	-	-	0.921	-	-	1.54
2.83	-	2.716	1.928	-	0.914	1.007	1.64
2.94	5.215	-	-	0.917	-	-	1.84
3.05	-	2.701	1.931	-	0.909	1.009	1.96
3.14	5.174	-	-	0.910	-	-	2.08
3.23	-	2.675	1.935	-	0.900	1.011	2.28
3.30	5.045	2.647	1.906	0.887	0.891	0.996	2.54
3.09	5.022	2.644	1.899	0.883	0.890	0.992	2.58
2.82	5.031	2.647	1.901	0.885	0.891	0.993	2.45
2.54	5.044	2.647*	1.905	0.887	0.891	0.996	2.30
2.27	5.057	2.668	1.896	0.889	0.898	0.990	2.12
1:99	5.065	2.678	1.891	0.891	0.901	0.998	1.94
1.72	5.114	2.685	1.905	0.899	0.903	0.995	1.72
1.44	5.199	2.696	1.928	0.914	0.907	1.008	1.46
1.17	5.219	2.717	1.920	0.918	0.914	1.003	1.26
0.89	5.310	2.739	1.939	0.934	0.922	1.013	0.88
0.62	5.389	2.761	1.951	0.948	0.929	1.019	0.61
0.34	5.515	2.787	1.979	0.970	0.938	1.034	0.37
0.07	5.567	2.809	1.981	0.979	0.945	1.035	0.20
0.0	5.609	2.820	1.989	0.986	0.949	1.039	0.68
0.0	5.583	2.825	1.976	0.981	0.951	1.032	0.68

* Shear wave values questionable below here due to poor signal

TABLE 4-1 (continued)

Sample #W3, Cycle #5, p_{CO_2} = 68 bars, $\dot{\varepsilon} = 10^{-5}$/sec

Stress kb	V_p km/sec	V_s km/sec	V_p/V_s	$V_p/(V_p)_o$	$V_s/(V_s)_o$	$(V_p/V_s)/(V_p/V_s)_o$	$e \times 10^{-3}$
0.0	5.645	2.965	1.904	1.-	1.-	1.-	0.44
0.11	5.639	-	-	0.999	-	-	0.30
0.19	-	2.961	1.905	-	0.999	1.000	0.25
0.36	5.646	-	-	1.000	-	-	0.18
0.47	-	2.963	1.905	-	0.999	1.001	0.14
0.65	5.623	-	-	0.996	-	-	0.14
0.79	-	2.953	1.904	-	0.996	1.000	0.14
0.94	5.565	-	-	0.986	-	-	0.20
1.07	-	2.936	1.896	-	0.990	0.996	0.22
1.18	5.533	-	-	0.980	-	-	0.26
1.29	-	2.922	1.893	-	0.985	0.994	0.29
1.44	5.481	-	-	0.971	-	-	0.36
1.52	-	2.903	1.888	-	0.979	0.992	0.40
1.63	5.431	-	-	0.962	-	-	0.46
1.75	-	2.879	1.887	-	0.971	0.991	0.54
1.87	5.369	-	-	0.951	-	-	0.62
1.97	-	2.855	1.881	-	0.963	0.988	0.70
2.11	5.322	-	-	0.943	-	-	0.80
2.20	-	2.812	1.893	-	0.948	0.994	0.88
2.29	5.259	-	-	0.932	-	-	0.96
2.38	-	2.779	1.893	-	0.937	0.994	1.06
2.49	5.188	-	-	0.919	-	-	1.16
2.55	-	2.758	1.881	-	0.930	0.988	1.20
2.55	5.170	2.758	1.874	0.916	0.930	0.985	1.20
2.55	5.170	-	-	0.916	-	-	1.23
2.70	-	2.739	1.888	-	0.924	0.991	1.36
2.84	5.097	-	-	0.903	-	-	1.42
2.92	-	2.718	1.876	-	0.917	0.985	1.62
3.05	5.094	-	-	0.903	-	-	1.76
3.13	-	2.693	1.892	-	0.908	0.994	1.92
3.23	5.040	-	-	0.893	-	-	2.06

TABLE 4-1 (continued)

Sample #W3, Cycle #5, p_{CO_2} = 68 bars, $\dot{\varepsilon} = 10^{-5}$/sec (continued)

Stress kb	V_p km/sec	V_s km/sec	V_p/V_s	$V_p(V_p)_o$	$V_s/(V_s)_o$	$(V_p/V_s)/(V_p/V_s)_o$	$\theta \times 10^{-3}$
3.35	-	2.656	1.898	-	0.896	0.997	2.24
3.42	5.000	-	-	0.886	-	-	2.34
3.52	-	2.617	1.911	-	0.883	1.004	2.48
3.52	4.889	2.584	1.892	0.866	0.872	0.994	2.58
3.50	4.865	2.582	1.884	0.862	0.871	0.990	2.64
3.48	4.850	2.562	1.893	0.859	0.864	0.994	2.74
3.25	4.853	2.561	1.895	0.860	0.864	0.995	2.62
2.98	4.852	2.561	1.894	0.860	0.864	0.995	2.50
2.70	4.854	2.567*	1.891	0.860	0.866	0.993	2.30
2.42	4.876	2.575	1.893	0.864	0.868	0.994	2.14
2.15	4.937	2.585	1.910	0.875	0.872	1.003	1.94
1.87	5.001	2.604	1.920	0.886	0.878	1.008	1.72
1.52	5.024	2.622	1.916	0.890	0.884	1.006	1.42
1.25	5.101	2.647	1.927	0.904	0.893	1.012	1.18
1.04	5.172	2.672	1.936	0.916	0.901	1.016	0.86
0.76	5.276	2.712	1.946	0.935	0.915	1.022	0.58
0.48	5.358	2.747	1.950	0.949	0.926	1.024	0.40
0.21	5.469	2.780	1.967	0.969	0.938	1.033	0.30
0.0	5.478	2.800	1.956	0.970	0.944	1.027	0.56
0.0	5.500	2.802	1.963	0.974	0.945	1.031	0.56
0.0	5.535	2.822	1.961	0.981	0.952	1.030	0.56

Sample #W3, Cycle #6, p_{CO_2} = 62 bars (transition) and lower at highest stress, $\dot{\varepsilon} = 10^{-5}$/sec

0.0	5.566	2.952	1.885	0.997	1.-	1.-	0.80
0.08	5.581	-	-	1.-	-	-	0.42
0.21	-	2.951	1.891	-	1.000	1.003	0.32
0.29	5.579	-	-	1.000	-	-	0.32

*Shear wave values questionable below here due to poor signal

TABLE 4-1 (continued)

Sample #W3, Cycle #6, p_{CO_2} = 62 bars (transition) and lower at highest stress, $\dot{\varepsilon} = 10^{-5}$/sec (continued)

Stress kb	V_p km/sec	V_s km/sec	V_p/V_s	$V_p/(V_p)_o$	$V_s/(V_s)_o$	$(V_p/V_s)/(V_p/V_s)_o$	$\theta \times 10^{-3}$
0.41	-	2.950	1.891	-	0.999	1.003	0.29
0.52	5.579	-	-	1.000	-	-	0.29
0.60	-	2.943	1.897	-	0.997	1.006	0.26
0.73	5.588	-	-	1.001	-	-	0.28
0.82	-	2.936	1.904	-	0.995	1.010	0.29
0.96	5.576	-	-	0.999	-	-	0.33
1.06	-	2.923	1.908	-	0.990	1.012	0.35
1.21	5.481	-	-	0.982	-	-	0.40
1.32	-	2.901	1.890	-	0.983	1.002	0.44
1.46	5.435	-	-	0.974	-	-	0.54
1.58	-	2.868	1.895	-	0.972	1.005	0.64
1.70	5.367	-	-	0.962	-	-	0.72
1.79	-	2.839	1.891	-	0.962	1.003	0.77
1.98	5.266	-	-	0.945	-	-	0.94
2.06	-	2.800	1.881	-	0.949	0.997	1.04
2.17	5.221	-	-	0.935	-	-	1.12
2.25	-	2.768	1.886	-	0.938	1.000	1.20
2.34	5.160	-	-	0.924	-	-	1.31
2.45	-	2.748	1.878	-	0.931	0.996	1.46
2.50	5.087	2.730	1.863	0.911	0.925	0.988	1.50
2.54	5.083	-	-	0.911	-	-	1.58
2.67	-	2.710	1.876	-	0.918	0.995	1.70
2.76	5.028	-	-	0.901	-	-	1.84
2.85	-	2.684	1.874	-	0.909	0.994	1.94
2.97	4.949	-	-	0.887	-	-	2.12
3.08	-	2.659	1.861	-	0.901	0.987	2.28
3.22	4.870	-	-	0.873	-	-	2.52
3.33	-	2.620	1.859	-	0.886	0.986	2.74
3.33	4.835	2.606	1.855	0.886	0.883	0.984	2.76
3.33	4.835	-	-	0.886	-	-	2.78

TABLE 4-1 (continued)

Sample #W3, Cycle #6, p_{CO_2} = 62 bars (transition) and lower at highest stress, $\dot{\varepsilon} = 10^{-5}$/sec (continued)

Stress kb	V_p km/sec	V_s km/sec	V_p/V_s	$V_p/(V_p)_o$	$V_s/(V_s)_o$	$(V_p/V_s)/(V_p/V_s)_o$	$e \times 10^{-3}$
3.44	-	2.601	1.860	-	0.881	0.986	3.00
3.51	4.790	-	-	0.858	-	-	3.15
3.60	-	2.573	1.862	-	0.871	0.988	3.48
3.60	4.749	2.548	1.864	0.851	0.863	0.989	3.72
3.60	4.706	2.541	1.852	0.843	0.861	0.982	3.82
3.59	4.690	2.537	1.849	0.840	0.859	0.981	3.90
3.58	4.636	2.533	1.830	0.831	0.858	0.971	4.00
3.56	4.634	2.526	1.834	0.830	0.856	0.973	4.08
3.55	4.624	2.521	1.834	0.829	0.854	0.973	4.16
commence p_{CO_2} drop							
3.55	4.628	2.526	1.832	0.829	0.856	0.972	4.24
3.55	4.624	2.525	1.831	0.829	0.855	0.971	4.24
3.55	4.619	2.524	1.830	0.828	0.855	0.970	4.24
3.53	4.619	2.523	1.830	0.828	0.855	0.971	4.28
3.53	4.630	2.522	1.836	0.830	0.854	0.974	4.28
3.53	4.626	2.519	1.836	0.829	0.853	0.974	4.28
3.53	4.615	2.511	1.838	0.827	0.851	0.975	4.28
3.53	4.588	2.496	1.838	0.822	0.846	0.975	4.28
3.53	4.519	2.482	1.820	0.810	0.841	0.965	4.28
3.53	4.483	2.481	1.806	0.803	0.840	0.958	4.26
3.53	4.483	2.483	1.805	0.803	0.841	0.957	4.26
3.53	4.502	2.485	1.811	0.807	0.842	0.961	4.26
3.53	4.508	2.489	1.811	0.808	0.843	0.960	4.24
3.53	4.523	2.491	1.815	0.810	0.844	0.963	4.24
3.53	4.523	2.492	1.815	0.810	0.844	0.962	4.24
3.53	4.533	2.494	1.817	0.812	0.845	0.964	4.20
3.53	4.544	2.496	1.820	0.814	0.846	0.965	4.20
3.53	4.568	2.499	1.828	0.818	0.847	0.969	4.16

TABLE 4-1 (continued)

Sample #W3, Cycle #6, p_{CO_2} = 62 bars (transition) and lower at highest stress, $\dot{\varepsilon} = 10^{-5}$/sec (continued)

Stress kb	V_p km/sec	V_s km/sec	V_p/V_s	$V_p/(V_p)_o$	$V_s/(V_s)_o$	$(V_p/V_s)/(V_p/V_s)_o$	$e \times 10^{-3}$
3.53	4.560	2.499	1.824	0.817	0.847	0.968	4.16
p_{CO_2} = 1 bar							
3.37	4.571	2.500	1.829	0.814	0.847	0.970	4.10
3.09	4.578	2.503	1.829	0.822	0.848	0.970	3.94
2.82	4.594	2.511	1.830	0.825	0.851	0.970	3.72
2.54	4.626	2.522	1.834	0.831	0.854	0.973	3.44
2.27	4.643	2.542	1.827	0.834	0.861	0.969	3.16
1.99	4.705	2.560	1.838	0.845	0.867	0.975	2.84
1.72	4.793	2.595	1.847	0.861	0.879	0.979	2.30
1.44	4.880	2.624	1.860	0.877	0.889	0.986	1.96
1.27	5.009	2.665	1.880	0.900	0.903	0.997	1.58
0.89	5.089	2.699	1.886	0.914	0.914	1.000	1.20
0.62	5.216	2.750	1.897	0.937	0.931	1.006	0.88
0.34	5.341	2.778	1.923	0.960	0.941	1.020	0.60
0.07	5.422	2.813	1.927	0.974	0.953	1.022	0.50
0.00	5.463	2.816	1.940	0.981	0.954	1.029	1.05
Sample #SMG1, Cycle #9, p_w = 350 bars, $\dot{\varepsilon} = 10^{-6}$/sec							
0.0	6.325	3.146	2.009	0.993	1.000	0.992	0.68
0.0	6.368	3.146	2.024	1.-	1.-	1.-	0.68
0.13	6.332	3.138	2.018	0.993	0.997	0.997	0.52
0.27	6.329	3.130	2.022	0.994	0.995	0.999	0.52
0.42	6.325	3.118	2.029	0.993	0.991	1.002	0.44
0.63	6.314	3.108	2.032	0.992	0.988	1.004	0.38
0.84	6.297	3.102	2.030	0.989	0.986	1.003	0.37
1.07	6.293	3.098	2.031	0.988	0.985	1.003	0.42

TABLE 4-1 (continued)

Sample #SMG1, Cycle #9, p_w = 350 bars, $\dot{\varepsilon} = 10^{-6}$/sec (continued)

Stress kb	V_p km/sec	V_s km/sec	V_p/V_s	$V_p/(V_p)_o$	$V_s/(V_s)_o$	$(V_p/V_s)/(V_p/V_s)_o$	$\varepsilon \times 10^{-3}$
1.25	6.293	3.087	2.039	0.988	0.981	1.007	0.43
1.46	6.280	3.086	2.035	0.986	0.981	1.005	0.48
1.67	6.274	3.082	2.036	0.985	0.980	1.006	0.49
1.92	6.266	3.077	2.036	0.984	0.978	1.006	0.56
2.09	6.232	3.070	2.030	0.979	0.976	1.003	0.59
2.30	6.232	3.064	2.034	0.979	0.974	1.005	0.64
2.51	6.193	3.053	2.028	0.973	0.970	1.002	0.70
2.72	6.174	3.042	2.030	0.970	0.967	1.003	0.74
2.84	6.149	3.034	2.027	0.966	0.964	1.001	0.78
2.99	6.150	3.026	2.032	0.966	0.962	1.004	0.83
3.09	6.145	3.013	2.039	0.965	0.958	1.007	0.89
3.22	6.102	3.004	2.031	0.958	0.955	1.003	0.92
3.13	6.128	2.991	2.049	0.962	0.951	1.012	0.99
3.42	6.106	2.968	2.057	0.959	0.943	1.016	1.11
3.22	6.007	2.941	2.043	0.943	0.935	1.009	1.29
3.21	6.025	2.916	2.066	0.946	0.927	1.021	1.40
3.20	6.008	2.895	2.075	0.943	0.920	1.025	1.45
3.19	5.946	2.885	2.061	0.934	0.917	1.018	1.65
3.19	5.946	2.857	2.081	0.934	0.908	1.028	1.81
3.17	5.922	2.842	2.071	0.930	0.903	1.023	2.01
3.16	5.916	2.814	2.102	0.929	0.894	1.039	2.17
3.14	5.856	2.764	2.119	0.920	0.897	1.047	2.53
3.13	5.829	2.727	2.138	0.915	0.867	1.056	2.75
3.11	5.810	2.691	2.159	0.912	0.855	1.067	3.03
3.10	5.801	2.671	2.172	0.911	0.849	1.073	3.17
2.72	5.767	2.656	2.247	0.906	0.844	1.110	3.13
2.30	5.750	2.635	2.182	0.903	0.838	1.078	3.13
1.88	5.767	2.618	2.149	0.906	0.832	1.062	3.13
1.46	5.728	2.600	2.203	0.899	0.826	1.088	3.07
1.05	5.748	2.577	2.231	0.903	0.819	1.102	3.05

TABLE 4-1 (continued)

Sample #SMG1, Cycle #9, p_w = 350 bars, $\dot{\varepsilon} = 10^{-6}$/sec (continued)

Stress kb	V_p km/sec	V_s km/sec	V_p/V_s	$V_p/(V_p)_o$	$V_s/(V_s)_o$	$(V_p/V_s)/(V_p/V_s)_o$	$e \times 10^{-3}$
0.63	5.769	2.542	2.269	0.906	0.808	1.121	3.01
0.21	5.780	2.535	2.280	0.908	0.806	1.126	2.93
0.0	5.785	2.558	2.262	0.908	0.813	1.118	2.75
0.0	5.918	2.721	2.175	0.929	0.865	1.074	2.09

Sample #SMG1, Cycle #3, Dry, $\dot{\varepsilon} = 10^{-6}$/sec

0.0	6.205	3.206	1.935	0.998	0.996	1.001	0.26
0.11	6.220	3.213	1.936	1.-	0.999	1.001	0.06
0.21	6.220	3.213	1.936	1.-	0.999	1.001	0.04
0.34	6.220	3.216	1.934	1.-	1.-	1.-	0.04
0.43	6.194	3.214	1.927	0.996	0.999	0.996	0.04
0.64	6.612	3.214	1.933	0.999	0.999	0.999	0.0
0.85	6.188	3.212	1.927	0.995	0.999	0.996	0.0
1.07	6.168	3.209	1.922	0.992	0.998	0.994	0.0
1.32	6.098	3.203	1.904	0.980	0.996	0.984	0.0
1.49	6.124	3.197	1.916	0.985	0.994	0.991	0.0
1.71	6.132	3.190	1.922	0.986	0.992	0.994	0.0
1.92	6.094	3.180	1.916	0.980	0.989	0.991	0.04
2.14	6.077	3.169	1.918	0.977	0.985	0.992	0.06
2.35	6.059	3.157	1.919	0.974	0.982	0.992	0.08
2.56	6.036	3.151	1.916	0.970	0.980	0.991	0.12
2.78	6.001	3.143	1.909	0.965	0.977	0.987	0.16
2.99	5.971	3.130	1.908	0.960	0.973	0.987	0.20
3.10	5.959	3.125	1.907	0.958	0.972	0.986	0.22
3.20	5.952	3.120	1.908	0.957	0.970	0.987	0.24
3.31	5.952	3.111	1.913	0.957	0.967	0.989	0.26
3.42	5.919	3.102	1.908	0.952	0.965	0.987	0.28
3.44	5.913	3.094	1.911	0.951	0.962	0.988	0.30
3.20	5.913	3.093	1.912	0.951	0.962	0.988	0.24

TABLE 4-1 (continued)

Sample #SMG1, Cycle #3, Dry, $\dot{\varepsilon} = 10^{-6}$/sec (continued)

Stress kb	V_p km/sec	V_s km/sec	V_p/V_s	$V_p/(V_p)_o$	$V_s/(V_s)_o$	$(V_p/V_s)/(V_p/V_s)_o$	$e \times 10^{-3}$
2.78	5.895	3.096	1.904	0.948	0.963	0.984	0.16
2.35	5.936	3.105	1.912	0.954	0.965	0.987	0.10
1.92	5.946	3.115	1.909	0.956	0.969	0.987	0.02
1.49	5.964	3.126	1.908	0.959	0.972	0.987	-0.06
1.07	5.992	3.147	1.904	0.963	0.979	0.984	-0.10
0.64	6.086	3.171	1.919	0.978	0.986	0.992	-0.17
0.21	6.119	3.200	1.912	0.984	0.995	0.989	-0.12
0.0	6.247	3.217	1.942	1.004	1.000	1.004	0.0
Sample #SMG1, Cycle #8, p_w = 1 bar (buffered), $\dot{\varepsilon} = 10^{-6}$/sec							
0.0	6.236	3.020	2.065	1.004	0.968	1.037	0.60
0.0	6.211	3.119	1.991	1.-	1.-	1.-	0.60
0.13	6.215	3.117	1.994	1.001	0.999	1.002	0.54
0.25	6.219	3.116	1.996	1.001	0.999	1.003	0.48
0.42	6.219	3.110	2.000	1.001	0.997	1.005	0.40
0.63	6.206	3.107	1.997	0.999	0.996	1.003	0.38
0.84	6.219	3.104	2.004	1.001	0.995	1.007	0.35
1.05	6.195	3.101	1.998	0.997	0.994	1.004	0.32
1.25	6.183	3.096	1.997	0.995	0.993	1.003	0.32
1.46	6.178	3.091	1.999	0.995	0.991	1.004	0.32
1.67	6.166	3.087	1.997	0.993	0.990	1.003	0.33
1.90	6.167	3.086	1.998	0.993	0.989	1.004	0.34
2.09	6.151	3.079	1.998	0.990	0.987	1.004	0.35
2.30	6.127	3.065	1.999	0.986	0.983	1.004	0.40
2.51	6.116	3.049	2.006	0.984	0.978	1.008	0.44
2.72	6.061	3.024	2.004	0.976	0.970	1.007	0.50
2.84	5.988	3.008	1.991	0.964	0.964	1.000	0.54
2.97	5.941	2.991	1.986	0.957	0.959	0.997	0.56
3.09	5.907	2.963	1.994	0.951	0.950	1.002	0.64

TABLE 4-1 (continued)

Sample #SMG1, Cycle #8, p_w = 1 bar (buffered), $\dot{\varepsilon} = 10^{-6}$/sec (continued)

Stress kb	V_p km/sec	V_s km/sec	V_p/V_s	$V_p/(V_p)_o$	$V_s/(V_s)_o$	$(V_p/V_s)/(V_p/V_s)_o$	$\theta \times 10^{-3}$
3.20	5.891	2.940	2.004	0.948	0.943	1.007	0.69
3.30	5.841	2.903	2.012	0.940	0.931	1.011	0.76
3.35	5.821	2.880	2.021	0.937	0.923	1.015	0.82
3.35	5.787	2.872	2.015	0.932	0.921	1.012	0.84
3.35	5.793	2.867	2.021	0.933	0.921	1.015	0.90
3.35	5.795	2.865	2.023	0.933	0.919	1.016	0.90
3.14	5.821	2.866	2.031	0.937	0.919	1.020	0.84
2.72	5.829	2.875	2.027	0.938	0.922	1.018	0.76
2.72	5.827	2.875	2.027	0.938	0.922	1.018	0.76
2.30	5.828	2.886	2.019	0.938	0.925	1.014	0.66
1.88	5.833	2.911	2.003	0.939	0.933	1.007	0.58
1.46	5.884	2.948	1.996	0.947	0.945	1.003	0.44
1.05	5.946	2.987	1.991	0.957	0.958	1.000	0.32
0.63	6.064	3.031	2.001	0.976	0.972	1.005	0.20
0.21	6.142	3.062	2.006	0.989	0.982	1.008	0.20
0.0	6.142	3.071	2.000	0.989	0.985	1.005	0.26
Sample #SMG1, Cycle #11, p_w = 1 bar (vented), $\dot{\varepsilon} = 10^{-4}$/sec							
0.0	6.276	3.078	2.039	0.999	0.994	1.004	1.13
0.0	6.285	3.095	2.031	1.-	1.-	1.-	1.13
2.02	6.081	3.006	2.023	0.996	0.971	0.996	1.72
2.02	6.037	3.002	2.011	0.961	0.970	0.990	1.74
2.02	6.120	3.003	2.038	0.974	0.970	1.003	1.74
2.35	5.953	2.929	2.032	0.947	0.946	1.000	1.96
2.35	5.918	2.923	2.025	0.942	0.944	0.997	2.04
2.75	5.620	2.819	1.994	0.894	0.911	0.982	2.37
2.75	5.643	2.816	2.004	0.898	0.910	0.987	2.47
0.0	6.118	2.994	2.043	0.973	0.967	1.006	1.20

TABLE 4-1 (continued)

Sample #SMG1, Cycle #11, p_w = 1 bar (vented), $\dot{\varepsilon} = 10^{-4}$/sec (continued)

Stress kb	V_p km/sec	V_s km/sec	V_p/V_s	$V_p/(V_p)_o$	$V_s/(V_s)_o$	$(V_p/V_s)/(V_p/V_s)_o$	$\epsilon \times 10^{-3}$
0.0	6.173	3.010	2.051	0.982	0.973	1.010	1.13
0.0	6.175	3.025	2.041	0.982	0.977	1.005	1.10
0.0	6.212	3.031	2.049	0.988	0.979	1.009	1.11
0.0	6.262	3.046	2.059	0.996	0.984	1.014	1.11
Sample #SMG1, Cycle #15, p_w = 1 bar (buffered), $\dot{\varepsilon} = 10^{-4}$/sec							
0.0	6.138	2.957	2.075	1.000	0.997	1.002	1.22
0.0	6.140	2.965	2.071	1.-	1.-	1.-	1.20
3.16	5.606	2.788	2.011	0.913	0.940	0.971	2.69
3.13	5.617	2.776	2.023	0.915	0.936	0.977	2.75
0.0	6.145	-	-	1.001	-	-	1.27
Sample #SMG1, Cycle #16, p_w = 1 bar (buffered, $\dot{\varepsilon} = 10^{-4}$/sec							
0.0	6.000	2.927	2.050	0.999	0.994	1.006	1.25
0.0	6.001	2.944	2.038	1.-	1.-	1.-	1.23
0.0	5.990	2.944	2.035	0.998	1.000	0.999	1.23
3.30	5.559	2.774	2.002	0.926	0.942	0.982	2.83
3.28	5.542	2.769	2.001	0.923	0.941	0.985	2.88
3.28	5.575	2.756	2.023	0.929	0.936	0.993	2.88

filled circles, Figure 4-3).

RESULTS

Results are presented in Table 4-1. In all samples studied, both shear and compressional wave velocities decreased with increasing dilatant volumetric strain, regardless of degree of saturation. For the same degree of saturation, velocities appear to be nearly monotonic functions of dilatant volumetric strain for a given rock type. This is somewhat surprising as one might have expected minor variations in crack geometry from sample to sample to introduce scatter in the measurements. At low pressures it is difficult to separate out the effect of different mineralogies from the effect of different crack and pore porosities in order to compare velocities between the gabbro and the granite, but the sensitivity of the individual velocities to θ seems to be similar for the two rocks. Moreover, in the range studied, the velocities are insensitive to effective confining pressure except as it alters θ. The run designated "variable" (Figure 4-5, crosses) had a pore pressure which was allowed to deviate from the initial 350 bar value in response to opening and closing of cracks within the rock. In fact it rose to 360 bars during initial loading and dropped to 307 bars at the peak axial load. Yet the behavior of velocities vs. θ during this loading cycle is nearly identical to that for the previous loading cycle (open circles, Figure 4-5), during which the pore pressure was held constant at 350 bars. Confining pressure in both cases was 390 bars. The

→ Pg 104

Figure 4-5. Change in seismic velocities with θ in saturated granite. Crosses, variable pore pressure; circles, 350 bars pore pressure.

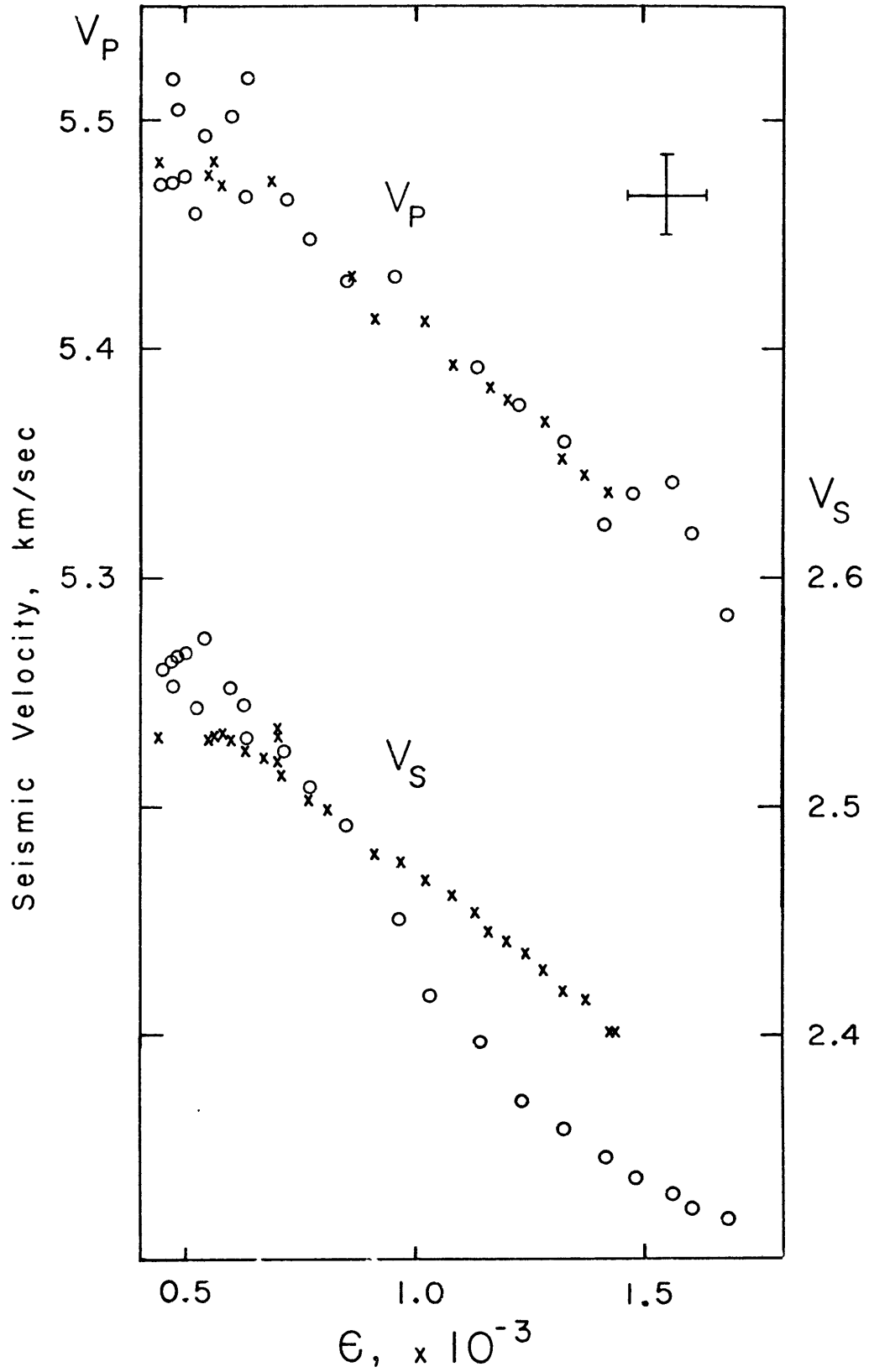
V_P
5.5
5.4
5.3
V_P
V_S
V_S
2.6
2.5
2.4
Seismic Velocity, km/sec
0.5
1.0
1.5
ϵ, x 10^{-3}

major difference between the two cycles is that less dilatant volumetric strain and less change in velocities were observed as a result of applying the same peak load when the pore pressure was allowed to vary; i.e. dilatancy hardening (Brace and Martin III, 1968) occurred. Similarly, the results of two dry runs, one conducted at 40 bars and one at 390 bars confining pressure, may be taken to show the independence of velocities on effective stress (Figure 4-6).

Hysteresis in Velocity-θ Curves. From Table 4-1, systematic differences may be noted in the velocity vs. θ relationship between the loading and unloading cycles. Such discrepancies occurred for both wet and dry stress cycles, with velocity invariably being less for a given value of θ during unloading. While some of the difference can be explained by time-dependent pore fluid migrations in wet rocks or time-dependent crack closure in wet and dry rocks, all of the hysteresis does not disappear with time. This is shown for a wet sample by the arrows in Figure 4-7.

During the first of the stress cycles illustrated (open circles), unloading was interrupted to follow the changes of θ, V_p and V_s with time. Similarly, during the second of the stress cycles illustrated (closed circles) the loading at 1.5×10^{-5}/sec was twice arrested and the migrations of θ followed for a two-hour interval under constant axial stress. There is no indication from the directions of migration that the observed hysteresis would disappear if loading and unloading were performed infinitely slowly.

Figure 4-6. Change in seismic velocities with e in dry granite. Crosses, 40 bars confining pressure; circles, 390 bars confining pressure.

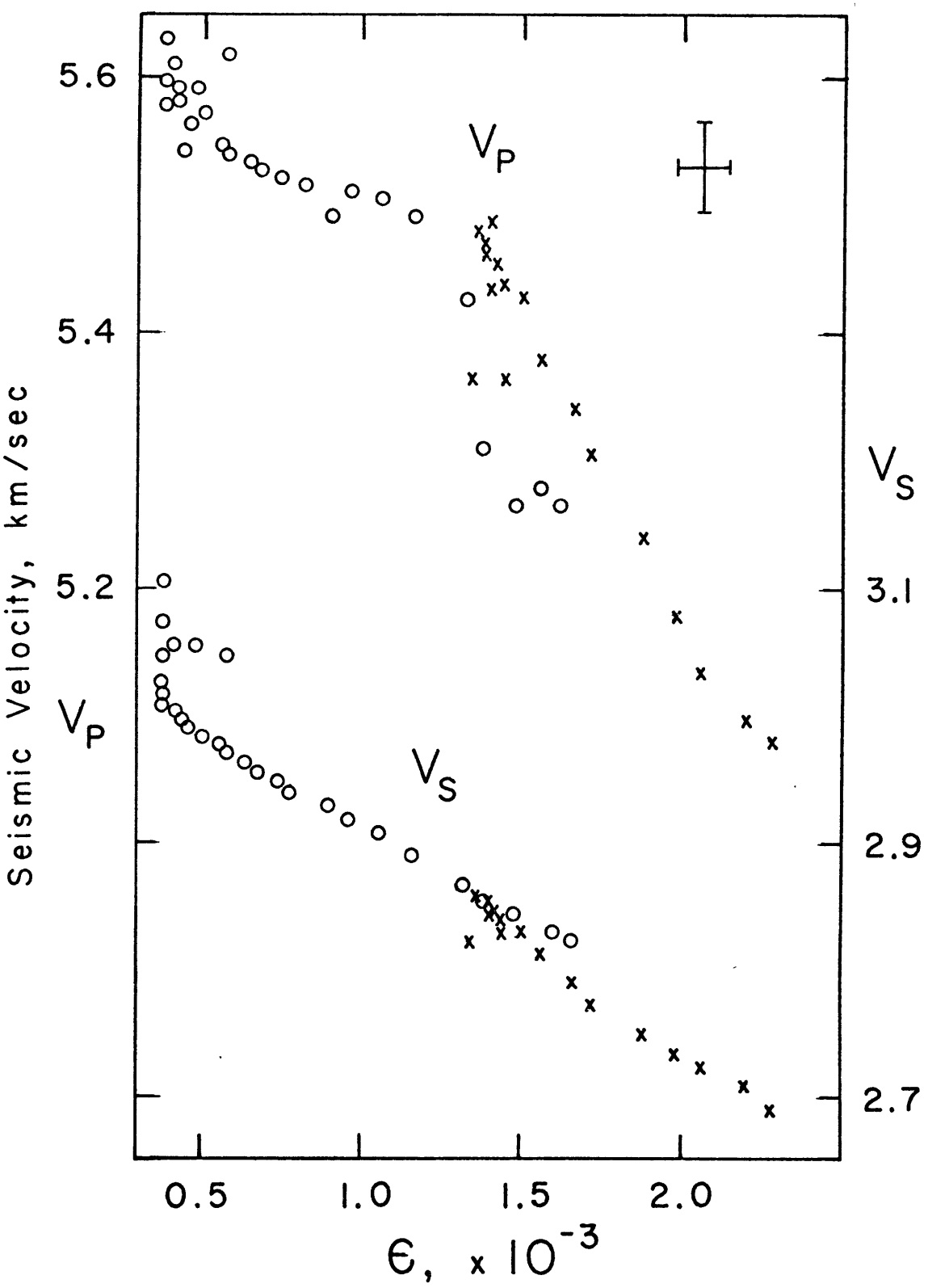
5.6
5.4
5.2
V_P
V_P
V_S
V_S
3.1
2.9
2.7
Seismic Velocity, km/sec
0.5
1.0
1.5
2.0
ϵ, x 10^{-3}

A second possibility, loosening of the transducer bond, can be ruled out as the zero stress velocities are more or less recoverable from cycle to cycle provided the dilatancy can be recovered.

The most likely explanation for the hysteresis lies in uncertainty as to the elastic line for unloading. Probably, frictional resistance must be overcome during unloading before dilatant cracks can close (Scholz and Kranz, 1974). This means that the rock will begin to unload "elastically", without undergoing significant changes in crack distribution or shape. The true dilatant volumetric strain should therefore not change much, contrary to what is found if one refers the stress-volumetric strain curve back to the elastic line for loading in computing ϵ. As long as the cracks remain open, seismic velocities should remain low. This appears to be what is happening at points A-C in Figure 4-7. Once the applied stress has dropped enough that the frictional resistance can be overcome, the velocities will begin to recover (somewhere between C and D in Figure 4-7). As unloading proceeds from D, cracks begin to close and the velocities should recover along the same path followed during loading. Regardless of rate, the V_p or V_s vs. ϵ curves should look identical during stress application and release, as long as the degree of saturation of the rock remains unchanged. That they fail to do so, as in Figure 4-7, is an artefact of using the linear elastic line for loading to determing the dilatant volumetric strain during unloading.

Except where noted, the rest of this paper will treat only

Figure 4-7. Hysteresis in seismic velocities vs. θ in granite with 350 bars pore pressure. See text for explanation.

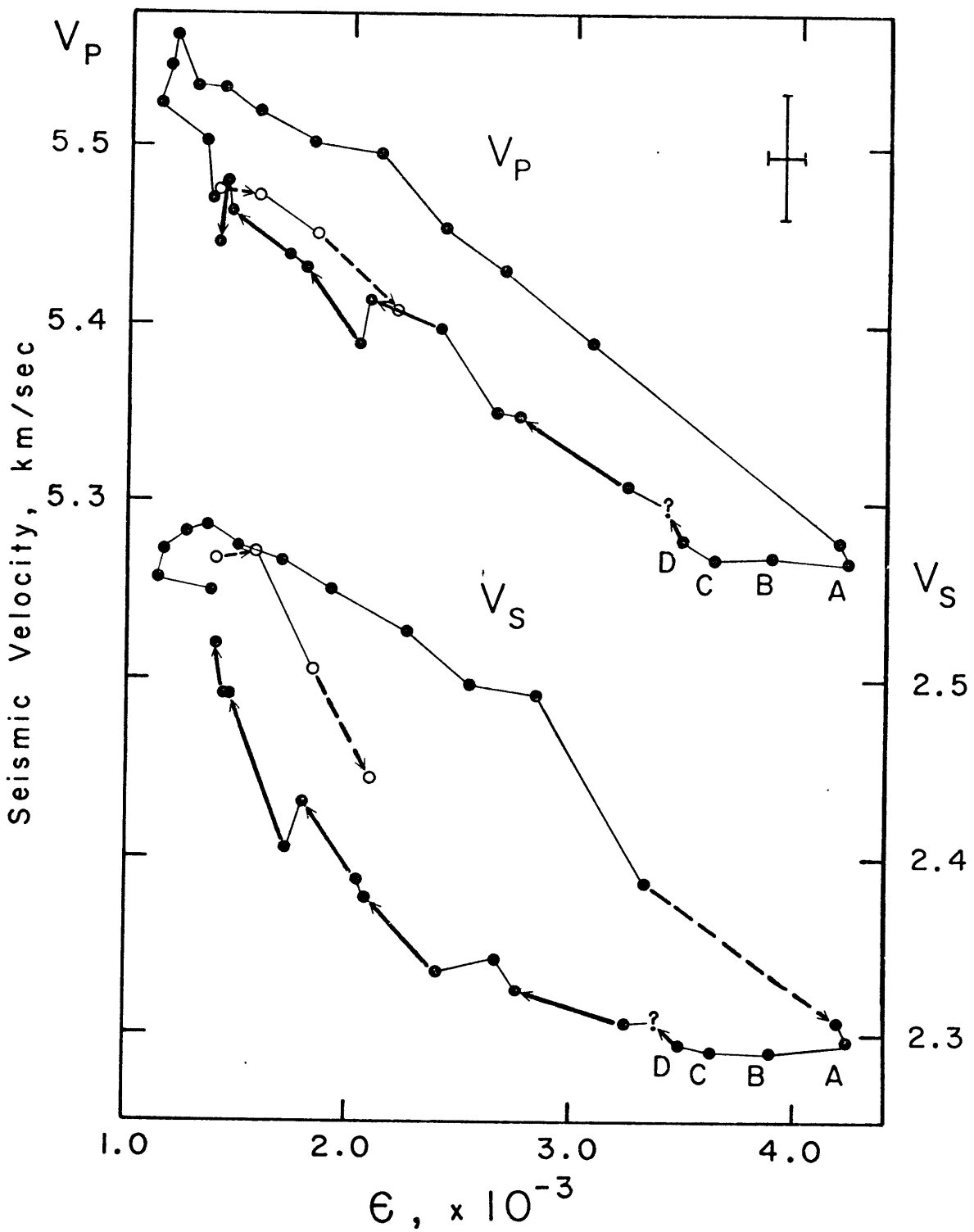
V_P
5.5
5.4
5.3
V_P
V_S
D
C
B
A
V_S
2.5
2.4
2.3
Seismic Velocity, km/sec
1.0
2.0
3.0
4.0
ϵ, x 10^{-3}

the results of measurements made on loading paths because of the uncertainty in the elastic line for unloading.

Velocity Ratios. Although differences in degree of saturation of the rock samples are not striking when one looks at the behavior of the individual velocities as a function of dilatant volumetric strain, a sharp distinction may be drawn between saturated, partially saturated and dry rocks based upon the behavior of the ratio V_p/V_s). If, for each stress cycle, we define the parameter $(V_p/V_s)_o$ to be the value of the velocity ratio when the shear wave velocity is a maximum, and if we take ϵ_o to be the dilatant volumetric strain corresponding tc that value of V_s (ϵ_o may be nonzero owing to crack orientation effects), then we may easily compare the variation of V_p/V_s and ϵ during different stress cycles by normalizing them with respect to these parameters. The percent change in the velocity ratio relative to the value it has at the shear wave velocity maximum is simply $(V_p/V_s)/(V_p/V_s)_o$-1. Results for dry rocks have been plotted in Figure 4-8; V_p/V_s drops at large dilatant strains. For rocks with high pore pressure (Figure 4-9) the ratio rises. These rocks presumably remain saturated. Again, there is evidence of the independence of velocity-dilatant strain behavior on rock type because the gabbro (closed circles, Figure 4-10) run at 1.5×10^{-6}/sec behaved comparably to the granites run at 1.5×10^{-5} and 1.5×10^{-6}/sec.

A further word about the gabbro is in order as its behavior may contradict some models of precursory phenomena of earthquakes (Brady, 1975). Points A and beyond (Figure 4-9) were obtained

Figure 4-8. Change in seismic velocity ratio with θ in dry rock. Strain rates 1.5×10^{-5} and 1.5×10^{-6}/sec. Open circles, granite, filled circles, gabbro. Numbers shown are maximum stress attained during loading cycle, in kbar.

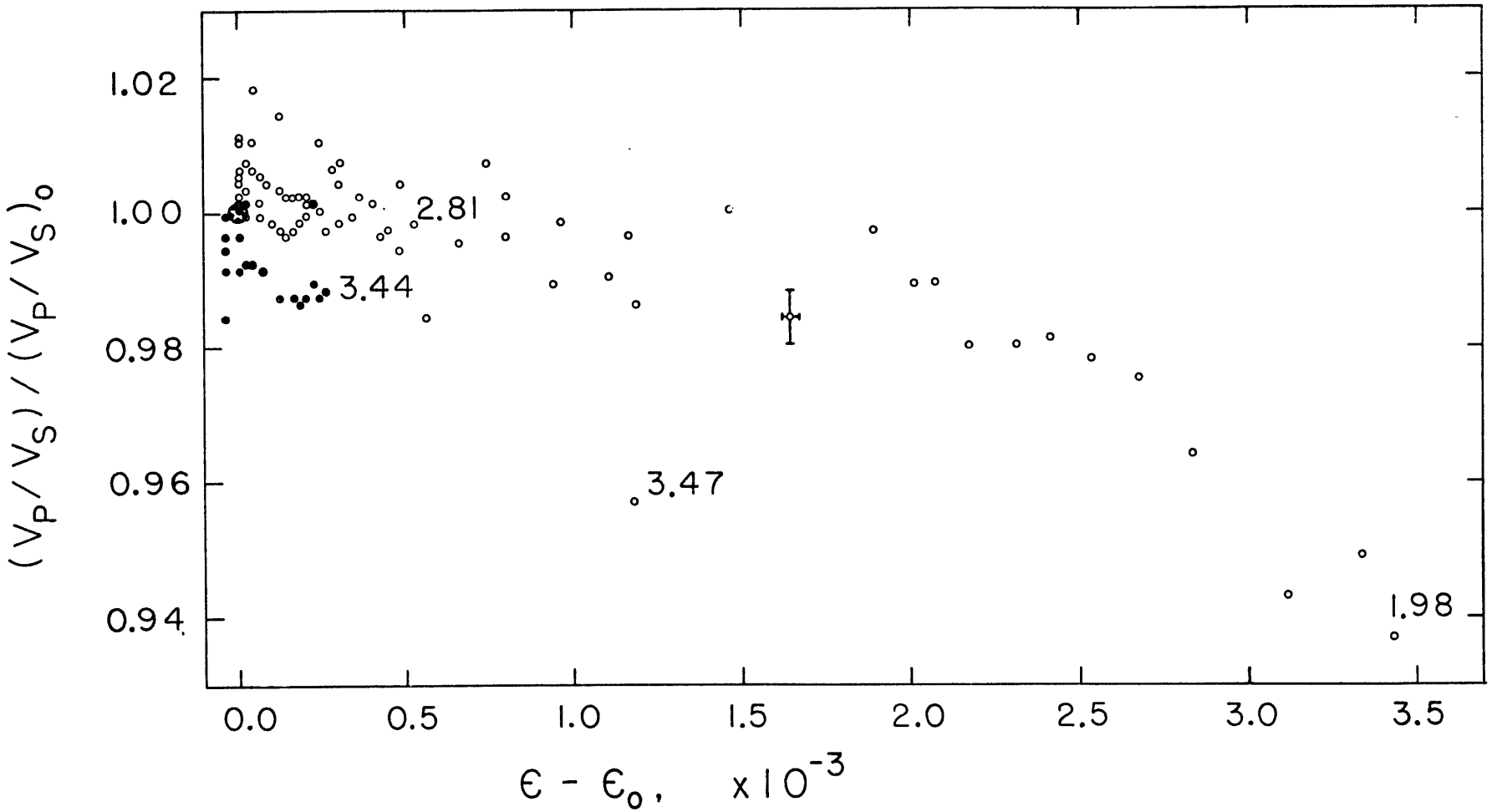
1.02
1.00
0.98
0.96
0.94
$(V_P/V_S)/(V_P/V_S)_o$
2.81
3.44
3.47
1.98
0.0
0.5
1.0
1.5
2.0
2.5
3.0
3.5
$\epsilon - \epsilon_o$, $\times 10^{-3}$

Figure 4-9. Change in seismic velocity ratio with ϵ in rocks with high pore pressure. Strain rates 1.5×10^{-5} and 1.5×10^{-6}/sec. Open circles, granite, 350 bars pore pressure; open squares, granite, variable pore pressure; filled circles, gabbro, 350 bars pore pressure. Numbers shown in figure are maximum stress attained during loading cycle, in kbar.

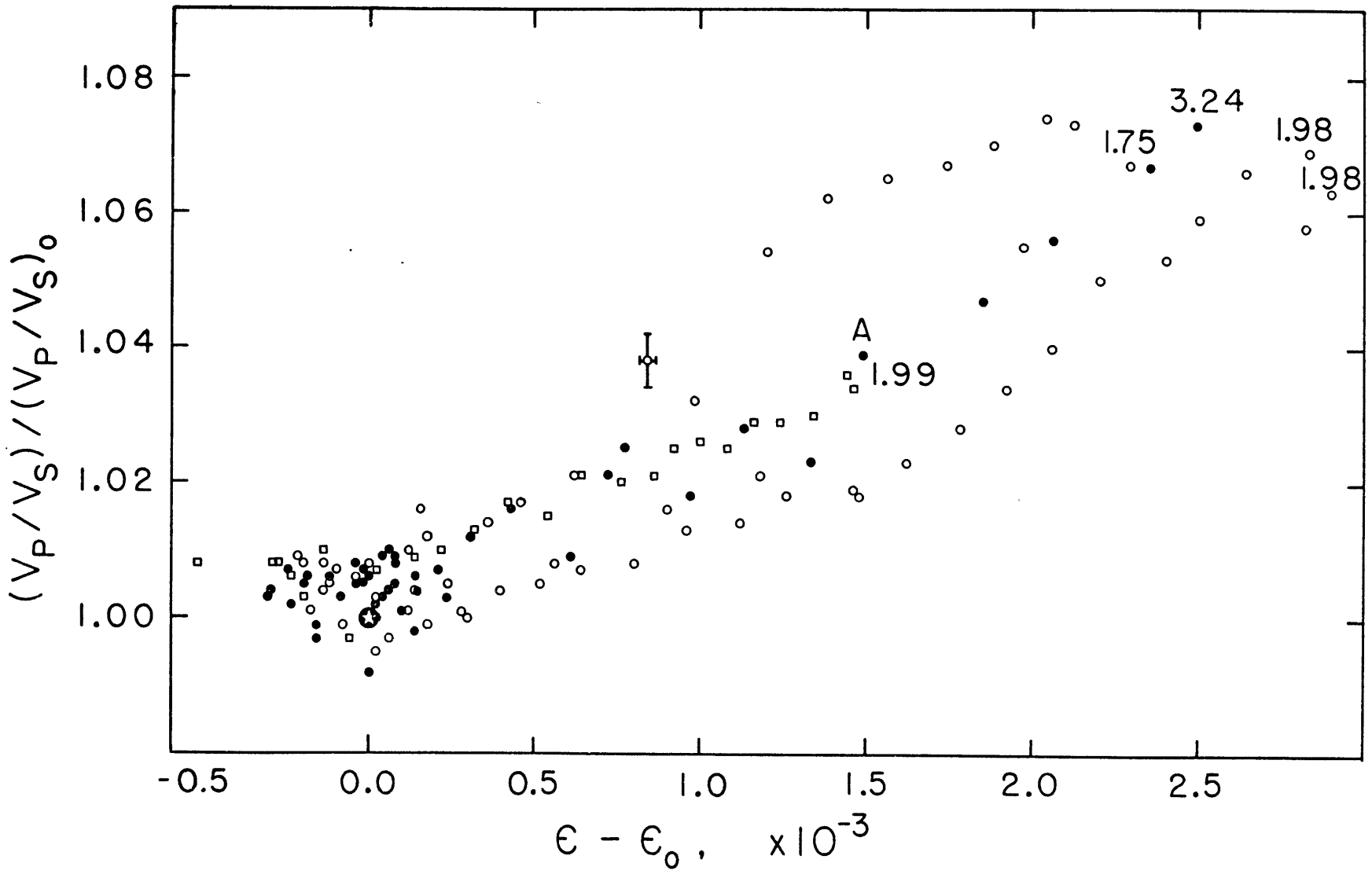
1.08
1.06
1.04
1.02
1.00
$(V_P/V_S)/(V_P/V_S)_o$
3.24
1.98
1.75
1.98
A
1.99
-0.5
0.0
0.5
1.0
1.5
2.0
2.5
$\epsilon - \epsilon_o$, $\times 10^{-3}$

in the post-peak stress region of the loading cycle. The loading was arrested at a maximum stress of 3.21 kbar and the rock allowed to relax for two hours due to accelerating creep. During this time, the stress dropped 140 bars, V_p decreased by 3.2 percent, but V_s decreased by 6.8 percent causing a new increase in V_p/V_s. It seems that a rather significant drop in stress would be required before cracks stopped propagating, let alone before frictional resistance could be overcome enough to permit crack closure and a V_s rise.

Results for stress cycles with 1 bar water pressure are rate-dependent (Figure 4-10), a phenomenon not observed in the dry and high pore pressure cases. At slow rates when the experiment was conducted with the pore fluid reservoir connected to the sample so that additional water was available to fill opening cracks, V_p/V_s rose. The rock properties followed the trend of the previous results for samples with 350 bars water pressure. At fast rates the results are more complex. When excess water was available, the V_p/V_s ratio tended to remain constant, but when the pore fluid reservoir was not connected to the rock the ratio dropped with increasing dilatant strain. However, the drop was not as pronounced as in the dry case. Under these fast rate conditions at the low pore pressure, the dilatant rock may be partially saturated, the amount of partial saturation depending upon the availability of additional pore fluid. The velocity ratio reflects the degree of partial saturation. This is in agreement with the theoretical results of O'Connell and Budiansky, (1974).

Figure 4-10. Change in seismic velocity ratio with θ in gabbro with 1 bar pore pressure. Squares, strain rate 1.5×10^{-4}/sec, pore fluid reservoir disconnected; circles, strain rate 1.5×10^{-4}/sec, reservoir connected; triangles, strain rate 1.5×10^{-6}/sec, reservoir connected. Numbers shown in figure are maximum stress attained during loading cycle, in kbar.

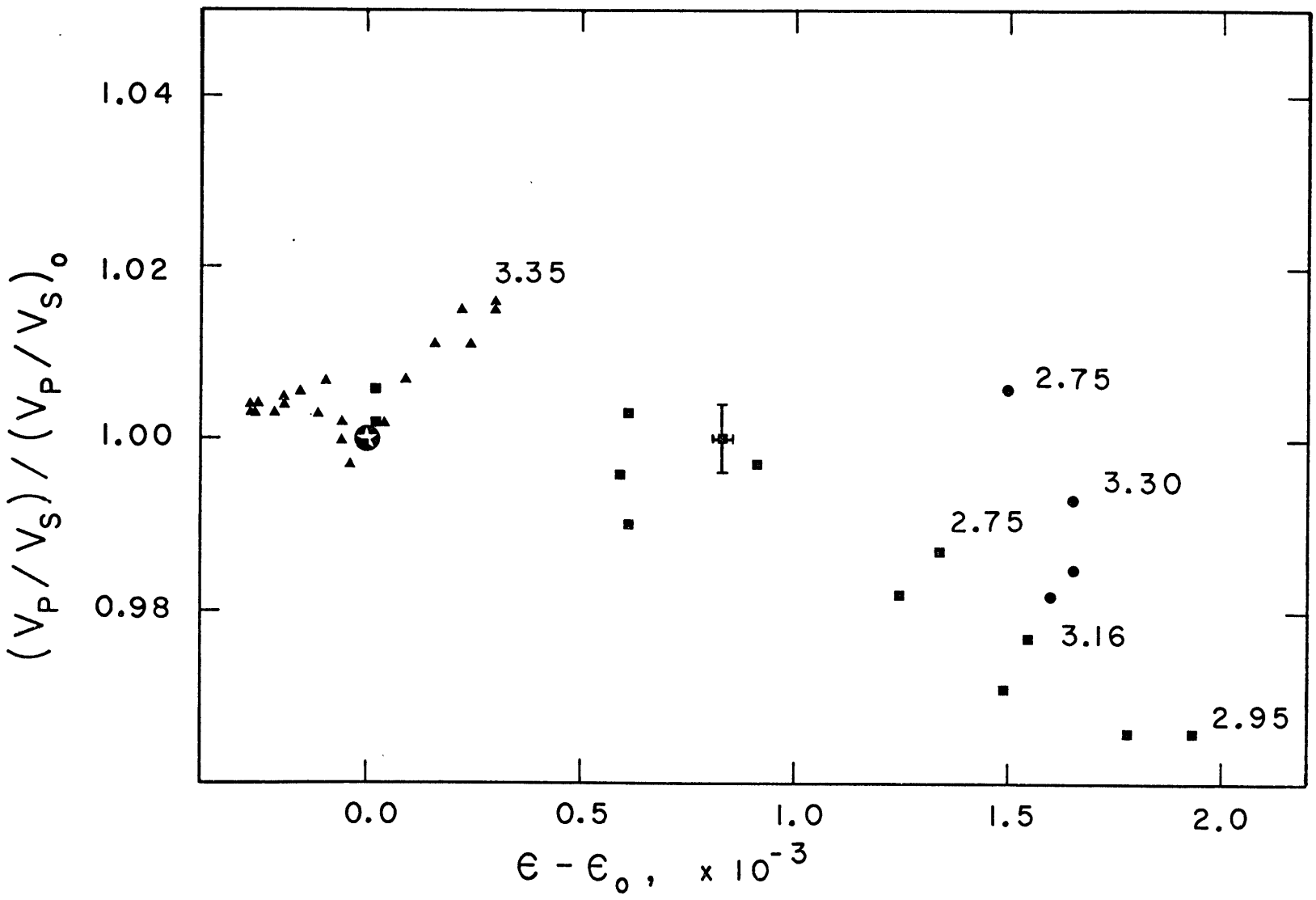
1.04
1.02
1.00
0.98
$(V_P/V_S)/(V_P/V_S)_o$
3.35
2.75
3.30
2.75
3.16
2.95
0.0
0.5
1.0
1.5
2.0
$\epsilon - \epsilon_o$, x 10^{-3}

The Liquid-Vapor Transition. The water-steam transition offers another possible mechanism for decreasing seismic velocity ratio. It is attractive because it provides an alternative to the opening of dry cracks in rock. Presumably, wet cracks would affect seismic velocities like dry cracks if the water in them could be converted to vapor through dilatancy-induced volume changes. Temperatures and hydrostatic pressures at mid-crustal depths are thought to be near the liquid vapor phase boundary for H_2O (Anderson and Whitcomb, 1974), so at any given temperature, only a negligible drop in pressure might suffice to vaporize the pore fluid. The resulting change in the compressibility of the pore fluid, and consequently, of the compressional wave velocity of the aggregate could be large.

Because our apparatus is unable to reach the liquid-vapor transition temperature of H_2O, CO_2 was used to model the water-steam transition. Although the room temperature viscosity of liquid CO_2 near the liquid-vapor transition is somewhat lower than that of liquid water at, say, 200°C (Washburn, 1929), the decrease in bulk modulus going through the transition is comparable (Kennedy and Holser, 1966; and Figure 4-11).

Some differences between the behavior of CO_2-saturated and water-saturated rocks are apparent from Figure 4-12. At p_{CO_2} = 112 bars, well above the transition pressure, the initial rise in V_p/V_s with dilatant volumetric strain appears to level off or reverse itself at higher strains. The cause of this is in doubt. Since no drop in V_p/V_s was observed for comparable →

Figure 4-11. Compressibility of carbon dioxide at 20°C.

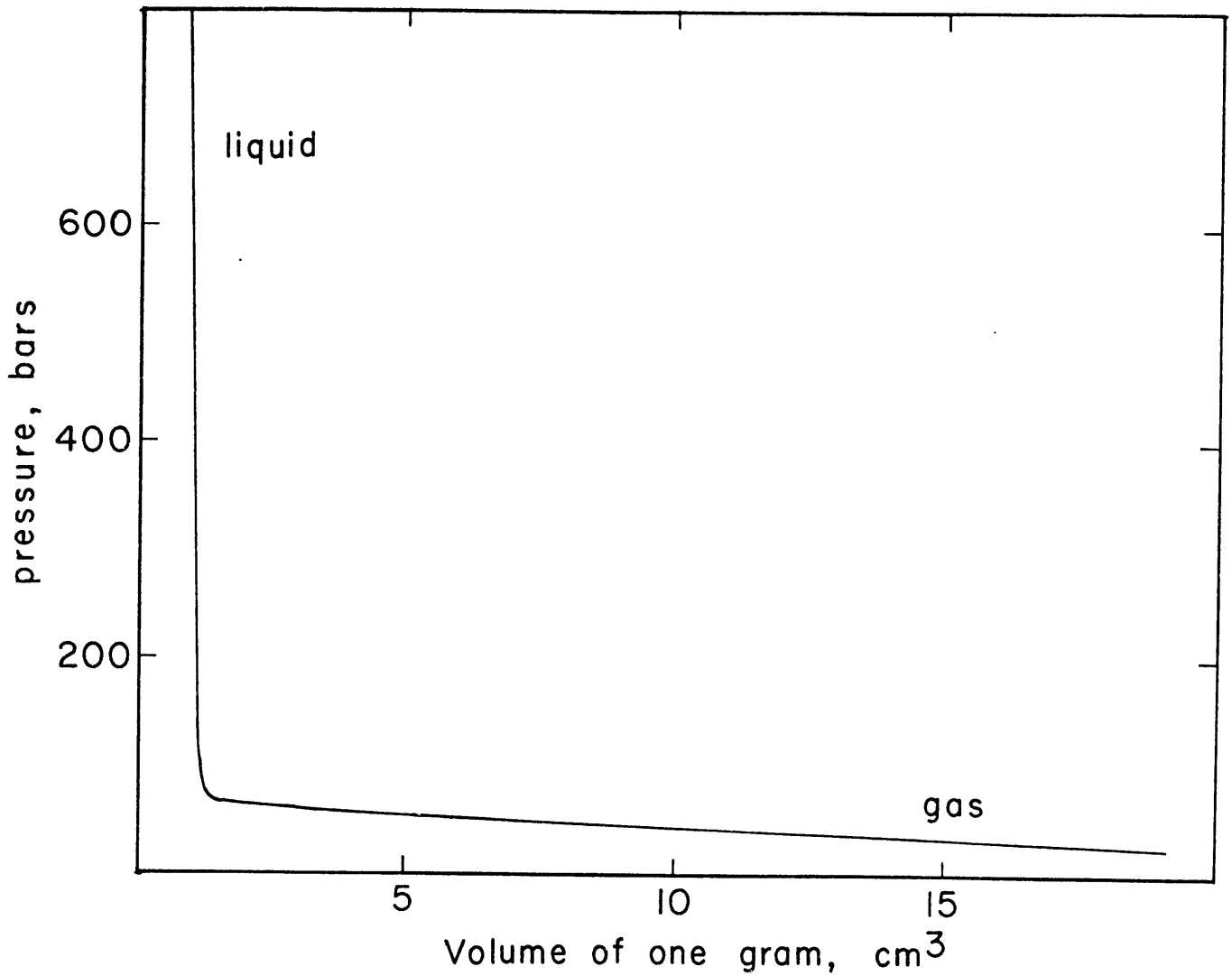
liquid
gas
600
400
200
pressure, bars
5
10
15
Volume of one gram, cm3

Figure 4-12. Change in seismic velocity ratio with e in granite with CO_2 pore fluid. Open circles, 112 bars CO_2 pressure; triangles, 68 bars CO_2 pressure; solid circles, 62 bars (liquid-vapor transition) CO_2 pressure. See text for explanation of stars.

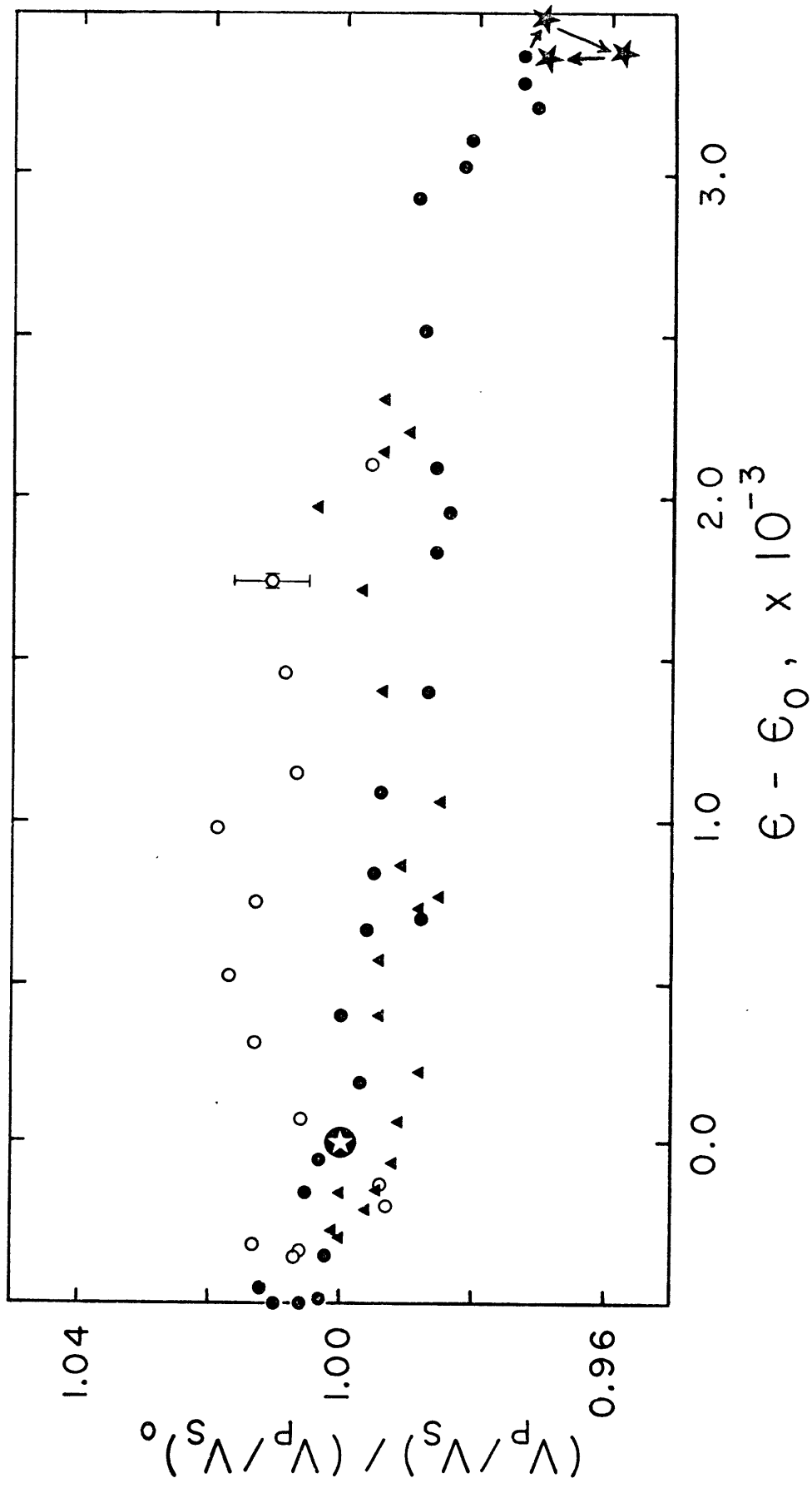
1.04
1.00
0.96
$(V_p/V_s) / (V_p/V_s)_o$
0.0
1.0
2.0
3.0
$\epsilon - \epsilon_o$, x 10^{-3}

dilatant volumetric strains when the starting CO_2 pore pressure was only slightly above the transition pressure, it is unsatisfying to try to explain the higher pore pressure behavior by appeal to the liquid-vapor transition. In fact, even running with CO_2 pore fluid at the transition pressure, the large drop expected in V_p/V_s failed to materialize. Although the drop in V_p was comparable to that for a dry rock with the same dilatant volumetric strain, the drop in V_s was somewhat larger so that the ratio of the velocities, although it decreased, decreased less than it would in a dry rock (compare Table 4-1, entry W1, cycle 12, with entry W3, cycle 6).

To remove any doubt about whether or not the liquid-vapor transition had been achieved in the dilatant rock with initial CO_2 pore pressure equal to 62 bars, the pore pressure system was reconnected to the sample at the peak of the loading cycle by opening a valve, and the reservoir pressure was monitored. After allowing time for any equilibration, the pore pressure was bled off deliberately. The velocity ratio-dilatant strain behavior followed the path shown by the arrows in Figure 4-12. The first star represents the point where the reservoir was reconnected to the sample. No change in velocities was observed within the 10-minute interval thereafter and the pore pressure held steady at 62 bars. The CO_2 was then bled off slowly. The second star in Figure 4-10 shows the last velocity ratio determination made while the pore pressure maintained its original 62 bar value. The third star represents the lowest value of V_p/V_s measured; pore pressure had by then dropped to 57 bars, clearly below the transition pressure. Thereafter,

V_p/V_s began to rise, finally reaching the value indicated by the last star at 1 bar pore pressure. The rise in V_p/V_s was due to an increase in Both V_p and V_s caused by crack closure in response to the increasing effective confining pressure on the rock sample.

DISCUSSION

Extrapolation of the Laboratory Results to the Earth. Although the relative magnitudes and the signs of the experimentally observed changes in V_p, V_s and their ratio may apply to the field, the absolute magnitudes may not. Near surface *in situ* velocities can be two to three orders of magnitude more sensitive to changes in ambient stress than velocities measured in the laboratory (DeFazio, *et al*. 1973; Reasenberg and Aki, 1974). If stress-strain behavior remains about the same in the laboratory and the field, then the conclusion is that rocks in the field may be two to three orders of magnitude more sensitive to ϵ than the results reported here suggest.

The most likely cause of this enhanced sensitivity is the difference in aspect ratio, width/length, of the cracks or joints *in situ* and those occurring in the laboratory rock samples. Walsh, (1965a, b, c) has shown that the effective elastic moduli vary as the crack length cubed; therefore long, thin cracks will have a greater effect on seismic velocities than short, fat ones for the same crack axis orientations and total crack volume. In the dry laboratory samples, for $\epsilon \simeq 10^{-3}$ only a 10 percent change in V_p is observed. Applying this

dependence directly to the field case requires that 10m of uplift be associated with a 20 percent drop in V_p assuming a dilatant volume with a radius of 10 km. This, clearly, is impossible. If, however, the average aspect ratio of cracks in the field were two or three orders of magnitude smaller than that in our granite and gabbro cylinders, then only 1 to 10 cm of uplift would suffice. Two orders of magnitude decrease in average aspect ratios from laboratory to field appears plausible not merely because of the greater length scales possible in situ, but because of the difference in lateral stiffness conditions between our experiments (constant confining pressure) and the earth (somewhere between constant confining pressure and uniaxial strain).

When looking for precursory changes in travel time ratios in the field, care must be taken to separate out differences due to changing path and/or polarization from those associated with changing crack density or degree of saturation of the material. The former need not signify a change in stress state in situ, while the latter probably do. The laboratory experiments, of course, are conducted under constant path and polarization conditions. Thus changes in V_p/V_s are related only to changing rock properties under loading. If, however, the polarization of the S wave had been changed by 90^o in these experiments, the decrease in shear wave velocity would have been about 60 percent of the observed value (Figure 4-5 and Bonner, personal communication). This means that decreases (increases) in the ratio V_p/V_s would have appeared to be greater (less) than were in fact measured (corresponding to a clockwise

rotation of the points in Figures 4-8 through 4-10 and 4-12).

The effect of measurement path on the magnitude of V_p/V_s can be considered most easily under the assumption of axial symmetry. If we make that simplification then from these experiments and those of Bonner (personal communication), Matsushima (1960a), and Gupta (1973a), V_p/V_s surfaces for the rock may be constructed (Figure 4-13b). These will be ellipsoids of rotation with the magnitude of the radius vector equal to the value of V_p/V_s measured in that direction. Because the magnitude of V_s is polarization as well as direction dependent, a range of values of V_p/V_s are possible in any one direction. If axial cracks (semi-major axis in the 3 direction) are opening in the dilatant material with random orientations of semi-minor axes (Figure 4-11a), then $V_{s_{13}}$* will be equal to $V_{s_{31}}$ ($=V_{s_{32}}$), while $V_{s_{12}}$ will be least of all. Similarly, V_{p_1} will be less than V_{p_3}; in fact, V_{p_3} will be nearly indistinguishable from the velocity in the unstressed material. For dry granite at about 400 bars p_c, Figure 4-11b illustrates the likely range of normalized V_p/V_s values.

In the field, the condition of axial symmetry may not be met. In a tectonic region, two of the three principal stresses need not generally be equal. Moreover, even a slight foliation such as is found in Westerly granite can produce more than 10 percent departures from axial symmetry of cracks if that foliation does not coincide with the unique stress direction. This means

*The first numerical subscript gives the propagation direction; the second, the polarization direction.

Figure 4-13. (a) Idealized representation of cracks in dilatant rock cylinder. (b) Normalized velocity ratio $[(V_p/V_s)/(V_p/V_s)_o]$ ellipsoid for dry granite with ϵ about 2 x 10^{-3} strain.

$\zeta = (V_{p3}/V_{s31})/(V_{p3}/V_{s31})_o = 1.01$;

$\xi = (V_{p1}/V_{s12})/(V_{p1}/V_{s12})_o = 0.97$

$\upsilon = (V_{p1}/V_{s13})/(V_{p1}/V_{s13})_o = 0.95$. Range of permissible normalized velocity ratios, υ' to ξ', in any given direction is indicated by the darkly-shaded region.

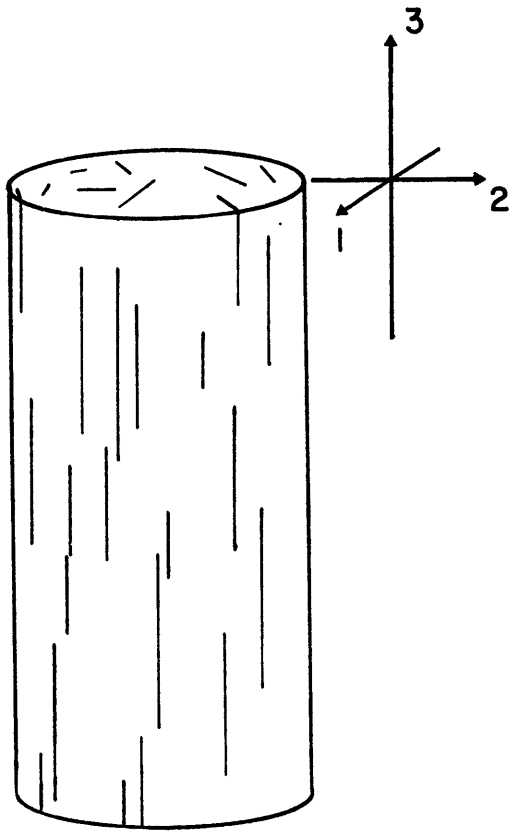

(a)

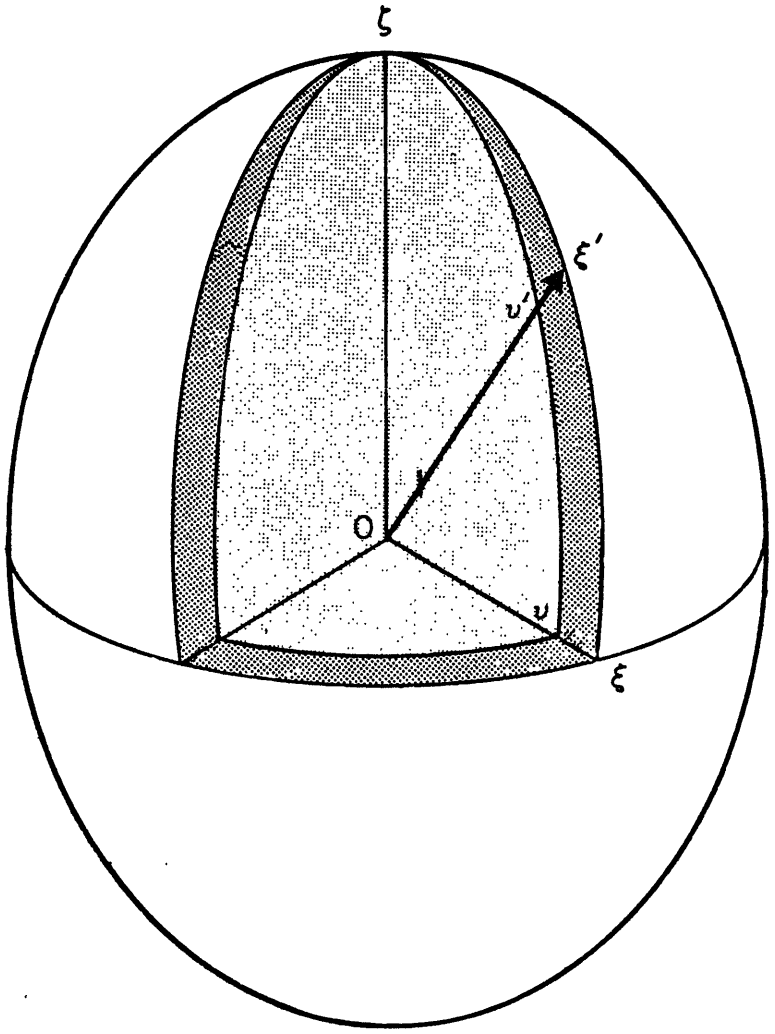

(b)

that the V_p/V_s surfaces will in general be quite complex, and that the principal axes of these surfaces need not coincide with the principal stress directions. However, the surfaces and their orientation can be determined for any rock with existing laboratory techniques. Although existing laboratory data are insufficient to permit such constructions at present, the means exist to separate out effects due to changing path from effects due to changing material properties.

CONCLUSIONS

At low confining pressures, changes in seismic velocity depend upon both dilatant volumetric strain, ϵ, and degree of saturation of the material. Both V_p and V_s decrease with increasing ϵ. V_p decreases more rapidly in saturated or nearly saturated rocks. Intrinsic velocity changes are completely overshadowed by the effect of cracks; thus seismic velocities are insensitive to changes in effective confining pressure except as they affect ϵ.

Seismic velocity ratios show a comparable dependence on ϵ in both the granite and the gabbro under similar conditions of saturation. Although a liquid-vapor transition will cause a decrease in V_p/V_s, the seismic velotity ratio drops over twice as much in dry rock for the same dilatant volumetric strain.

In initially-saturated material, decreases in seismic velocity ratio occur under rather limited conditions. If strain rates of 10^{-4}/sec are required to lower V_p/V_s in dilatant

laboratory specimens where the distance to the reservoir was 6 cm, then to produce this effect in the earth, where strain rates are likely to be at least 6 to 8 orders of magnitude lower, either the distances over which pore fluid must equilibrate are on the order of 10 to 100 km, or the average permeability of the rock *in situ* is 6 to 8 orders of magnitude less than that of repeatedly stressed laboratory samples of San Marcos gabbro. The first alternative appears more likely. Fluid source to fluid sink distances of 6 km are not grossly out of line with anomalous zones of about 10 km linear dimension, such as are suggested by certain field data. However, if the earth's surface is taken to be a fluid source, then significant dry crack space cannot occur in initially saturated material at depths shallower than about 6 km. Dilatant zones forming in saturated regions of the crust at depths less than 6 km will not cause decreases in seismic velocity ratio.

Since dilatant porosity increases probably do not exceed 10-100 percent *in situ* (Hanks, 1974), a liquid-vapor transition is not an attractive means of generating V_p/V_s decreases, as only a small fraction of the pore fluid could be vaporized by the enlargement of liquid-filled cracks. Thus, even if *in situ* velocities are much more sensitive to changes in pore fluid state than those measured in the laboratory, the effect of a liquid-vapor transition is likely to be small. However, it would be in the right direction to produce the observed premonitory decreases in travel time ratios, and large changes in the individual seismic velocities can be involved.

Because the opening of dry cracks produces a much larger drop in V_p/V_s than any other mechanism, the introduction of dry cracks *in situ* must be regarded as the most effective means of generating anomalously low travel time ratios. Of all the possible combinations of dilatancy and pore fluids studied in our experiments, dry cracks can most easily reproduce the relative drops in V_p and V_s reported in the field. In certain localities such as Blue Mountain Lake where hypocentral temperatures are less than 100°C, or in places where uplift data sharply constrain the amount of new crack space that can be accommodated in the *in situ* material, opening of dry cracks may be the only one of the currently understood mechanisms capable of explaining the seismic observations.

CHAPTER 5

COMPARISON OF CALCULATED AND OBSERVED CRACK DENSITIES AND SEISMIC VELOCITIES IN WESTERLY GRANITE

INTRODUCTION

In rock at confining pressures below several kilobars, variations in seismic velocities with pressure, stress or measurement path are due largely to variations in crack density and crack orientation. Classical bounding theories are useless for approaching this type of problem owing to the large differences in moduli between the solid rock and the vapor or liquid filled inclusions. Moreover, these theories (Voigt, 1910; Reuss, 1929; Hill, 1952, 1963) take volume fraction as their input parameter whereas Walsh (1965a, b), Nur (1973)and O'Connell and Budiansky (1974) have shown that elastic constants do not uniquely depend upon volume fraction when the included phase is fluid.

In the past 10 years many theoretical descriptions of the effects of cracks on elastic properties of rocks have been formulated. Thus far agreement between almost all of these analyses and laboratory data has been good (Brace, 1965; O'Connell and Budiansky, 1974; Toksöz et al., 1975), but in view of our near-total ignorance of actual crack geometries, important input parameters to the theories, it is not surprising that calculated elastic constants or seismic velocities could be fit to the measured values. Numbers for total crack and pore porosity are available for many rocks but these data

alone are insufficient. Matrix and fluid phase moduli being constant, seismic velocities will not uniquely depend upon porosity but rather upon crack density, ϵ , $\equiv (1/V) \sum w^3$, where w is a characteristic crack length and V is the aggregate volume. This ϵ is a function not only of porosity but of the crack shapes. New crack geometry measurements in Westerly Granite thus provide a necessary additional constraint in calculating seismic velocities.

Early theoretical treatments of the effect of cracks on bulk properties applied only to dilute concentrations of ellipsoidal voids (Walsh, 1965a, b, 1968, 1969). Kuster and Toksöz (1974) used a dynamic rather than a static approach to obtain elastic constants of a body with an isotropic void distribution. Garbin and Knopoff (1973, 1975a, b) formulated the problem dynamically for the limiting case $\alpha \rightarrow 0$ (α = aspect ratio = semi-minor/semi-major axis of the ellipsoid) in a form which can be extended to anisotropic crack distributions. In the long wavelength limit, their results are identical with Walsh's (1969). Anderson et al. (1974) considered the specific case of transverse anisotropy: a parallel array of oblate spheroidal cracks in an otherwise isotropic medium while Nur (1971) investigated velocity anisotropy due to crack closure during uniaxial loading of a material containing an initially isotropic distribution of cracks. Nur's analysis actually has two parts, one treating the effect of cracks on velocity; the other treating the effect of stress on the crack distribution.

Recently, self-consistent methods have been employed. In these formulations, the elastic constants of the matrix material are replaced by the effective elastic constants of the crack + matrix aggregate in order to calculate the change in strain energy of the body due to the presence of an individual crack (O'Connell and Budiansky, 1974; Budiansky and O'Connell, 1975). This extends the range of validity of the results to higher crack densities although cracks are still treated as isolated flaws within an infinite, homogeneous, isotropic matrix. The accuracy of the self-consistent method cannot be determined from theoretical principles. Comparison with experimental data is the only way to assess the maximum crack density for which a self-consistent solution will be appropriate.

This paper examines the accuracy of the self-consistent approach of O'Connell and Budiansky and the non-interactive approach of Kuster and Toksöz by comparing the two model predictions with laboratory data and with each other (Figure 5-1). Cheng (Toksöz *et al.*, 1975) has developed a formula based on Eshelby's (1957) analysis for determining crack aspect ratio distribution $\alpha_i(p)$ *vs.* $\phi_i(p)$ from $\alpha_i(p_o)$ *vs.* $\phi_i(p_o)$ where ϕ_i is the porosity attributable to spheroidal pores of aspect ratio α_i. Since for spheroids,

$$\epsilon = \frac{3}{4\pi}(\phi_i / \alpha_i) \qquad (1)$$

we may construct $\epsilon(p)$ from considerations of elastic crack closure. For the hydrostatic case then 3 types of comparison

Figure 5-1. Flow chart of the procedure. Solid lines indicate inputs; dashed lines show comparisons.

HYDROSTATIC

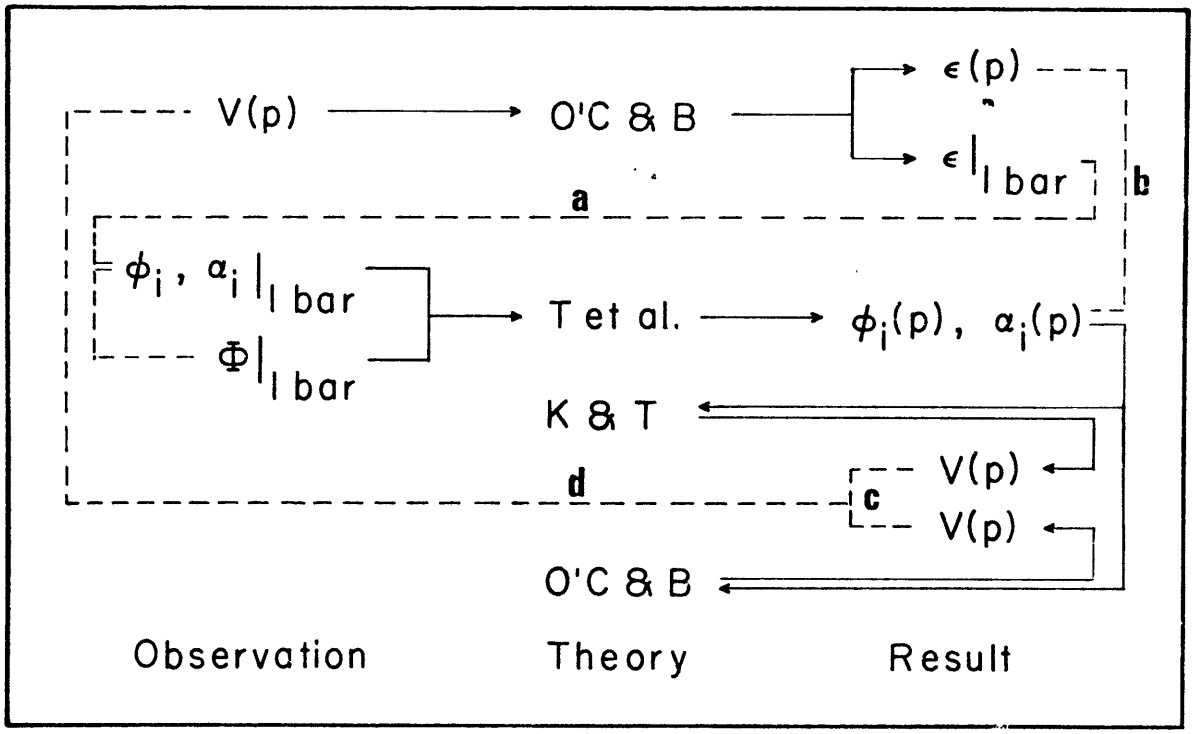

STRESSED

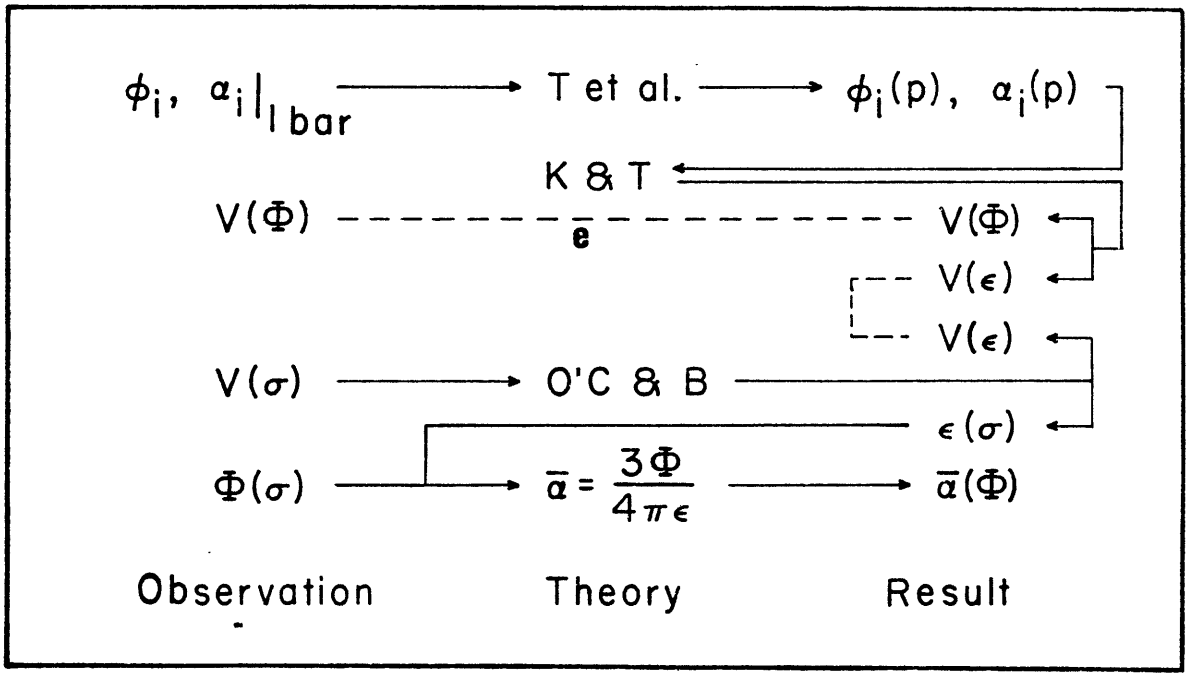

between theory and observation are possible:

1) ϵ(1 bar) as determined with the SEM may be directly compared with crack densities predicted from velocity theories (a, Figure 5-1).

2) $\epsilon(p)$ obtained from crack closure calculations may be compared with $\epsilon(p)$ independently obtained from measured seismic velocities (b, Figure 5-1).

3) Lastly, seismic velocities from the self-consistent and non-interactive models may be compared with each other and with measured values as a function of pressure (c and d, Figure 5-1).

Encouraged by the good agreement between observed and calculated velocities and crack densities in the hydrostatic case, I went on to apply the theories to stressed rock. Unfortunately, there is currently no way of calculating $\epsilon(\sigma)$, where σ is differential stress, independently of seismic velocity data. Thus the only direct comparison between measured and theoretically obtained values are for $V_p(\Phi)$ or $V_s(\Phi)$, where the calculated functions are constructed from $V_p(p)$ or $V_s(p)$ and $\Phi(p)$ ie, Figure 5-1). Agreement between calculated and observed seismic velocities vs. porosity is only to be expected if the crack aspect ratios in stressed and hydrostatically loaded rocks are similar functions of porosity. It seems more fruitful at this stage therefore to accept the theories in the non-hydrostatic case as adequate approximations to reality and to use them, combined with dilatant volumetric strain measurements to obtain information about average aspect ratios in grantie under triaxial load.

THEORETICAL MODELS

The two theories used in this study were developed for isotropic distributions of ellipsoidal inclusions in an otherwise homogeneous, isotropic matrix (O'Connell and Budiansky, 1974; Budiansky and O'Connell, 1975; Toksöz et al., 1975; Kuster and Toksöz, 1974). The formulation of O'Connell and Budiansky is strictly valid only for thin cracks whereas the model of Kuster and Toksöz can handle equant pores as well. The degree of anisotropy which can be tolerated by such isotropic formulations has not been tested heretofore. Since in most rocks under low confining pressures cracks will control variations in elastic properties, preferred orientation of matrix grains contributes only secondarily unless crack directions are tied to crystal morphology (Birch, 1961; Nur and Simmons, 1969). Thus, treating the matrix as isotropic should not lead to difficulties; rock anisotropy will be almost entirely due to the voids.

The model of Kuster and Toksöz depends on a non-interactive scattering analysis and consequently is appropriate only for a sparse distribution of cracks. In an elastic analysis of an infinite array of cracks under simple shear, Koiter (1961) found that the strain energy associated with cracks separated by one crack length was 10 percent greater than for cracks infinitely separated. England and Green (1963) have also demonstrated that strain energy goes up rapidly for cracks opening under uniform pressure as the ratio of crack spacing to crack length decreases from 1. Such studies would require a

characteristic crack length less than 1/2 for reliable solutions, or an ϵ of 0.2. These solutions apply to ordered arrays of cracks, and the results could be quantitatively different if cracks are randomly distributed. Nonetheless, the sparse distribution theory might best be applied cautiously when crack densities are 0.2 or greater.

The scheme of O'Connell and Budiansky is self-consistent; crack interactions are approximated by regarding the material surrounding each crack as a homogeneous, isotropic body having the effective elastic constants of a crack + matrix aggregate. These effective elastic constants can be calculated if the crack density is known. This method should be valid to higher crack densities than that of Toksöz et al. By analogy with resistor array theory, O'Connell and Budiansky (1974) suggest that the self-consistent elastic solutions may be reliable up to crack densities of 0.4.

The formulation of O'Connell and Budiansky requires that seismic velocity of the uncracked matrix, degree of saturation of the voids and ϵ be specified at each interval for which aggregate seismic velocities are to be determined. Alternatively, a unique value of ϵ can be inferred from the aggregate and matrix seismic velocities, independently of the state of saturation of the material (Budiansky and O'Connell, 1975).

$$\epsilon = (2 - \bar{\nu})\frac{9(1 - 2\bar{\nu})(1 + 3\nu)(1 - \bar{K}/K) - 45(\nu - \bar{\nu})}{32(1 - \bar{\nu}^2)(1 - 2\nu)} \qquad (2)$$

where $\bar{\nu} = (2 - (\bar{V}_p/\bar{V}_s)^2)/(2(1 - (\bar{V}_p/\bar{V}_s)^2))$, etc. Barred

quantities refer to aggregate properties, while the others are those of the solid matrix.

Toksöz et al., require a more complete specification of crack density than the single input of O'Connell and Budiansky. Specifically, the aspect ratio distribution and the porosity, ϕ_i, due to voids of a given α_i must be known. But their computer-implemented model will then calculate seismic velocities and aspect ratio distributions at specified pressure increments with only the bulk modulus and density of the phase filling the cracks as additional input parameters. Their theory actually consists of two separate parts. Firstly, $\phi_i(p)$ and $\alpha_i(p)$ are calculated following Eshelby (1957) under the assumption that $d\phi_i/\phi_i = d\alpha_i/\alpha_i$ and that the concentration of voids is dilute ($\phi_i \ll \alpha_i$). Expressions for α_i are evaluated numerically at each pressure increment. Voids of a given aspect ratio are presumed to close when the fractional change is greater than or equal to 1. In calculating $d\alpha_i/\alpha_i$ the matrix material is assumed to have the effective moduli of the rock with all voids of aspect ratio α_j, $j \neq i$. Thus, the first part of the theory incorporates an approximation similar to the self-consistent one. Secondly, the seismic velocities at pressure p are computed from the elastic constants of the effective medium having the previously calculated $\alpha_i(p)$ and $\phi_i(p)$ (Kuster and Toksöz, 1974):

$$V_p = \left(\frac{K^* + \frac{4}{3}\mu^*}{\rho^*} \right)^{\frac{1}{2}}$$

$$V_s = \left(\frac{\mu^*}{\rho^*} \right)^{\frac{1}{2}}$$

$$\rho^* = \rho(1 - \Phi) + \Phi\rho'$$

$$\frac{K^* - K}{3K^* + 4\mu} = \frac{1}{3} \frac{K' - K}{3K - 4\mu} \sum_{i=1}^{N} \phi_i T_{jjkk}(\alpha_i)$$

$$\frac{\mu}{6\mu^*(K + 2\mu) + \mu(9K - 8\mu)} = \frac{\mu' - \mu}{25\mu(3K + 4\mu)} \sum_{i=1}^{N} \phi_i \left(T_{jkjk}(\alpha_i) - \frac{1}{3}(T_{jkjk}(\alpha_i)\right.$$

where T_{jjkk} and T_{jkjk} are scalar functions of K, μ, ρ, K', μ', ρ', and α_i, Ks are bulk moduli, μs are shear moduli and ρs densities. Unsuperscripted variables refer to the matrix properties; primed variables refer to the inclusion properties and starred variables to the effective aggregate properties (Toksöz et al., 1975). To solve the velocity equations at any particular pressure it turns out that only crack density rather than the complete spectrum of ϕ_i and α_i is required.

INPUT PARAMETERS

Crack densities. The SEM micrographs used in this study are reproduced in Figures 5-2 through 5-4. The actual size of the collages used was 41.6 x 58.9 cm^2 and 37.9 x 57.0 cm^2 for

the prestressed rock and 35.4 x 41.0 cm^2 for the unstressed rock. Magnification was about 400x. The prestressed sections were oriented parallel to the maximum stress direction. Crack lengths in both the prestressed and unstressed granite were measured from the photographs. A single crack was defined to be any open flaw of aspect ratio less than 1 which did not change orientation by more than 20 degrees over any significant portion of its length and which was either continuously open or bridged by material of exposed thickness no more than 3 crack widths or one tenth the total crack length, whichever was less. Crack widths in the unstressed sample were measured on the SEM using higher magnification than that at which the photographs were taken. Crack widths were taken directly from the micrographs of the prestressed rock either by measuring the gap with a scale or, for the very narrow cracks, by comparison with the appearance of cracks in the micrograph of the virgin rock. Crack widths so determined were spot checked using the SEM at 23,000x. Agreement was in all cases within a factor of 3 and usually within a factor of 2. The accuracy of the measurements is no better than this whatever the precision. Cracks may intersect the plane of the micrograph obliquely; they may not be cut at their widest point and they often vary in width considerably and irregularly along their trace.

The smallest crack width that can be resolved is about 0.03 μm owing to the thickness of the conductive coating on the SEM section (Brace et al., 1972; Sprunt and Brace, 1974).

→ Pg 144.

Figure 5-2. Scanning electron micrograph of unstressed Westerly Granite.

100 μm

Figure 5-3. Scanning electron micrograph of Westerly Granite T.5, prestressed to 3 kbar at 500 bars confining pressure.

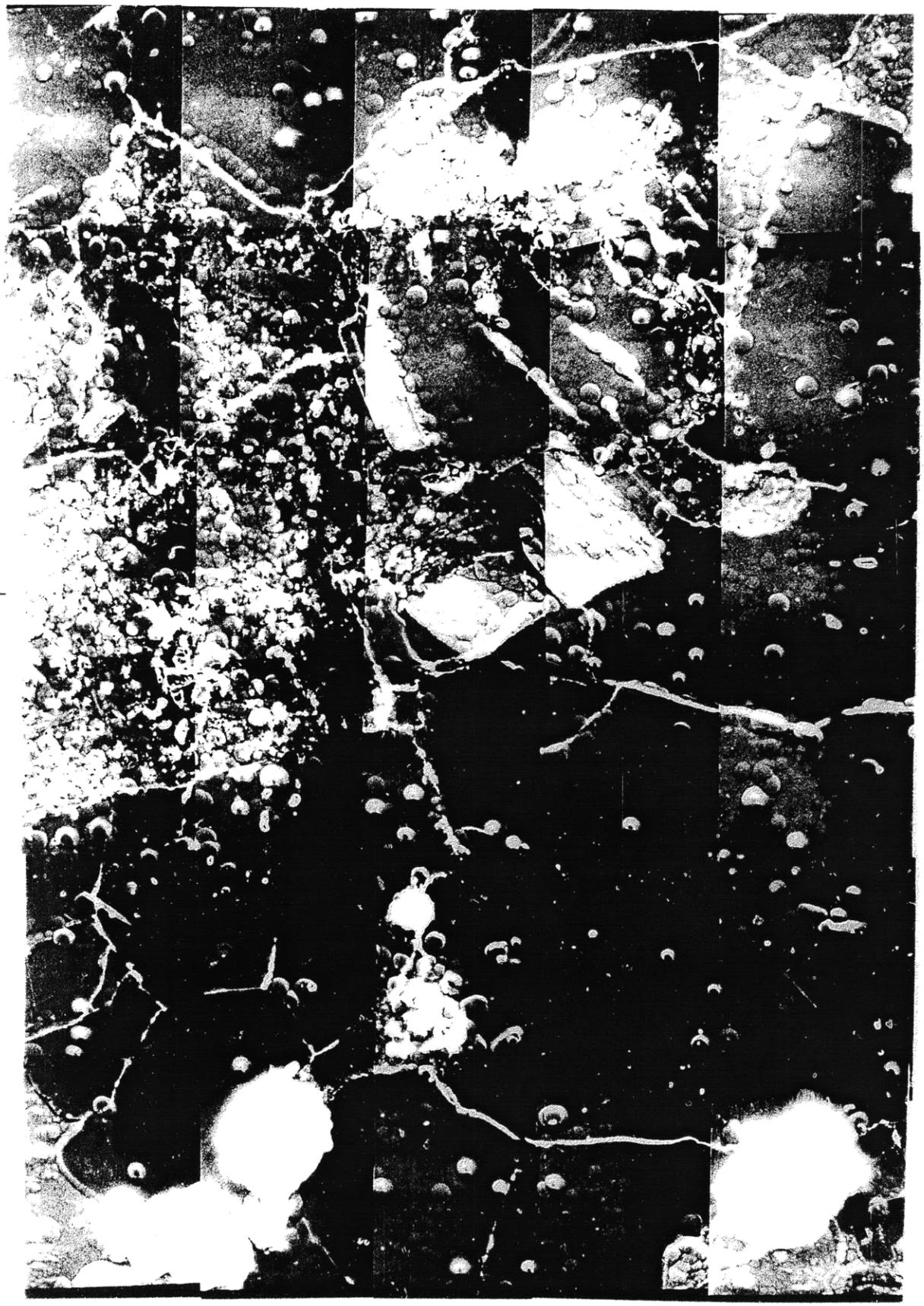

200 μm

Figure 5-4. Scanning electron micrograph of Westerly Granite W.5, previously stressed to beyond failure at 800 bars confining pressure.

100 μm

Figure 5-5a. Crack length distribution. Heavy lines, unstressed granite; shaded area, pre-stressed granite, T.5.

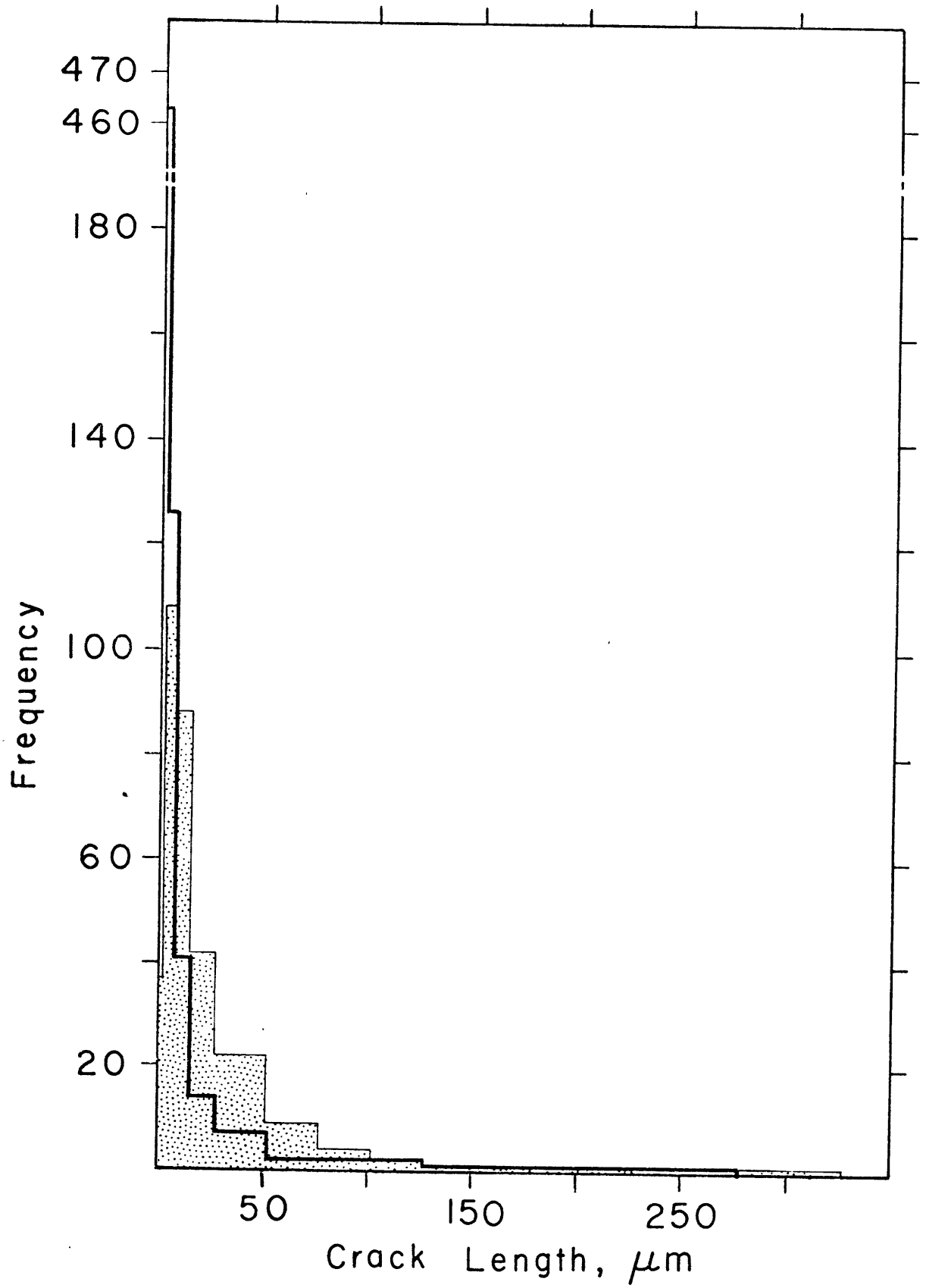
470
460
180
140
100
60
20
Frequency
50
150
250
Crack Length, μm

Figure 5-5b. Crack length distribution. Heavy lines, unstressed granite; shaded area, pre-stressed granite, W.5.

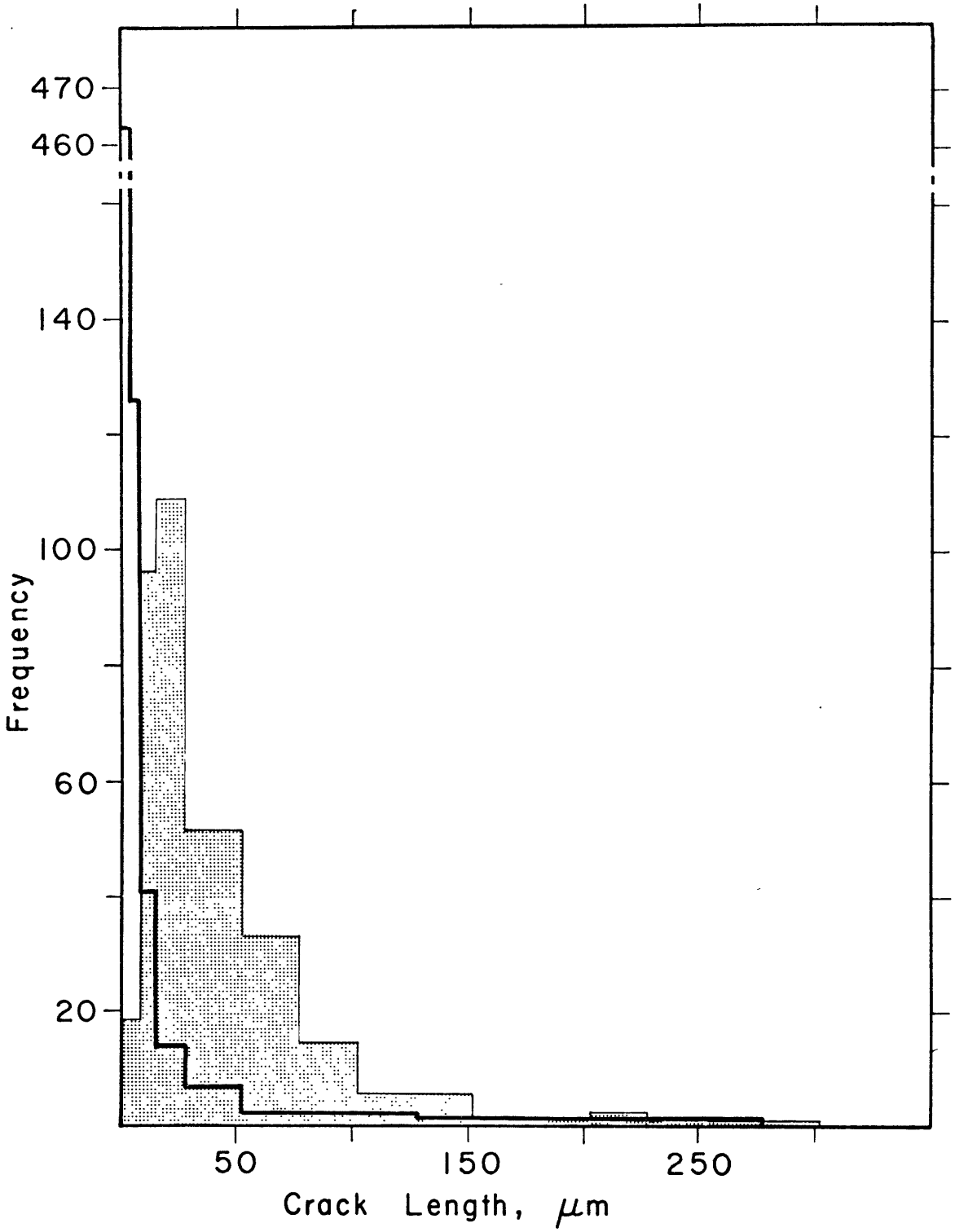
470
460
140
100
60
20
Frequency
50
150
250
Crack Length, μm

Figure 5-6a. Crack aspect ratio distribution. Heavy lines, unstressed granite; shaded area, prestressed granite, T.5.

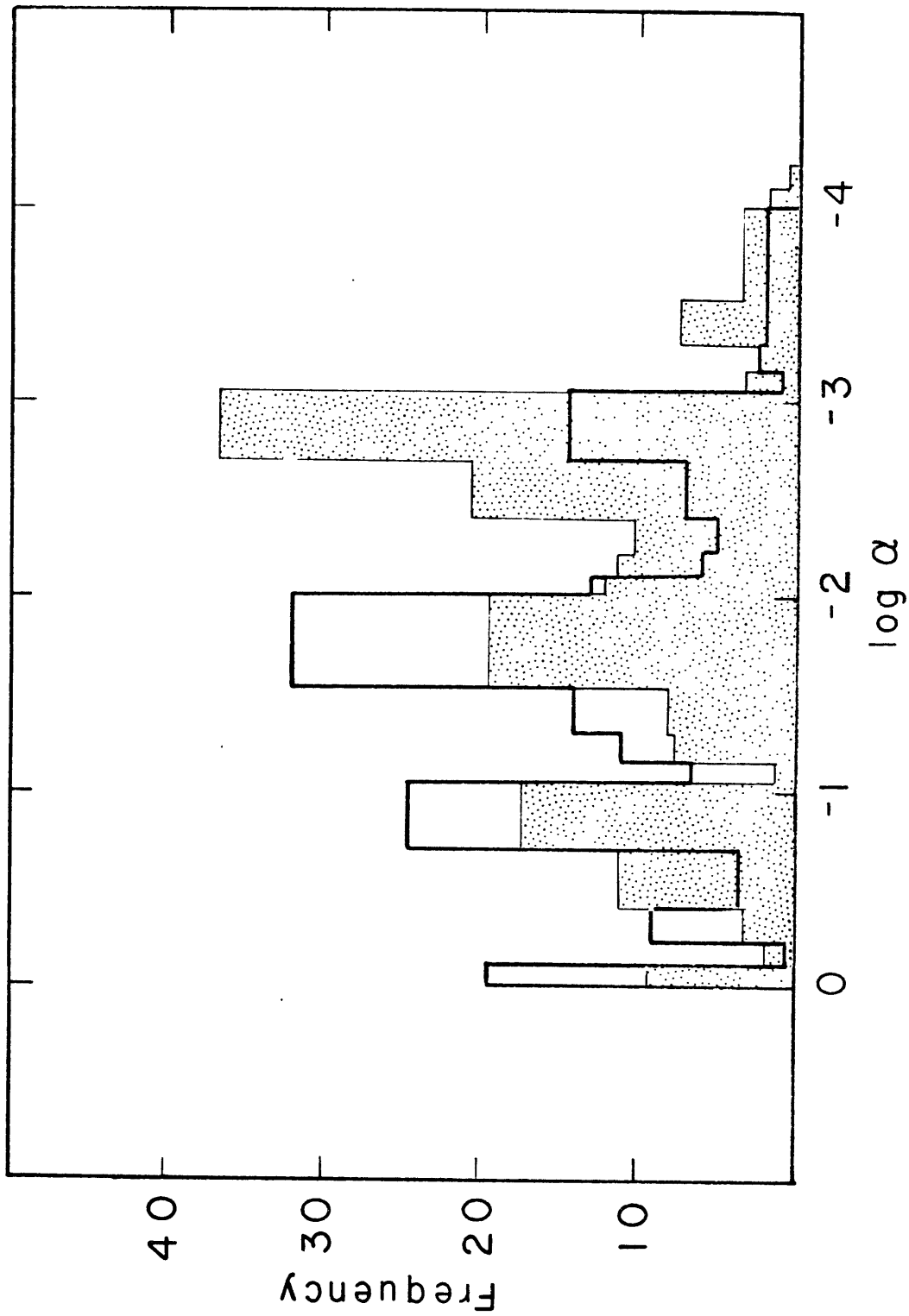
Frequency
40
30
20
10
log α
0
-1
-2
-3
-4

Figure 5-6b. Crack aspect ratio distribution. Heavy lines, unstressed granite; shaded area, prestressed granite, W.5.

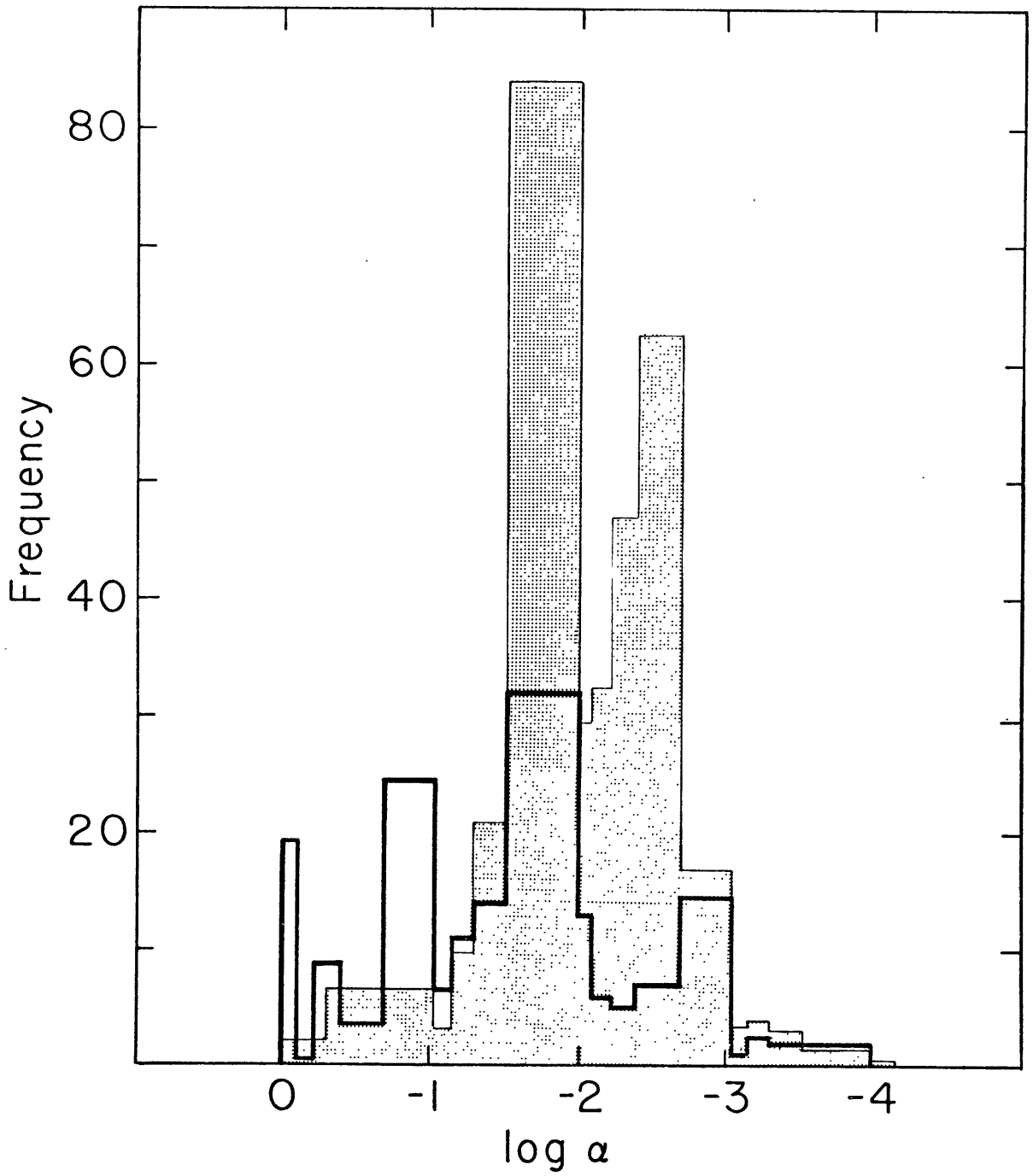
80
60
40
20
Frequency
0
-1
-2
-3
-4
log α

Figure 5-7. Crack aspect ratio vs. percent porosity. Heavy lines, area average approximation; shaded area, volume average approximation.

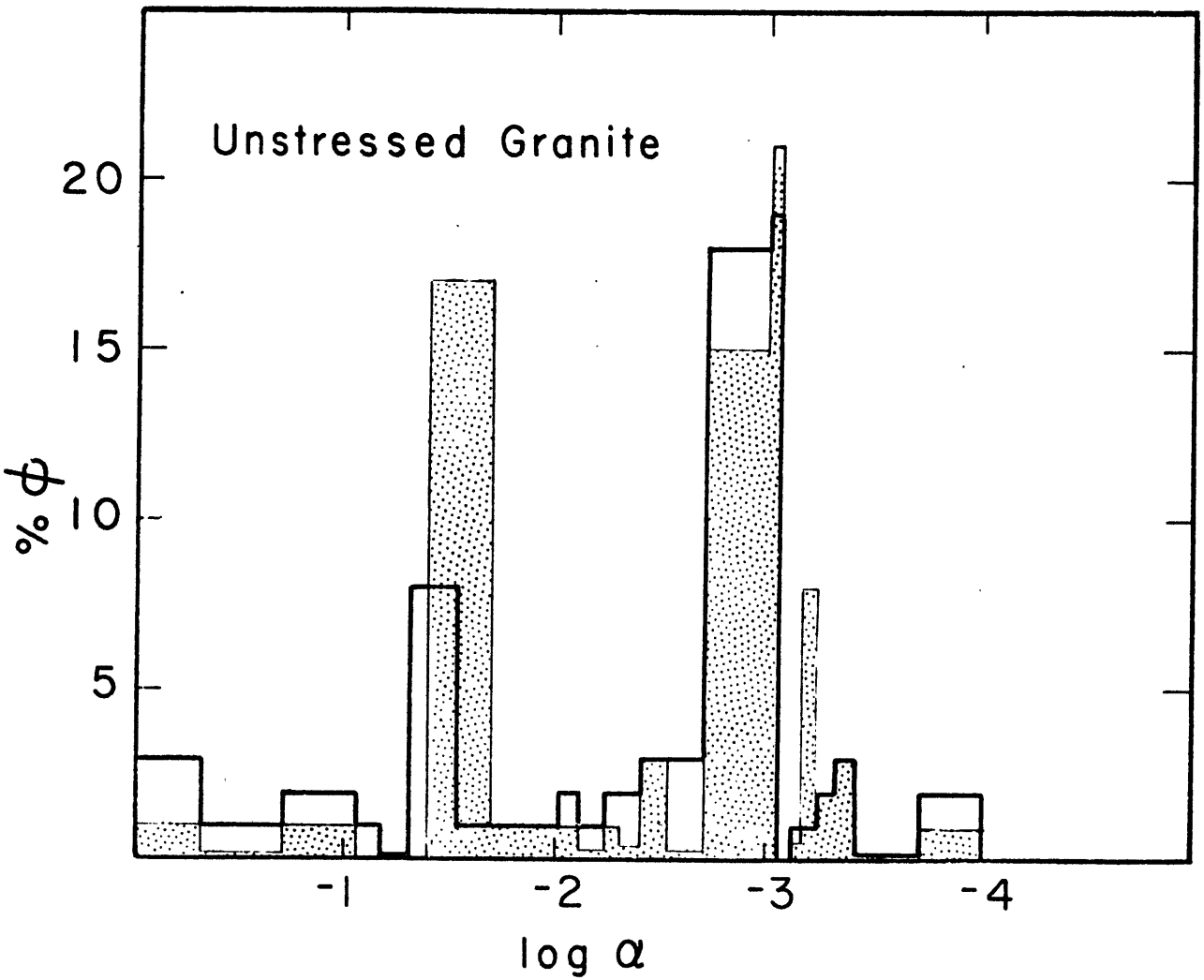
Unstressed Granite
20
15
10
5
% φ
-1
-2
-3
-4
log α

Figure 5-8a. Same as Figure 5-7 for prestressed granite, T.5.

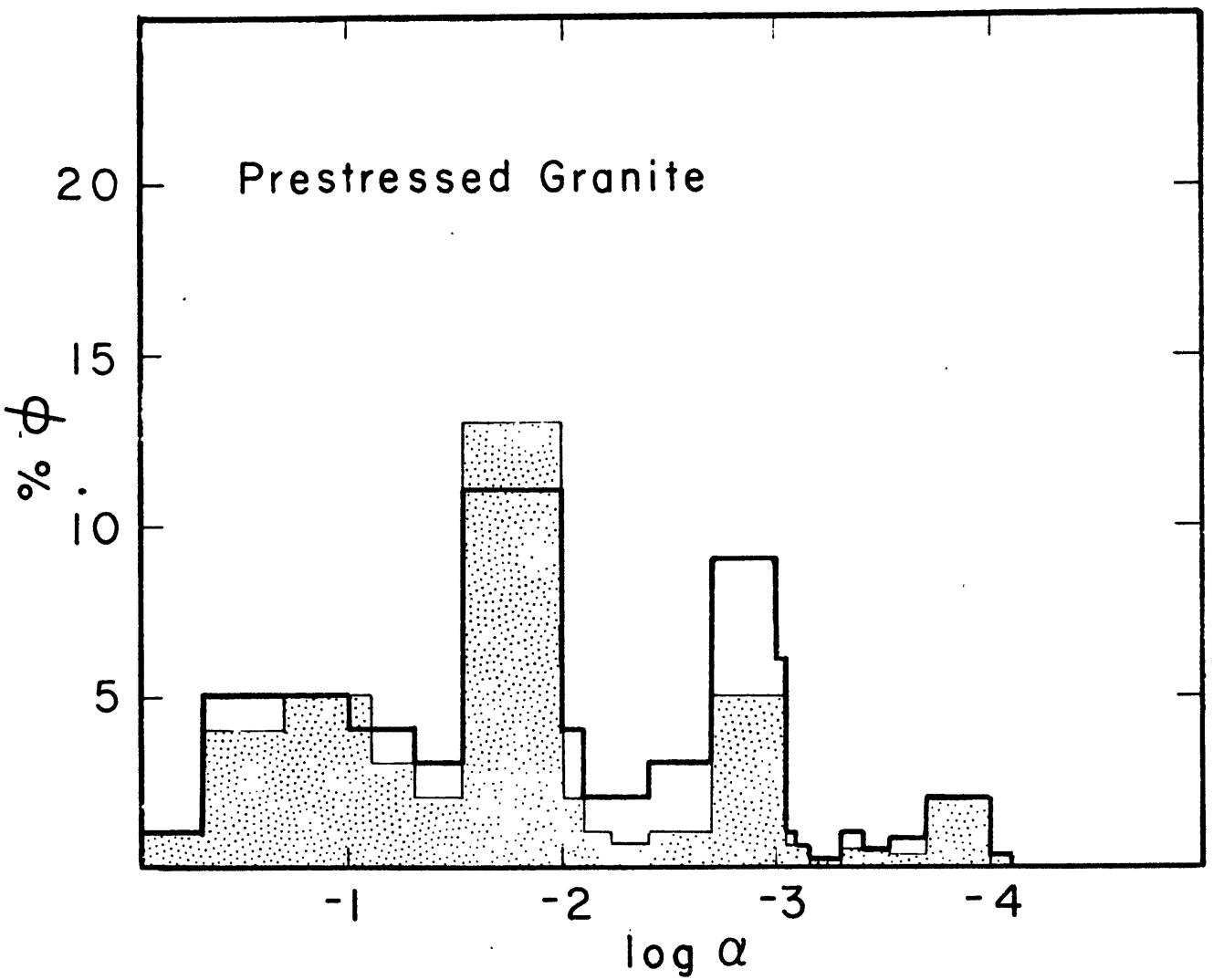
Prestressed Granite
20
15
10
5
% φ
-1
-2
-3
-4
log α

Figure 5-8b. Same as Figure 5-7 for prestressed granite, W.5.

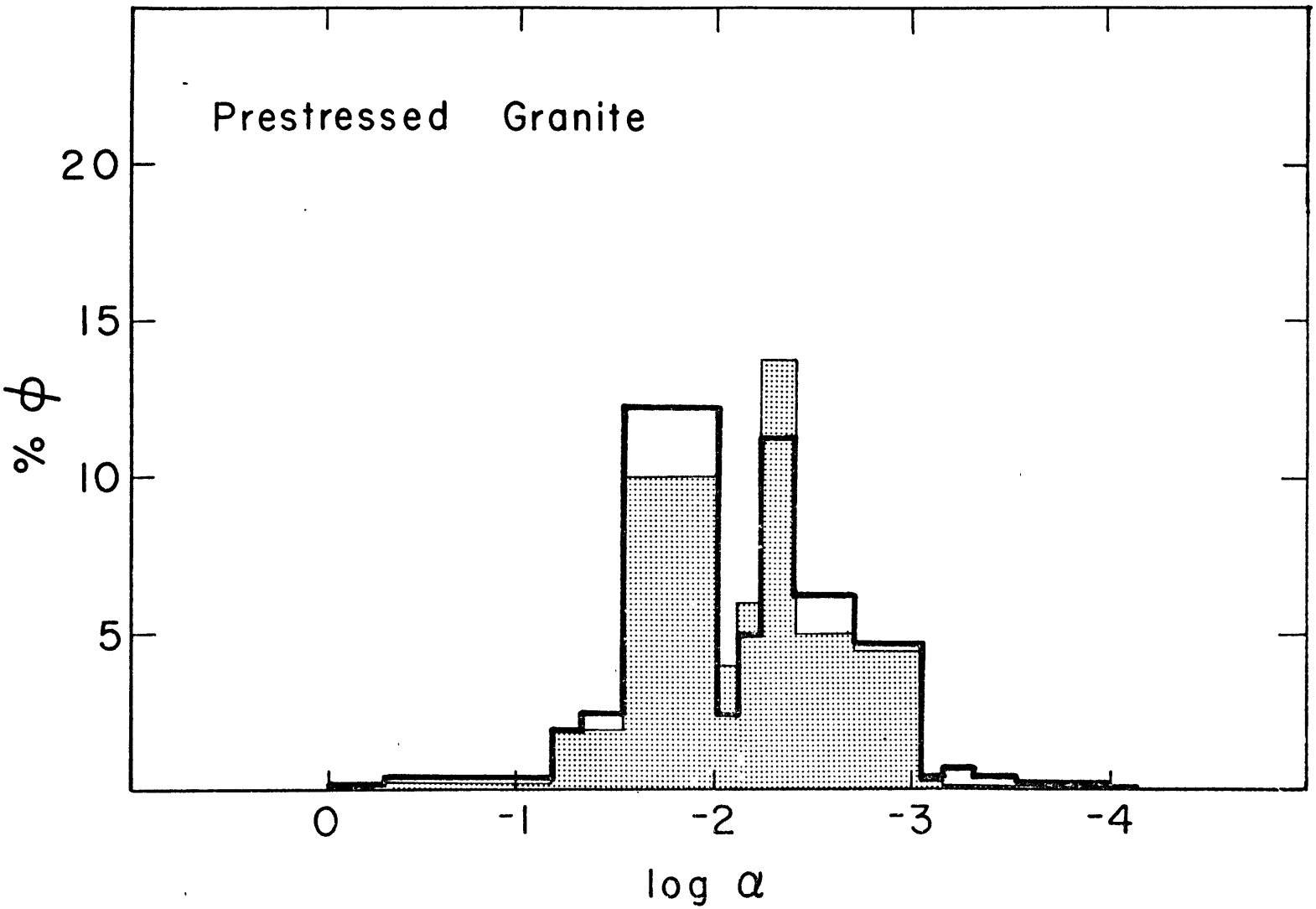
Prestressed Granite
20
15
10
5
% φ
0
-1
-2
-3
-4
log α

The longest observed crack was 565 μm in length. The smallest aspect ratio that could therefore have been seen is about 5×10^{-5}. Because the average crack length was considerably less than 565 μm (Figure 5-5, Table 5-1), many cracks with aspect ratio less than 10^{-3} may have been missed.

Measured void length and aspect ratio distributions are given in Figures 5-5 and 5-6. In Figures 5-7 and 5-8 the crack aspect ratio distribution is expressed as a percentage of the total crack porosity. For purposes of scale equant ($\alpha = 1$) intragranular pores have not been included, but their measured contribution to porosity may be found in Table 5-1. Because information on the third dimension is unavailable, two different schemes were employed to relate the measured two-dimensional values to volumetric quantities. Using an area average approximation,

$$\phi_{iA} = \frac{\pi \alpha_i}{4A} a_j a_j \qquad (3)$$

where the repeated index indicates summation and A is the area of the micrograph scanned. With the volume average approximation,

$$\phi_{iV} = \left(\frac{\pi \alpha_i}{4A} \right) a_j^{1.5} a_j^{1.5} a_j^{1.5} \qquad (4)$$

If the void distribution is isotropic, ϕ_{iA} will be equal to the true porosity as equation (4) amounts to assuming that the observed voids extend completely through the specimen in the third dimension. The volume approximation assumes ellipsoidal cavities with b, the axis in the third dimension equal to

$(\frac{1}{2})(\pi ac)^{\frac{1}{2}}$. ϕ_{iA} will always be greater than ϕ_{iV} but because $\phi_a > \phi_V$, the percentage of porosity attributable to voids of a certain aspect ratio may be either greater or less in the two approximations. For the rocks investigated, however, these differences are not large.

Because agreement between the porosities I determined using the SEM and previously measured values is poor, as is discussed below, I used not merely the directly observed ϕ_i, but also

$$\phi_i' = (\Phi / \phi)\, \phi_i \qquad (5)$$

as inputs to the theoretical formulations, where Φ is some previously determined porosity. If pores were explicitly included in the velocity calculations Φ was $.009 \pm .001$; if not, Φ was taken as $.002 \pm .0005$ (Brace et al., 1965). Normalized crack porosities for stressed rock (pores excluded) are given as a function of crack orientation and aspect ratio in Tables 5-2 and 5-3.

Crack density can be obtained directly from the void geometry. For spheroidal cavities, equation (1) is appropriate (O'Connell and Budiansky, 1974). If α_i and ϕ_i are not available, either of two statistical formulae for ϵ may be used in place of equation (1). For a rock with cracks of any identical convex shape but uniform size:

$$\epsilon = 8M \langle a \rangle^2 / \pi^3 \qquad (6)$$

while for a distribution of sizes and shapes in which size and

→ Pg 155

TABLE 5-1

DATA FOR DEFORMED AND UNDEFORMED WESTERLY GRANITE

Quantity	Prestressed Rock		Unstressed Rock
	W.5	T.5	
Confining pressure	800 bars	500 bars	-
Max. differential stress	6.8 kbar	3.0 kbar	-
$\langle a \rangle$	28.9 ± 0.002 μm	30.6 ± 0.002 μm	17.7 ± 0.002 μm
$\langle a^2 \rangle$	2949 ± 0.003 μm	4890 ± 0.002 μm	1960 ± 0.004 μm
M	$(8.8 \pm 0.9) \times 10^{-4}$ μm^{-2}	$(4.2 \pm 0.4) \times 10^{-4}$ μm^{-2}	$(3.8 \pm 0.4) \times 10^{-4}$ μm^{-2}
e (eq. (6))	0.19 ± 0.08	0.10 ± 0.05	0.03 ± 0.01
e (eq. (7))	0.62 ± 0.27	0.49 ± 0.05	0.18 ± 0.02
e (eq. (1), $\phi = \phi_A$)	0.54 ± 0.04	0.25 ± 0.04	0.16 ± 0.04
ϕ_A (cracks only)	$(0.68 \pm 0.07) \times 10^{-2}$	$(0.34 \pm 0.04) \times 10^{-2}$	$(0.13 \pm 0.02) \times 10^{-2}$
ϕ_V (cracks only)	$(0.54 \pm 0.05) \times 10^{-4}$	$(0.18 \pm 0.02) \times 10^{-4}$	$(0.86 \pm 0.09) \times 10^{-5}$
ϕ_A (intragranular pores only)	$(0.70 \pm 0.07) \times 10^{-4}$*	$(0.14 \pm 0.01) \times 10^{-2}$	assumed comparable to T.5 values because plagioclase content of section is similar, ≈ 30 percent.
ϕ_V (intragranular pores only)	$(0.93 \pm 0.09) \times 10^{-7}$*	$(0.33 \pm 0.03) \times 10^{-5}$	

*Plagioclase content of this section is less than 5 percent

TABLE 5-2a

SAMPLE T.5 POROSITY

NORMALIZED AREA AVERAGE APPROXIMATION ($x10^6$)

Aspect Ratio	Orientation ($a \wedge \sigma_{max}$) (degrees)								
	-90- <-70	-70- <-50	-50- <-30	-30- <-10	-10 - <+10	+10 - <+30	+30 - <+50	+50- <+70	+70- < +90
<1.0-0.5	94.2	16.2	122.	39.5	41.4	27.2	1.58	0.0	29.9
<0.5-0.1	128.	144.	111.	39.6	77.0	63.1	58.1	37.6	287.
$<10\text{-}7x10^{-2}$	18.5	2.95	77.0	2.95	9.31	0.0	229.	110.	39.1
$<7\text{-}5x10^{-2}$	85.7	27.3	10.4	7.59	39.0	8.09	124.	2.00	8.88
$<5\text{-}3x10^{-2}$	43.1	7.89	17.6	18.4	4.08	2.70	8.70	12.8	9.25
$<3\text{-}1x10^{-2}$	94.0	50.2	281.	26.3	93.1	13.8	291.	73.9	32.5
$<10\text{-}8x10^{-3}$	12.2	0.986	6.07	13.7	14.9	0.0	0.986	3.32	2.51
$<8\text{-}6x10^{-3}$	41.8	30.5	2.09	7.27	8.63	0.591	39.6	66.1	0.789
$<6\text{-}4x10^{-3}$	17.8	71.4	19.3	29.7	25.7	10.5	2.90	4.59	8.63
$<4\text{-}2x10^{-3}$	162.	25.0	72.6	12.7	15.8	93.6	36.4	106.	18.9
$<2\text{-}1x10^{-3}$	4.47	11.6	62.0	20.5	46.2	18.4	59.7	14.7	7.68
$<10\text{-}9x10^{-4}$	0.0	0.829	58.9	2.17	0.769	2.26	0.355	0.0	0.0
$<9\text{-}8x10^{-4}$	0.0	15.3	0.0	0.888	0.0	9.46	0.0	0.0	0.0

TABLE 5-2a (continued)

SAMPLE T.5 POROSITY

NORMALIZED AREA AVERAGE APPROXIMATION ($x10^{-6}$)

Aspect Ratio	Orientation (a Λ σ_{max}) (degrees)								
	-90- <-70	-70- <-50	-50- <-30	-30- <-10	-10- <+10	+10- <+30	+30- <+50	+50- <+70	+70- <+90
$<8\text{-}7x10^{-4}$	0.474	0.0	0.0	2.95	0.0	0.0	0.0	0.0	0.0
$<7\text{-}5x10^{-4}$	1.30	3.94	4.81	10.9	7.01	0.0	10.4	32.3	0.0
$<5\text{-}4x10^{-4}$	5.94	0.217	2.88	5.43	0.0	0.197	5.81	0.0	0.0
$<4\text{-}3x10^{-4}$	6.58	0.0	0.0	25.7	0.0	0.0	1.47	0.0	0.0
$<3\text{-}2x10^{-4}$	0.0	0.0	0.0	101.	0.0	0.0	2.37	0.0	0.0
$<2\text{-}1x10^{-4}$	0.0	0.0	0.532	0.0	0.0	0.0	1.42	0.0	0.0
$<1x10^{-4}$	0.0	0.0	0.0	0.0	0.0	0.0	3.65	0.0	0.0

TABLE 5-2b

SAMPLE T.5 POROSITY

NORMALIZED VOLUME AVERAGE APPROXIMATION ($x10^6$)

Aspect Ratio	Orientation ($a \wedge \sigma_{max}$) (degrees)								
	-90- <-70	-70- <-50	-50- <-30	-30- <-10	-10- <+10	+10- <+30	+30- <+50	+50- <+70	+70- <+90
<1.0-0.5	81.7	4.93	67.0	22.3	23.5	12.9	0.231	0.0	18.8
<0.5-0.1	74.9	69.9	55.6	11.9	41.7	42.4	37.7	10.6	134.
$<10\text{-}7x10^{-2}$	4.37	0.593	74.6	0.593	2.40	0.0	375.	87.7	28.4
$<7\text{-}5x10^{-2}$	97.3	12.7	2.93	1.32	18.4	1.90	144.	0.329	3.09
$<5\text{-}3x10^{-2}$	22.7	2.02	5.53	7.16	0.563	0.381	1.93	3.84	1.80
$<3\text{-}1x10^{-2}$	99.4	12.4	418.	8.72	21.8	3.10	243.	39.8	11.2
$<10\text{-}8x10^{-3}$	3.50	0.114	1.68	3.80	4.18	0.0	0.114	0.532	0.267
$<8\text{-}6x10^{-3}$	23.9	17.3	0.212	1.27	2.46	0.038	21.1	38.1	0.056
$<6\text{-}4x10^{-3}$	5.51	49.7	5.34	9.22	8.70	3.54	0.436	0.571	1.29
$<4\text{-}2x10^{-3}$	28.3	4.92	30.6	2.28	2.74	70.7	11.8	43.5	3.31
$<2\text{-}1x10^{-3}$	0.624	2.39	28.3	6.06	56.5	4.48	33.9	3.92	1.93
$<10\text{-}9x10^{-4}$	0.0	0.088	50.1	0.371	0.079	0.398	0.025	0.0	0.0
$<9\text{-}8x10^{-4}$	0.0	5.17	0.0	0.097	0.0	3.40	0.0	0.0	0.0

TABLE 5-2b (continued)

SAMPLE T.5 POROSITY

NORMALIZED VOLUME AVERAGE APPROXIMATION ($x10^6$)

Aspect Ratio	Orientation ($a \wedge \sigma_{max}$) (degrees)								
	-90- < -70	-70- < -50	-50- < -30	-30- < -10	-10- < +10	+10- < +30	+30- < +50	+50- < +70	+70- < +90
$<8\text{-}7x10^{-4}$	0.038	0.0	0.0	0.593	0.0	0.0	0.0	0.0	0.0
$<7\text{-}5x10^{-4}$	0.173	0.913	1.07	2.87	1.25	0.0	2.89	12.5	1.13
$<5\text{-}4x10^{-4}$	1.52	0.012	0.428	1.47	0.0	0.010	1.56	0.0	0.0
$<4\text{-}3x10^{-4}$	1.96	0.0	0.0	13.6	0.0	0.0	0.137	0.0	0.0
$<3\text{-}2x10^{-4}$	0.0	0.0	0.0	11.8	0.0	0.0	0.280	0.0	0.0
$<2\text{-}1x10^{-4}$	0.0	0.0	0.045	0.0	0.0	0.0	0.140	0.0	0.0
$<1x10^{-4}$	0.0	0.0	0.0	0.0	0.0	0.0	0.089	0.0	0.0

TABLE 5-3a

SAMPLE W.5 POROSITY

NORMALIZED AREA AVERAGE APPROXIMATION ($x10^6$)

Orientation ($a \wedge \sigma_{max}$) (degrees)

Aspect Ratio	-90- <-70	-70- <-50	-50- <-30	-30- <-10	-10- <+10	+10- <+30	+30- <+50	+50- <+70	+70- <+90
<1.0-0.5	6.18	9.85	0.0	0.0	4.14	4.03	16.2	6.60	1.57
<0.5-0.1	0.0	54.3	12.6	12.0	47.0	77.3	6.26	3.82	10.4
$<10\text{-}7x10^{-2}$	3.08	8.88	0.062	0.0	22.5	0.0	0.0	12.7	19.1
$<7\text{-}5x10^{-2}$	0.415	26.6	19.2	134.	15.8	23.9	195.	10.1	15.4
$<5\text{-}3x10^{-2}$	7.69	40.9	72.6	16.6	45.4	208.	137.	9.83	63.8
$<3\text{-}1x10^{-2}$	123.	168.	425.	405.	699.	236.	284.	187.	41.7
$<10\text{-}8x10^{-3}$	11.3	12.0	181.	93.7	331.	103.	100.	31.5	4.62
$<8\text{-}6x10^{-3}$	50.5	32.2	551.	72.1	144.	127.	56.9	13.7	6.91
$<6\text{-}4x10^{-3}$	15.8	19.0	741.	116.	1040.	175.	21.6	149.	98.6
$<4\text{-}2x10^{-3}$	31.7	38.7	53.5	83.1	474.	78.4	34.0	213.	271.
$<2\text{-}1x10^{-3}$	9.18	24.0	7.85	8.09	109.	28.8	561.	10.5	0.0
$<10\text{-}9x10^{-4}$	4.89	0.0	8.46	0.0	31.4	0.0	0.0	231.	0.0
$<9\text{-}8x10^{-4}$	3.28	0.0	0.0	0.0	6.66	0.0	8.11	10.2	0.0

TABLE 5-3a (continued)

SAMPLE W.5 POROSITY

NORMALIZED AREA AVERAGE APPROXIMATION ($x10^6$)

Orientation ($a \wedge \sigma_{max}$) (degrees)

Aspect Ratio	-90- <-70	-70- <-50	-50- <-30	-30- <-10	-10- <+10	+10- <+30	+30- <+50	+50- <+70	+70- < +90
$<8\text{-}7x10^{-4}$	0.0	1.72	0.0	31.2	0.0	6.45	0.0	0.0	0.0
$<7\text{-}5x10^{-4}$	0.0	11.7	0.0	0.0	61.6	0.0	2.48	2.32	0.0
$<5\text{-}4x10^{-4}$	0.0	3.06	1.39	0.0	23.1	0.0	0.0	0.0	0.0
$<4\text{-}3x10^{-4}$	0.0	36.2	0.0	0.0	18.8	1.44	0.0	0.0	0.0
$<3\text{-}2x10^{-4}$	0.0	0.0	0.0	1.98	9.58	5.86	0.0	0.0	0.0
$<2\text{-}1x10^{-4}$	0.0	0.0	0.0	0.0	20.0	0.0	0.0	0.0	0.0
$<1x10^{-4}$	0.0	3.40	0.0	0.0	0.0	11.3	0.0	0.0	0.0

TABLE 5-3b

SAMPLE W.5 POROSITY

NORMALIZED VOLUME AVERAGE APPROXIMATION ($x10^{-6}$)

Orientation (a Λ σ_{max}) (degrees)

Aspect Ratio	-90- <-70	-70- <-50	-50- <-30	-30- <-10	-10- <+10	+10- <+30	+30- <+50	+50- <+70	+70- <+90
<1.0-0.5	1.38	2.72	0.0	0.0	0.726	0.942	4.12	1.41	0.229
<0.5-0.1	0.0	34.4	3.58	2.55	23.9	61.2	1.29	0.711	3.89
<10-7x10^{-2}	0.602	2.52	1.80	0.0	8.28	0.0	0.0	4.58	9.67
<7-5x10^{-2}	0.031	14.6	5.75	173.	3.81	10.5	272.	3.71	6.43
<5-3x10^{-2}	1.48	14.5	34.0	483.	19.5	204.	164.	2.46	26.9
<3-1x10^{-2}	196.	74.1	564.	323.	730.	170.	182.	153.	14.1
<10-8x10^{-3}	2.61	3.47	183.	48.5	596.	66.4	74.5	18.2	0.749
<8-6x10^{-3}	27.3	10.9	1370.	49.3	102.	81.6	34.9	3.46	1.23
<6-4x10^{-3}	3.10	3.63	1550.	73.7	1270.	220.	5.84	107.	59.7
<4-2x10^{-3}	8.24	8.71	17.7	70.3	401.	23.3	8.28	231.	439.
<2-1x10^{-3}	1.99	5.27	1.81	2.69	58.4	7.90	485.	2.30	0.0
<10-9x10^{-4}	1.26	0.0	2.05	0.0	13.4	0.0	0.0	520.	0.0
<9-8x10^{-4}	0.564	0.0	0.0	0.0	1.44	0.0	26.9	3.80	0.0

TABLE 5-3b (continued)

SAMPLE W.5 POROSITY

NORMALIZED VOLUME AVERAGE APPROXIMATION ($x10^6$)

Aspect Ratio	Orientation ($a \wedge \sigma_{max}$) (degrees)								
	-90- < -70	-70- < -50	-50- < -30	-30- < -10	-10- < +10	+10- < +30	+30- < +50	+50- < +70	+70- < +90
$<8\text{-}7x10^{-4}$	0.0	0.264	0.0	20.3	0.0	1.90	0.0	0.0	0.0
$<7\text{-}5x10^{-4}$	0.0	3.69	0.0	0.0	28.0	0.0	0.444	0.400	0.0
$<5\text{-}4x10^{-4}$	0.0	0.627	0.190	0.0	13.0	0.0	0.0	0.0	0.0
$<4\text{-}3x10^{-4}$	0.0	20.7	0.0	0.0	8.43	0.201	0.0	0.0	0.0
$<3\text{-}2x10^{-4}$	0.0	0.0	0.0	0.333	3.47	1.65	0.0	0.0	0.0
$<2\text{-}1x10^{-4}$	0.0	0.0	0.0	0.0	10.4	0.0	0.0	0.0	0.0
$<1x10^{-4}$	0.0	0.729	0.0	0.0	0.0	4.44	0.0	0.0	0.0

shape are uncorrelated and b/a < 0.1,

$$\epsilon = 3M\langle a^2\rangle/(4\pi) \qquad (7)$$

where $\langle a\rangle$ is the average crack length, $\langle a^2\rangle$ the average of the square of the crack length and M the number of crack traces per unit area. For the stressed and unstressed granites considered here, equations (6) and (7) yield quite different results at 1 bar pressure. Comparison with results from equation (1) (Table 5-1) suggests that equation (7) is more nearly correct. Since this is the more general of the two statistical expressions one might have expected it to be more accurate a priori.

Moduli of the matrix and fluid phases. The bulk modulus, K, and density of air used in this study are given in Table 5-4 at various pressures. For the purposes of calculation, pore pressure was assumed to be $\frac{1}{4}$ of the confining pressure in hydrostatic examples with vapor-filled cracks. This is an overestimate; although the mass of air in the pore space was kept constant during the experiments of Nur and Simmons (1969b) from which the velocity data have been taken, the framework is far less compressible than the gas filling the pores. However, resulting velocities are not very sensitive to changes in K_{air} given the small crack densities and the large contrast in moduli between rock and air over the range of values of K_{air} taken. When prestressed ϕ_i and α_i were used K_{air} was set equal to $K_{air}\big|_{1\ bar}$ at all pressures because the pore system was vented to the atmosphere when velocities were

TABLE 5-4+

PROPERTIES OF AIR

Pressure (bar)	Bulk Modulus (bar)	Density (gm/cm^3)
0	1.50	0.0011
50	325	0.07
100	500	0.12
150	610	0.17
200	663	0.22
250	700	0.27
300	725	0.31
350	750	0.34
400	778	0.37
450	880	0.40
500	950	0.43

+ Values calculated from Baehr and Schwier (1961).

measured. In saturated examples, liquid moduli were computed from Kennedy and Holser's (1966) pressure-volume-temperature data.

Matrix density of the granite is 2.62 gm/cm^2 (Birch, 1966). Shear and bulk moduli are 0.33 ± 0.01 and 0.56 ± 0.01 mbar respectively (Birch, 1960, 1966; Simmons, 1964).

Seismic velocities. Hydrostatic seismic velocities came from Nur and Simmons (1969b). Seismic velocities in stressed Westerly Granite were taken from Hadley (1975) with a 10 percent correction added to the reported shear wave velocities as suggested in the text. This correction was necessary as ϵ is not linearly dependent upon seismic velocities and therefore relative changes in velocity cannot be used to determine changes in ϵ; absolute values of velocities must be used.

HYDROSTATIC RESULTS

A comparison of measured velocities with those calculated after Toksöz et al., is presented in Figure 5-9 for wet and dry granite. Area average and volume average approximations to ϕ_i were used to calculate the velocities. In Figure 5-10, the observed ϕ_i have been replaced in the velocity computation by ϕ_i, as given by equation (5). Values calculated after O'Connell and Budiansky using the $\epsilon(p)$ given by Toksöz et al., with the area average approximation are compared in Figures 5-11 and 5-12 with the measured velocities and those calculated after Kuster and Toksöz. At low pressures, O'Connell and Budiansky's method results in consistently lower values of seismic velocities than the non-interactive analysis. Jumps in the computed

→ 162

Figure 5-9. Seismic velocity vs. pressure. Solid symbols, equant intragranular pores included in the porosity and 10 kbar values assigned to matrix moduli; open symbols, intragranular porosity excluded and 4 kbar values assigned to matrix moduli. Triangles, volume average approximation; circles, area average. Error in velocities is ± 0.05 km/sec. Solid curves, experimental observations of Nur and Simmons (1969). Error $\pm$ 2 percent.

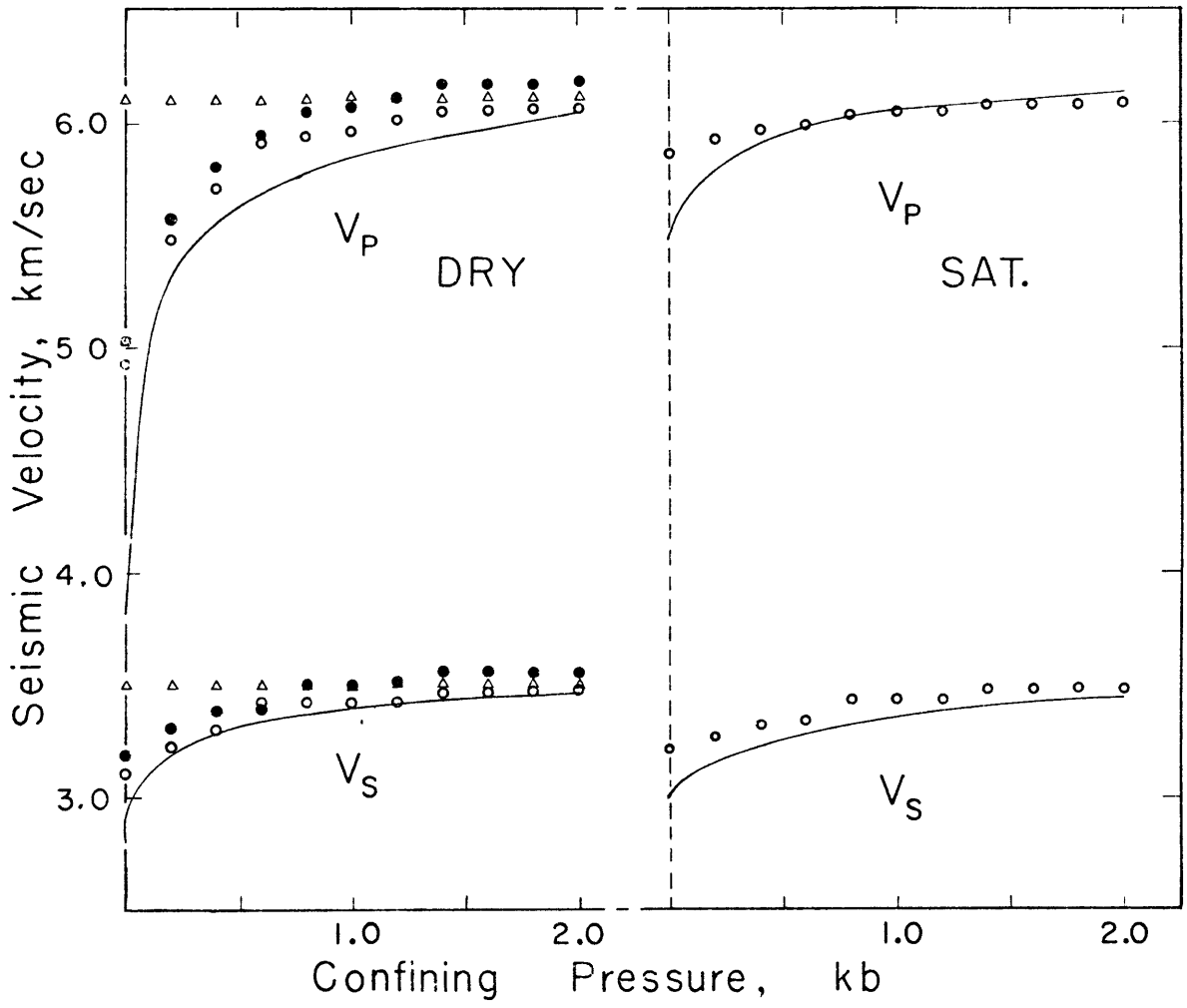
Seismic Velocity, km/sec
6.0
5.0
4.0
3.0
V_P
DRY
V_S
V_P
SAT.
V_S
1.0
2.0
1.0
2.0
Confining Pressure, kb

Figure 5-10. Same as Figure 5-9 except that observed porosity has been replaced by normalized porosity to compute seismic velocities. Solid symbols, normalized with respect to previously reported total porosity; open symbols, normalized with respect to previously reported crack porosity only.

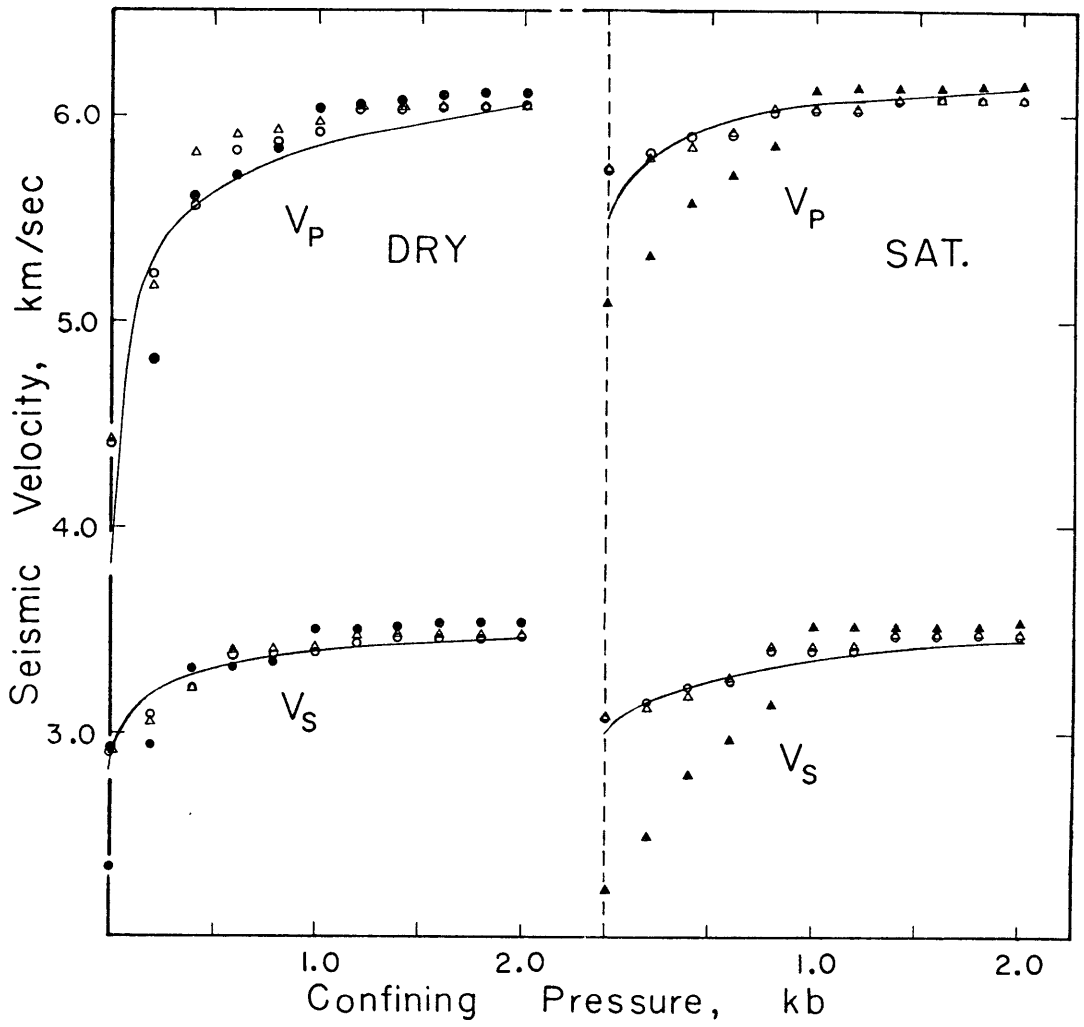
6.0
5.0
4.0
3.0
Seismic Velocity, km/sec
V_P DRY
V_S
V_P SAT.
V_S
1.0
2.0
1.0
2.0
Confining Pressure, kb

Figure 5-11. Same as Figure 5-9 except that x's correspond to seismic velocities computed after O'Connell and Budiansky (1974), using e(p) calculated from the elastic crack closure analysis of Toksöz et al., (1975).

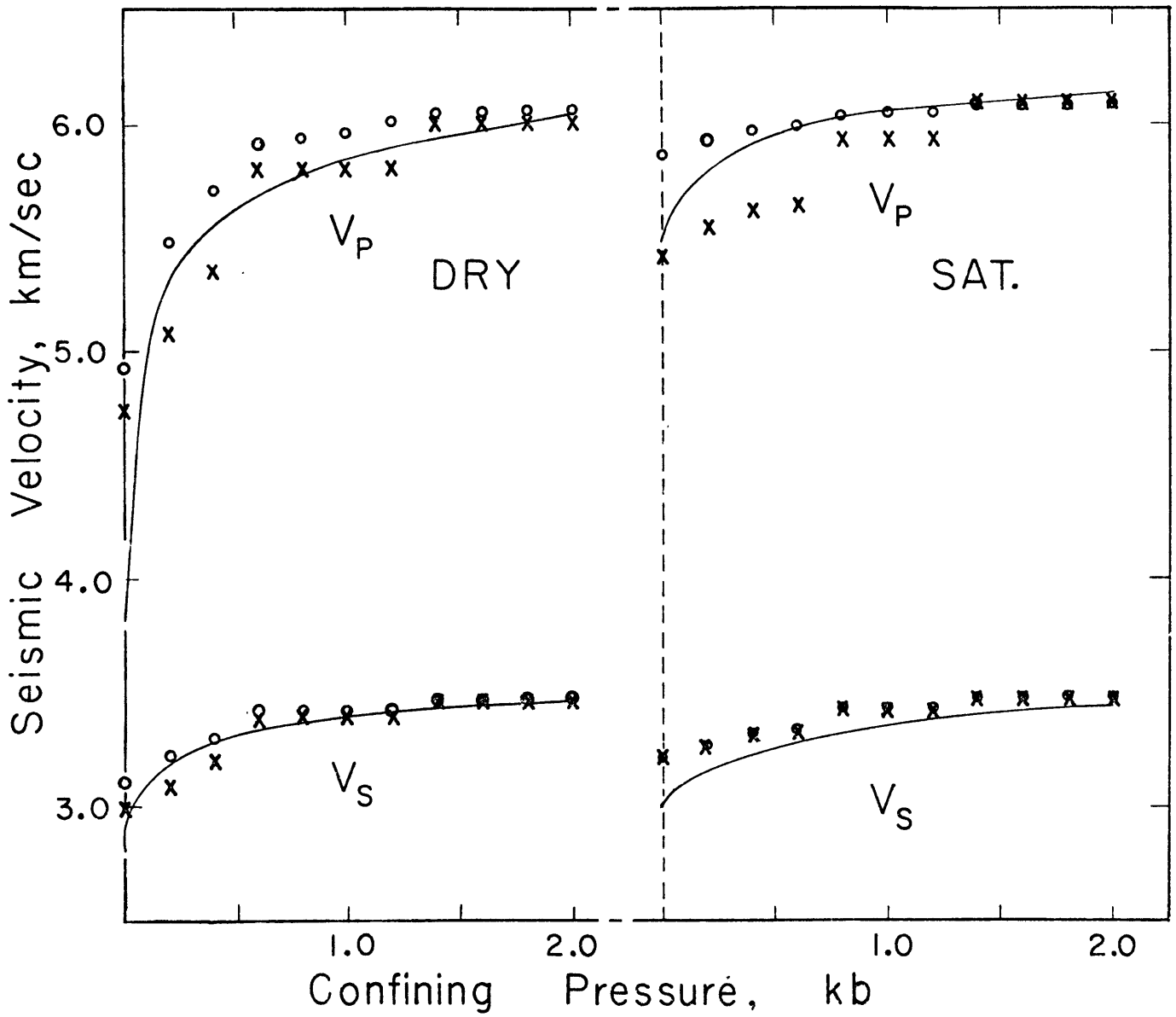
Seismic Velocity, km/sec
6.0
5.0
4.0
3.0
V_P
DRY
V_S
V_P
SAT.
V_S
1.0
2.0
1.0
2.0
Confining Pressure, kb

Figure 5-12. Same as Figure 5-11 except that observed porosity has been replaced by normalized porosity to compute seismic velocities.

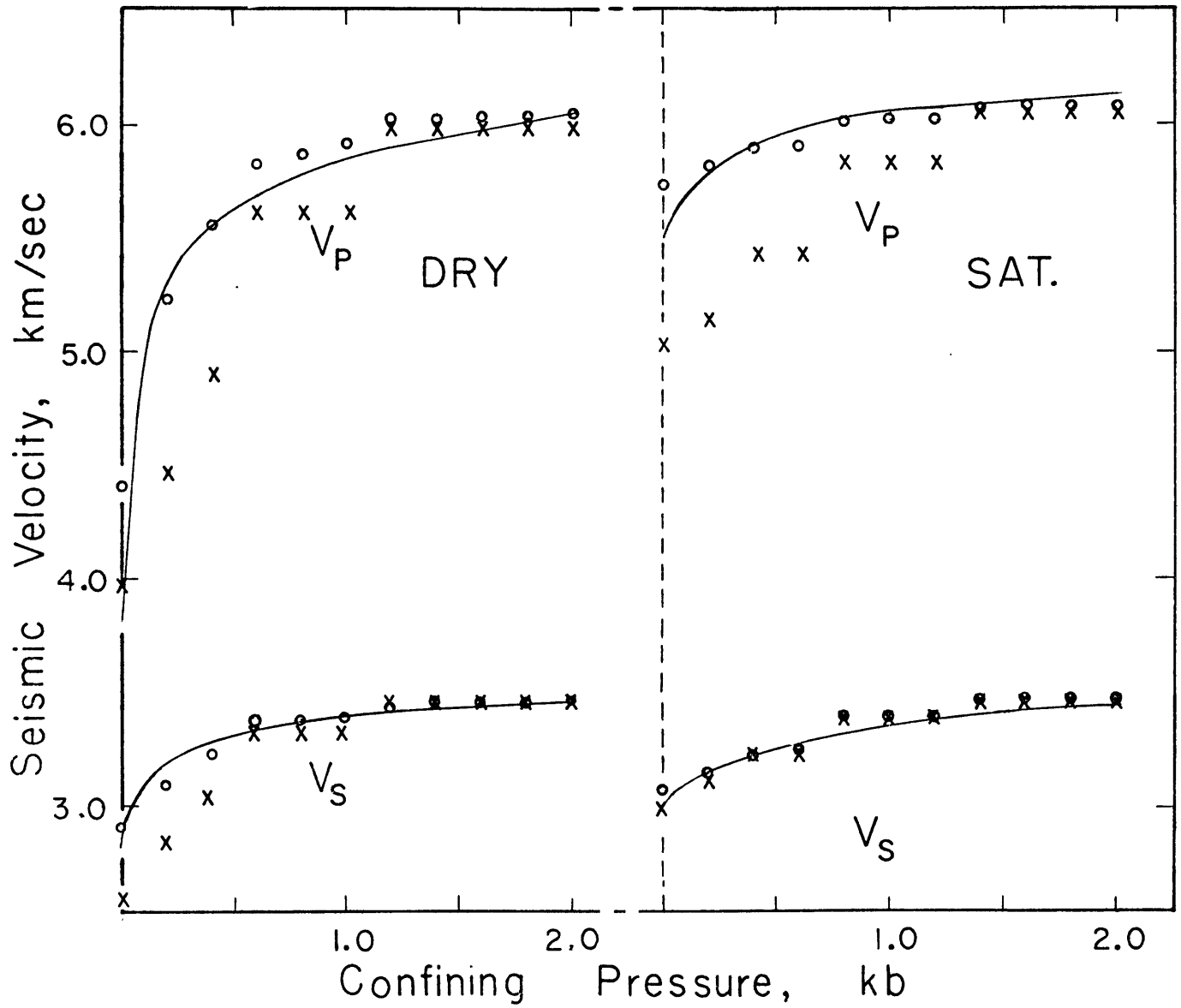
6.0
5.0
4.0
3.0
Seismic Velocity, km/sec
V_P
DRY
V_S
V_P
SAT.
V_S
1.0
2.0
1.0
2.0
Confining Pressure, kb

velocity values are artifacts of the discrete nature of the aspect ratio distribution used. If smaller divisions in aspect ratio had been taken a smoother curve would have resulted.

Crack densities as a function of pressure are shown in Figure 5-13. The zero pressure values of ϵ in the elastic crack closure scheme of Toksöz et al., have been constrained to equal those calculated from the SEM micrograph data when total crack porosity is normalized with respect to previously reported values. At higher pressures, they have been derived from the computer aspect ratio distribution using equation (1). With the single exception of the zero pressure dry crack density calculated using the formula of O'Connell and Budiansky, the agreement between the two theories and between theory and the single measured value of ϵ is very good.

NON-HYDROSTATIC RESULTS

Attempts to predict seismic velocity variation with stress using hydrostatic formulae met with no success because it is difficult to know how to relate pressure and stress. However, porosity computed from Toksöz et al., can be equated with dilatant volumetric strain and if the isotropic, hydrostatic theory is adequate, seismic velocities calculated at a given porosity should match the observed values at a corresponding dilatant volumetric strain. They do not (Figure 5-14). To determine something about the cause of the disagreement, plots of V_p and V_s vs ϵ calculated from velocity data using equation (2) have been compared with curves of V_p and V_s vs. ϵ computed

Figure 5-13. Crack density vs. pressure. Circles, O'Connell and Budiansky's method; shaded area and region bounded by heavy lines, Toksöz et al.'s. Range of values in latter method arises from choice of volume or area average approximations to normalized porosity.

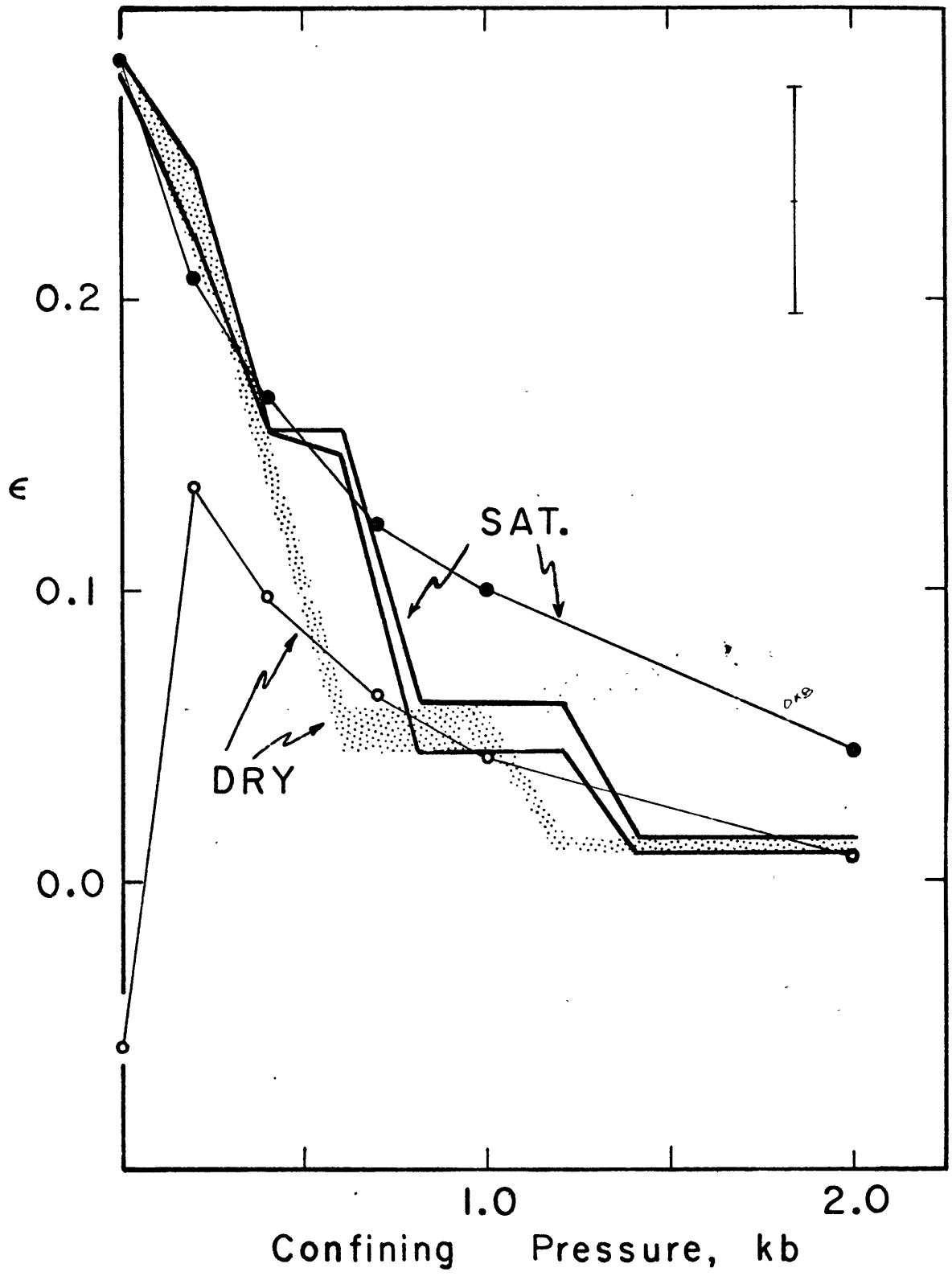
0.2
0.1
0.0
ϵ
SAT.
DRY
1.0
2.0
Confining Pressure, kb

Figure 5-14. Seismic velocity vs. porosity. Curves A-C calculated from Toksöz et al., using observed area average, normalized volumetric average and normalized area average approximations to porosity respectively. These are for dry rock. For saturated rock, only a single curve, W, is shown as whatever scheme is used to estimate porosity, calculated values are nearly identical. Errors for solid curves (T.5) and dashed curves (W.5) are $\pm$ 0.09 km/sec. Open circles, observed velocities in dry stressed granite; filled circles, observed velocities in stressed granite with pore water pressure.

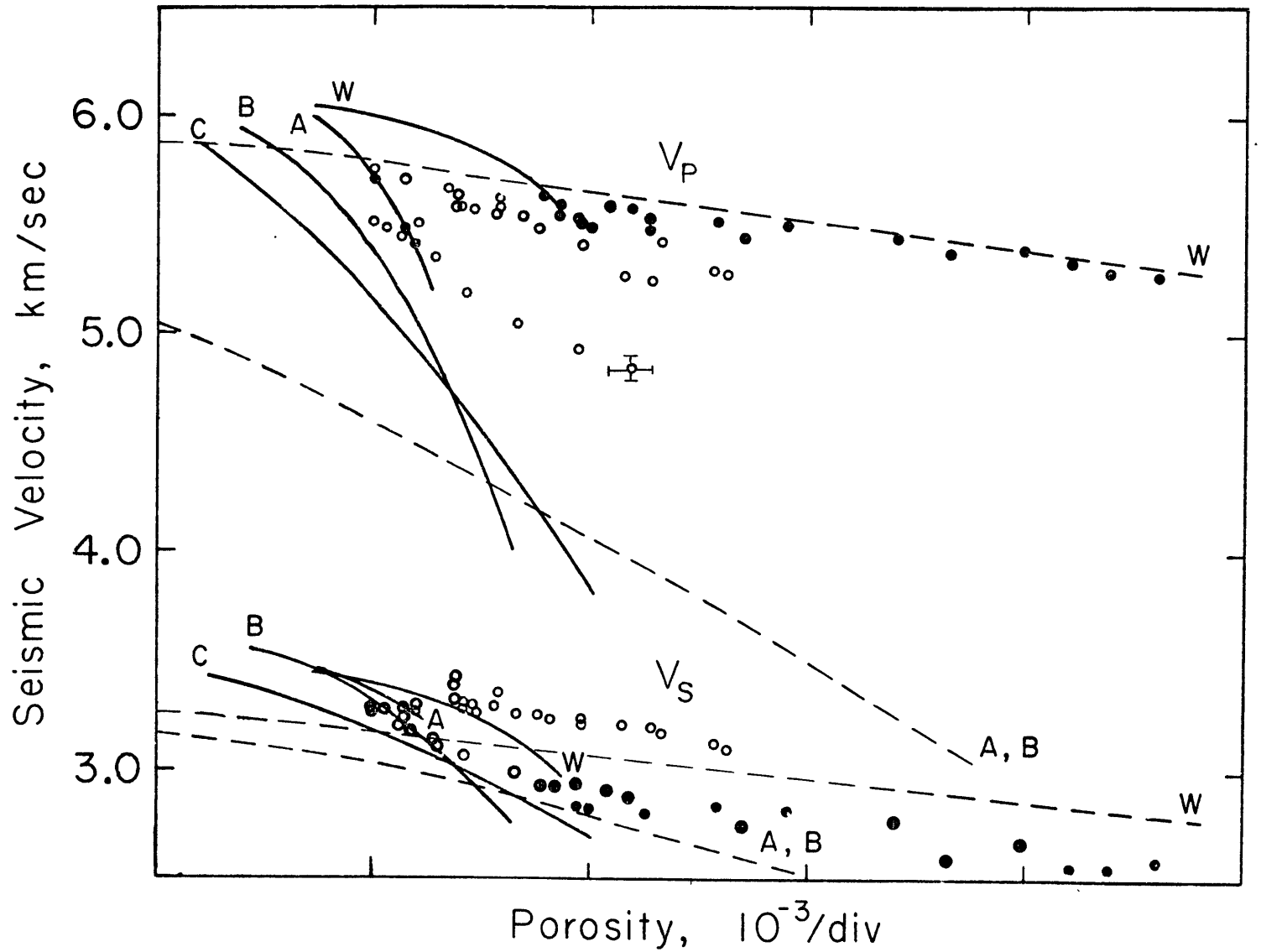
Seismic Velocity, km/sec
6.0
5.0
4.0
3.0
Porosity, 10^{-3}/div
V_P
V_S
W
B
A
C
A, B

after Toksöz et al., using the normalized SEM micrograph aspect ratio distribution for prestressed rock (Figure 5-15). The non-self-consistent formulation uniquely relates seismic velocities and crack density for a given degree of saturation while the self-consistent method gives results dependent upon the orientation of measured seismic velocity paths. Because crack density is a bulk property it should not depend upon the observational path. But a directional dependence is implicit in the aspect ratio and this produces difficulties when cracks are preferentially oriented. In a rock under stress sufficient to cause the compressional wave velocity to decrease, the crack density must be increasing. Yet it appears not to if the shear wave velocity used in the calculation is polarized parallel to the direction of maximum compression (Figure 5-15,x's). However, if the shear wave velocity is measured with a wave polarized perpendicular to the maximum stress direction (circles, Figure 5-15) the self-consistent plots of velocity vs. ϵ agree well with the non-interactive results. The agreement between the two methods is actually much worse in the hydrostatic case (Figure 5-16). Since the self-consistent method predicts the lower values of velocity at a given crack density in the hydrostatic case, and the higher values in the stressed case, the actual saturation of the experimental materials is probably influencing the results. It will be recalled that in the hydrostatic case, the properties of air were changed with pressure in the model of Toksöz et al., while no such change was incorporated into O'Connell and Budiansky's method as

Figure 5-15. Seismic velocity in stressed Westerly Granite as a function of crack density. Filled symbols, saturated rock; open circles and x's, dry rock. Squares calculated using the method of Toksöz et al., with 1 bar pressure prestressed granite crack aspect ratio distributions. Circles observed seismic velocities of Hadley (1975) and crack densities calculated from those velocities using equation (2). x's, same as circles but shear wave polarization parallel to the maximum stress direction. Shear wave polarization for circles is perpendicular to the maximum stress direction.

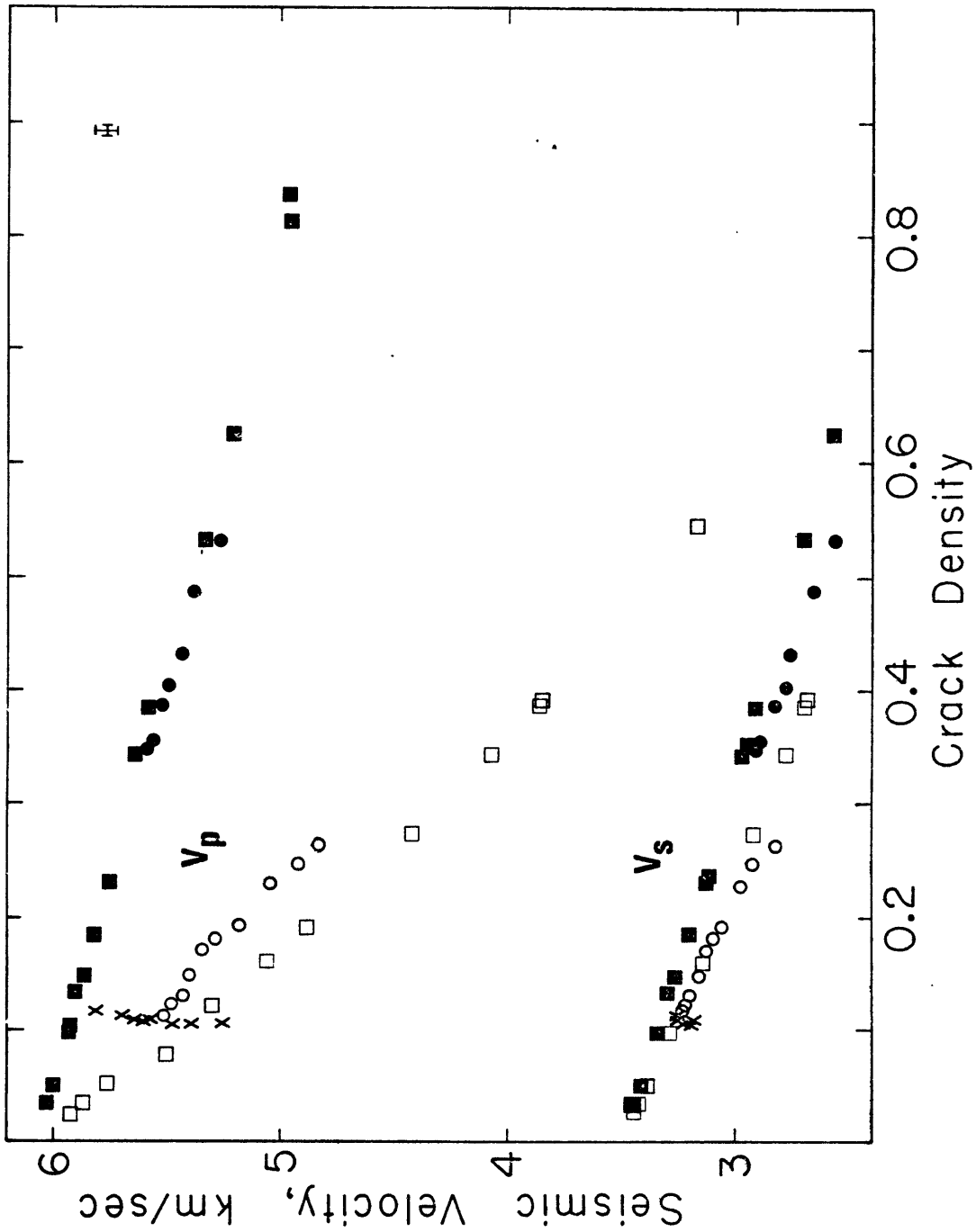
Seismic Velocity, km/sec
6
5
4
3
0.2
0.4
0.6
0.8
Crack Density
V_p
V_s

Figure 5-16. Seismic velocity in hydrostatically loaded Westerly Granite as a function of crack density. Filled symbols, saturated rock; open circles, dry rock. Squares calculated using the method of Toksöz et al., with 1 bar unstressed granite aspect ratio distributions. Circles, observed seismic velocities of Nur and Simmons (1969b) and crack densities calculated from those velocities using equation (2).

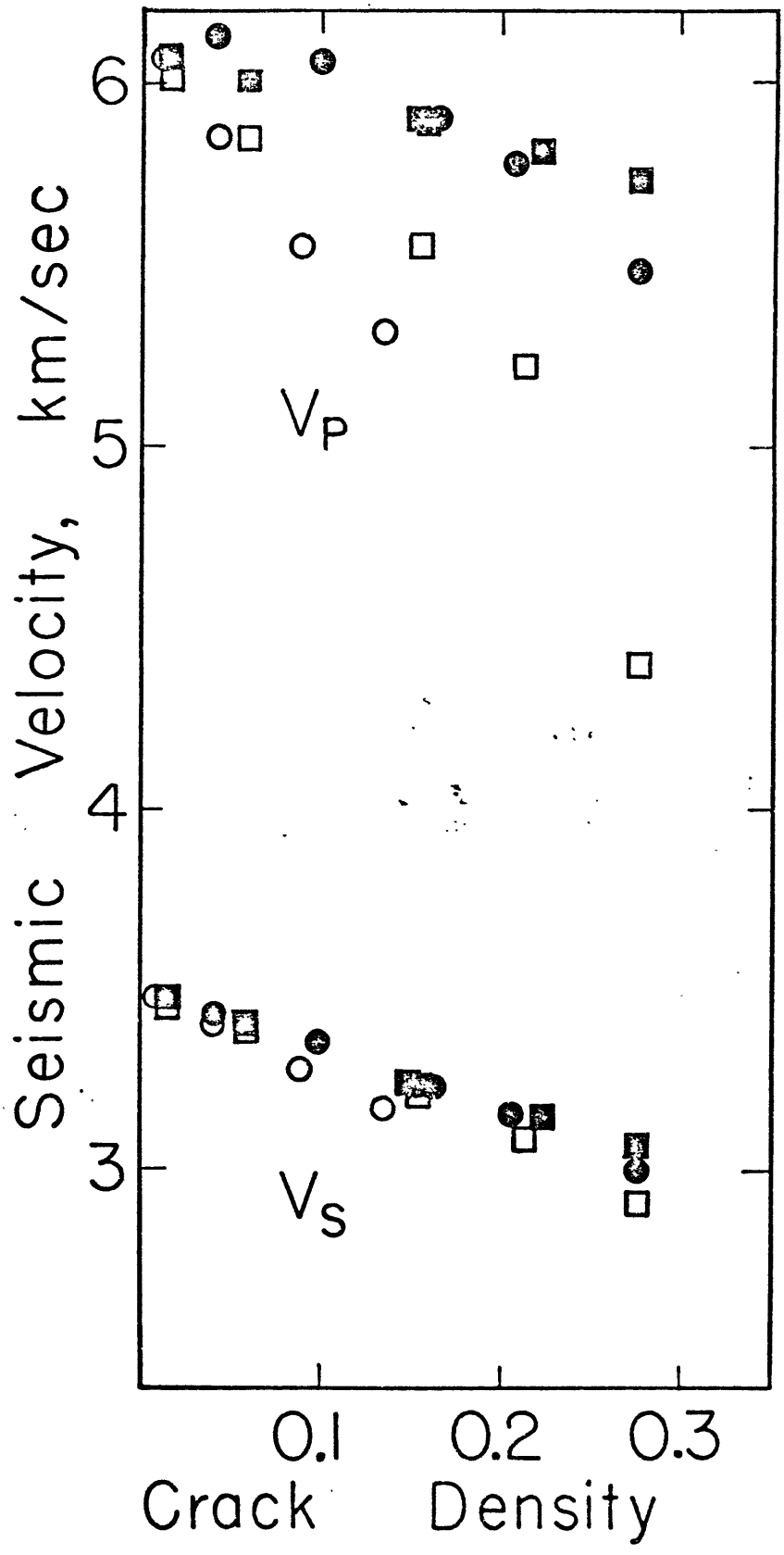
Seismic Velocity, km/sec
6
5
4
3
V_P
V_S
0.1
0.2
0.3
Crack Density

employed here (equation (2)).

In Figure 5-17 the self-consistent data of Figure 5-14 have been replotted making use of the simplified relationship

$$e = (3\Phi)/(4\pi\bar{\alpha}), \tag{8}$$

where $\bar{\alpha}$ is an average aspect ratio such that

$$(\bar{\alpha})^{-1} = \Phi^{-1} \frac{\phi_i}{\alpha_i}$$

In granite under stress, $\partial\bar{\alpha}/\partial\Phi$ is positive, i.e. the average aspect ratio increases with increasing porosity. This is in contrast to the hydrostatic behavior.

DISCUSSION

SEM observation of cracks and pores. In previous SEM observations of microcavities in Westerly Granite Sprunt and Brace (1974) and Brace et al., (1971) state that "the porosity, as observed directly with the SEM...is approximately in accord with the total porosity as measured by immersion, and crack porosity by elastic measurements under pressure...Westerly Granite as seen with the aid of the SEM has both abundant high and low aspect ratio cavities..." The quantitative results presented here suggest that much of the porosity -- more than half -- is not seen. Since the sample areas chosen for study were selected as being representative of all that were seen, it seems most probable that the cracks and pores were there but unresolvable owing to their small widths. Crack porosities

Figure 5-17a. Average aspect ratio vs. porosity in stressed and hydrostatically confined granite.

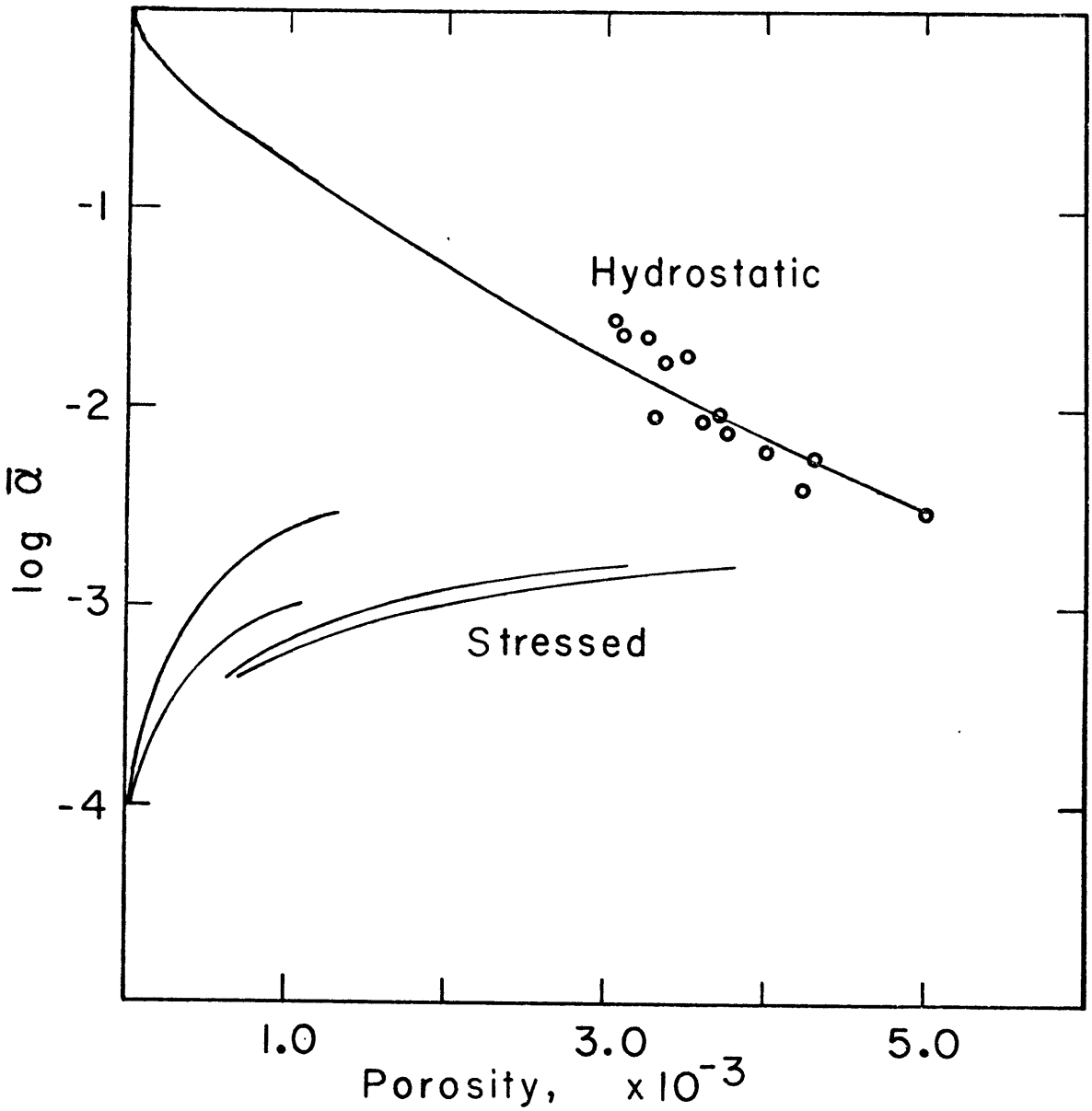
Hydrostatic
Stressed
log α
-1
-2
-3
-4
1.0
3.0
5.0
Porosity, x10⁻³

Figure 5-17b. Enlargement of stressed curves of Figure 5-17a with linear aspect ratio scale. Circles, shear wave polarization parallel to the maximum stress direction; x's, shear wave polarization perpendicular to the maximum stress direction.

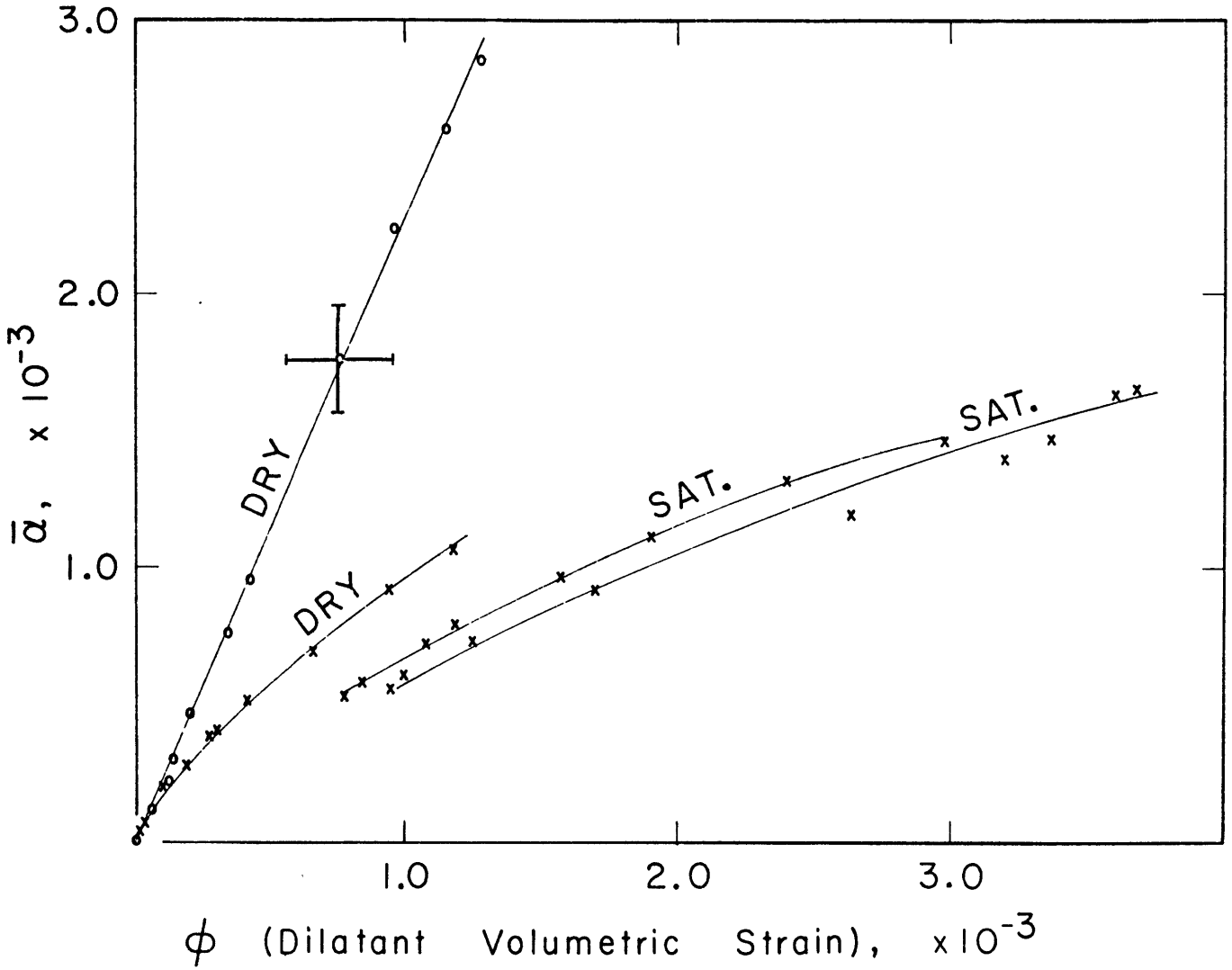
3.0
2.0
1.0
$\bar{\alpha}$, x 10^{-3}
DRY
DRY
SAT.
SAT.
1.0
2.0
3.0
ϕ (Dilatant Volumetric Strain), x 10^{-3}

are only slightly below previously reported values: $1.3 \pm 0.2 \times 10^{-3}$ as opposed to $2.0 \pm 0.5 \times 10^{-3}$ (Brace et al., 1965), but pore porosity, space caused by equant intragranular voids is here reported to be of the same order as crack porosity, $1.4 \pm 0.1 \times 10^{-3}$, whereas Brace et al., published $7 \pm 1 \times 10^{-3}$. In Chelmsford Granite Sprunt and Brace (1974) were able to account for the previously reported pore porosity using SEM observation, so how generally pore space may be overlooked with the SEM is not known. In granites pores seem to concentrate in the feldspars, and in Westerly Granite almost exclusively in the plagioclase. My sample T.5 had less than 5 percent plagioclase in the section and so was atypical of the bulk rock. But even multiplying the reported rock porosity by 10 (fictitiously raising the feldspar content to 30 percent) would still leave it an order of magnitude less than the previously reported value (Table 5-1).

The intragranular porosity of the most porous plagioclase in my micrographs varied from 0.8 to 1.3 percent. These numbers do not compare unfavorably with the most porous value of 1.8 percent reported by Montgomery and Brace (1975) for plagioclase in Westerly Granite. Of that porosity, one half to one third could be attributed to equant voids. If plagioclase makes up one third of the rock then the whole rock porosity should be at least 0.13 - 0.30 percent (including only equant voids) or 0.6 percent (including all intragranular cavities.) This

assumes that all the plagioclase is as porous as the most porous grains; in fact even contiguous highly porous grains may exhibit considerable variability. No attempt has as yet been made to identify the least porous plagioclase in granitic rocks. Thus, the true range of plagioclase porosities and the true contribution of plagioclase porosity to the whole rock porosity is not known. The location and size of the "missing" pores in my granite samples is also not known. It may be that the pores were there but unresolvable; it may be that the minerals scanned were atypically pore-free; or it may be that the missing porosity exists as a small number of rather large holes sparsely distributed in the rock.

It is difficult to compare the crack length and aspect ratio distributions reported here with those of Sprunt and Brace (1974). They chose a "random sample of 80 cavities" in their SEM micrographs whereas every crack and pore visible in the areas I selected for study has been included in the present compilations. One likely result of the previous technique is that pores will be overlooked in favor of cracks. This can be seen from both the aspect ratio and cavity length data in Table 5-5 where I give their results and mine, the latter normalized to sum to 80 (or 77 in one case). However, basic consistencies between the two sets of data are observed.

TABLE 5-5

COMPARISON OF THE PRESENT RESULTS WITH THOSE OF SPRUNT AND BRACE (1974)

Aspect Ratio

Division	Unstressed			Stressed				
	pores included	pores not included		pores included		pores not included		
	This study		Sprunt & Brace	This study				Sprunt & Brace
				T.5	W.5	T.5	W.5	
1.0-0.6	70	12	28	68	12	5	1	26
0.5-0.2	2	11	21	2	3	11	3	15
0.1-0.06	2	12	9	1	3	6	3	6
0.05-0.02	3	21	6	2	21	12	24	11
0.01-0.006	1	9	3	2	13	11	16	11
0.005-0.002	1	9	8	3	22	22	26	8
$0.001\text{-}6\times10^{-4}$	1	4	2	1	5	8	6	2
$\leq 5\times10^{-4}$	0	2	2	1	1	5	1	1

TABLE 5-5 (continued)

COMPARISON OF THE PRESENT RESULTS WITH THOSE OF SPRUNT AND BRACE (1974)

Cavity Length

Division µm	Unstressed			Stressed				
	pores included	pores not included		pores included		pores not included		
	This study		Sprunt & Brace	This study				Sprunt & Brace
				T.5	W.5	T.5	W.5	
≦1	-	24	22	57	1	1	0	14
1-5	-	25	14	10	22	2	16	17
5-10	-	10	27	3	18	16	20	20
10-50	-	11	5	8	17	49	19	11
50-100	-	3	6	1	19	9	22	12
100-500	-	5	3	1	3	3	3	5
500-1000	-	0	0	0	0	0	0	1

Firstly, we are dealing with the same general range of aspect ratios and cavity lengths. Seven percent of the cracks I observed in virgin Westerly Granite had lengths in excess of the maximum reported by Sprunt and Brace, 100 μm. All of the cracks I saw, however, were less than 275 μm long. The conclusion that crack lengths are substantially less than the grain size is thus supported by the present examination. Secondly, both studies show a shift toward longer cavities in the prestressed material. The shifts reported here are more pronounced. This could have resulted from the different experimental stress conditions; the samples used for this study were loaded to 60 percent of peak strength at 500 bars confining pressure (T.5) and to post-peak strength at 800 bars confining pressure (W.5) whereas the prestressed sample in the previous work was recovered intact after loading to more than 95 percent of the fracture strength at 1500 bars. However, most of the previous SEM work was done at 100x so that fine cracks may have been overlooked. Thirdly, both studies reveal a tendency toward lower aspect ratios in the prestressed material although again the trend is more pronounced in the present work.

It should be noted that despite the increase in the number of low aspect ratio cracks, the percentage of porosity attributable to low aspect ratio voids ($\alpha < 10^{-3}$) is about the same in the prestressed material as in the unstressed rock. In the sample loaded to 60 percent of peak strength there are only about 10 percent more cracks per unit area, M, than are observed in the virgin material but ϕ_A increases nearly 150

percent. In the sample loaded beyond peak strength however, M increases 100 percent while ϕ_A goes up by a factor of 5 (Table 5-1). Moreover, the cracks become much more highly oriented (Tables 5-2 and 5-3). These findings suggest that stress-induced porosity begins with the extension and widening of pre-existing cavities although substantial numbers of new cracks are created later in the failure process. The new cracks may account for the bulk of the stress induced porosity near peak strength. This is in agreement with earlier observations of Tapponnier (1974).

Hydrostatic velocity results. Comparison of measured seismic velocities with those computed from observed crack and pore porosities using the non-interactive model indicates that porosity has been greatly underestimated from my SEM sections. However, agreement of measured seismic velocities and theoretical values is good when my measured aspect ratio distributions are normalized with respect to previously reported crack porosity. This suggests that the aspect ratio distribution of these narrow voids is similar to the ones shown in Figures 5-6 and 5-7. Disagreement between measured and computed seismic velocities at low pressures may as likely result from the breakdown of the non-interactive approximation as from my failure to observe and include very low aspect ratio cavities. In fact, when the observed aspect ratio distributions including intragranular pores are normalized with respect to previously reported total porosity, calculated velocities are lower than observed values at low pressure and higher at high pressure.

Therefore, if the measured aspect ratio distributions are not representative, they err rather in underestimating the high aspect ratio than the low aspect ratio void fraction. This is in accord with earlier comparisons of the crack and pore porosities measured with the SEM and the values given by Brace et al., (1965).

A different story emerges if measured seismic velocities are compared with the results of the self-consistent analysis. Looking at Figures 5-11 and 5-12, the self-consistent results suggest that crack porosity is not underestimated at 0.13 percent. Except at the very lowest pressures where theory and experiment both are subject to considerable uncertainty, agreement between observed velocities and those calculated from the as observed crack porosities is better than the fit obtained by normalizing the crack porosity to sum to 0.20 percent. Pore porosity is presumably still underestimated though as the higher pressure portions of the experimental curves in Figures 5-11 and 5-12 were fit by neglecting equant void space entirely and taking 4 kbar values for the matrix moduli.

Is crack porosity underestimated then? Probably somewhat. From Figure 5-13 it is seen that crack densities are apparently different for dry and saturated rock as a function of (effective) confining pressure. This is a real flaw in the elastic crack closure model of Toksöz et al. Such a situation is physically unrealistic. However, the theory of O'Connell and Budiansky does not incorporate any assumptions about crack closure and

should therefore give the same $\epsilon(p)$ regardless of the degree of saturation of the material. The systematic differences in Figure 5-13 most probably occur because the conditions of saturation under which seismic velocities were measured in the laboratory were not as advertised. Dry rocks probably have residual water or machine oil in them which will result in variations in the local void saturation, while saturated rocks may have some residual air in them. This explanation is consistent with earlier findings of O'Connell and Budiansky (1974) although in the present case, owing to the formal independence of ϵ on the degree of saturation of the void space (equation (2)), an appeal must be made to local and persistent variation in fluid content within the test samples. Such small variations as would be necessary, 5 to 10 percent, seem highly plausible.

To within experimental error then, ϵ calculated from seismic velocities in dry and saturated rock matches that calculated from the normalized SEM aspect ratio distribution using elastic crack closure theory. This is a fundamental and important comparison. At the highest value of ϵ in the dry case where there is an extreme difference in moduli between the cracks and the intact rock, the self-consistent velocity theory may break down. Unfortunately, the velocity data used in determining the 1 bar dry rock crack density are subject to considerable uncertainty (compare Nur and Simmons's values with those cited by Press, 1966) so the validity of the theory has not truly been tested. Serious disagreement between actual

and calculated values of ϵ (or of velocity, in the direct problem) may not occur until around $\epsilon = 0.4$ as suggested by O'Connell and Budiansky (1974).

Non-hydrostatic results. The relationship of seismic velocities measured under triaxial stress to those computed from isotropic, hydrostatic theory is not clear as the effect of existing crack anisotropy cannot be separated from the effect of stress as opposed to pressure. If there were an anisotropic, hydrostatic theory then it would be possible to test the equivalence of stress increase with confining pressure decrease on a preferentially oriented array of cracks. Nevertheless, several points can be made using and concerning existing theories.

There is no agreement between calculated seismic velocities and those observed in stressed rock as a function of porosity. Measurement paths and polarization were chosen to yield the greatest change in velocity with porosity yet observed seismic velocities are generally less sensitive to stress-induced, oriented porosity than predicted from the isotropic, hydrostatic theory. While this could result from the neglect of crack interactions in the calculated values, crack aspect ratio distributions determined from sample W.5 yielded decreased sensitivity of calculated velocities (dashed lines, Figure 5-14). This sample was recovered post-failure and had a higher crack density and larger unconfined porosity than the other pre-stressed sample (solid lines, Figure 5-14). Thus, the failure of the hydrostatic, non-self-consistent theory to be able to

model velocities in rock under stress seems to arise rather because crack aspect ratios in stressed and unstressed rock are different functions of porosity.

Self-consistent and non-interactive theories predict the same relationship between crack density and seismic velocities for a given degree of water saturation. This is true for both stressed and hydrostatically loaded rocks.* If we then compare the behavior of average aspect ratio vs. porosity as predicted by self-consistent theory for hydrostatically loaded and stressed granite, the two are indeed quite different. Under hydrostatic loading the average aspect ratio increases with <u>decreasing</u> porosity approaching 1 at zero porosity, consistent with the idea of pore closure at a confining pressure of the order of αE (Walsh, 1965a), where E is Young's modulus of the matrix phase. In stressed rock, despite the obvious and fictitious dependence of ϵ on measurement path and shear wave polarization direction the average aspect ratio always increases with <u>increasing</u> porosity and generally at a decelerating rate. Such behavior was to be anticipated. Cracks which open under stress initially should

*This result was unexpected since the crack densities involved are as high as 0.4 for dry rock and 0.5 for water saturated material. However, the self-consistent formulation is a static calculation while the non-interactive model of Toksöz <u>et al</u>., is a dynamic one. This static-dynamic difference should offset the self-consistent-non-interactive aspects of the two theories (Warren and Trice, 1975).

widen as the load is increased more easily than they extend, but at some point cracks must propagate and link up if the sample is to fail. $d\bar{\alpha}/d\sigma$ should therefore be positive but decreasing. Since $d\Phi/d\sigma$ is positive in dilatant rock, for $d\bar{\alpha}/d\sigma$ to be positive requires $d\bar{\alpha}/d\Phi > 0$. Similarly for $d^2\bar{\alpha}/d\sigma^2$ to be negative, $d^2\bar{\alpha}/d\Phi^2$ must be negative, as observed.

It should be pointed out that different assumptions are involved in the stressed and hydrostatic cases. Stressed cracks are assumed to have zero porosity in the unloaded state. The stressed rock curves in Figure 5-14 therefore represent only the contribution to average aspect ratio and porosity made by cracks opening and extending under stress. In the hydrostatic case, the rock is assumed to have a finite porosity in the unconfined state, 0.2 percent.

CONCLUSIONS

I failed to detect more than half the pore space of Westerly Granite using SEM observation. It is not known whether that porosity was there but unresolvable, or whether the sections scanned were unusually pore-free. Aspect ratio distributions of observable cracks seem representative of those which were not seen, although the fraction of equant voids is seriously underestimated. Dilatant porosity near peak strength seems to be attributable mainly to the creation of new cracks although widening and extension of pre-existing cracks dominates in the early stages of dilatancy.

To describe hydrostatic velocity behavior in rocks such

as granite self-consistent theory is not needed. At very low confining pressures both self-consistent and non-interactive theories may be inadequate to describe velocity behavior while at pressures of 200 bars or more either theory will do. Inability of present theories to predict velocity changes in stressed rock results mainly from lack of knowledge of crack geometries under nonhydrostatic conditions. Static self-consistent and dynamic non-interactive models give the same results for velocities as a function of stressed rock crack densities.

Despite the obvious conflict in using isotropic theory to model a demonstrably anisotropic situation, average aspect ratios computed from self-consistent methods can be reasonably related to dilatant volumetric strain or differential stress provided the seismic velocities used in computation are measured along selected paths. Aspect ratios so determined increase with stress from zero at zero stress to 2 to 3 parts in 10^3 at about 80 percent of the intact rock fracture strength. This is in contrast to hydrostatic results in which average aspect ratio decreases from 1 at high pressure to a few parts in 10^3 in the unconfined state.

CONCLUSION

Suggestions for Future Work

From our present results, it could be concluded that stresses of the order of kilobars are required to produce dilatancy in the earth. But if faults in the earth move under low shear stresses, as is suggested by the heat flow data, then either the effective normal stress must be low or the fault zone weakened by gouge. If the first alternative is correct then the relevant behavior to assume for the in situ stress to cause dilatancy is that observed in low pressure laboratory experiments. Some low effective pressure stress cycling experiments under different conditions of confining and pore pressure would add credence to such an assumption. If the second alternative holds, we currently have no idea of the in situ stress required to produce dilatancy as we know almost nothing about the mechanical properties of gouges, clay or otherwise. Further work on the deformation behavior of gouges is important.

Crustal temperatures may reach 400°C or more, yet the effect of temperature on dilatancy is still largely unknown. In preliminary stress-strain investigations, granite at 2 kbar confining pressure and 400°C behaved similarly to granite under the same confining pressure at room temperature but more thorough experiments on this and other rock types should be performed. The strain rate sensitivity of dilatancy at different temperatures also deserves attention.

It may one day be possible to observe developing cracks in rocks under uniaxial stress with the scanning electron microscope. The interpretation of such observations may be open to some question due to the immediate proximity of the free surface. Nevertheless, the information obtained may be invaluable in constructing theories of crack formation and crack growth in dilatant materials. Without such theories, the *in situ* behavior of brittle rocks under stress and the reasons for any changes observed in their physical properties can at best be a matter for informed speculation.

Existing theories of the effect of dry or fluid filled cracks on seismic velocities can adequately explain present experimental observations, yet the question of what causes the precursory V_p/V_s anomalies has not been settled. Some further laboratory experiments on sedimentary rocks might be useful at this stage as clay reactions with water may dramatically lower seismic velocities and marbles, being more ductile under crustal conditions than the rocks I investigated, may behave somewhat differently. More importantly, however, we need to know more about the properties of rocks *in situ* in tectonic crustal regions. What is the predominant degree of saturation and what the average aspect ratio of the voids, joints as well as microcracks? What about the permeability? This information can only come from extensive field observations.

We have some uplift data that put severe constraints on the dilatancy model (Castle *et al.*, 1974). And now we have some experimental and theoretical results which suggest that

Pg 185 missing

the average aspect ratio of the in situ voids causing velocity anomalies has to be less than 10^{-5} and that these cracks, joints or fissures had better be dry or less than 60 percent saturated (O'Connell and Budiansky, 1974). Are they?

We may need to drill more than a few wells to satisfactorally answer this question, although a certain amount of information is available in the mining and tunnelling literature. There is also a large body of data on downhole oil and gas pressures and flow rates, most of it proprietary, which would provide information about variations in permeability and fluid pressure over time.

Drilling holes in the ground is a rather expensive proposition, but some information doesn't come cheap. We have constrained the dilatancy model well enough to go into the field looking for two numerical quantities. If these check out, then the dilatancy model as we understand it checks out; if they don't, then it doesn't. At this time there seems to be no point in performing vast series of relatively inexpensive laboratory experiments, refining our knowledge of seismic velocity changes in stressed rock to the third or fourth decimal place until we know for sure that the process we are investigating is applicable in the earth. For a little more money, we can find that out.

APPENDIX

The effect of gauge length on measured strain has been determined by computer calculation. Four strain gauges of initial length s are mounted at angles $(\psi_2 - \psi_1)/2$ around an initially circular cylinder of radius R_o. The circular cross-section is then given a specified elliptical deformation with a being the resultant semi-minor axis length, oriented along $\psi = 0$, and b being the semi-major axis length. Using elliptical integrals, the strained length, s', of each gauge is computed from

$$s' = \int_{\psi_1'}^{\psi_2'} (a^2\sin^2\theta + b^2\cos^2\theta)^{-1/2} d\theta \qquad \text{(i)}$$

and the ψ_i' are determined from the ε_{12} in the direction of the initial (unstrained) ψ_i. The strain recorded by the gauge is then

$$\frac{s' - s}{s} \qquad \text{(ii)}$$

These strains are used to calculate the strain ellipse and the measured ε_θ compared with the specified ones. Results are given in Figures A and B for various values of s/R_o. The geometry used in our experiments gives $s/R_o = 0.8$. The apparent orientation of the observed strain ellipse for $s/R_o = 0.8$ lies in all cases within 0.1° of actual. Since, in the actual laboratory specimen, the strain gauge midpoints can only be oriented to within $\pm 10^\circ$ of the fault trace, the misorientation of the circumferential strain ellipse due to a finite strain gauge length is insignificant.

Figure A. Comparison of semi-minor (A) and semi-major (B) axes of observed and true strain ellipses as a function of original strain gauge length to sample radius ratio. B/B_{true}: Lower boundary of region is for 0.036 percent strain, upper for 0.36 percent strain. A/A_{true}: Upper boundary of region is for 0.036 percent strain, lower boundary is for 0.36 percent strain.

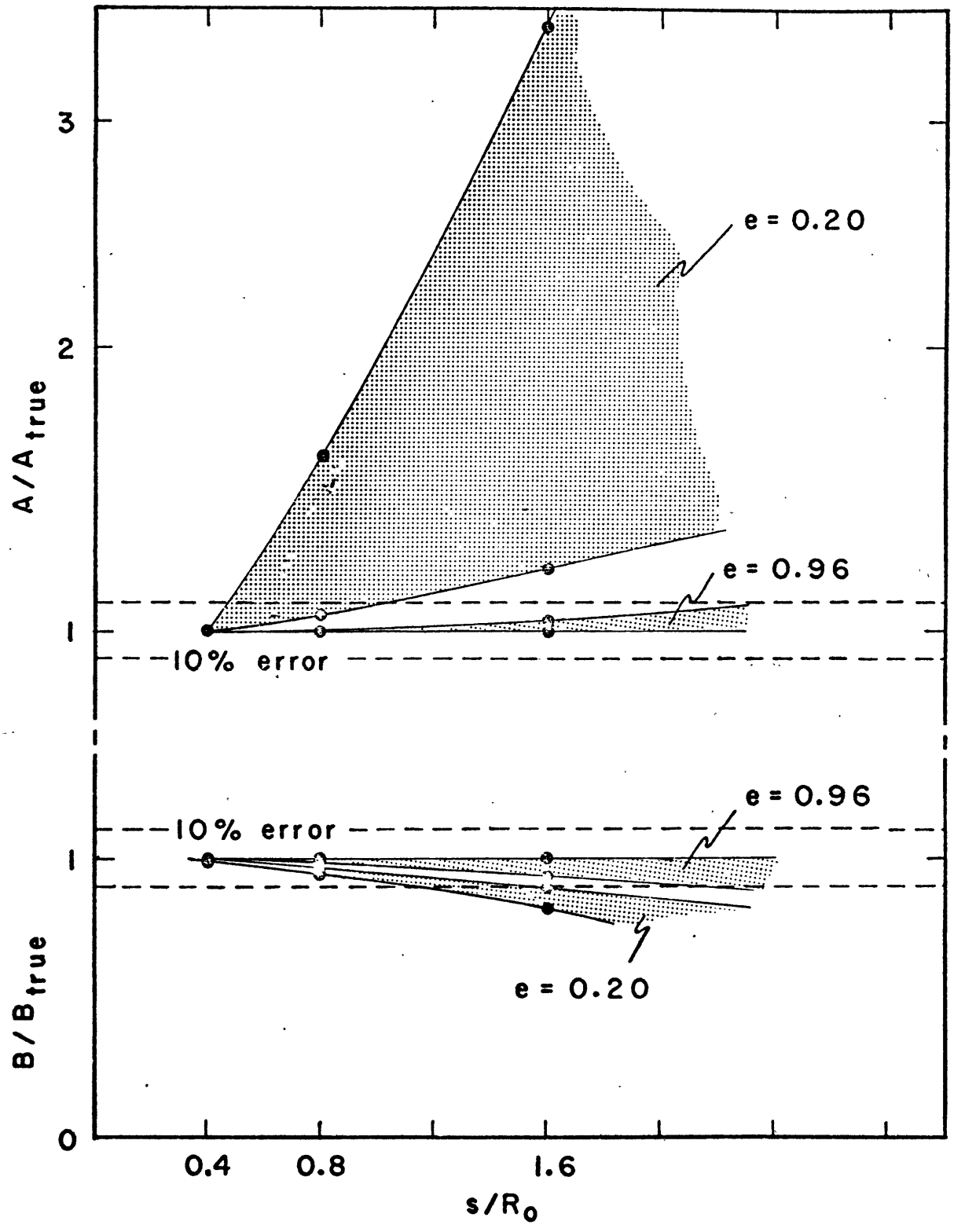
3
2
1
A/A true
e = 0.20
e = 0.96
10% error
10% error
e = 0.96
1
B/B true
e = 0.20
0
0.4
0.8
1.6
s/R0

Figure B. Comparison of actual and observed strain anisotropy, $(\varepsilon_{max} - \varepsilon_{min})/\varepsilon_{min}$, as a function of initial strain gauge length to sample radius ratio.

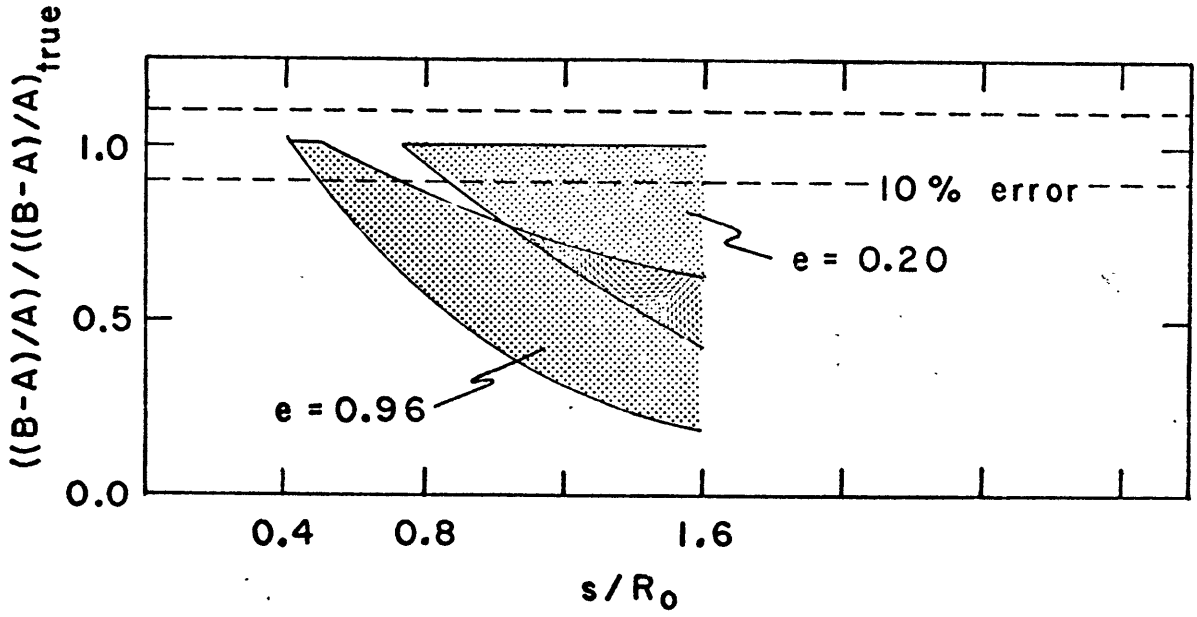
((B-A)/A) / ((B-A)/A)true
1.0
0.5
0.0
10 % error
e = 0.20
e = 0.96
0.4
0.8
1.6
s/R0

ACKNOWLEDGMENTS

To the U.S. Geological Survey for supporting this work under contract numbers 14-08-0001-13229 and 14-08-0001-14551, to the Army Research Office for supporting this work under contract number PNDGDAHC04-73-C-001 and to the National Science Foundation for supporting me.

To W.F. Brace, my advisor, for his patient assistance in all phases of the thesis from experimental design to grammatical construction.

To Gordon Marlatt for inspiring me to attempt a dissertation in the first place and to my grandparents Hadley who made the attempt possible.

To C.B. Raleigh and Barclay Kamb, whose continued interest brought me through the dark times, and to the Meadows for their refuge at Cedarholm.

C. Goetze, T.R. Madden and C.H. "Arthur" Cheng made helpful suggestions in technique and interpretation. P. Tapponnier, C.H. Scholz and Y.P. Aggarwal assisted in some of the work. Discussions with all of the above and R.J. O'Connell, B. Budiansky, A. Nur, B. Bonner, J.D. Byerlee, M. Zoback, R. Stesky and M. Wyss contributed immensely to the finished product.

REFERENCES

Aggarwal, Y.P., L.R. Sykes, D.W. Simpson and P.G. Richards (1975). Spatial and temporal variations in t_s/t_p and in p-wave residuals at Blue Mountain Lake, New York: Application to earthquake prediction., J. Geophys. Res., 80, 718-732.

Anderson, D.L. and J.H. Whitcomb (1973). The dilatancy-diffusion model of earthquake prediction, in Proc. Conf. Tectonic Problems of the San Andreas Fault System, R.L. Kovack and A. Nur, eds., Stanford University Press, Stanford, CA, 417-426.

Anderson, D.L. and J.H. Whitcomb (1975). Time dependent seismology, J. Geophys. Res., 80, 1497-1503.

Anderson, D.L., B. Minster and D. Cole (1974). The effect of oriented cracks on seismic velocities, J. Geophys. Res., 79, 4011-4015.

Baehr, H.D. and K. Schwier (1961). Die Thermodynamischen Eigenschaften der Luft, Springer-Verlag, Berlin. 136 pp.

Beaumont, C. and J. Berger (1975). Earthquake prediction: Modification of the earth tide tilts and strains by dilatancy, preprint.

Birch, F. (1960). The velocity of compressional waves in rocks to 10 kbar, Part I, J. Geophys. Res., 65, 1083-1102.

Birch, F. (1961). The velocity of compressional waves in rocks to 10 kilobars, Part II, J. Geophys Res., 66, 2199-2224.

Birch, F. (1966). Compressibility; elastic constants, in Handbook of Physical Constants, S.P. Clark, ed. Geol. Soc. Am., Mem. 97, 97-176.

Bonner, B. (1974). Shear wave birefringence in dilating granite, Geophys. Res. Lett., 1, 217-220.

Bonner, B. (1975). V_p/V_s in saturated granodiorite loaded to failure, Pageoph, in press.

Brace, W.F. (1964). Effect of pressure on electric-resistance strain gages, Exp. Mechanics, 4 (37), 212-216.

Brace, W.F. (1965). Some new measurements of linear compressibility of rocks, J. Geophys. Res., 70, 391-398.

Brace (1973). Personal communication.

Brace, W.F. (1975). Dilatancy-related electrical resistivity changes in rocks, Pageoph, in press.

Brace, W.F. and R.J. Martin III (1968). A test of the law of effective stress for crystalline rocks of low porosity, Int. J. Rock Mech. Min. Sci., 5, 415-426.

Brace, W.F. and A.S. Orange (1968). Further studies of the effects of pressure on electrical resistivity of rocks, J. Geophys. Res, 73, 5407-5420.

Brace, W.F. and R.M. Stesky (1973). Time dependence of frictional sliding in gabbro at high temperature and pressure, E⊕S, Trans. A.G.U., 54, 466.

Brace, W.F., A.S. Orange and T.R. Madden (1965). The effect of pressure on the electrical resistivity of water-saturated crystalline rocks, J. Geophys. Res., 70, 5669-5678.

Brace, W.F., B.W. Paulding, Jr. and C. Scholz (1966). Dilatancy in the fracture of crystalline rocks, J. Geophys. Res., 71, 3939-3953.

Brace, W.F., J.B. Walsh and W.T. Frangos (1968). Permeability of granite under high pressure, J. Geophys. Res., 73, 2225-2236.

Brace, W.F., E. Silver, K. Hadley and C. Goetze (1972). Cracks and pores: a closer look, Science, 178, 162-164.

Brady, B.T. (1975). Theory of earthquakes, Part I: A scale independent theory of rock failure, Pageoph, 112, 701-725.

Brune, J.N., T.L. Henyey and R.F. Roy (1969). Heat flow, stress, and rate of slip along the San Andreas Fault, California, J. Geophys. Res., 74, 3821-3827.

Budiansky, B. and R.J. O'Connell (1975). Elastic moduli of a cracked solid, preprint.

Byerlee, J.D. (1966). The frictional characteristics of Westerly Granite, PhD. Thesis, M.I.T.

Byerlee, J.D. (1967). Frictional characteristics of granite under high confining pressure, J. Geophys. Res., 72, 3639-3648.

Byerlee, J.D. (1973). Personal communication.

Byerlee, J.D. and R. Summers (1975). The effect of fault gauge on fault stability, Int. J. Rock. Mech. Min. Sci., in press.

Carslaw, H.S. and J.C. Jaeger (1959). Conduction of heat in solids, 2nd ed., Oxford Univ. Press, Oxford, 510 pp.

Castle, R.L., J.N. Alt, J.C. Savage and E.I. Balazs (1974). Elevation changes preceding the San Fernando earthquake of February 9, 1971, Geology, 2, 61-66.

Crouch, S.L. (1970). Experimental determination of volumetric strains in failed rock, Int. J. Rock Mech. Min. Sci., 7, 589-603.

DeFazio, T.L., K. Aki and J. Alba (1973). Solid earth tide and observed change in the in situ seismic velocity, J. Geophys. Res., 78, 1319-1322.

England, A.H., and A.E. Green (1963). Some two-dimensional punch and crack problems in classical elasticity, Proc. Camb. Phil. Soc., 59, 489-500.

Garbin, H.D., and L. Knopoff (1973). The compressional modulus of a material permeated by a random distribution of circular cracks, Quart. Appl. Math., 30, 453-464.

Garbin, H.D. and L. Knopoff (1975). The shear modulus of a material permeated by a random distribution of free circular cracks, preprint.

Garbin, H.D., and L. Knopoff (1975b). Elastic moduli of a medium with liquid-filled cracks, preprint.

Goodman, R.E. and J. DuBois (1972). Duplication of dilatant behavior in the analysis of jointed rocks, Technical Report #11, Contract DACA45-70-C-0088, U. Cal., Berkeley.

Griggs, D.T., D.D. Jackson, L. Knopoff and R.L. Shreve (1975). Earthquake prediction: modeling the anomalous V_p/V_s source region, Science, 187, 537-540.

Gupta, I.N. (1973a). Seismic velocities in rock subjected to axial loading up to shear fracture, J. Geophys. Res., 78, 6936-6942.

Gupta, I.N. (1973b). Premonitory variations in S-wave velocity anisotropy before earthquakes in Nevada, Science, 182, 1123-1129, 1973.

Hadley, K. (1973). Laboratory investigation of dilatancy and motion on fault surfaces at low confining pressures in Proc. Conf. Tectonic Problems of the San Andreas Fault System, R.L. Kovach and A. Nur eds., Stanford Univ. Press, Stanford, CA, 427-435.

Hadley, K. (1975). V_p/V_s variations in dilatant rocks, Pageoph, in press.

Haimson, B.C. (1974). Mechanical behavior of rock under cyclic loading, Proc. Third Internat Cong., Vol. 2, Part A, Internat. Soc. Rock Mech., in press.

Handin, J. (1973). Mechanical properties of rocks affecting earthquake generation, Semi-annual Progress Report No. 2, Parts I and II, Contract No. 14-08-0001-12723, Texas A&M Research Foundation, College Station.

Hanks, T.C. (1974). Constraints on the dilatancy diffusion model of the earthquake mechanism, J. Geophys. Res., 79, 3023-3025.

Hearmon, R.F.S. (1961). Applied anisotropic elasticity, Oxford Univ. Press, London, 136 pp.

Henyey, T.L. and G.J. Wasserberg (1971). Heat flow near major strike-slip faults in California, J. Geophys. Res., 76, 7924-7946.

Hill, R.J. (1952). The elastic behavior of a crystalline aggregate, Proc. Phys Soc. London, Ser. A, 65, 349-354.

Hill, R.J. (1963). Elastic properties of reinforced solids: some theoretical principles, J. Mech. Phys. Solids, 11, 357-372.

Jaeger, J.C. (1959). The frictional properties of joints in rock, Geofis. Pura Appl., 43, 148-158.

Jaeger, J.C. (1971). Friction of rocks and stability of rock slopes, Geotechnique, 21 (2), 97-134.

Kennedy, G.C. and W.T. Holser (1966). Pressure-volume-temperature and phase relations of water and carbon dioxide, in Handbook of Physical Constants, S.P. Clark, ed., Geol. Soc. Am Mem. 97, 317-384.

Koiter, W.T. (1961). An infinite row of parallel cracks in an infinite elastic sheet, in Problems of Continuum Mechanics, M.A. Lavrent'ev, ed., Soc. Industr. Appl. Math., Philadelphia, 246-259.

Kuster, G.T. (1972). Seismic wave propagation in two-phase media and its application to the earth's interior, Ph.D. Thesis, M.I.T., Cambridge.

Kuster, G.T. and M.N. Toksöz (1974). Velocity and attenuation of seismic waves in two-phase media: Part I, theoretical formulations, Geophysics, 39, 587-606.

Lachenbruch, A.H. and J.H. Sass (1973). Thermo-mechanical aspects of the San Andreas Fault system, Proc. Conf. Tectonic Problems of the San Andreas Fault System, R.L. Kovach and A. Nur, eds., Stanford Univ. Press, Stanford, CA, 192-205.

Martin, R.J. III (1972). Time-dependent crack growth in quartz and its application to the creep of rocks, J. Geophys. Res., 77, 1406-1419.

Matsushima, S. (1960a). Variation of the elastic wave velocities of rocks in the process of deformation and fracture under high pressure, Disaster Prevention Res. Inst., Kyoto Univ., Bull., 32, 1-8.

Matsushima, S. (1960b). On the deformation and fracture of granite under high confining pressure, Disaster Prevention Res. Inst., Kyoto Univ., Bull., 32, 11-20

Mjachkin, V.I., W.F. Brace, G.A. Sobolev and J.H. Dieterich (1975). Two models for earthquake forerunners, Pageoph, in press.

Mogi, K. (1966). Some precise measurements of fracture strength of rocks under uniform compressive stress, Rock Mech. Eng. Geol., 4 (1), 41-55.

Mogi, K. (1968). Source locations of elastic shocks in the fracturing process in rocks (1), Bull. Earthquake Res. Inst., Univ. Tokoyo, 46, 1103-1125.

Nersesov, I.L., A.N. Semenov and I.G. Simbireva (1969). Space-time distribution of the travel time ratios of transverse and longitudinal waves in the Garm area, in The Physical Basis of Foreshocks, Nauka Publ., Moscow.

Nur, A. (1971). The effect of stress on velocity anisotropy in rocks with cracks, J. Geophys. Res., 76, 2022-2034.

Nur, A. (1972). Dilatancy, pore fluids and premonitory variations of t_s/t_p travel times, Bull. Seismol. Soc. Am., 62, 1217-1222.

Nur, A. and G. Simmons (1969a). Stress-induced velocity anisotropy in rock: an experimental study. J. Geophys. Res., 74, 6667-6674.

Nur, A. and G. Simmons (1969b). The effect of saturation on velocity in low porosity rocks, Earth Plan. Sci. Lett., 7, 183-193.

Nur, A., M.L. Bell, and P. Talwani (1973). Fluid flow and faulting, 1: a detailed study of the dilatancy mechanism and premonitory velocity changes, in Proc. Conf. Tectonic Problems of the San Andreas Fault System, R.L. Kovach and A. Nur, eds., Stanford Univ. Press, Stanford, CA, 391-404.

Nye, J.F. (1957). Physical Properties of Crystals, Oxford Univ. Press, Oxford, 322 pp., esp. 158-168.

O'Connell, R.J. and B. Budiansky (1974). Seismic velocities in dry and saturated cracked solids, J. Geophys. Res., 79, 5412-5426.

Press, F. (1966). Seismic velocities, in Handbook of Physical Constants, S.P. Clark, ed., Geol. Soc. Am., Mem. 97, 197-218.

Reasenberg, P. and K. Aki (1974). A precise, continuous measurement of seismic velocity for monitoring in situ stress, J. Geophys. Res., 79, 399-406.

Reuss, A. (1929). Berechuung die Fließgrenze von Mischkristallen auf Grund der Plastizitatsbedingung für Einkristallen, Z. Angew. Math. Mech., 9, 49-58.

Scholz, C.H. (1968a). Microfracturing and the inelastic deformation of rock in compression, J. Geophys. Res., 73, 1417-1432.

Scholz, C.H. (1968b). Experimental study of the fracturing process in brittle rock, J. Geophys. Res., 73, 1447-1454.

Scholz, C.H. and R. Kranz (1974). Notes on dilatancy recovery, J. Geophys. Res., 79, 2132-2135.

Scholz, C.H., L.R. Sykes and Y.P. Aggarwal (1973). Earthquake prediction: a physical basis, Science, 181, 803-810.

Semenov, A.N. (1969). Variations in the travel time of transverse and longitudinal waves before violent earthquakes, Izv. Phys. Solid Earth, 3, 245-248.

Simmons, G. and H. Wang (1971). Single crystal elastic constants and calculated aggregate properties, M.I.T. Press, Cambridge, 370 pp.

Sprunt, E. and W.F. Brace (1974). Direct observation of microcavities in crystalline rocks, Int. J. Rock Mech. Min. Sci, 11, 139-150.

Stesky, R.M. Frictional strength of faults in granite and gabbro at high temperature and pressure, E⊕S, Trans Am. Geophys. Union, 54, 465.

Stesky, R.M., W.F. Brace, D.K. Riley and P.-Y.F. Robin (1974). Friction in faulted rock at high temperature and pressure, Tectonophys., 23, 117-203.

Stuart, W. and J. Dieterich (1975). Continuum theory of rock dilatancy, in Advances in Rock Mechanics, Proc. 3rd Congress of Internat. Soc. for Rock Mechanics, Vol. 2, Part A, Denver, in press.

Tapponnier, P. (1974). A closer look at dilatant microcracks, E⊕S, Trans. Am. Geophys. Union, 56, 1196.

Thill, R.E. Acoustic methods for monitoring failure in rock, in Proc. of 14th Symposium on Rock Mech., H.R. Hardy, Jr. and R. Stefanko, eds., Am. Soc. Civil Eng., New York. 649-487.

Tocher, D. (1957). Anisotropy in rocks under simple compression, Am. Geophys. Union Trans., 38, 89-94.

Toksöz, M.N., C.H. Cheng and A. Timur (1975). Velocities of seismic waves in dry, saturated and frozen rocks, preliminary draft.

Voigt, W. (1910). Lehrbuch der Kristallphysik, Teubner, Berlin. 1004 pp.

Walsh, J.B. (1965a). The effect of cracks on the compressibility of rocks, J. Geophys. Res., 70, 381-389.

Walsh, J.B. (1965b). The effect of cracks on the uniaxial compression of rocks, J. Geophys. Res., 70, 399-411.

Walsh, J.B. (1965c). The effect of cracks on Poisson's ratio, J. Geophys. Res., 70, 5249-5257.

Walsh, J.B. (1968). Attenuation in partially melted material, J. Geophys. Res., 73, 2209-2216.

Walsh, J.B. (1969). New analysis of attenuation in partially melted rocks, J. Geophys. Res., 74, 4333-4337.

Warren, N. and R. Trice (1975). Correlation of elastic moduli systematics with texture in lunar metarials, preliminary draft.

Washburn, E.W., ed., (1929). International Critical Tables: Vol V., McGraw-Hill, N.Y., for the National Research Council.

Wawersik, W.R. and W.F. Brace (1971). Post-failure behavior of a granite and diabase, Rock Mech., 3, 61-85.

Whitcomb, J.H., J.E. Garmany and D.L Anderson. Earthquake prediction: variation of seismic velocities before the San Fernando earthquake, Science, 180, 632-635.

Wu, F.T., L. Blatter and H. Robertson (1975). Clay gauges in the San Andreas Fault system and their possible implications, preprint.

Zoback, M. and J.D. Byerlee (1975). The effect of cyclic differential stress on dilatancy in Westerly Granite under uniaxial and triaxial conditions., J. Geophys. Res., 80, 1526-1530.

Zoback, M. (1975). Personal communication.